AURORAL DATA ANALYSIS

J. David Winningham

Gordon G. Shepherd

The University of Texas at Dallas
P. O. Box 688
Richardson, Texas 75080

Final Report for Period 1 August 1975 - 31 January 1979

31 January 1979

Approved for public release; distribution unlimited

Prepared for

AIR FORCE GEOPHYSICS LABORATORIES
AIR FORCE SYSTEMS COMMAND
UNITED STATES AIR FORCE
HANSCOM AFB, MASSACHUSETTS 07131

79

SECURITY CLASSIFICATION OF THIS PAGE *(When Data Entered)*

REPORT DOCUMENTATION PAGE

READ INSTRUCTIONS BEFORE COMPLETING FORM

1. REPORT NUMBER: AFGL-TR-79-0071	2. GOVT ACCESSION NO.
3. RECIPIENT'S CATALOG NUMBER	
4. TITLE *(and Subtitle)*: Auroral Data Analysis	5. TYPE OF REPORT & PERIOD COVERED: Final Report 1 Aug 1975-31 January 1979
6. PERFORMING ORG. REPORT NUMBER	
7. AUTHOR(s): J. David Winningham, Gordon G. Shepherd *	8. CONTRACT OR GRANT NUMBER(s): F19628-76-C-0005
9. PERFORMING ORGANIZATION NAME AND ADDRESS: The University of Texas at Dallas, P. O. Box 688, Richardson, Texas 75080	10. PROGRAM ELEMENT, PROJECT, TASK AREA & WORK UNIT NUMBERS: 62101F, 7663 08AC
11. CONTROLLING OFFICE NAME AND ADDRESS: Air Force Geophysics Laboratory, Hanscom AFB, Massachusetts 01731, Captain Edward J. Weber/PHI/Monitor	12. REPORT DATE: March 26, 1979
	13. NUMBER OF PAGES: 148
14. MONITORING AGENCY NAME & ADDRESS *(if different from Controlling Office)*	15. SECURITY CLASS. *(of this report)*: Unclassified
	15a. DECLASSIFICATION/DOWNGRADING SCHEDULE

16 DISTRIBUTION STATEMENT *(of this Report)*

Approved for public release; distribution unlimited.

17. DISTRIBUTION STATEMENT *(of the abstract entered in Block 20, if different from Report)*

18. SUPPLEMENTARY NOTES

* York University, 4700 Keele St. Downsview, Ontario, Canada

19 KEY WORDS *(Continue on reverse side if necessary and identify by block number)*

AURORAL PARTICLES, MAGNETOSPHERE - IONOSPHERE INTERACTIONS

20 ABSTRACT *(Continue on reverse side if necessary and identify by block number)*

Based on the ISIS-1 and 2 data set it has been possible to meet the goals set forth in this contract. The particle-optical empirical relationships derived can be used to relate 6300A emissions to low-energy (< 300 eV) fluxes in a quantitative way and vice-versa. If suitable ionization production models were available, then < 300 eV energy fluxes 'images' derived from concurrent 6300A images, could be utilized to predict F-region behavior. One possible result would be the derivation of an estimate of FoF_2 during darkened conditions. This result along with the local time position of the trough would allow an estimate

DD FORM 1 JAN 73 1473/1 EDITION OF 1 NOV 65 IS OBSOLETE

SECURITY CLASSIFICATION OF THIS PAGE *(When Data Entered)*

of the severity of scattering from the steep poleward wall of the trough and the fluctuations embedded in it. Knowledge of the IMF B_z component in near real-time would allow a dynamic 'prediction' of the trough wall. Such a prediction could be used to allow reconfiguration of systems affected by the trough wall and fluctuations at or near it.

It is recommended that

1. Verification tests of the derivation of < 300 eV electron fluxes based on 6300A images should be undertaken. This could be achieved with either existing or new data sets.

2. Model calculations of ionospheric parameters based on particle and optical data should be undertaken. The results should be compared with concurrently obtained ionospheric data. If positive the results of such calculations could be used to predict ionospheric parameters based on satellite images. This technique would be extremely powerful if high-altitude 6300A cinematography were available. A first attempt at this could be made with results from the NASA Dynamics Explorer A & B particle and cinematography data.

3. Verification tests of the accuracy of trough wall prediction based on IMF B_z data and the empirical relations derived in the work should be undertaken. Such verification tests would probably lead to further refinements of the 'predicative' formulas. If proved reasonably accurate these empirical predictions could form the basis for operational decisions for systems affected by the physics occurring at the trough wall.

4. If the results derived under this contract are proven to be 'reliable' and the derivable results relevant to Air Force needs then high-altitude (> $2R_E$) satellite imaging should be considered as a test mission. Such a test could be used to define the operational utility of a real-time, fine time scale (< 10 min) monitoring of auroral emissions.

TABLE OF CONTENTS

I.	Introduction	1
II.	6300 A - Electron Flux Empirical Relation	
	A. Introduction	2
	B. Data	4
	C. The Analysis Approach	10
	D. Results	17
	E. Estimation of energy fluxes from optical emissions	20
	F. Discussion and Conclusions	21
III.	Comparison of Particle, Optical, and Electron Density Data	23
IV.	Dynamical Effects	25
V.	Summary and Conclusions	28
VI.	Recommendations	29
VII.	Published Papers	31
VIII.	Papers in Press	140
IX.	Oral Presentations at Meetings	143
X.	References	145
	Personnel	147

I. Introduction

Research performed during the period of this contract represents a continuation of work begun under AFGL contracts F19628-72-C-0230 and F19628-75-C-0032. Technical reports AFCRL-TR-74-0379 and TR-75-0404 should be consulted as background references.

The objectives of this contract are: (1) to relate the 6300A emissions as observed by the ISIS-2 scanning photometer to the causative electron fluxes which are simultaneously observed by the ISIS-2 Soft Particle Spectrometer. The energy sub-region of the electron flux which is primarily responsible for the 6300A emissions will be delineated to the accuracy available with the ISIS-2 instrumentation. It is hoped that an empirical relation can be derived that relates electron energy flux to 6300A flux. (2) To compare the particle fluxes and 6300A emissions (and the conclusions derived in Item 1) with simultaneous electron density profiles obtained by the ISIS-2 topside sounder. The basic goal of such a comparison will be to ascertain if it is possible to infer gross characteristics of the ionosphere (e.g. f_0F_2, plasma trough boundaries) from 6300A and particle flux measurements. (3) To relate, where possible, the results obtained in Items 1 and 2 to the dynamical effects produced by substorms. Specifically we will evaluate if it is possible to infer the motion of boundaries such as the poleward edge of the low-altitude plasma trough from indirect measurements. (4) To analyze the simultaneous data obtained with ISIS-2, the AFGL Airborne Ionospheric Laboratory, and the Defense Meteorological Satellite System. Again the

goal will be to ascertain if ionospheric parameters can be determined by indirect means. In the following sections it will be shown how each of these goals were accomplished.

Copies of the nine papers published with the support of this contract are enclosed in Section VII. In addition two papers are in press but are not included as part of this report. They will be sent to AFGL upon receipt of the reprints. The reader will be referred to the published papers for detailed information during the course of this report.

II. 6300A - Electron Flux Empirical Relation.

A. Introduction:

Considerable attention has been given to the calculation of optical auroral emissions from a knowledge of the primary electron spectrum, and reasonable success seemed to have been obtained for the major emissions (Rees and Luckey, 1974). However, at that time adequate experiments to test the validity of the calculations had not been done. A coordinated experiment with this objective was conducted by Rees et al. (1977) and they obtained from satellite measured primary spectra reasonable agreement for the 3914 A N_2^+ emission, excellent agreement for the 6300 A atomic oxygen emission, and poorer agreement for the 5577 A atomic oxygen emission. In a subsequent analysis of the same experiment, but using the secondary electron spectrum measured on the rocket, Sharp et al. (1979) found the calculated 6300 A emission an order of magnitude too low, and concluded that the excitation mechanism for the 6300 A emission was unknown. Still more recently, Rusch et al. (1979) proposed that energy

transfer from $N(^2D)$ to O_2 would produce enough $O(^1D)$ to explain the results. If the above were confirmed, the puzzle would be solved, but at the present time one cannot confirm that the 6300 A excitation processes are fully understood.

The difficulties with the 5577 A emission have extended over a longer period of time, beginning with the rocket measurements of Donahue et al. (1968). Ten years later, Deans and Shepherd (1978) made rocket measurements that were nearly self-consistent, using energy transfer from $N_2(A^3\Sigma_u^+)$ to $O(^3P)$ as the major source (in contrast Rees et al. (1977) found it unnecessary to use this reaction). Solheim and Llewellyn (1978) and Yau and Shepherd (1978) have proposed energy transfer from $O_2(A^3\Sigma_u^+, C^3\Delta_u$, or $c^1\Sigma_u^-)$ as an important mechanism, with the former authors considering it to be the dominant mechanism, with $O_2(c^1\Sigma_u^-)$ the only important agent. So the 5577 A puzzle may also be solved, though it is probably too early to be sure of that as well.

An interesting aspect of the puzzle is that the older Rees and Luckey (1974) formulation seems to give the correct I(6300)/I(5577) intensity ratio. This point has been discussed by Arnoldy and Lewis (1977), and examples of situations where it seems to work are given by M. M. Shepherd and Eather (1976) and by McEwen and Bryant (1978). The use of ISIS-2 satellite maps of these emissions (Shepherd et al. 1973) in morphological interpretation requires some procedure for converting optical emissions to particle fluxes. Auroral spectroscopists have long known that this was possible in principle, but the difficulties with the mechanisms described

seemed to preclude a satisfactory quantitative formulation. In view of these theoretical difficulties it was decided to make an empirical determination, using the optical and particle detectors on the same spacecraft. This has the practical advantage that any calibration or like factors are self-consistent from the parameter determination to the morphological interpretative analyses. (The accuracy of the particle flux determination will still be dependent on the precision of the particle spectrometer calibration). The Rees et al. (1977) and Sharp et al. (1979) studies when taken together raise the very important question as to whether the primary electrons observed by a higher altitude satellite do in fact produce secondary electrons measured at lower altitudes by a rocket through simple ionization and energy degradation processes or whether some other acceleration or plasma instability processes are at work. If the latter is true, then the ISIS results derived here may be at variance with those of other experiments, especially rockets, and may not apply in all situations, nor may they agree with theoretical calculations. Nevertheless, such comparisons are important for this very reason, and may serve as a guide to further work. However the prime motivation for this work is the establishment of an empirical procedure that will work for satellite data analysis.

B. Data:

Figure 1 shows an example of what might be considered raw optical data. The intensity of the 6300 A emission is shown on a linear scale, plotted versus Universal Time (UT). The spacecraft was in a cartwheel mode for these data, so that the perpendicular viewing photometer (Shepherd et

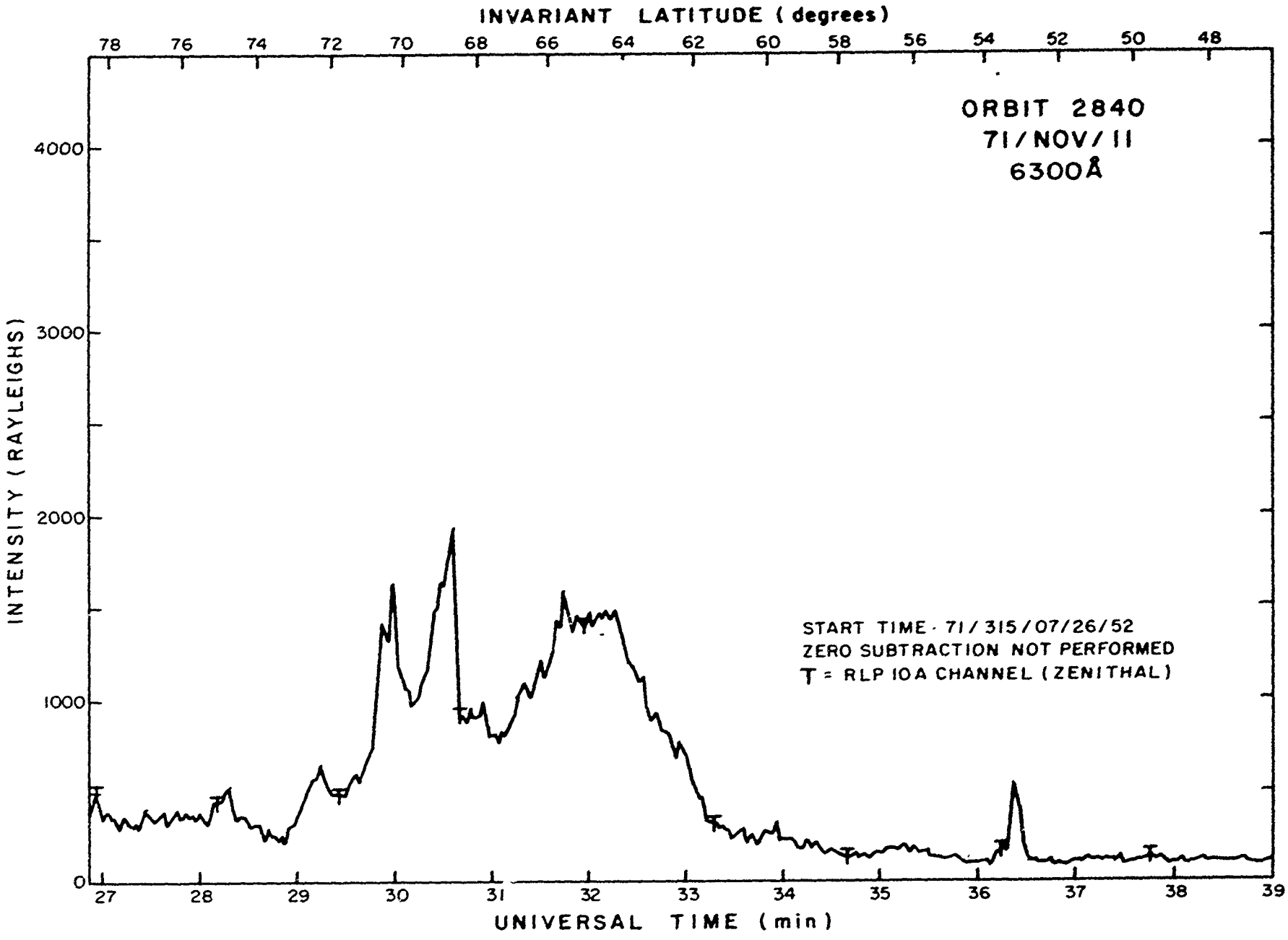
INVARIANT LATITUDE (degrees)
78 76 74 72 70 68 66 64 62 60 58 56 54 52 50 48
ORBIT 2840
71/NOV/11
6300Å
INTENSITY (RAYLEIGHS)
4000
3000
2000
1000
0
START TIME - 71/315/07/26/52
ZERO SUBTRACTION NOT PERFORMED
T = RLP 10A CHANNEL (ZENITHAL)
27 28 29 30 31 32 33 34 35 36 37 38 39
UNIVERSAL TIME (min)

Figure 1

al., 1973) sees the same emitting region on many successive spacecraft spins. For each latitude viewed, the data are selected from the spacecraft rotation which yields the minimum time delay between the optical viewing of that latitude, and the crossing of the spacecraft past the magnetic field line that intersects this latitude point at the emission altitude. In this "minimum-time-delay" analysis the delay can never be more than one-half spin period which means a maximum of ten seconds in general. This continuous curve is therefore composed of segments of data spliced from many rotations: thus the time scale at the bottom does not correspond to the viewing time, but is the smoothly varying time of the spacecraft, for which the invariant latitude is shown at the top.

Figure 2 (bottom frame) shows the same minimum time delay 6300 A trace again, except that the scale is logarithmic, and the 5577 A emission and the N_2^+ 3914 A emission from Dr. C. D. Anger's Auroral Scanning Photometer (Anger et al., 1973) have been added as well. The upper part of the diagram contains data from the Soft Particle Spectrometer (Heikkila et al. 1970) which we now discuss.

For reasons that will become clear later, the electron spectra have been integrated over energy into four directional energy flux bands, which from bottom to top correspond to 5-60 eV, 60-300 eV, 300 eV - 1 keV, and 1-15 keV. The SPS looks perpendicular to the spin axis and in this cartwheel mode a full range of pitch angles is scanned; the pitch angle sawtooth is shown at the top such that a downward tooth corresponds to downgoing electrons. In these instantaneous fluxes one can see the nature of the pitch angle distributions. For the 1-15 keV channel (the top trace)

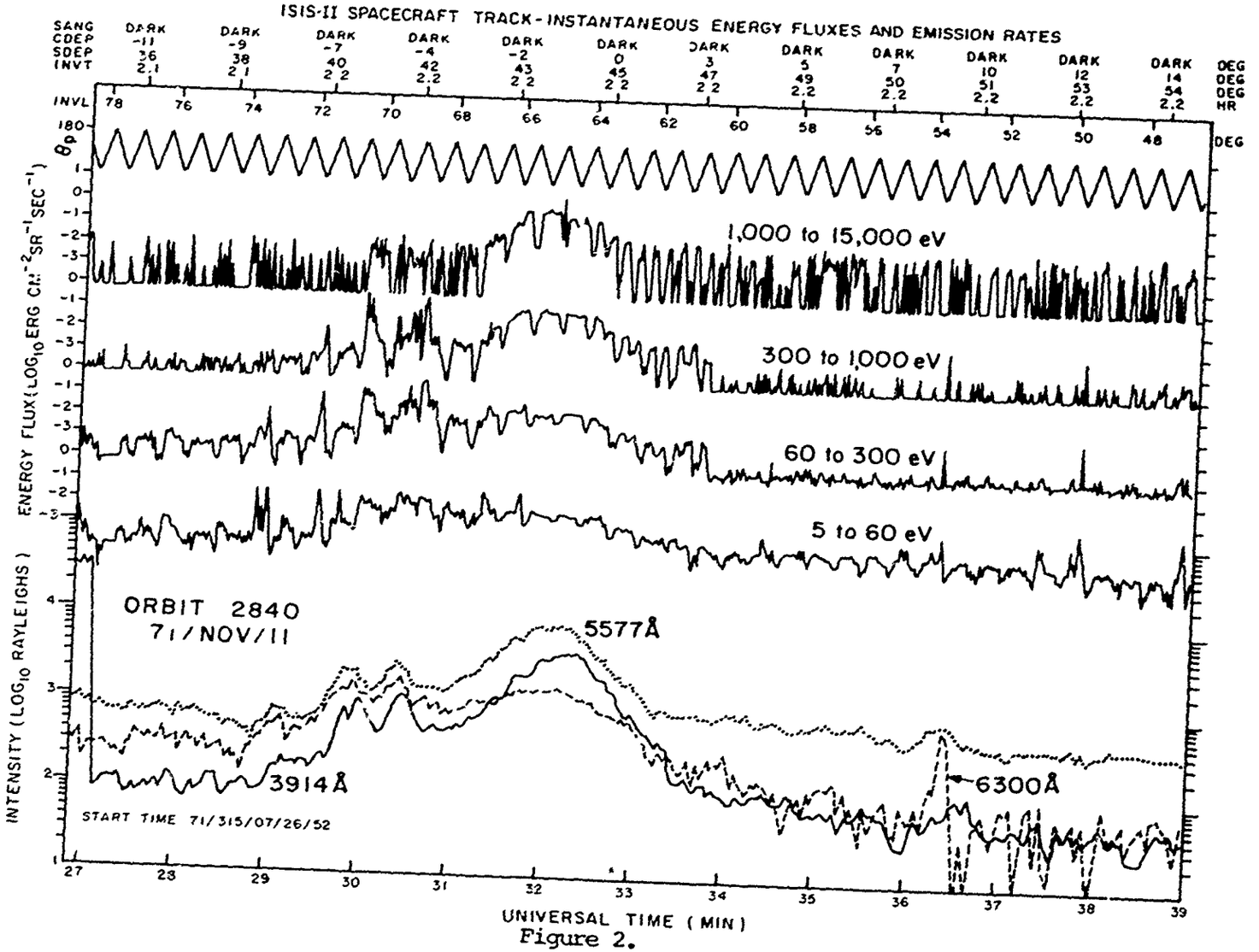
ISIS-II SPACECRAFT TRACK-INSTANTANEOUS ENERGY FLUXES AND EMISSION RATES
SANG
CDEP
SDEP
INVT
INVL
θ_p
1,000 to 15,000 eV
300 to 1,000 eV
60 to 300 eV
5 to 60 eV
ENERGY FLUX (LOG$_{10}$ ERG CM^{-2} SR^{-1} SEC^{-1})
INTENSITY (LOG$_{10}$ RAYLEIGHS)
ORBIT 2840
71/NOV/11
5577Å
3914Å
6300Å
START TIME 71/315/07/26/52
UNIVERSAL TIME (MIN)
DEG
DEG
DEG
HR

Figure 2.

the fluxes form a smooth symmetrical narrow region centered at 65° Invariant; this is the continuous (diffuse) auroral belt. The distributions appear isotropic in the poleward half of this distribution but going equatorward from the center the loss cone deepens and the flux peaks are at 90°, finally corresponding to trapped particles. For the 0.3-1 keV channel there is a similar distribution, except that anisotropy sets in further equatorward than at higher energies. More importantly, there are now large structured irregular fluxes in the 68-73° invariant region, where the 1-15 keV fluxes were small. This is the discrete aurora, which appears as a region of low-energy, enhanced precipitation in ISIS data viewed this way. The same trends continue in the 60-300 eV band, with the discrete auroral fluxes substantially higher than for the diffuse region, and with the flux extended both further equatorward and poleward. Isotropic fluxes in this band continue the trend seen in the other bands, i.e. lower energy particles remain isotropic over a wider latitudinal range as a function of decreasing latitude. The discrete and diffuse auroral patterns are readily seen in the linear 6300 A data of Figure 1.

The lowest energy channel, 5 - 60 eV, continues the same trend, except that there seems to be no equatorward limit to the flux. This effect is explained by noting the additional scales at the top of Fig. 2. "INVT" stands for invariant time, "SDEP" for solar depression at the viewed point, "CDEP" for the solar depression in the conjugate hemisphere to the viewed point and "SANG" denotes sun angle, the angle between the photometer axis at the time of viewing and the satellite-sun line. The indication "DARK" means that the spacecraft was in darkness and so SANG is not

relevant. The solar depression angles show that the local ionosphere is very dark, but that it is twilight in the conjugate hemisphere. The conjugate sun sets at 63.5° invariant but the 5-60 eV fluxes continue undiminished to a conjugate solar depression of 10° at 52.7° invariant - beyond this the fluxes decrease as expected. These are clearly fluxes of conjugate photoelectrons. Additional evidence for this fact is provided by the minimum in the energy flux at 180° pitch angle, i.e. upcoming fluxes.

These plots of "instantaneous" fluxes and intensities are interesting and useful in their own right, but for quantitative flux and optical emission comparisons further analysis is required. To improve the quantitative aspect of the data we have calculated the precipitated energy flux. For each energy band the precipitated flux is integrated over the loss cone - this is done for the two halves of the cone - ascending and descending from the zenith. These two values are the same in a region of stable precipitation; their difference gives a measure of this stability. For the optical emissions corrections must be made for airglow background and for earth albedo. The airglow is subtracted by manually selecting baseline regions outside the auroral region, on one or preferably both sides of the aurora. A linear interpolation is used inside the auroral region. An albedo correction is made using the method of Hays and Anger (1978). As applied to the 6300 A emission the method assumes that the aurora is of uniform intensity in the east-west direction. An albedo of 0.5 was used, as larger values gave evidence of overcorrection. The data resulting from these corrections are plotted against invariant latitude,

one data point per spin as shown in Figure 3. For the electron fluxes, each half-cone flux is shown by a short bar, with the bars connected with a vertical line. These values are also stored in an on-line data base for an analysis to be described later. Values of optical emission rate averaged over the corresponding time regions are also stored in the data base along with other temporal and spatial parameters.

C. The Analysis Approach:

Earlier analyses by Bunn (1974) had shown non-linear relationships between total energy flux and 6300 A emission rate, in agreement with the known energy dependence of excitation of the emission. More energetic precipitation penetrates to lower levels of the atmosphere where the $O(^1D)$ level is more heavily quenched by N_2 (Hays, 1978) and yields correspondingly less emission. The non-linear plots obtained by Bunn (1974) are interesting in that they imply a systematic relationship between energy spectrum and energy flux but that will not be pursued here. However, for a given energy band, if it may be assumed monoenergetic, there must be a linear relationship between the precipitated energy ard the amount of emission it produces. For the ith energy band we can therefore define a production coefficient as follows:

$$I_i = e_i F_i \qquad (1)$$

where I_i is the emission intensity and F_i is the energy flux for the ith band. For the units used here the production coefficient e_i will be in Rayleighs erg^{-1} cm^2 sec. A given aurora may then be represented by a linear superposition of energy fluxes giving some total intensity I:

$$I = \sum_{i=1}^{N} e_i F_i \qquad (2)$$

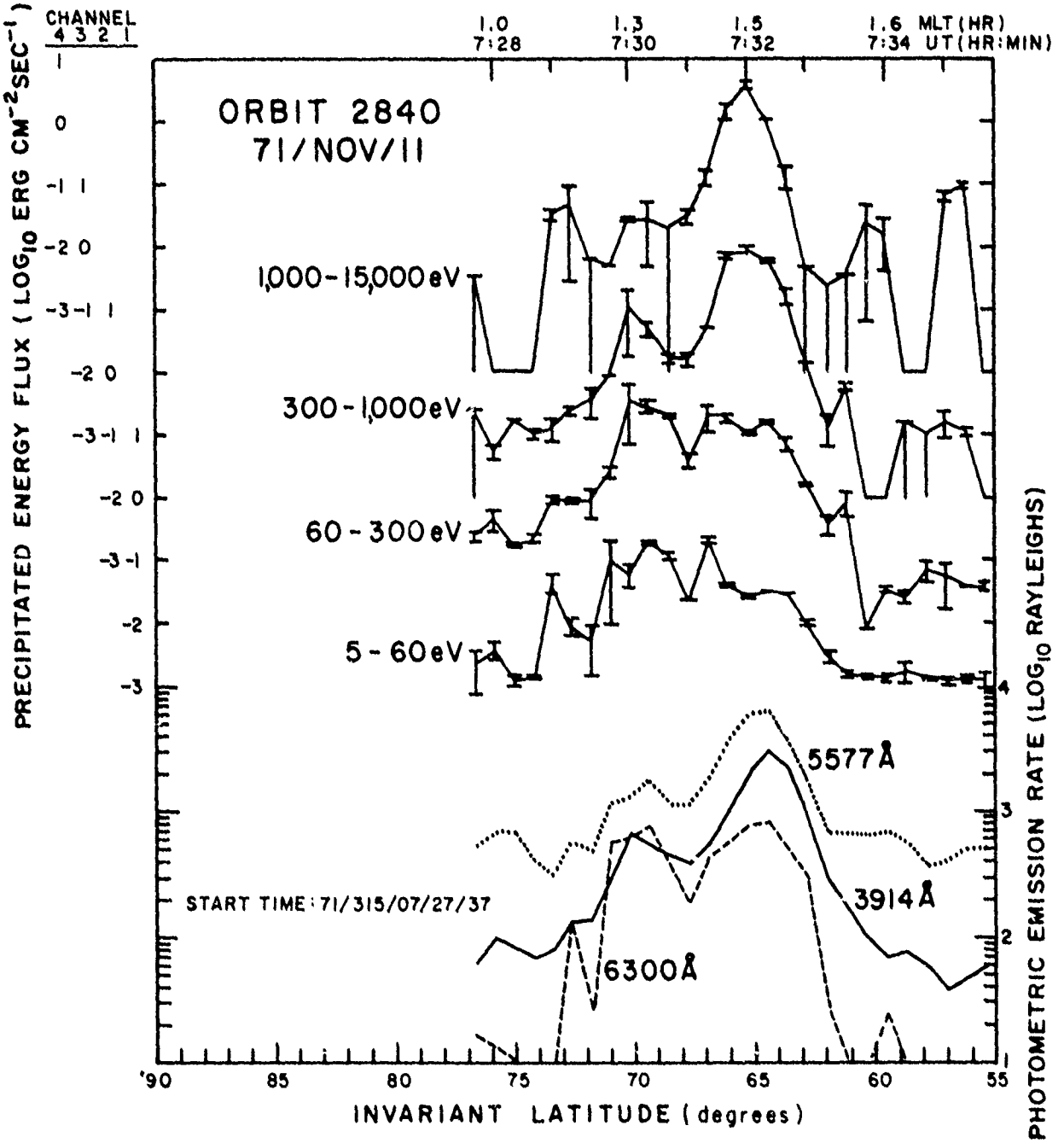
CHANNEL
4 3 2 1
PRECIPITATED ENERGY FLUX (LOG10 ERG CM-2SEC-1)
1.0
7:28
1.3
7:30
1.5
7:32
1.6 MLT(HR)
7:34 UT(HR:MIN)
ORBIT 2840
71/NOV/11
1,000-15,000eV
300-1,000eV
60-300eV
5-60eV
5577Å
3914Å
6300Å
START TIME: 71/315/07/27/37
90
85
80
75
70
65
60
55
INVARIANT LATITUDE (degrees)
PHOTOMETRIC EMISSION RATE (LOG10 RAYLEIGHS)

Figure 3

We had originally proposed to determine the coefficients e_i by a regression analysis of the data base, using the stored values of I and F_i; it was later discovered that four bands was about as many as the method and data would cope with, at least for an initial study. The bands were originally divided in a way that allocates roughly the same energy flux to each band, and that associates certain geophysical significance (e.g. photoelectrons, E & F-region energy deposition) with each. The result was the four bands shown in Figures 2 and 3. A regression analysis was perfomed, to minimize the sum of the squares of the differences between the observed intensity, I_{OBS}, values and the right side of equation (2). To illustrate the quality of the results, Figure 4 shows plots for each band of F_i versus I_i, where I_i is calculated from:

$$I_i = I_{OBS} - \sum_{j \neq i} e_j F_j \qquad (3)$$

Logarithmic plots are used even though the regression was linear and thus the value fitted by regression is constrained to be a line of constant slope, as shown by the regression-determined line on each plot. The logarithmic scale makes the scatter look worse than it is and scatters it unequally about both sides of the fitted line - the fitted line tends to follow the upper limit of the data points. It should also be pointed out that the actual I_i values cannot be calculated since the regression is simultaneous on all four plots; the total error is thrown into each plot individually and is not the sum of all of the scatter on all of the plots. Bearing in mind then that the plots are illustrative the following comments are in order. From a larger number of candidate orbits, 12 orbits were

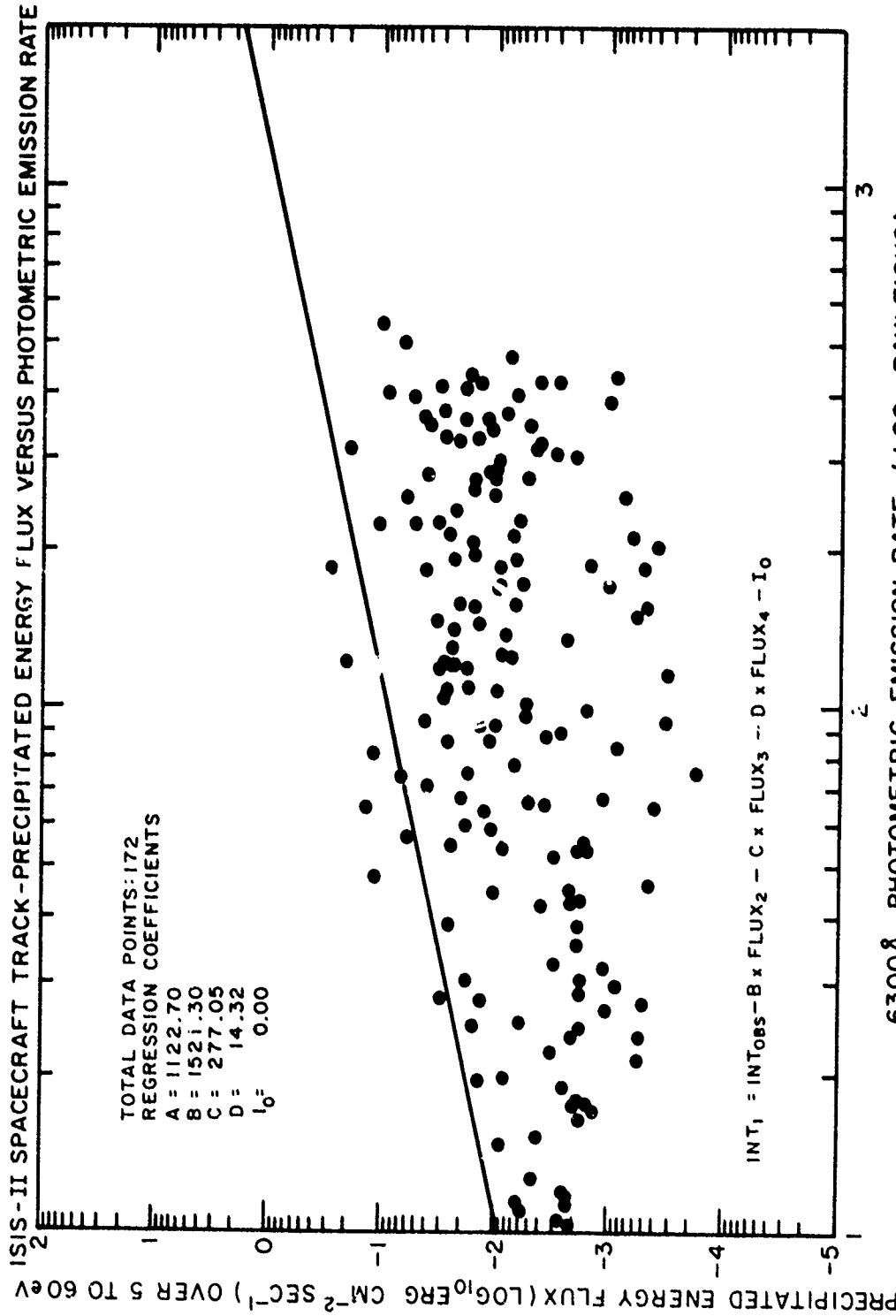
ISIS-II SPACECRAFT TRACK-PRECIPITATED ENERGY FLUX VERSUS PHOTOMETRIC EMISSION RATE
TOTAL DATA POINTS: 172
REGRESSION COEFFICIENTS
A = 1122.70
B = 1521.30
C = 277.05
D = 14.32
I_o = 0.00
$INT_1 = INT_{OBS} - B \times FLUX_2 - C \times FLUX_3 - D \times FLUX_4 - I_o$
PRECIPITATED ENERGY FLUX (LOG_{10} ERG CM^{-2} SEC^{-1}) OVER 5 TO 60 eV
6300Å PHOTOMETRIC EMISSION RATE (LOG_{10} RAYLEIGHS)
2
1
0
-1
-2
-3
-4
-5
3

Figure 4

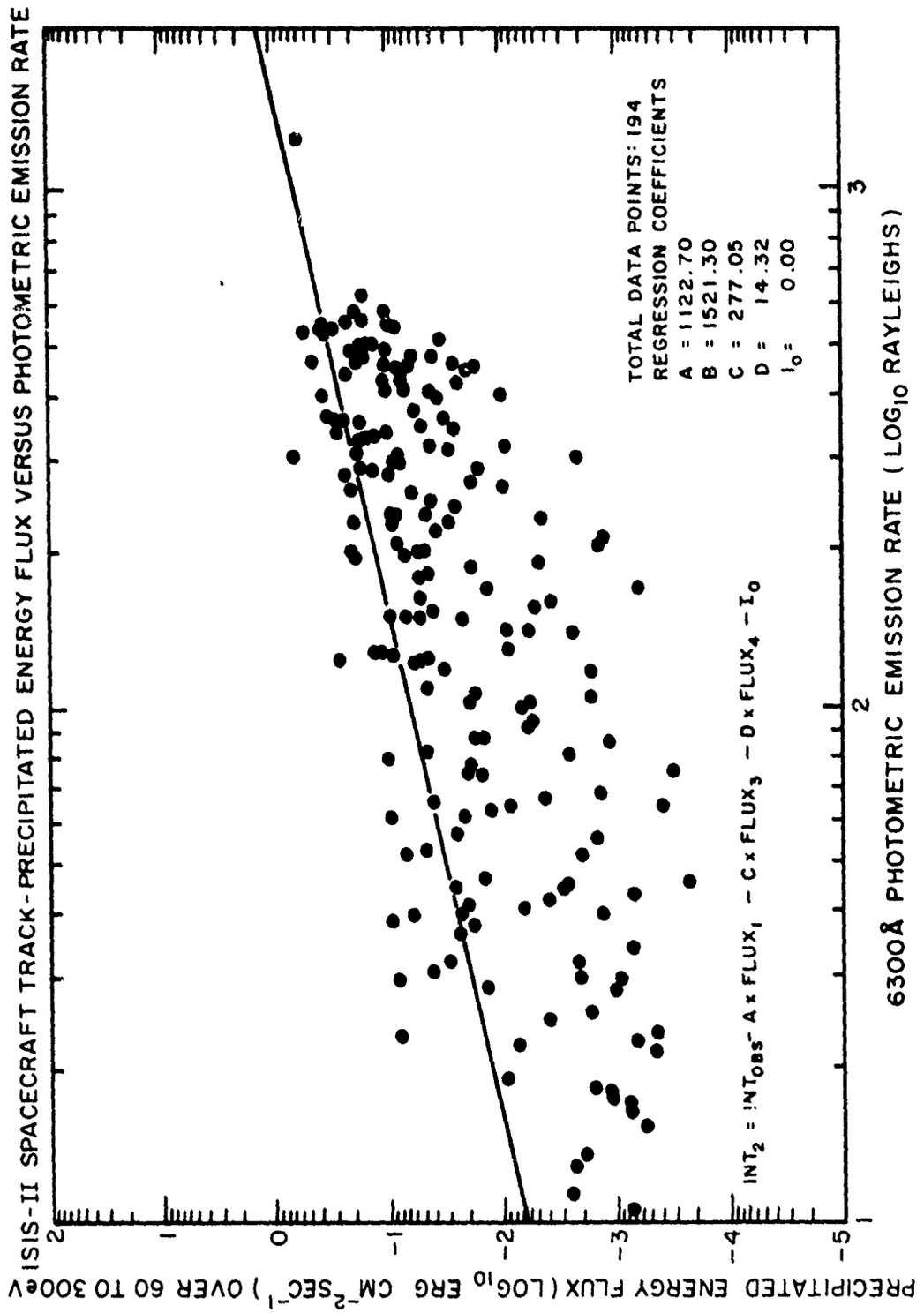
ISIS-II SPACECRAFT TRACK-PRECIPITATED ENERGY FLUX VERSUS PHOTOMETRIC EMISSION RATE
TOTAL DATA POINTS: 194
REGRESSION COEFFICIENTS
A = 1122.70
B = 1521.30
C = 277.05
D = 14.32
I_0 = 0.00
$INT_2 = INT_{OBS} - A \times FLUX_1 - C \times FLUX_3 - D \times FLUX_4 - I_0$
PRECIPITATED ENERGY FLUX (LOG_{10} ERG $CM^{-2}SEC^{-1}$) OVER 60 TO 300eV
6300Å PHOTOMETRIC EMISSION RATE (LOG_{10} RAYLEIGHS)

Figure 4b

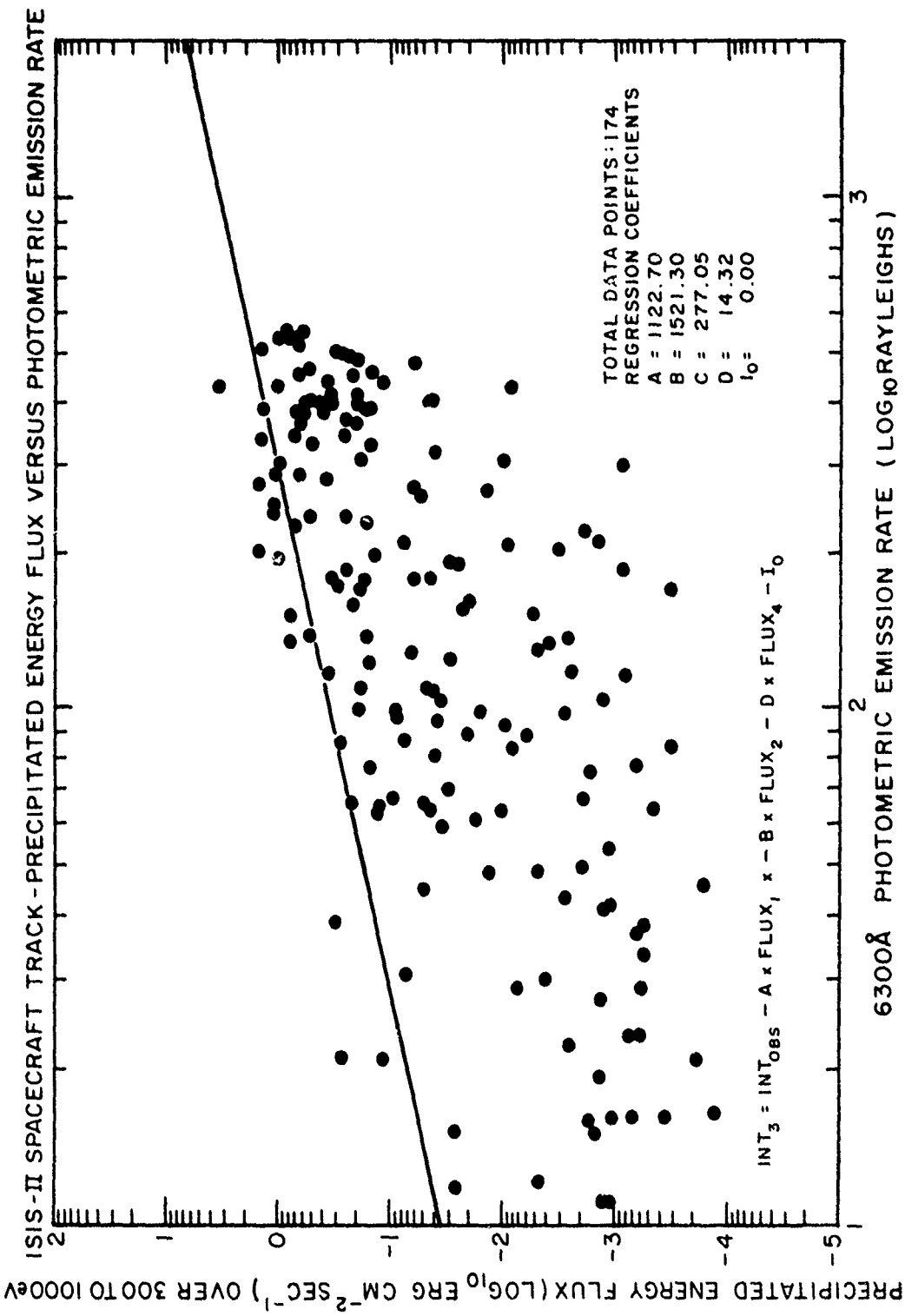
ISIS-II SPACECRAFT TRACK-PRECIPITATED ENERGY FLUX VERSUS PHOTOMETRIC EMISSION RATE
TOTAL DATA POINTS: 174
REGRESSION COEFFICIENTS
A = 1122.70
B = 1521.30
C = 277.05
D = 14.32
I_o = 0.00
$INT_3 = INT_{OBS} - A \times FLUX_1 \times - B \times FLUX_2 - D \times FLUX_4 - I_o$
PRECIPITATED ENERGY FLUX (LOG_{10} ERG $CM^{-2}SEC^{-1}$) OVER 300 TO 1000eV
6300Å PHOTOMETRIC EMISSION RATE (LOG_{10} RAYLEIGHS)

Figure 4c

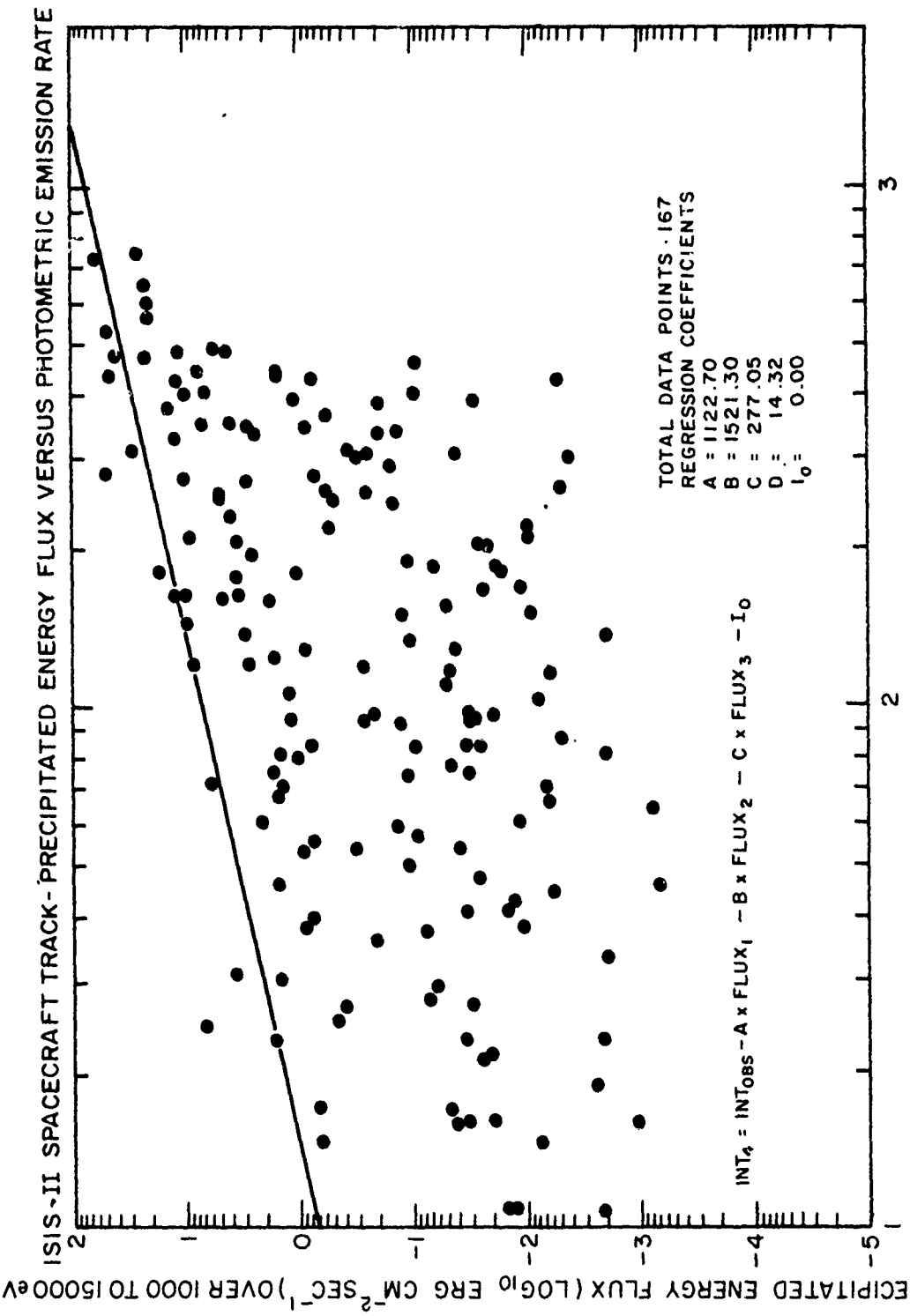
ISIS-II SPACECRAFT TRACK-PRECIPITATED ENERGY FLUX VERSUS PHOTOMETRIC EMISSION RATE
PRECIPITATED ENERGY FLUX (LOG10 ERG CM-2SEC-1) OVER 1000 TO 15000 eV
6300Å PHOTOMETRIC EMISSION RATE (LOG10 RAYLEIGHS)
TOTAL DATA POINTS · 167
REGRESSION COEFFICIENTS
A = 1122.70
B = 1521.30
C = 277.05
D = 14.32
I0 = 0.00
INT4 = INTOBS - A x FLUX1 - B x FLUX2 - C x FLUX3 - I0

Figure 4d

selected for the regression analysis, yielding 172 data points. These orbits were between Oct. 2 and Nov. 24, 1971, so that a rather narrow range of season and local time is represented. Returning to Figure 4 (b), the 60-300 eV band shows a convincing regression fit, in terms of the linearity within this band. Figures 4 (c) and 4 (d), which show the .3-1 keV and 1-15 keV bands respectively, show less convincing but nevertheless satisfactory relations. For the 5-60 eV band shown in Figure 4 (a) the intensities seem rather independent of the fluxes and one cannot have as much confidence in the value, but because of the low energies involved this band did not contribute much to the regression and the coefficients obtained for the other bands.

D. Results:

The production coefficients obtained are shown in Table 1, in Rayleighs erg^{-1} cm^2 sec, along with their probable errors and limits on the regression estimate.

Table 1

6300A Production of Coefficients Determined by Regression Analysis

	Energy			
	5-60 eV	60-300 eV	.3-1 keV	1-15 keV
6300A production Coefficients R $erg^{-g^{-1}}$ cm^2 s	1120	1520	277	14.3
Probable error	262	84	22	1.2
Lower limit	603	1354	231	11.8
Upper limit	1462	1688	322	16.7
Weighted mean energy	30 eV	200 eV	.5 keV	5 keV
Production Efficiency Photons/electrons	0.05	0.49	0.22	0.11

A more fundamental way to express the production efficiency is in terms of the number of photons that are emitted from a 1 cm^2 column for each incident electron that enters the column at the top (unit incident flux). The production coefficients are also given in these units in this table, but since the conversion factor is energy dependent it is necessary to assign an "average" energy to each band to make the conversion. We have assigned subjective weighted average values that reflect the shape of the spectrum within each band, and these values are given as well.

Although as explained in the introduction we do not wish to become embroiled in a discussion of excitation mechanisms, it is still appropriate to make some comparisons with theoretical calculations. In Figure 5 the values of production coefficient are shown as a function of energy for the 6300 A data of Figure 4, for the calculations of Banks et al. (1974), for the calculations of Mantas and Walker (1976), and for an in situ rocket measurement into conjugate photoelectrons by Shepherd et al. (1978). The values of Rees and Luckey (1974) cannot be compared directly because their results are for power- exponential spectra. But taking their production coefficient for the 4278 A N_2^+ band at 1 kR emission rate of 160 erg^{-1} cm^2 sec and their I(6300)/ I(4278) ratios as a function of characteristic energy, α , and using the average energy which is 2α , we obtain the points shown in the figure (a constant I(3914)/I(4278) = 3 was applied). The agreement between all of these is surprisingly good, considering that no attention has been paid to standardization of model atmospheres, ionospheric electron densities, reaction rates and the like, and further considering the order of magnitude discrepancies cited in the introduction.

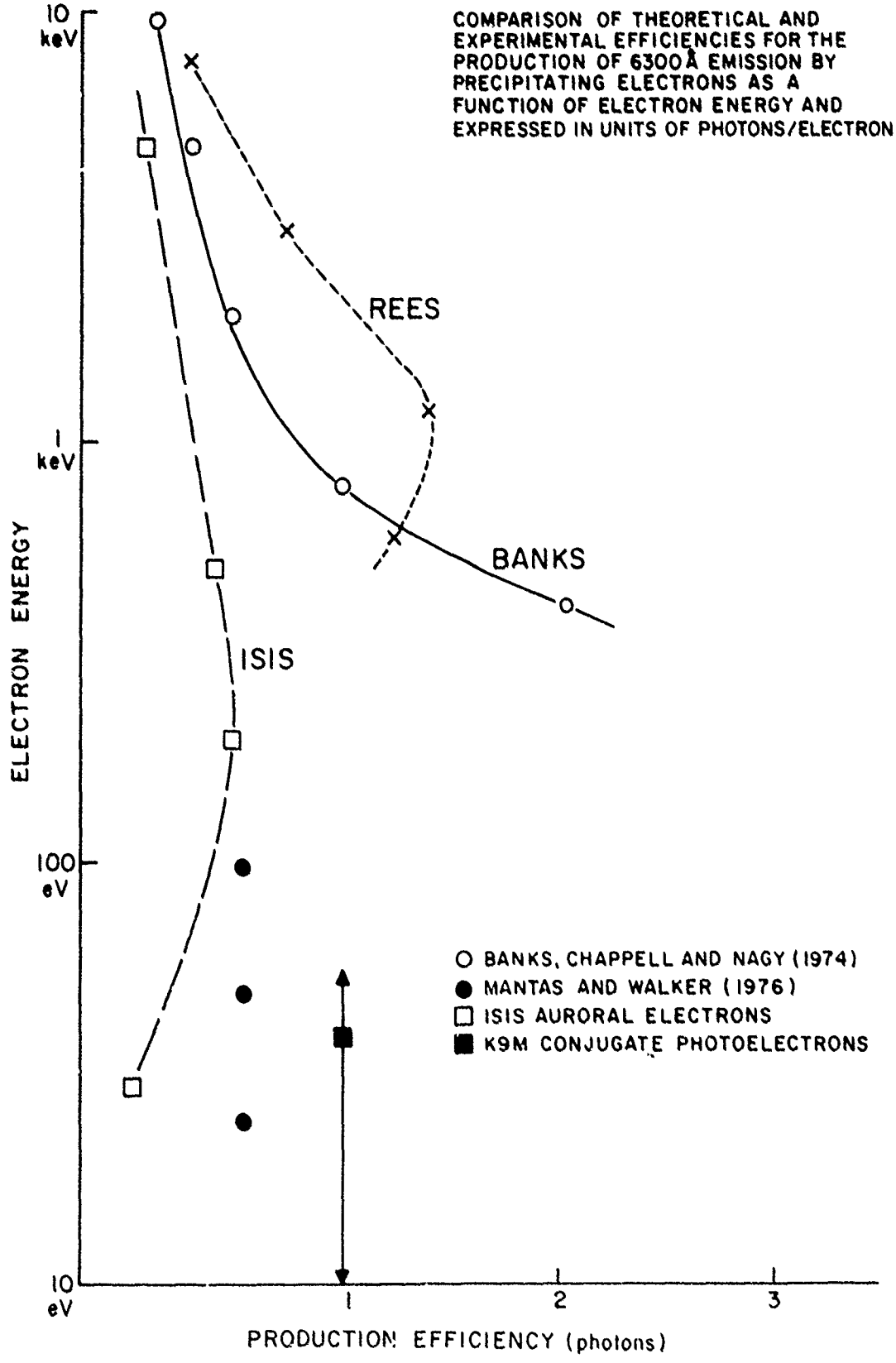
COMPARISON OF THEORETICAL AND EXPERIMENTAL EFFICIENCIES FOR THE PRODUCTION OF 6300Å EMISSION BY PRECIPITATING ELECTRONS AS A FUNCTION OF ELECTRON ENERGY AND EXPRESSED IN UNITS OF PHOTONS/ELECTRON.
10 keV
1 keV
100 eV
10 eV
ELECTRON ENERGY
REES
BANKS
ISIS
O BANKS, CHAPPELL AND NAGY (1974)
● MANTAS AND WALKER (1976)
□ ISIS AURORAL ELECTRONS
■ K9M CONJUGATE PHOTOELECTRONS
1
2
3
PRODUCTION EFFICIENCY (photons)

Figure 5

E. Estimation of energy fluxes from optical emissions:

As an initial test of the regression fit, we show in Figure 6 the calculated 6300 A emission for orbit 2848 obtained from using the measured energy fluxes and the fitted coefficients. The agreement is entirely satisfactory, giving one confidence in the procedure. It may be noted that the regression coefficients obtained when orbit 2840 is deleted from the data set are essentially identical in e_2, e_3, and e_4 and show only some variation in e_1, so that the agreement is an indication of the stability of the whole dataset, not just the regeneration of a limited amount of data from itself.

In applying this information to deduce energy fluxes from optical emissions one notes from Table 1 that a large fraction of the 6300 A emission comes from the 60-300 eV band. If it all came from only this band then the 6300 A emission could be used to calculate the 60-300 eV flux very simply. To improve this procedure one notes that for most energy spectra, at least on the nightside, that most of the precipitated flux lies outside the 60-300 eV band. Since the 3914 A emission is a measure of the total energy flux, this emission can be used to determine the energy flux above 300 eV and to correct for the amount of 6300 A emission produced by electrons above this energy. Unfortunately we cannot distinguish between the .3-1 keV and 1-15 keV flux channels in this way, but since the latter is wider and carries most of the energy it does not matter too much. Combining the 160 R erg^{-1} cm^2 sec efficiency for 4278 A emission from Rees and Luckey (1974), the I(3914)/I(4278) ratio of 3 and the

production coefficients of 1520 and 14 R erg^{-1} cm^2 sec for the 60-300 eV and 1-15 keV bands respectively one obtains:

$$F(60\text{-}300eV) = (1/1520)\ (I_{6300} - I_{3914}/30)\ erg\ cm^{-2}\ sec^{-1} \quad (4)$$

Figure 6 shows a comparison between the calculated and measured fluxes, but as we might have expected, the agreement is better if we compare the predicted fluxes with the sum of the two low energy bands, 5-300 eV. The above equation can therefore be applied to the calculation of the F(E<300 eV) flux. The agreement is satisfactory, although the calculated fluxes are consistently higher. This probably results from neglecting the .3-1 keV band. We make an upward adjustment by a factor of 2.5 to bring these curves into agreement and the final equation is therefore:

$$F(E<300\ eV) = 2.63 \times 10^{-4}\ I(6300) - 8.77 \times 10^{-6}\ I(3914)\ erg\ cm^{-2}sec^{-1} \quad (5)$$

F. Discussion and Conclusions:

At the present time we have in the data base only low resolution preliminary values of the 3914 A emission, uncorrected for albedo. When corrected 3914 A values are incorporated it will be possible to refine the above equation further. While the formulation has been based on approximate arguments one can see that it could be determined from a strictly empirical "inverse" regression from the data base, where the coefficients of the optical intensities in equation (5) are found by regression against the flux in the two lowest energy bands.

Although our confidence in the method is limited to use with ISIS data, there is in principle no reason why it cannot be applied in general, and specifically with ground-based data. However, one would like to calibrate this application and the only comparisons we have are those using

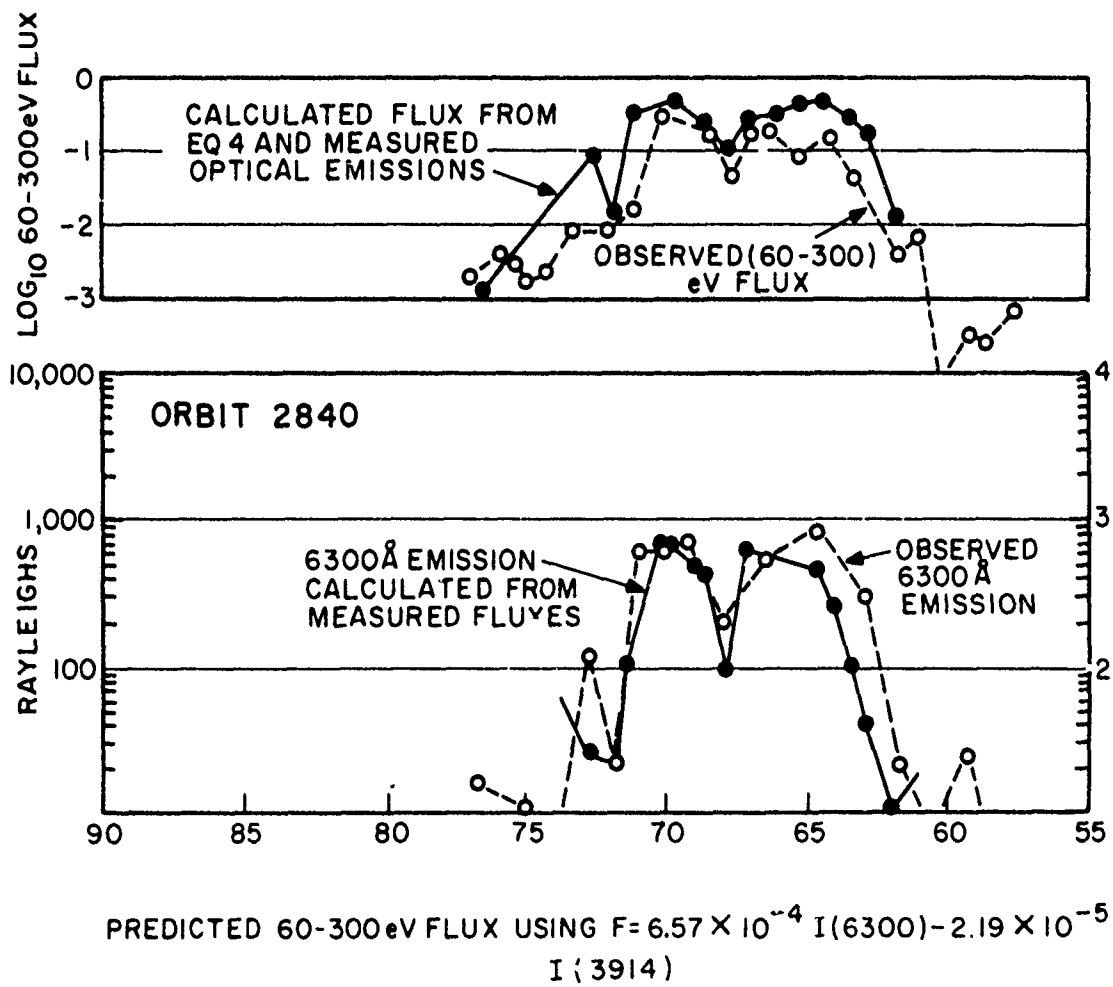
LOG10 60-300eV FLUX
0
-1
-2
-3
CALCULATED FLUX FROM EQ 4 AND MEASURED OPTICAL EMISSIONS
OBSERVED(60-300) eV FLUX
10,000
1,000
100
RAYLEIGHS
4
3
2
ORBIT 2840
6300Å EMISSION CALCULATED FROM MEASURED FLUXES
OBSERVED 6300Å EMISSION
90
85
80
75
70
65
60
55
PREDICTED 60-300eV FLUX USING F= 6.57 X 10^-4 I(6300)-2.19 X 10^-5 I(3914)

Figure 6

rocket data, which as explained, seem at variance with satellite data. Applying our formulation to the estimation of 6300 A emission rate, using the measured fluxes of Arnoldy and Lewis (1977), Rees et al. (1977), and Sivjee and McEwen (1976), values obtained are lower by at least an order of magnitude than observed experimentally. This is surprising, but is at least consistent with the result that the ISIS data and theoretical calculations agree, and the theory is an order of magnitude too low compared with rocket results.

III. Comparison of Particle, Optical, and Electron Density Data

Item 2 of the contract has as its basic goal the inference of gross characteristics of the ionosphere such as the trough poleward boundary from optical and particle data from satellites. Item 4 had the same basic goal, i.e. to ascertain ionospheric parameters by indirect means, as item 2 except that joint data analysis of DMSP, ISIS, and AFGL Airborne Ionospheric Laboratory was to be the means. These basic goals were accomplished in the paper 'A Case Study of the Aurora, High-Latitude Ionosphere, and Particle Precipitation During Near Steady State Conditions' (See Appendix). The abstract for this paper is given below.

> An ISIS-2 pass is singled out for a detailed examination of the particle fluxes, optical emissions, and ionospheric parameters observed during a quiescent period (late recovery) between two substorms. This pass was chosen because it was part of a coordinated data acquisition period between the Air Force Geophysics Laboratory (AFGL) Airborne Ionospheric Observatory, ISIS-2, and DMSP (Defense Meteorological Satellite Program). As a result, both long-duration measurements (aircraft) and transient, snapshot (spacecraft) data are available. This allows, on a macroscopic level, the separation of space and time effects.

On the basis of the joint data set it was established that the latitudinal morphology observed by the satellite is basically spatial in nature. It is concluded that the observed particle fluxes are most easily understood in terms of precipitation from the quiet time plasma sheet without intervening acceleration. The observed optical emissions and ionospheric parameters are found to be in good qualitative and quantitative agreement (within experimental error) with the electron fluxes, although establishment of this point has required careful determination of the viewing direction of the optical instruments, removal of scattered light (albedo) from underlying cloud and snow, and consideration of the effects of photon-counting statistics on contour plots of the optical data.

Figure 4 (see Section VII) of this paper graphically summarizes the results obtained for this winter pass. Panel E provides a measure of the particle energy fluxes in two bands corresponding roughly to E & F region energy deposition. Comparison of panel E with the electron densities at various heights given in panels A & B clearly demonstrates that the equatorward edge of precipitating electrons corresponds to the poleward trough wall and poleward precipitation boundary to the polar cap. It can be seen in panel C that the equatorward precipitation boundary also corresponds to the onset of 6300 A (and also 5577 & 3914) auroral emissions.

As would be expected the maximum E region response (See panel D) observed by the aircraft occurs at the point of highest average electron energy observed by ISIS. The stars in panel D are calculated $f_o E_a$ based on the observed particles. Good agreement is observed between the calculated and observed values. The aircraft also observed FLIZ over the particle flux region that it sampled.

Based on the data presented in this paper one can derive the following conclusions.

1. The poleward trough boundary corresponds to the equatorward edge of >100 eV electron precipitation during local sunset conditions.
2. The equatorward edge of enhanced 6300 A emissions coincides with the equatorward edge of >100 eV electron precipitation and thus with the poleward trough wall.
3. One can infer the instantaneous latitude of the poleward trough wall as a function of local time from 6300 satellite images during sunset.
4. If high-altitude cinematography of 6300 A were available then the gross dynamics of the trough could be ascertained.

IV. Dynamical Effects

The ultimate goal of this contract is expressed in item 3, namely the determination of the dynamical position of the poleward trough wall by indirect means.

It has been shown in the previous sections that

(1) it is possible to define an empirical relationship between <300 eV electron fluxes and 6300 A fluxes based on ISIS-2 results.

(2) the equatorward boundary of enhanced 6300 A emissions and low-energy electrons coincide and that both coincide with the concurrently observed poleward trough wall during sunset periods.

What is needed now is to relate one of the observed ISIS particle or optical boundaries to substorm and IMF variations in order to evaluate the dynamic behavior of the coincident poleward trough wall. We have chosen the electron fluxes as the unifying (and obviously causative) agent. In the paper "A Statistical Study of the 'Instantaneous' Nightside Auroral Oval: The Equatorward Boundary of Electron Precipitation as Observed by the ISIS 1 and 2 Satellites" (See Section VII) this goal was accomplished. The abstract of the paper is reproduced below and the reader is referred to Section VII for the entire text.

> Electron spectrograms from 351 passes of the ISIS 1 and 2 satellites were utilized to study statistically the effects of the interplanetary magnetic field (IMF), substorm activity, and the earth's dipole tilt angle on the latitude of the equatorward boundary of the nightside (2000-0400 magnetic local time) 'instantaneous' auroral oval. The boundary location (in invariant latitude) of the instantaneous oval at hourly local time intervals was identified in terms of the equatorward boundary of the diffuse > 100 eV electron precipitation. The following characteristics were noted: (1) The north-south component (B_z) of the IMF plays the dominant role in controlling the motion of this boundary. The invariant latitude of the boundary is shown to shift by approximately 4° depending on the direction of the IMF (northward and southward, respectively) relative to its position corresponding to $B_z = 0$. This indicates an inward motion of the associated boundary in the magnetotail by about 5 earth radii when the IMF changes its direction from northward to southward with large magnitude. There is a significant difference in the amount of the shift between the evening and morning sectors: i.e., for the same decrease in B_z value the boundary moves more equatorward in the morning sector than in the evening sector. When the obtained oval particle boundary was projected onto the equatorial plane of the magnetotail along magnetic field lines, good agreement was found between the projected boundary and the drift boundary (the Alfven layer) of low-energy electrons in the presence of the dawn-dusk electric

field. Thus this agreement gives new evidence showing that the diffuse electron precipitation that produces the diffuse aurora originates near and at the inner boundary of the plasma sheet. (2) Substorm activity seems to have a separate role in determining the latitude of the equatorward boundary of the nightside auroral precipitation region. The boundary during substorm periods is statistically found to be 2^{o} - 3^{o} lower in invariant latitude than that during quiet times. Even a simple classification into quiet and disturbed conditions improves the accuracy with which the auroral oval location can be inferred. By combining the IMF effect and the substorm effect it is indicated that the boundary is located at the lowest latitudes when a substorm takes place during a southward IMF with large magnitude, whereas the boundary is located in the highest latitudes when the IMF has a northward component during quiet times. (3) The equatorward boundary of the nightside auroral oval is located at higher latitudes in the winter hemisphere than in the summer hemisphere, although this effect of the earth's dipole tilt is usually smaller than the effects of the IMF and substorm activity.

Figures 3a to c and Table 1 of this paper provide an empirical relationship that relates the > 100 eV equatorward boundary of precipitating electrons to the IMF B_z component. These relationshhips can be used in conjunction with knowledge of the IMF B_z component to 'predict' the location of the > 100 eV electron boundary and thus the poleward trough wall for darkened conditions. However, the following caveats must be remembered.

(1) Substorm effects are not uniquely separated. If concurrent knowledge of the AE or better index is available then the values predicted by the coefficients in Table 1 should be revised downward by 1 to 3^{o} depending on substorm magnitude.

(2) D_{ST} effects were purposefully excluded from this study and thus caution must be used when applying the formulas for 'predictive' purposes during very disturbed periods.

With the above caveats in mind one can now 'predict' the poleward trough wall during darkened conditions in the local time range 2000 to 0400, based on near real-time knowledge of the one-hour average IMF B_z component.

If one wishes to 'measure' the local time, latitude location of the poleward trough wall during dark periods then 6300 A images obtained in near real-time by polar orbiting satellites can be used. Such data can be used to refine the predictions based on averaged IMF B_z. These 'images' provide an 'instantaneous' position independent of magnetic activity of the low-energy electron boundary and thus the trough wall. One caveat should be applied to the above, namely that during periods of decreasing activity the trough wall could be at slightly lower latitudes as a result of recombination hysterisis.

If no optical data is available then electron data obtained in the 2000 to 0400 LT sector could be used to measure the local trough position and extrapolations to other local times based on Table 1 could be made. If both low-energy electron data and 6300 A images are concurrently available, then cross checks can be made. This also holds true for checking the prediction based on IMF data if the one hour average of B_z is concurrently available with the polar satellite data.

V. Summary and Conclusions

Based on the ISIS 1 and 2 data set it has been possible to meet the goals set forth in this contract. The relationships derived in section 2 can be used to relate 6300 A emissions to low-energy (<300 eV) fluxes in a quantitative way and vice-versa. If suitable ionization production models were available then < 300 eV energy fluxes 'images', derived from concurrent 6300 A images, could be utilized to predict

F-region behavior. One possible result would be the derivation of an estimate of FoF_2 during darkened conditions. This result along with the local time position of the trough would allow an estimate of the severity of scattering from the steep poleward wall of the trough and the fluctuations embedded in it. Knowledge of the IMF B_z component in near real-time would allow a dynamic 'prediction' of the trough wall. Such a prediction could be used to allow reconfiguration of systems affected by the trough wall and fluctuations at or near it.

VI. Recommendations

1. Verification tests of the derivation of < 300 eV electron fluxes based on 6300 A images should be undertaken. This could be achieved with either existing or new data sets.

2. Model calculations of ionospheric parameters based on particle and optical data should be undertaken. The results should be compared with concurrently obtained ionospheric data. If positive the results of such calculations could be used to predict ionospheric parameters based on satellite images. This technique would be extremely powerful if high-altitude 6300 A cinematography were available. A first attempt at this could be made with results from the NASA Dynamics Explorer A & B particle and cinematography data.

3. Verification tests of the accuracy of trough wall prediction based on IMF B_z data and the empirical relations derived in the work should be undertaken. Such verification tests would probably lead to further refinements of the 'predicative' formulas. If proved reasonably accurate these empirical predictions could form the basis for operational decisions for systems affected by the physics occurring at the trough wall.

4. If the results derived under this contract are proven to be 'reliable' and the derivable results relevant to Air Force needs then high-altitude (>$2R_E$) satellite imaging should be considered as a test mission. Such a test could be used to define the operational utility of a real-time, fine time scale (< 10 min) monitoring of auroral emissions.

VII. PUBLISHED PAPERS

VOL. 82, NO. 35 JOURNAL OF GEOPHYSICAL RESEARCH DECEMBER 1, 1977

A Statistical Study of the 'Instantaneous' Nightside Auroral Oval: The Equatorward Boundary of Electron Precipitation as Observed by the Isis 1 and 2 Satellites

Y. KAMIDE[1]

Cooperative Institute for Research in Environmental Sciences, University of Colorado, NOAA, Boulder, Colorado 80302
Geophysical Institute, University of Alaska, Fairbanks, Alaska 99701

J. D. WINNINGHAM

Center for Space Sciences, University of Texas at Dallas, Richardson, Texas 75080

Electron spectrograms from 351 passes of the Isis 1 and 2 satellites were utilized to study statistically the effects of the interplanetary magnetic field (IMF), substorm activity, and the earth's dipole tilt angle on the latitude of the equatorward boundary of the nightside (2000–0400 magnetic local time) 'instantaneous' auroral oval. The boundary location (in invariant latitude) of the instantaneous oval at hourly local time intervals was identified in terms of the equatorward boundary of the diffuse >100-eV electron precipitation. The following characteristics were noted: (1) The north-south component (B_z) of the IMF plays the dominant role in controlling the motion of this boundary. The invariant latitude of the boundary is shown to shift by approximately ±4° depending on the direction of the IMF (northward and southward, respectively) relative to its position corresponding to $B_z = 0$. This indicates an inward motion of the associated boundary in the magnetotail by about 5 earth radii when the IMF changes its direction from northward to southward with large magnitude. There is a significant difference in the amount of the shift between the evening and morning sectors; i.e., for the same decrease in B_z value the boundary moves more equatorward in the morning sector than in the evening sector. When the obtained oval particle boundary was projected onto the equatorial plane of the magnetotail along magnetic field lines, good agreement was found between the projected boundary and the drift boundary (the Alfvén layer) of low-energy electrons in the presence of the dawn-dusk electric field. Thus this agreement gives new evidence showing that the diffuse electron precipitation that produces the diffuse aurora originates near and at the inner boundary of the plasma sheet. (2) Substorm activity seems to have a separate role in determining the latitude of the equatorward boundary of the nightside auroral precipitation region. The boundary during substorm periods is statistically found to be 2°–3° lower in invariant latitude than that during quiet times. Even a simple classification into quiet and disturbed conditions improves the accuracy with which the auroral oval location can be inferred. By combining the IMF effect and the substorm effect it is indicated that the boundary is located at the lowest latitudes when a substorm takes place during a southward IMF with large magnitude, whereas the boundary is located in the highest latitudes when the IMF has a northward component during quiet times. (3) The equatorward boundary of the nightside auroral oval is located at higher latitudes in the winter hemisphere than in the summer hemisphere, although this effect of the earth's dipole tilt is usually smaller than the effects of the IMF and substorm activity.

INTRODUCTION

The 'classical' auroral oval (or belt), which is defined as the locus of high frequency (>75%) of auroral appearance [*Feldstein*, 1963, 1966], has been used extensively to order geophysical data. *Eather* [1973] has pointed out several pitfalls in this usage. He states that it is the instantaneous region of visual and subvisual auroral emissions that is most relevant. Hereafter, the term auroral oval should be interpreted to mean the 'instantaneous' region of particle-produced optical emissions, both diffuse and discrete. The 'classical' auroral oval will be that defined by Feldstein.

The size of the auroral oval is not fixed but varies with magnetic activity. During geomagnetically active periods the classical auroral oval expands equatorward, reaching the latitude of the auroral zone, while it contracts poleward during periods of low activity [*Feldstein and Starkov*, 1967]. Since *Dungey*'s [1961] suggestion, that a southward interplanetary magnetic field (IMF) results in a net magnetic flux transfer from the dayside to the nightside, the equatorward shift of the auroral oval has been actively discussed [e.g., *Coroniti and Kennel*, 1973]. Indeed, an extensive study of auroral and magnetic substorms and the dynamics of the classical auroral oval, based on data from a meridian chain of all-sky cameras and magnetometers, suggests that the north-south component of the IMF controls the size of the auroral oval [*Akasofu et al.*, 1973, *Kamide and Akasofu*, 1974]. However, there is a difficulty in examining whether the location of the auroral oval depends solely on the north-south component of the IMF or on both the IMF and the substorm activity, because of the close relationship between the southward component of the IMF and geomagnetic activity [*Fairfield and Cahill*, 1966, *Schatten and Wilcox*, 1967, *Hirshberg and Colburn*, 1969]. Recently, *Kamide et al.* [1976] reported separate effects of these two parameters on the location of the cleft (the dayside portion of the auroral oval), while no such systematic study on the nightside has yet been made.

Another difficulty in previous all-sky camera studies of the classical auroral oval is that even the combined 'field of view' of the cameras was not extensive enough to study the auroral distribution simultaneously over the entire polar region. This difficulty has been removed to a significant extent by auroral imagery from scanning photometers aboard the Isis 2 and DMSP satellites [*Anger et al.*, 1973, *Lui and Anger*, 1973, *Pike*

[1] On leave of absence from Kyoto Industrial University, Kyoto 603, Japan.

Paper number 7A0716

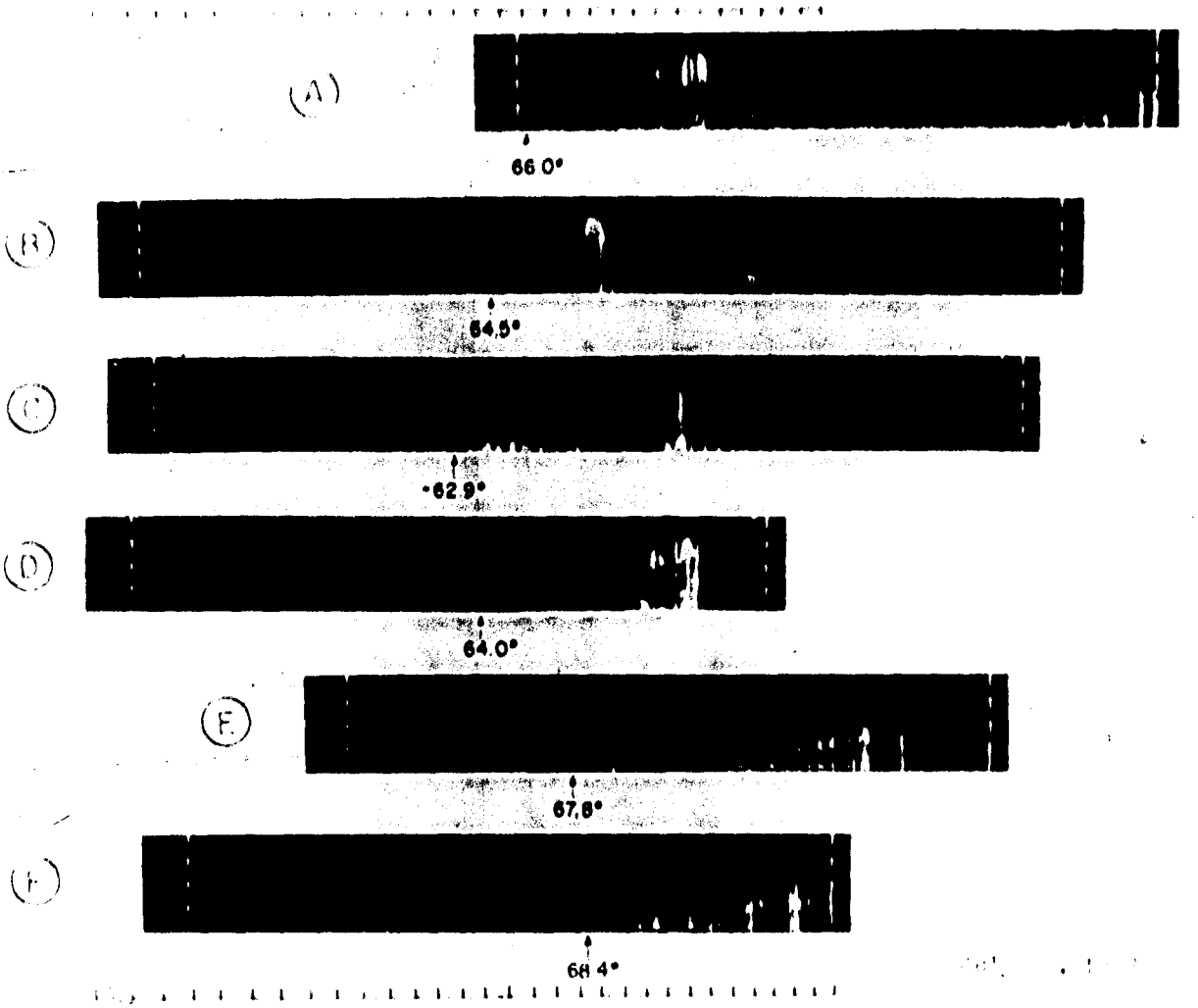

Fig. 1a. Electron spectrograms for six Isis 1 orbits on July 26, 1969, based on data from the soft particle spectrometer (SPS). The ordinate is the log$_{10}$ of the electron energy in electron volts. The invariant latitude scale is correct at 68° for all orbits, slight differences occurring each pass at latitudes above and below 68°. The location of the equatorward boundary of the diffuse ~100-eV electron precipitation is indicated by an arrow for each pass. Note that pass C occurred in the southern hemisphere.

and Whalen, 1974; *Snyder et al.*, 1974; *Akasofu*, 1974]. These instruments construct a map of auroral luminosity from horizon-to-horizon scans of the atmosphere and the earth below the satellites and perpendicular to the orbital path. Even research utilizing low-altitude polar orbiting satellites does not eliminate all difficulties, since the orbital period (100–120 min) is much longer than the average lifetime of substorms. Therefore it is not possible to examine in detail how the pattern of the auroral emissions and particle precipitation varies over the complete polar region during successive phases of an individual substorm. We can, however, determine how the average 'instantaneous' pattern varies during quiet and substorm times by examining a large number of individual passes to construct a composite picture [*Hoffman and Burch*, 1973; *Snyder et al.*, 1974; *Winningham et al.*, 1975; *Lui et al.*, 1975, 1977].

The purpose of this study is to obtain statistically the latitudinal changes of the nightside auroral oval in response to the IMF, substorm activity, and the earth's dipole tilt. In this paper we will be concerned only with the equatorward boundary of the auroral oval that is defined by us as the equatorward edge of ~100 eV electron precipitation at low altitudes (~ 1500 km) as observed by the Isis 1 and 2 satellites. It is noted that the equatorward boundary is a more convenient parameter with which to determine the size of the auroral oval than the position of discrete electron precipitation (auroras), the equatorward boundary of the diffuse auroral belt is relatively steady, while discrete auroras undergo considerable structural changes making it difficult to assign a single value for their latitude.

This paper is in some ways similar to one by *Lui et al.* [1975]. They examined the auroral distribution as a function of geomagnetic activity on the basis of Isis 2 scanning photome-

ter pictures and determined the equatorward boundary of the diffuse 3914-Å and 5577-Å auroral belt at magnetic local midnight to the nearest latitudinal degree for 58 satellite passes. The equatorward boundary of >100-eV electron precipitation studied in this paper would be more closely related to the 6300-Å diffuse aurora. When the latitudinal patterns presented in *Winningham et al.* [1975] are considered, the >100-eV electron boundary will be equatorward (approximately 1°) of that determined from the 3914-Å and 5577-Å emission lines. The accuracy of the boundary determination in the present study is approximately 0.1°.

We first examine a long period during which the data were taken on successive orbits. Then, on the basis of a large data set (a total of 351 Isis 1 and 2 passes) covering a wider area of the nightside auroral region, we examine quantitatively the dependence of the equatorward boundary not only on geomagnetic activity but also on the IMF and the earth's dipole tilt angle.

Analysis

In this study we used data from the following periods: June 7 to July 26, 1969 (Isis 1 data), May 29 to August 20, 1971 (Isis 2 data), and October 18, 1971, to January 13, 1972 (Isis 2 data). We chose the 351 satellite passes for this particular study by the following criteria:

1. The satellite pass occurred over the auroral region within 2000-0400 MLT (magnetic local time).

2. The equatorward boundary of the diffuse auroral precipitation along the satellite pass could be determined with little difficulty in the electron spectrogram (see Figure 1*a*).

3. Simultaneous IMF values were measured by the Explorer 33 and 35, Imp-G (Imp 5), or Imp-I (Imp 6) satellites for an interval of at least 1 hour preceding the Isis pass over the auroral oval.

4. The *Dst* index [*Sugiura and Poros*, 1971, 1972] during the entire period across the auroral region was above $-40\ \gamma$ (= nT, nanotesla). High-*Dst* intervals were excluded to eliminate a possible effect of the large magnetospheric inflation due to the storm time ring current [cf. *Akasofu and Chapman*, 1963].

Details of the Isis soft particle spectrometer (SPS) can be found in the work by *Heikkila et al.* [1970], *Heikkila and Winningham* [1971], *Winningham et al.* [1973], and *Lui et al.* [1977]. For details of the format of electron spectrograms based on data from the SPS, see *Winningham et al.* [1975, Figure 1*a*].

Latitudinal Morphology of Nightside Electron Precipitation

In Figure 1*a* we show a series of Isis electron spectrograms for six passes which occurred on July 26, 1969. The Isis SPS measures electrons between 10 eV and 12 keV in 22 bands as opposed to 5 eV and 13 keV in 38 contiguous samples for Isis 2. The data are presented in an 'energy-time' spectrogram format, in which the number of electrons per $\frac{1}{16}$ s is logarith-

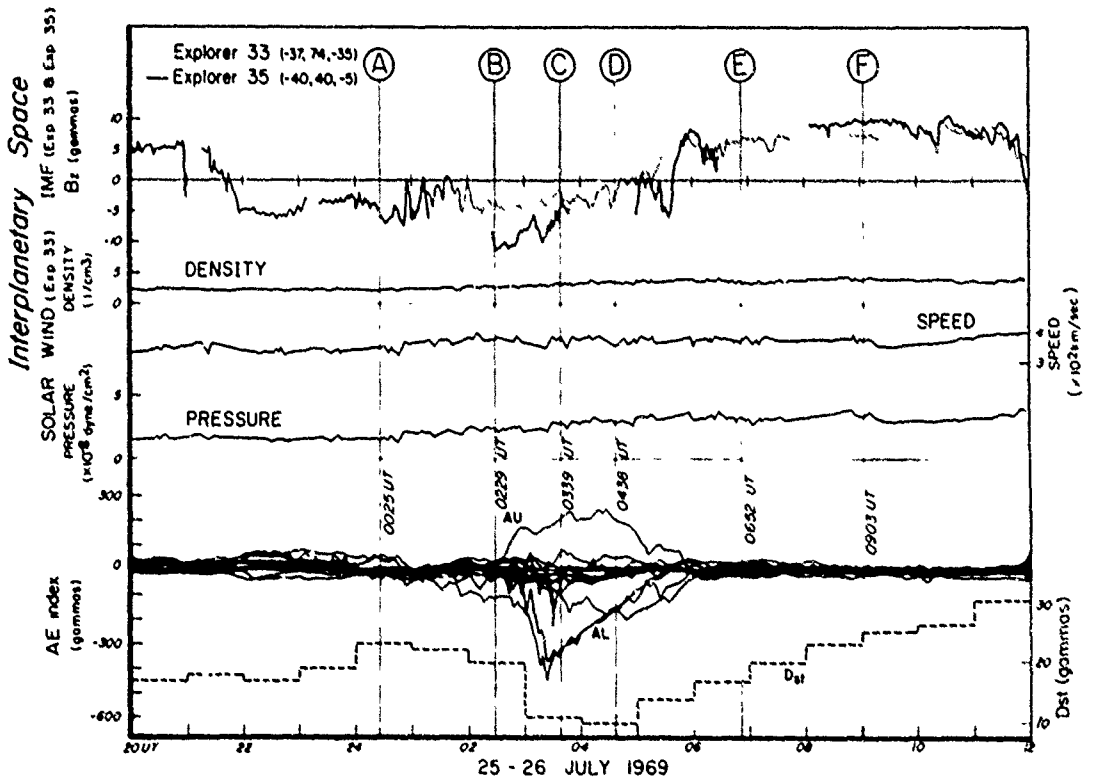

Fig. 1*b* Solar wind parameters and geomagnetic activity indices (*AE* and *Dst*) for July 25-26, 1969. The IMF is given by the B_z component in solar magnetospheric coordinates observed by two satellites. The times of the six Isis 1 passes, whose SPS data are shown in Figure 1*a*, are indicated by vertical lines A-F. The *AE* index is given by the separation between the upper and lower envelopes of the superposition of the *H* component magnetic records at auroral latitudes. Here, we used data from 11 observatories, which are College, Barrow, Cape Wellen, Tixie Bay, Cape Chelyuskin, Dixon Island, Abisko, Leirvogur, Narssarssuaq, Great Whale River, and Fort Churchill

mically coded as a shade of gray, with larger counts indicated by increasing whiteness. The ordinate is a logarithmic scale of energy, and the abscissa is linear in increasing spacecraft time. The scale of invariant latitude given at the top and the bottom of the spectrograms is adjusted to be most accurate at 65° for all the satellite orbits but becomes less accurate (although not seriously) at higher and lower latitudes. The magnetic local time of the satellite varied between 2000 and 2300 on these six passes.

In the SPS data shown in Figure 1*a* we can see two latitudinally separated precipitation regions with different characteristic patterns, the region of relatively uniform precipitation (with gradually increasing energy toward higher latitude) and the region of intense and highly structured precipitation located on the poleward edge of the auroral oval. Throughout the entire region of auroral precipitation the energy flux of protons was at least 1 order of magnitude lower than the electron energy flux [*Klumpar et al.*, 1976, *Lui et al.*, 1977]. *Winningham et al.* [1975] referred to the uniform precipitation region as the central plasma sheet (CPS) and to the intense and structured precipitation region as the boundary plasma sheet (BPS). In this paper we use the equatorward edge of the diffuse >100-eV electron precipitation (CPS) as the equatorward boundary of the diffuse aurora, which is indicated by an arrow for each pass. Note that the approximate collocation of the belt of the diffuse optical aurora and diffuse electron precipitation has recently been identified by the simultaneous observations by the auroral scanner and the SPS aboard the Isis 2 satellite [*Deehr et al.*, 1976; *Lui et al.*, 1977].

The corresponding interplanetary and geomagnetic data are shown in Figure 1*b*, plotted here, from the top, are the north-south component of the IMF in solar magnetospheric coordinates (Explorer 33 and 35), the solar wind density, velocity, and pressure (Explorer 33), the superposition of auroral zone *H* component magnetograms, and the *Dst* index. The IMF data show well-defined southward and northward turnings at about 2145 UT on July 25 and 0540 UT on July 26, respectively. Thus the southward field lasted for more than 7 hours, except for occasional brief northward turnings. There was no significant change in the number density, velocity, and pressure of the solar wind throughout the period of our interest. During the period of the predominantly southward-directed IMF, there occurred only one isolated substorm of medium intensity, at least 3 hours after the well-defined southward turning.

These six traverses of the nightside auroral precipitation zone by the satellite during this period are indicated by six vertical lines, denoted by A, B, C, D, E, and F in Figure 1*b*. Pass A took place about 3 hours after the southward turning, well before the ground magnetic records showed any sign of substorm activity (unfortunately, the Isis 1 data are not available for at least 12 hours prior to pass A). It is quite likely that the magnetosphere had adjusted itself to the IMF southward field by the time of pass A. Further, since there was then no appreciable geomagnetic activity, the latitude of the equatorward boundary of the diffuse auroral precipitation observed during pass A may be taken to be a typical value for a southward IMF of about 5 γ. On the other hand, pass F took place well after the northward turning and also during no substorm activity, so that the latitude of the equatorward boundary observed during pass F may be taken to be a typical value for a northward IMF of about 8 γ.

The equatorward boundary of the electron precipitation during passes B, C, D, and E may be affected by substorm activity, as well as by the IMF north-south component. During pass C a significant equatorward shift (~3.1°) of the equatorward boundary from the location observed during pass A occurred during the maximum phase of the substorm. It should be noted that pass C occurred over the southern hemisphere auroral region. As will be seen in the statistical examination given in the following section, the latitude of the equatorward boundary in the winter hemisphere (southern hemisphere in this particular example) tends to be higher than that in the summer hemisphere (northern hemisphere) by 1°-2°. Thus it may well be that the actual equatorward boundary in the northern hemisphere was located at somewhat lower latitudes than what was observed in the southern hemisphere. Unfortunately, there is a large difference in the B_z values observed at Explorer 33 and 35 at the time of pass B. If we assume that the Explorer 33 data reproduce closely the IMF near the magnetosphere, which controlled the state of the magnetosphere during this period, there was no significant difference of the B_z values between the times of passes B and C. Thus the shift (~1.6° or more) observed between the two passes may be attributed to the effect of the substorm. On the other hand, if we assume that the Explorer 35 data reproduce the needed values better than the Explorer 33 data do, we may infer that the shift associated with the substorm was partially masked by a significant decrease of the southward component, which could have caused a poleward shift of the oval, that is to say, the substorm-associated shift could have been larger than what the observed value of shift indicates. Thus in either case the observed equatorward shift during pass C may be attributed to the effect of the substorm. However, the northward shift observed during pass D took place during the period when the substorm was recovering and the magnitude of the southward component of the IMF was decreasing, so that it is difficult to separate the contributions of both effects.

The examples shown here point out the need for us to sort out the independent effect that the IMF and substorm activity have on the latitudinal shift of the nightside auroral precipitation region. Most of the observations for southward IMF were made during substorms, and thus it is difficult in individual cases to differentiate the latitudinal movement of the auroral belt caused by the IMF and by the development of a substorm. In the next section we will examine statistically the shift of the equatorward boundary of the electron precipitation on the basis of a large number of satellite passes.

STATISTICAL NIGHTSIDE AURORAL OVAL DATA SET

Appendix 1 summarizes the conditions under which all the 351 Isis 1 and 2 traverses occurred. It appears that the cases were collected quite uniformly and in sufficient numbers over such parameters as magnetic local time, polarity of the IMF, season, and substorm activity. Thus we believe that the present data set allows us to make some statistical tests.

We have utilized solar magnetospheric coordinates in describing the IMF. Here, we used the north-south component of the IMF (denoted by $\overline{B_z}$) averaged for 1 hour preceding the time of the satellite passage over the equatorward boundary of the diffuse auroral particle precipitation identified in the soft particle spectrogram data for each of the Isis passes. In calculating the 1-hour average IMF value the transit time for the interplanetary signal to the magnetopause (which was assumed to be located at $X = 10\ R_E$) was taken into account in each case, by assuming the solar wind speed to be 400 km s.

The observations were grouped into quiet periods and sub-

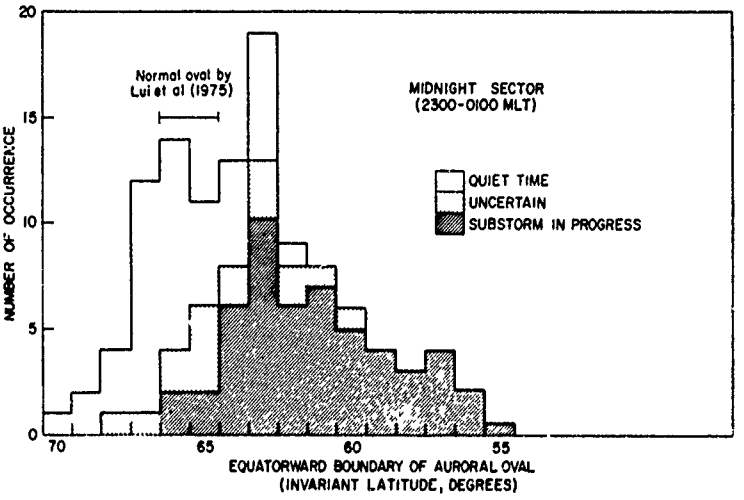

Fig. 2 Histogram showing the latitudinal distribution of the equatorward boundary of the diffuse electron precipitation in the midnight sector. The intervals of latitude θ (in degrees) are defined such that θ represents $\theta \pm 0.5$. Symbols for different categories of substorm activity are defined in the inset. The latitudinal area of the normal auroral oval defined by *Lui et al.* [1975] on the basis of 58 auroral images is also indicated.

storm times. This division was made primarily by referring to the presence of a sharp increase of the *AE* index [*Allen et al.*, 1974, 1975*a*, *b*] and of structured discrete auroral precipitation in the SPS data; for the typical pattern of the spectrogram corresponding to quiet and substorm times, see *Winningham et al.* [1975] We also checked carefully individual magnetograms whenever it was necessary. It was, however, sometimes impossible to determine, from the *AE* index and available geomagnetic records at individual observatories and the SPS data, whether there occurred polar substorms or just minor fluctuations. These cases are represented by 'uncertain' in Appendix 1.

Distribution of the Oval Latitude Around Midnight

The histogram in Figure 2 shows the latitudinal distribution of the equatorward electron boundary defining the auroral oval near magnetic midnight. This was obtained from a partial data set (113 satellite passes) in which the boundary crossing occurred between 2300 and 0100 MLT. The histogram is essentially the same as Figure 2*b* of *Lui et al.* [1975], except that they classified substorm conditions into three categories (quiet condition, bright aurora, and substorm in progress) in terms of global auroral features, whereas we defined them by geomagnetic activity and the pattern of the auroral particle precipitation. The invariant latitude of the boundary is found to vary between 55° and 70°, the most probable latitude being 63° for this particular data set. Although there is general agreement with *Lui et al.* [1975], it appears that the latitudes of these data are distributed somewhat lower than those presented by *Lui et al.* [1975] This apparent difference may be explained by the different data sets used in the two independent studies Namely, our data set includes more disturbed periods than that examined by *Lui et al* [1975], and they examined only data from the winter season in which the auroral oval is found to lie in higher latitudes than it does in summer season data Also, as was mentioned earlier, their study involved the 3914-Å and 5577-Å emission lines which are most indicative of >1-keV electrons Our study delineates the >100-eV electron boundary which would more closely relate to the 6300-Å line. The work of *Winningham et al.* [1975] demonstrated the softness of the electron spectrum at the equatorward edge of the CPS.

It is one of the striking features in Figure 2 that with the decrease of latitude the probability of seeing a substorm increases while the probability of observing a quiet oval decreases. The probability of observing a substorm along the expanded oval (i.e., <60°) is essentially 100%. It is also noticeable that the probability of seeing substorm activity decreases to about 50-60% along the oval which is located at 63°-64° invariant latitude. It is, however, uncertain at present whether this probability of seeing substorms by the Isis satellites represents the probability of substorm occurrence. We must be careful in discussing these two probabilities by taking the following facts into account: First, substorms along the contracted oval tend to recover faster than the intense ones along the expanded oval [*Montbriand*, 1971], so that data taken every 2 hours by a polar-orbiting satellite cannot properly monitor the substorm occurrence frequency. Second, *Kamide and Akasofu* [1974] have shown that weak substorms tend to occur along the contracted oval, whereas intense ones tend to occur along the expanded oval. Thus it may well be that some of the cases which we identified as 'uncertain' take place during weak substorms of which the latitudinal pattern of the auroral particle is somewhat different from that of the normal substorm.

We also applied the same method to the data of the other local time sectors and found results similar to the above. This work will be the subject of a separate paper.

Effect of the Interplanetary Magnetic Field

In Figure 3*a* the invariant latitudes of the equatorward boundary of the diffuse aurora are plotted as a function of the corresponding B_z values of the IMF (averaged over 1 hour preceding the satellite passage time) for the 33 orbits available between 2000-2100 MLT. The observations made during quiet periods are shown by open circles (for summer season) or open squares (for winter season), and those made during substorms

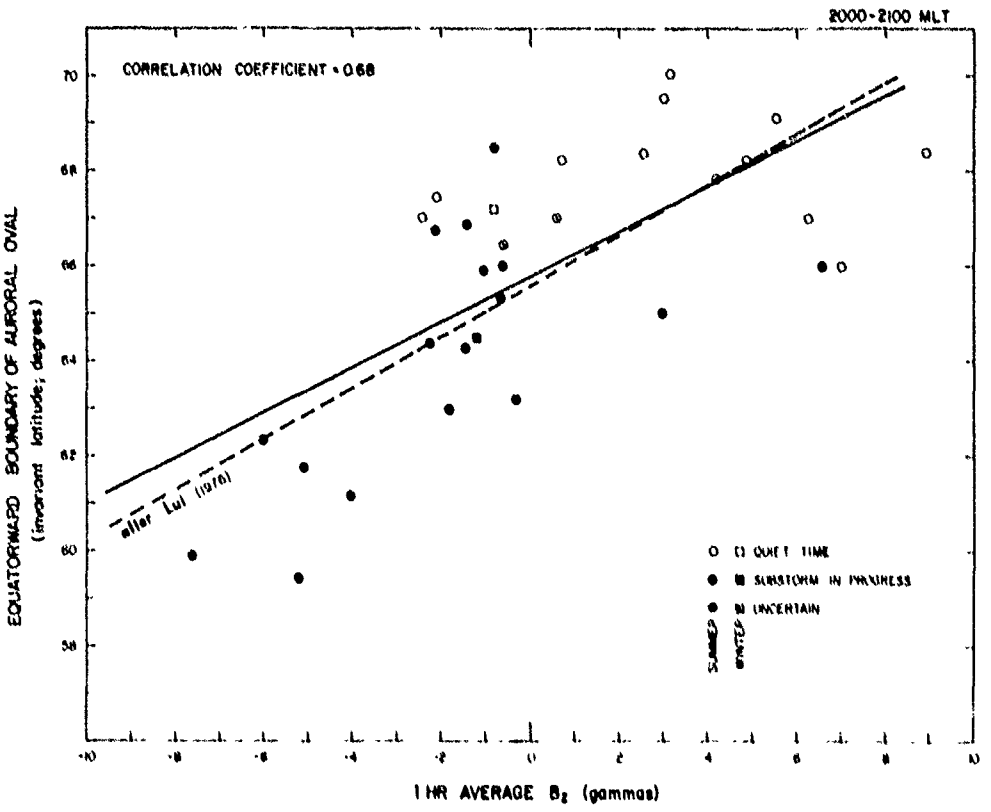

Fig. 3a. Equatorward boundary of the >100-eV electron precipitation plotted on the corresponding B_z value of the IMF for 2000-2100 MLT. The symbols used to distinguish different substorm activities are defined in the inset. The least squares fit is indicated by the solid line, whereas the relationship obtained by A. T. Y. Lui (unpublished manuscript, 1976) for 2000 MLT is shown by the dashed line.

are marked by solid circles or solid squares. For two cases we found some small magnetic disturbances in the AE variation, but we could not determine whether these were substorm effects. These points are identified by double circles and double squares. Most points are well confined to an area whose center line can roughly be expressed by

$$\text{invariant latitude (deg)} = 0.48\bar{B}_z(\gamma) + 65.8$$

This fit was determined by the least squares method and is shown by a solid line. Also shown in Figure 3a, by a dashed line, is a linear relationship (A. T. Y. Lui, unpublished manuscript, 1976). Lui used 31 Isis 2 auroral images to identify the equatorward boundary of the diffuse aurora at 2000 MLT as a function of the corresponding B_z values of the IMF. These two independently obtained relations are found to be in good agreement.

We have obtained similar relationships between the oval location and the B_z component of the IMF for every 1-hour MLT interval from 2100 to 0400. The statistical results are given in Table 1. In Figures 3b and 3c we show, as further examples, the relationships for 2200-2300 and 0100-0200 MLT, respectively.

It should be noted that a substorm effect (see the next subsection) is possibly contaminated in the results presented in Figures 3a-3c, especially in determining the average IMF dependence. In fact, one may claim that if only the quiet time data are treated, there would be little or no dependence on B_z discernible in the scattered points in Figures 3a-3c. However, we show in Figure 3d that there is really a systematic equatorward (or poleward) motion of the nightside auroral oval in conjunction with the decrease (or increase) in the B_z value. After eliminating all times with substorm activity or when minor magnetic disturbances were present, Figure 3d shows the distribution of all quiet time data for the evening and morning sectors, separately. Observational points made in the same hemisphere within 6 hours are connected with solid lines. Although some scatter would be expected because of the wide local time span (4 hours) and unknown magnetospheric configuration associated with magnetic conditions prior to the

TABLE 1. Statistical Characteristics of the Nightside Electron Precipitation Boundary Λ as a Function of the B_z Component of the IMF

MLT Range	a	Λ_0	Correlation Coefficient	Cases
2000-2100	0.48	65.8	0.68	31
2100-2200	0.50	65.7	0.61	51
2200-2300	0.49	65.4	0.71	56
2300-2400	0.46	64.5	0.51	56
0000-0100	0.74	63.4	0.56	57
0100-0200	0.76	64.1	0.53	45
0200-0300	0.61	63.1	0.42	43
0300-0400	1.38	64.6	0.63	8
Total	0.60	64.5	0.55	151

Coefficients are obtained by the least squares fit Λ (deg) = $aB_z(\gamma) + \Lambda_0$.

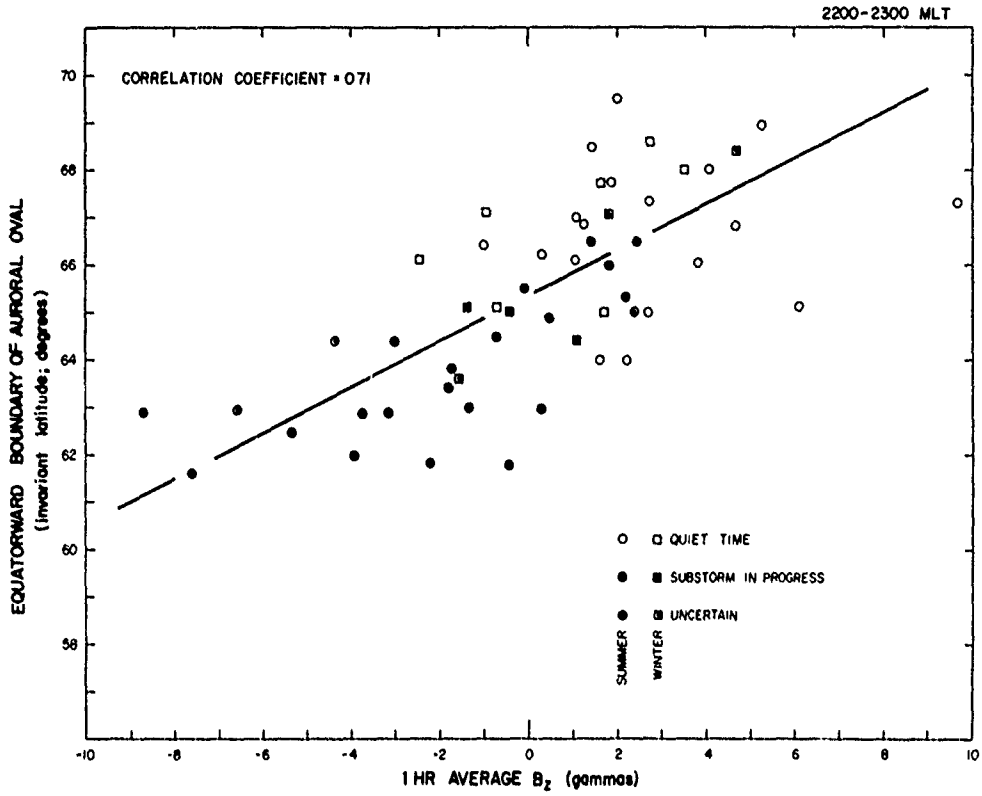

Fig. 3b Same as Figure 3a except for local time sector 2200–2300 MLT

'quiet times,' the previously noted B_z dependence can clearly be seen with few exceptions, especially when successive data points are considered.

From Figures 3a–3d we note the following characteristics: (1) The north-south component of the IMF is one of the important factors that controls the location of the equatorward boundary of the nightside auroral oval. Even when the IMF is directed northward, a significant equatorward shift of the auroral oval boundary is observed in conjunction with the decrease in the magnitude of the B_z component. (2) For a given B_z value (say, $B_z = 0$) the equatorward boundary of the auroral oval is generally located at lower latitudes in the morning sector than in the evening sector. This is in good agreement with the 'classical' optical auroral oval as given by *Feldstein and Starkov* [1967] and *Starkov* [1969]. (3) The magnitude of the shift in invariant latitude at various local times is not statistically the same for a given change in the B_z value but has a significant local time dependence. It was found from the least squares fits that the equatorward boundary of the auroral oval shifts equatorward by 0.49° and 0.76°, corresponding to the 1-γ decrease of the B_z value in the 2100–2200 and 0100–0200 MLT sectors, respectively; note that the correlation coefficient in the morning sector is rather low. In order to show that this local time dependence of the oval response to the IMF is not the effect of the biased data set in terms of the B_z (or B_y) component of the IMF we show the distribution of all the observation points in (MLT, B_z) coordinates in Figure 4. It can be seen that there is no biased relationship between MLT and B_z in the present particular data set, all 351 points are distributed quite uniformly over the parameters.

Figure 5 shows the average location of the equatorward boundary of the auroral oval in invariant latitude-MLT coordinates for three different B_z values, 5 γ, 0 γ, and −5 γ. It can be seen clearly in this diagram that the IMF dependence of the oval location in the morning sector is stronger than that in the evening sector. When the B_z value decreases from 5 γ to −5 γ, the boundary tends to move equatorward from about 68° to 60° in the morning sector and only from 68° to 63° in the evening sector. This motion of the auroral oval will be discussed in more detail later in conjunction with the drift boundary of low-energy plasma sheet particles.

Substorm Effect

The magnetospheric substorm may be another factor which controls the location of the equatorward boundary of the nightside auroral oval. However, it is generally difficult to single out this effect in individual events, since other factors such as the north-south component of the IMF are also involved in complicated ways. Only a statistical analysis will define any possible substorm effect.

It is clear in Figure 3 that almost all the points observed during substorms lie below the solid lines. It should be remembered that the solid lines represent the average latitude of the >100-eV electron boundary determined empirically on the basis of the B_z values of the IMF only. In contrast, the oval equatorward boundary during quiet times is located at higher latitudes than the statistical solid lines. This feature can be clearly seen in the range of $-2\ \gamma < B_z < 2\ \gamma$, where the sample number for quiet times is almost the same as that for disturbed

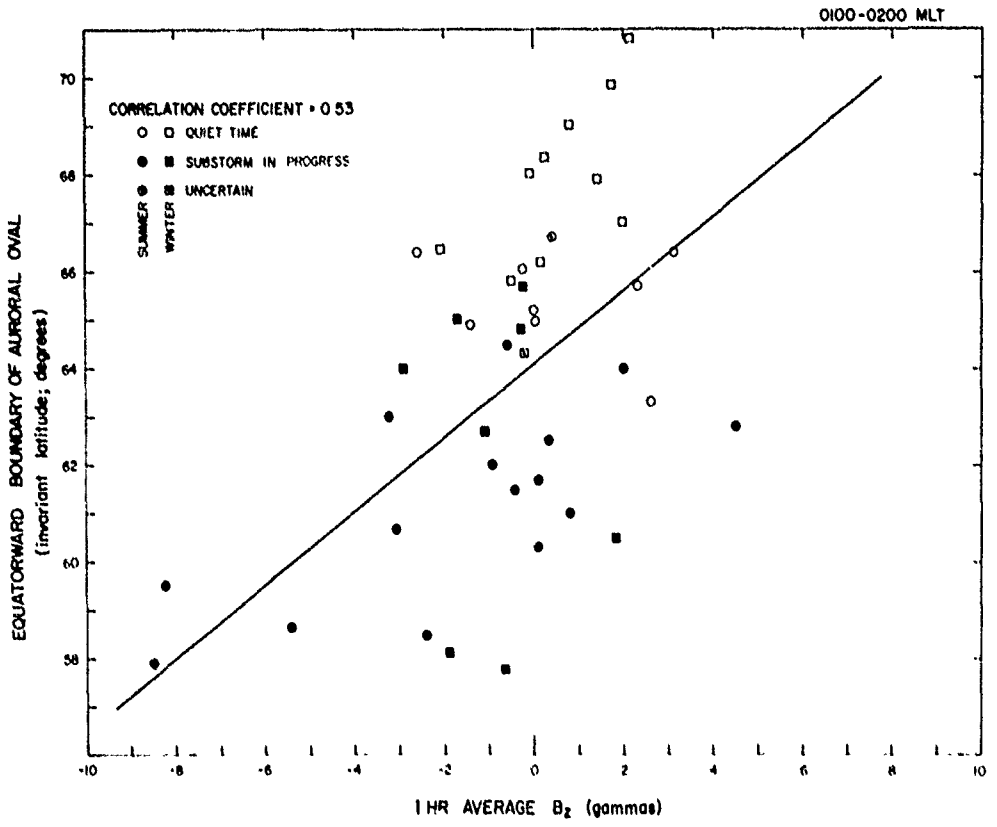

Fig. 3c Same as Figure 3a except for local time sector 0100-0200 MLT

times The fact that almost all the passes for the southward IMF with large amplitude took place during substorms makes separation of the IMF and substorm effects difficult.

In Figure 6 we show the invariant latitude of the equatorward boundary of the auroral electrons in the sector 2300-0100 MLT as a function of the *AL* index, which may represent the maximum intensity of the westward electrojet. Since we first eliminated all times during magnetic storms, the *AL* index ranges from quiet to moderately disturbed activity values There is a considerable scatter in the latitude for a given *AL* value Nevertheless, there is a trend for the latitude (in particular, the highest latitude for a given *AL* value approximated by the dashed line) to move equatorward for greater electrojet activity The scatter of the points may be explained by one or both of the following reasons

1 The *AL* index is not the most suitable index for monitoring properly the substorm intensity mainly because of an inadequate network of the present observatories along the auroral belt Thus it may well be that the actual auroral electrojet is more intense than what the index indicates In other words, if we could plot the real value of the electrojet intensity as abscissa, the distributed points would tend to be shifted towards the left hand side approaching the dashed line

2 As has been shown previously, the north south component of the IMF has the main role in controlling the latitude of the auroral oval, and its effect is included in Figure 6 If we could identify the separate roles of the IMF and substorm activity (although it is difficult), some of the scattered points would tend to be moved upward, thus approaching again the dashed line

Effect of Earth's Dipole Tilt (Seasonal Change)

The tilt angle dependence of the equatorward boundary of the nightside auroral oval has also been studied, after eliminating all times when there was a southward IMF and a northward IMF with large magnitude (greater than 4 γ) We have also eliminated all cases before 2100 and after 0300 MLT, since the number of samples in these local time sectors is not large enough to allow us to single out the seasonal effect Note, however, that the data set is still not uniform enough over seasons and universal time for us to examine the dependence on the wide range of the tilt angle (±35°), since our data were taken mostly from two different seasons June, July, and August, and November, December, and January Nevertheless, a systematic seasonal dependence was found In Figure 7 we show the average location of the equatorward boundary of the diffuse aurora as a function of MLT for the winter and summer hemispheres, separately In a total of 129 cases (82 for the summer hemisphere and 47 for winter) there is a seasonal shift of 1°-2° in the invariant latitude, which is found to be a little weaker tilt angle dependence than that for the cleft latitude *Burch* [1972] has shown that there is a total seasonal shift of 4° in the cleft latitude even for quiet time observations Note that the sign of the seasonal shift is reversed between the cleft and

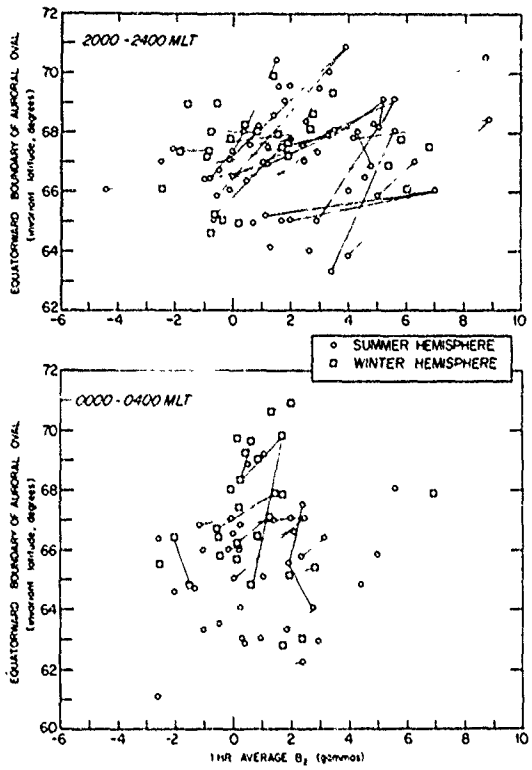

Fig. 3d. Equatorward boundary of the auroral precipitation during quiet periods plotted on the corresponding B_z value of the IMF for the evening and morning sectors (2000–2400 and 0000–0400 MLT, respectively). Symbols used to distinguish different seasons are defined in the inset. The observations made within 6 hours in the same hemisphere are connected with solid lines.

nightside oval latitudes, in agreement with the field line configuration modeled by *Mead and Fairfield* [1975].

This same summer-winter asymmetry can be found in Figure 3, where cases for the winter season are marked by squares. Points in the winter season generally lie in higher latitudes than points in the summer season, except for several points in the 0100–0200 MLT sector (Figure 3c) which occurred during substorms.

On the basis of the magnetospheric configuration model obtained by *Mead and Fairfield* [1975], *Fairfield and Mead* [1975] calculated the latitudes where field lines originating from the synchronous satellite orbit at 6.6 R_E in the equatorial plane intersect the earth for different tilt angles, see Figure 8 of *Fairfield and Mead* [1975]. They found that the earth intersection location is approximately 1° higher in the winter hemisphere than in the summer hemisphere, which is in good agreement with the present observations by the Isis satellites given in Figure 7.

Discussion

Limitations of the Present Study

In this study we have constructed the statistical configuration of the equatorward boundary of the nightside >100-eV electron precipitation at hourly local time intervals as functions of the north-south component of the IMF, substorm activity, and the dipole tilt angle. However, several factors limit the usefulness of the location of the nightside auroral oval presented in this paper. First of all, only the equatorward boundary of the diffuse auroral particle precipitation is presented to characterize the size of the auroral oval. We have not considered the boundaries of the discrete aurora, which are usually located near the poleward boundary of the diffuse aurora. This is simply because the equatorward boundary of the diffuse aurora is relatively steady in comparison with the boundaries of the discrete aurora. Thus the use of the discrete aurora boundary from a polar-orbiting satellite with the long orbital period is inadequate for a statistical study; the electron and proton flux distribution over the discrete auroral region is highly variable during a polar substorm. In particular, if the satellite passes through the auroral surge or torch structure, which is one of the main substorm features of the discrete aurora, the poleward boundary of the discrete aurora depends strongly on which portion of this structure is traversed latitudinally by the satellite. In such a case a 5° error can be easily introduced.

Second, the obtained oval location can only represent an average configuration of the equatorward boundary and cannot represent the rapid change that might take place between successive satellite orbits [*Eather*, 1973; *Creutzberg*, 1976]. This is limited by the availability of the data, as well as by the method of calculating the IMF value. Although in this study an average value of the IMF over 1 hour was used as a typical value of the IMF, different values can of course be obtained by choosing different combinations of time delay (of the oval in response to the IMF) and time interval (over which the IMF is averaged). Such an extension to include time variations at different local times would obviously be highly desirable.

Finally, no *Dst* effect was taken into consideration in the present statistical analysis by eliminating cases in which the *Dst* was below −40 γ. In the 351 cases examined, no significant dependence of the oval location on the *Dst* index was found. In other words, the *Dst* effect, if any, is small in this *Dst* range. *Akasofu and Chapman* [1963] showed that the latitude of the equatorward boundary of the 'classical' auroral oval varied for different intensities of magnetic storms, sometimes being as low as 50° in geomagnetic latitude during large storms. Since there is a close relationship between *Dst* and the IMF (and also substorm activity), it is at present uncertain whether the *Dst* effect indicated by *Akasofu and Chapman* [1963] is included in the IMF and substorm effects examined in this study. This point could be checked by using a larger data set including a variety of magnetic storms.

Equatorward Boundary of the Diffuse Aurora

Lui et al. [1975] found the equatorward boundary of the diffuse auroral belt at local midnight to be a useful parameter in characterizing the size of the auroral oval and thus of the polar cap. We have amplified their results to all local times of the night sector and by including the IMF effect.

It should be stressed that the distinction between the diffuse and discrete auroras is important in studying auroral physics and associated magnetospheric structure. Although it is not the intent here to repeat the description of the characteristic difference between these two types of auroras, we would like to note that the equatorward boundary of the diffuse aurora corresponds to the inner (earthward) edge of the plasma sheet [*Eather and Mende*, 1971; *Lassen*, 1974; *Winningham et al.*, 1975; *Lui et al.*, 1977]. As is shown in the examples in Figure 1a, there is a gradual decrease in the energy of plasma particles with decreasing latitude in the diffuse aurora region. Similar 'softening' of the electrons has been reported near the inner

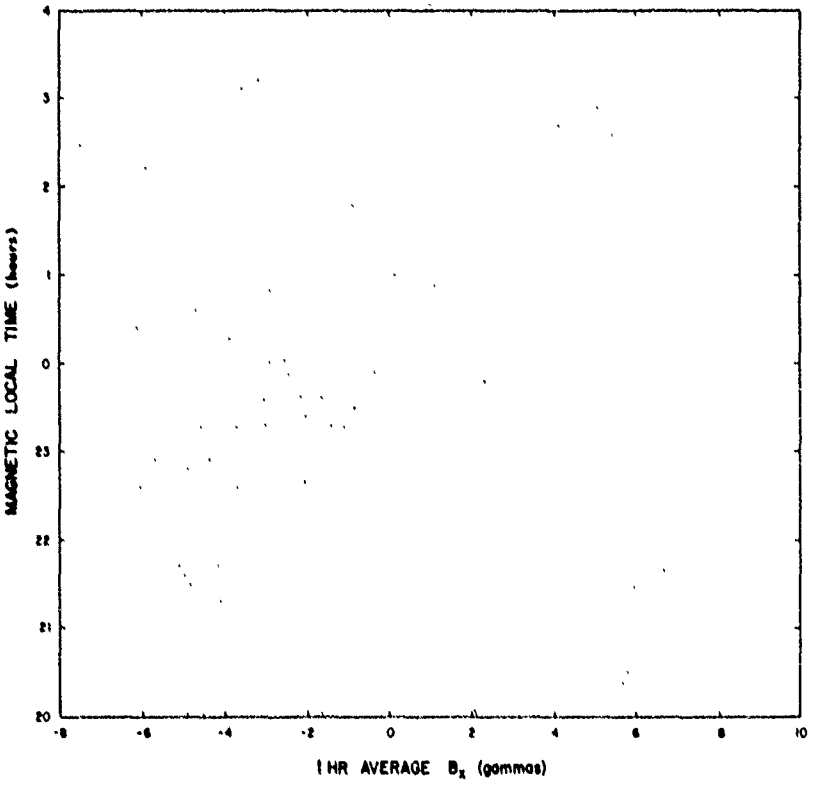

Fig. 4 Distribution of 351 passes in the 'MLT, B_z' coordinates. It is seen in this diagram that all points are distributed quite uniformly.

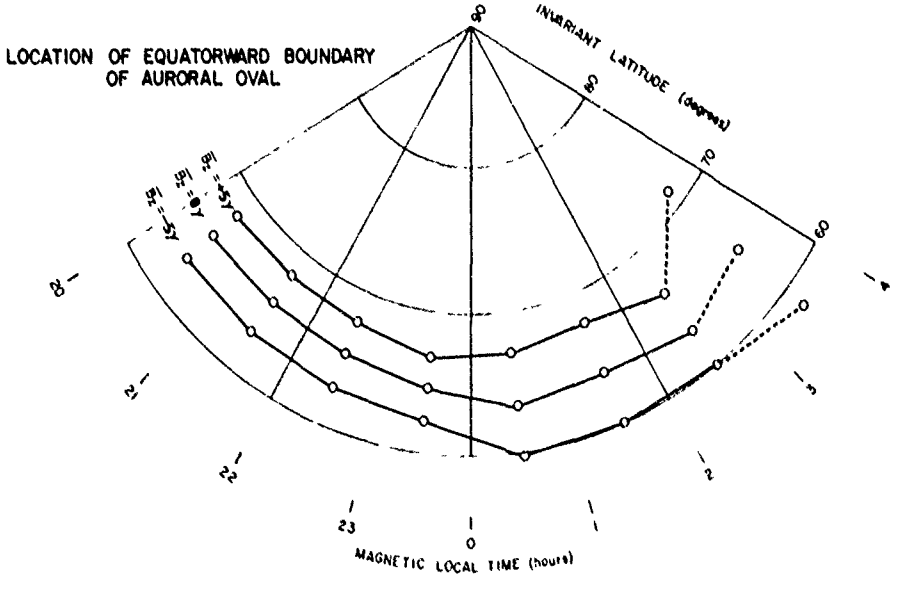

Fig. 5 Location of the equatorward boundary of the diffuse electron precipitation at different local times in the dark sector for three B_z values of the IMF. Since only eight data points were used in the statistics for the 0300-0400 MLT interval, the B_z dependence is shown by dashed lines in this local time sector.

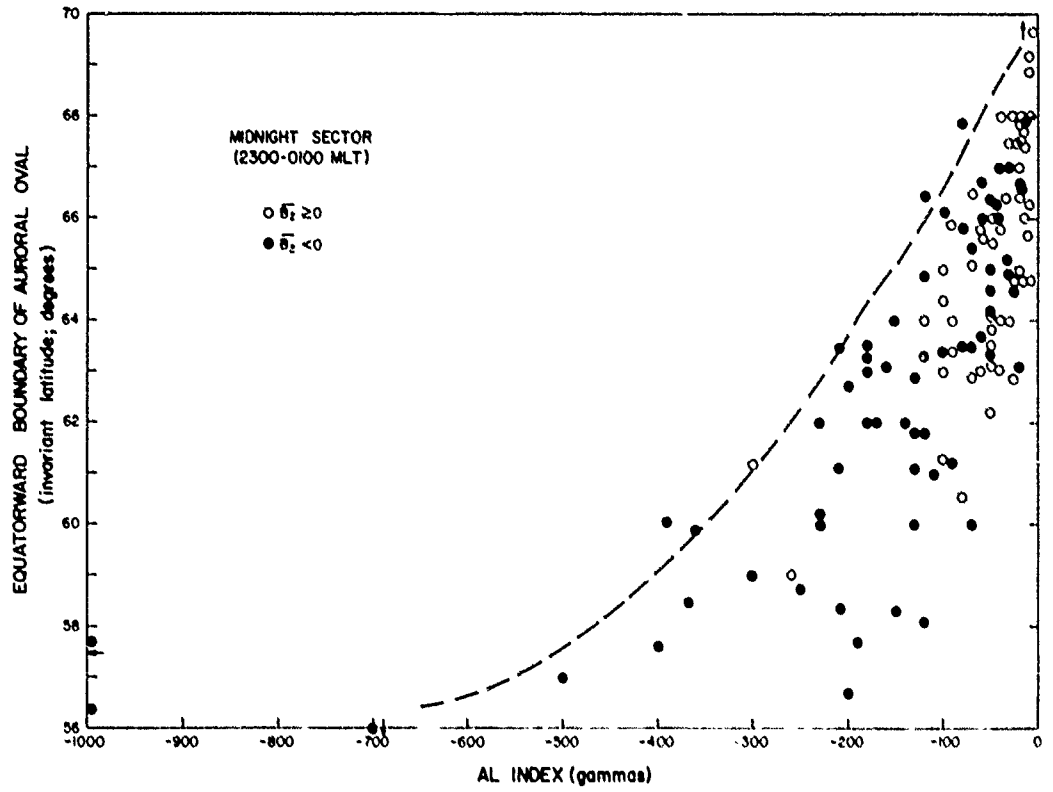

Fig. 6. Location of the equatorward boundary of the diffuse electron precipitation in the dark sector as a function of the auroral electrojet AL index. Symbols used to distinguish the sign of the B_z component of the IMF are defined in the inset. The dashed line indicates the maximum electrojet activity for a given latitude of the precipitation boundary.

edge of the plasma sheet by *Vasyliunas* [1968], *Frank* [1971], and others.

Effect of the Interplanetary Magnetic Field

Several workers [*Burch*, 1972, 1973, *Yasuhara et al.*, 1973, *Kamide et al.*, 1976] have presented clear evidence of an equatorward shift of the cleft associated with the southward IMF. This paper has statistically shown that the north-south component of the IMF plays the dominant role in determining the location of the nightside auroral oval. The equatorward boundary of the diffuse auroral precipitation during periods of southward IMF is found at lower latitudes than during northward IMF. This IMF effect is observed at all local times in the dark sector.

The role of the southward IMF in initiating magnetospheric convection and the net transport of the magnetic flux into the magnetotail has been discussed in the literature [*Coroniti and Kennel*, 1973, *Burch*, 1973, *Kan and Akasofu*, 1974]. That is, the efficiency of the flux transport depends on the amount of the southward IMF flux impinging on the magnetosphere. One of the manifestations of the process near the earth is the enhancement of the electric field across the polar cap, and another is the expansion of the polar cap. The latter has recently been confirmed by *Holzworth and Meng* [1975], who correlated the area of the polar cap with the IMF. It may be noted that a significant equatorward shift of the oval boundary is observed in association with the decrease in the B_z magnitude even during the northward IMF (see Figure 3). This fact indicates that the dawn-dusk electric field does not vanish when $B_z = 0$. This indication does not seem to be in accord with the suggestion by *Burton et al.* [1975] and *Caan et al.* [1977], who showed that only the southward-oriented IMF is important in the development of substorms and storms.

Our statistical analysis has indicated that the magnitude of the latitudinal shift in conjunction with the IMF change is not necessarily the same at all local times but has a local time dependence as shown in Figures 3 and 5. For a given change in the B_z component of the IMF, the response of the auroral oval in the morning sector seems stronger than in the evening sector. To recapitulate, we show in Figure 8 for each of the B_z values (+5, 0, and −5 γ) the approximate location in the equatorial plane of the magnetosphere that corresponds to the equatorward boundary of the nightside auroral oval. Here we have projected the boundary latitude obtained from the Isis satellites along the magnetic field lines given as MF73D (for $Kp = 2$) by *Fairfield and Mead* [1975]. The use of different magnetospheric models has been found to make no significant change in the gross features, except for $B_z = -5$ γ in which the corresponding boundary is in the distant tail. The evening-morning asymmetry is evident in that for a change in the B_z value from +5 to −5 γ the boundary moves approximately from $L = 9$ to $L = 5$ at 2100 MLT, whereas it changes from $L = 12$ to $L = 4$ at 0300 MLT. Similar characteristics can be noticed in the inner boundary of the plasma sheet observed by *Vasyliunas* [1968], although he examined the boundary crossing by satellite only in the premidnight sector; there is a tendency for the radial distance of the plasma sheet inner edge to decrease with increasing local time, i.e., approaching mid-

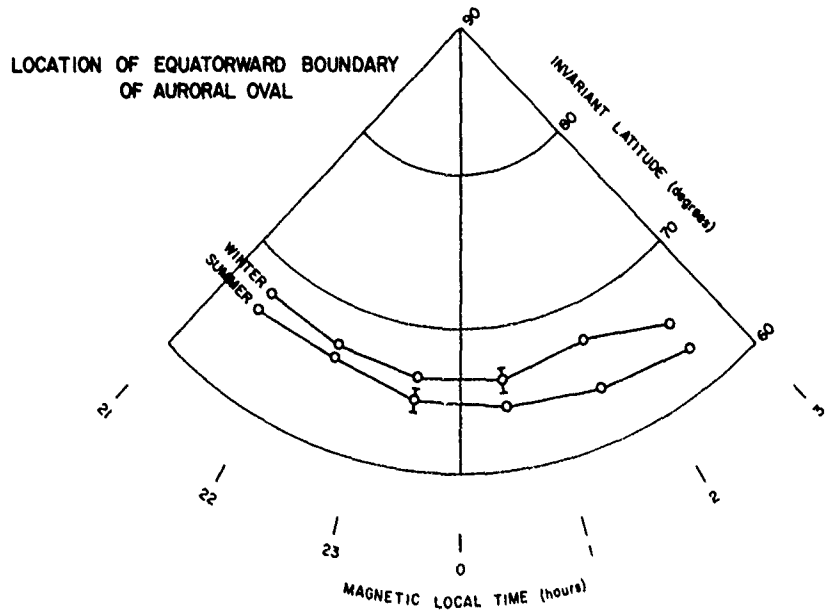

Fig. 7. Location of the equatorward boundary of the diffuse electron precipitation at different local times in the dark sector for the winter and summer hemispheres. Standard deviations are also given.

night; see his Figures 20 and 24. More recently, *Mauk and McIlwain* [1974] and *Freeman* [1974] have shown that the injection of low-energy particles at geostationary orbit is observed at earlier local times at higher *Kp* index. Since the *Kp* index is highly correlated with the dawn-dusk electric field [*Mozer and Lucht*, 1974; *Kivelson*, 1976], those observations indicate that for a given uniform dawn-dusk electric field the injection boundary is located closer to the earth at later local times.

This local time dependence of the location of the plasma sheet inner boundary inferred from the present study of the auroral precipitation boundary may be accounted for by the low-energy plasma motion in the magnetotail in which a large-scale uniform electric field is superimposed on the corotation electric field. In such a situation, plasmas drifting from the distant tail toward the earth terminate at the boundary called the Alfven layer [*Alfvén*, 1939; *Alfvén and Fälthammar*, 1963]. Inside the boundary the drift orbits of particles encircle the earth. The location of the Alfvén layer can be obtained for a particle of magnetic moment μ by tracing the particle trajectories [*Kavanagh et al.*, 1968; *Schield et al.*, 1969; *Chen*, 1970] A simple discussion of the particle drift boundary is included in Appendix 2.

The two dotted lines in Figure 8 represent the locations of the Alfvén layers for electrons and protons with $\mu = 0$ in the presence of the 0.4-mV/m and 0.17-mV/m electric fields in the tail to compare them with our oval boundaries for $\bar{B}_z = -5\ \gamma$ and $0\ \gamma$, respectively. The 0.4-mV/m and 0.17-mV/m values are derived from an empirical relation [*Gonzalez and Mozer*, 1974] between $\bar{B}_z$ and the electrostatic field (see Appendix 2) Note that the Alfvén layer for electrons with higher μ (for example, $\mu = 0.005$ keV/γ corresponding to 100-eV electrons in the tail) is located slightly outward of the shown boundary for each electric field strength A good agreement can be seen between the Alfvén layers and the auroral oval boundaries, which are projected onto the equatorial plane of the magnetosphere along the field lines Displacement of the plasma sheet boundary more inward in the morning sector than in the evening sector can be simply explained by considering that the drifts of particles (except high-energy protons) due to the tail electric field and the corotation electric field supplement each other in the morning sector, whereas they oppose each other in the evening sector. Thus this good agreement gives new evidence indicating that the diffuse electrons originate in the inner boundary of the plasma sheet.

It is noted, however, that there is no reason to believe that the electric field that was assumed in obtaining the drift boundaries is uniform across the entire magnetotail Furthermore, an asymmetry of the magnetic field between the morning sector and evening sector may not be neglected in the explanation of the local time dependence of the IMF response of the plasma sheet boundary. That is, the magnetic field in the evening sector is always inflated owing to the partial ring current which develops in conjunction with the southward IMF [*Kamide*, 1974], thus indicating the stronger magnetic field there than at the same L value in the morning sector. This difference between the morning and evening sectors causes a difference in the drift velocity of plasma sheet particles, which is faster in the morning sector than in the evening sector

The following points should further be noted in interpreting the statistical results presented in this paper: First, although the statistical behavior of the oval boundary was obtained in terms of the IMF, this may include the substorm effect in particular for cases with the southward IMF with large magnitude. Thus the evening-morning asymmetry of the response may actually be affected by the particular behavior of the tail particles in response to the substorm expansion Second, there are some errors in using the static magnetospheric configuration to project the ionospheric points to the equatorial plane of the magnetotail

Substorm Effect

In this study we have also identified the separate role of substorm activity from the IMF effect in controlling the lati-

tude of the electron precipitation boundary It has been indicated that the occurrence of substorms has been shown to add noticeably to the equatorward shift of the boundary, although it is not easy to distinguish the substorm effect from the IMF effect during individual cases. This equatorward motion of the region of the diffuse aurora by a few degrees can clearly be identified in all cases shown by *Snyder and Akasofu* [1972], who examined the 'cross section' of the auroral oval as observed by the Alaskan meridian chain of all-sky cameras

Vasyliunas [1968] showed the radial distance of the Ogo 1 crossings of the plasma sheet inner boundary in the evening sector with the division into two classes, quiet time and substorm time. It was found that all the observed crossings at times of substorm activity occurred earthward of those with no activity. This is also in agreement with our results.

The substorm effect (mainly an increase in flux producing the diffuse aurora) has been reported by *Winningham et al.* [1975]. Its pattern is relatively stable during substorms in comparison with the structured discrete aurora The enhancement of the brightness of the diffuse aurora during substorms can easily be found in the auroral images observed repeatedly by Isis 2 and DMSP satellites

It is not obvious why the equatorward boundary of the nightside auroral oval during substorms is located more equatorward than its quiet time position, regardless of the well-known 'poleward expansion' of the discrete aurora during the expansive phase of substorms. There is, however, at least one possibility of explaining the process which causes the equatorward shift of the boundary In their recent model calculation for a substorm, *Yasuhara et al* [1975] have shown that a three-dimensional current system can shift the nightside auroral oval poleward by several degrees This current system, proposed by *Akasofu* [1972], *Kamide and Fukushima* [1972], *Crooker and McPherron* [1972], and *McPherron et al.* [1973] to explain the ground magnetic distribution occurring in the course of substorms, consists of a flow into the morning part of the auroral oval along magnetic field lines, along the auroral oval, and out from the evening part of the oval along field lines On the other hand, the Triad satellite observations have recently revealed that the field-aligned current system is not so simple as above but is of double structure in all local times, consisting of two oppositely directed currents [*Zmuda and Armstrong*, 1974]. Indeed, *Kamide and Akasofu* [1976] have shown that in the evening sector the region of the upward field-aligned current on the poleward side of the oval coincides well with the region of the discrete aurora and that the downward field-aligned current on the equatorward side of the oval corresponds to the diffuse aurora. Thus the enhancement of this field-aligned current system on the equatorward half of the oval (upward in the morning sector and downward in the evening sector) during substorms can produce the equatorward motion of the equatorward half of the oval by a few degrees, since such a system produces the inflation of the magnetic field there.

Contracted Oval

The present study confirms the earlier works by *Feldstein and Starkov* [1967], *Stringer and Belon* [1967], *Starkov* [1969], *Lassen* [1972], and *Lui et al.* [1975] indicating that the auroral oval is quite dynamic, it expands and contracts, as is evident from the histogram given in Figure 2 *Berkey and Kamide* [1976] showed by use of DMSP auroral photographs during quiet periods that the size of the auroral oval is highly sensitive even to relatively small changes in the geomagnetic activity Our study has shown the minimum size of the auroral oval to be located at 70° in invariant latitude near midnight It should be noted that the parameter we have used in this paper to characterize the 'size of the oval' is the latitude of the equatorward boundary of the diffuse aurora Therefore since the width of the diffuse auroral belt is usually of a few degrees and there is the discrete aurora poleward of it, the actual size of the polar cap, which seems to relate more directly to the IMF, is a few degrees smaller than what Figure 2 indicates.

The equatorward boundary of the diffuse aurora at the 70° invariant latitude around midnight can be mapped to the inner termination of the plasma sheet at 12–17 R_E (depending on different models) by using recent magnetospheric configuration models constructed by *Mead and Fairfield* [1975] The

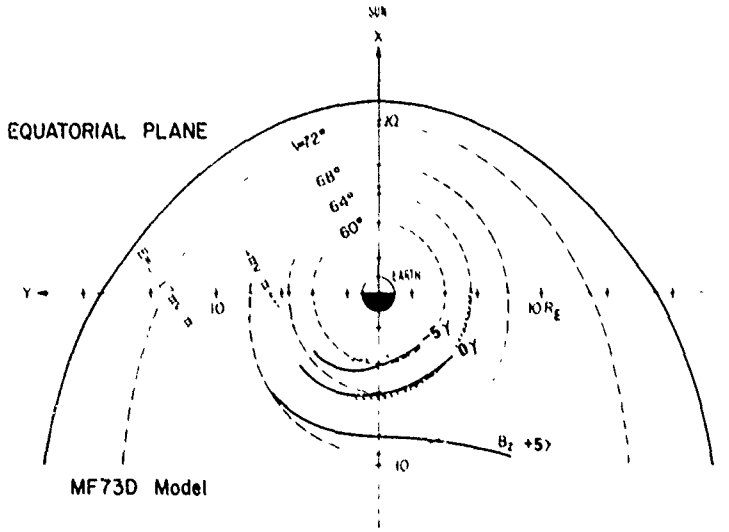

Fig 8 Location of the oval boundary for different B_z values of the IMF The boundary location in the equatorial plane was obtained by projecting the location of the electron precipitation boundary along magnetic field lines of MF73D model [*Mead and Fairfield* 1975] The Alfven layers for electrons and protons with μ (magnetic moment) equal to 0 in the presence of 0.4 mV m and 0.17-mV m dawn-dusk electric fields are shown by dotted lines (see Appendix 2)

contracted oval is probably associated with a weaker dawn-to-dusk electric field across the magnetotail. It has been shown that if a substorm takes place along the contracted oval, it is weak in terms of the optical energy and Joule heat energy [*Kamide and Akasofu*, 1974; *Akasofu and Kamide*, 1976].

It has also been shown in Figure 2 that the probability of seeing substorms decreases as the oval contracts. This is in good agreement with the finding of *Lui et al.* [1975], who identified the occurrence of a substorm in terms of the auroral pattern. As has been suggested by *Lui et al.* [1975], the probability of seeing substorms is not equivalent to their probability of occurrence. However, since the probability of observing substorms along the expanded oval is 100% (see Figure 2) and substorms are absent during a prolonged period of a large northward IMF [*Akasofu*, 1975], it is not unreasonable to assume that there is a latitudinal dependence of the substorm occurrence frequency.

APPENDIX 1

The following tabulation summarizes conditions during the 351 satellite passes used in this analysis. The number of cases associated with each condition is shown.

Magnetic local time	
Evening (2000–2400)	198
Morning (0000–0400)	153
Interplanetary magnetic field	
Northward ($\bar{B}_z \geq 0$)	169
Southward ($\bar{B}_z < 0$)	182
Toward sector ($\bar{B}_y \geq 0$)	178
Away sector ($\bar{B}_y \leq 0$)	173
Season	
Summer	223
Winter	128
Geomagnetic activity	
Quiet time	135
Substorm in progress	170
Uncertain	46

APPENDIX 2

The Alfvén layer is defined for a particle of magnetic moment μ as a flow boundary, inside which the drift orbit that completely encircles the earth lies, in the presence of a dawn-dusk electric field. Particle orbits and the Alfvén layers in a dipole magnetic field and a uniform electric field have been calculated by *Kavanagh et al.* [1968] and *Chen* [1970]. The inner edge of the plasma sheet then corresponds to the drift boundary evaluated for the low-energy end of the range of energies found in the plasma sheet (100 eV to 1 keV). It is noted that for these 100-eV electrons the correction to the zero energy solution is negligible [*Kivelson and Southwood*, 1975] and that the Alfvén layer for 1-keV electrons is found 1–2 R_E outward of the zero energy boundary depending on local time.

There are several papers which describe the derivation of the electric potential induced by the reconnection between geomagnetic field and the arbitrary IMF [*Hill*, 1973; *Sonnerup*, 1974, *Gonzalez and Mozer*, 1974; *Cowley*, 1974]. It is not easy to estimate an upper limit of the electric field strength used for obtaining the Alfvén layer, since this value is highly variable depending on different assumptions. Here we estimate the dawn-dusk electric field intensity in the magnetotail produced by the IMF on the basis of the work by *Gonzalez and Mozer* [1974] because (1) they compared their models with the observed polar cap electric field and (2) they obtained the field intensities as functions of the B_z values of the IMF which can readily be compared with our results. For $B_z = -5\ \gamma$ (with $B_y = 0$) they obtained the maximum potential difference Φ_m across the entire tail as about 290 kV. By using the best empirical fit $\Phi = 0.35\Phi_m$ (see their equation (17)), we can get $\Phi = 102$ kV. When we assume a 40-R_E magnetotail thickness, the average electric field E across the tail is estimated to be 0.4 mV/m. In a similar way, $\Phi = 43$ kV and $E = 0.17$ mV/m are obtained for the IMF condition $B_z = 0$ with $|B_y| = 5\ \gamma$; see Figures 8 and 10 of *Gonzalez and Mozer* [1974]. These estimated potential differences are in reasonable agreement with *Heppner*'s [1972, 1977] measurements of the integrated potential drop across the polar cap, which ranged from 20 to 100 kV. In this fashion, in Figure 8 we plot the Alfvén layers for $E = 0.4$ mV/m and 0.17 mV/m and compare them with our auroral oval boundaries (projected into the equatorial plane) for $B_z = -5\ \gamma$ and $0\ \gamma$, respectively.

By using the empirical expression E (kV/R_E) = $0.44/(1 - 0.097Kp)^3$ given by *Kivelson* [1976], Kp values can be estimated to be 6 and 4– for $B_z = -5\ \gamma$ and $0\ \gamma$, respectively. These values are in basic accord with the observational relationship between Kp and IMF parameters obtained by *Schatten and Wilcox* [1967] and *Hirshberg and Colburn* [1969].

Acknowledgments. We wish to acknowledge numerous helpful discussions with S.-I. Akasofu. We are also obliged to F. Yasuhara for his assistance given in the early phase of the work. The work of Y. Kamide was supported in part by NSF grants DES74-23832 and GA-37094 and in part by AFGL contract F19628-72-C-0301 to the Geophysical Institute of the University of Alaska. The work of J. D. Winningham was supported by AFGL contract F19628-76-C-005 and NASA grants NGR 44-004-150 and NSGS 5085 to the University of Texas at Dallas.

The Editor thanks K. Lassen and C.-I. Meng for their assistance in evaluating this paper.

REFERENCES

Akasofu, S.-I., Magnetospheric substorms: A model, in *Solar Terrestrial Physics*, edited by J. R. Dyer, pp. 131–151, D. Reidel, Hingham, Mass., 1972.

Akasofu, S.-I., A study of auroral displays photographed from the DMSP-2 satellite and from the Alaska meridian chain of stations, *Space Sci. Rev.*, *16*, 617, 1974.

Akasofu, S.-I., The roles of the north-south component of the interplanetary magnetic field on large-scale auroral dynamics observed by the DMSP satellite, *Planet. Space Sci.*, *23*, 1349, 1975.

Akasofu, S.-I., and S. Chapman, The lower limit of latitude (US sector) of northern quiet auroral arcs and its relation to *Dst* (*H*), *J. Atmos. Terr. Phys.*, *25*, 9, 1963.

Akasofu, S.-I., and Y. Kamide, Substorm energy, *Planet. Space Sci.*, *24*, 223, 1976.

Akasofu, S.-I., P. D. Perreault, F. Yasuhara, and C.-I. Meng, Auroral substorms and the interplanetary magnetic field, *J. Geophys. Res.*, *78*, 7490, 1973.

Alfvén, H., A theory of magnetic storms and auroras, 1, *Kgl. Sv. Vetenskapsakad. Handl.*, *18*(3), 1939.

Alfvén, H., and C.-G. Fälthammar, *Cosmical Electrodynamics*, 2nd ed., p. 56, Oxford University Press, New York, 1963.

Allen, J. H., C. C. Abston, and I. D. Morris, Auroral electrojet magnetic activity indices *AE* (11) for 1969, *Rep. UAG-31*, World Data Center A for Solar Terr. Phys., NOAA, Boulder, Colo., 1974.

Allen, J. H., C. C. Abston, and I. D. Morris, Auroral electrojet magnetic activity indices *AE* (11) for 1971, *Rep. UAG-39*, World Data Center A for Solar Terr. Phys., NOAA, Boulder, Colo., 1975a.

Allen, J. H., C. C. Abston, and I. D. Morris, Auroral electrojet magnetic activity indices *AE* (11) for 1972, *Rep. UAG-45*, World Data Center A for Solar Terr. Phys., NOAA, Boulder, Colo., 1975b.

Anger, C. D., I. Lancott, J. McNally, and H. S. Kerr, The ISIS-2 scanning auroral photometer, *Appl. Opt.*, *12*, 1753, 1973.

Berkey, F. T., and Y. Kamide, On the distribution of global auroras during intervals of magnetospheric quiet, *J. Geophys. Res., 81*, 4701, 1976.

Burch, J. L., Precipitation of low-energy electrons at high latitudes: Effects of interplanetary magnetic field and dipole tilt angle, *J. Geophys. Res., 77*, 6696, 1972.

Burch, J. L., Rate of erosion of dayside magnetic flux based on a quantitative study of the dependence of polar cusp latitude on the interplanetary magnetic field, *Radio Sci., 8*, 955, 1973.

Burton, R. K., R. L. McPherron, and C. T. Russell, An empirical relationship between interplanetary conditions and *Dst*, *J. Geophys. Res., 80*, 4204, 1975.

Caan, M., R. L. McPherron, and C. T. Russell, The statistical magnetic signatures of magnetospheric substorms, *Planet. Space Sci., 25*, in press, 1977.

Chen, A. J., Penetration of low-energy protons into the magnetosphere, *J. Geophys. Res., 75*, 2458, 1970.

Coroniti, F. V., and C. F. Kennel, Can the ionosphere regulate magnetospheric convection?, *J. Geophys. Res., 78*, 2837, 1973.

Cowley, S. W. H., On the possibility of magnetic fields and fluid flows parallel to the *X* line in a reconnection geometry, *J. Plasma Phys., 12*, 319, 1974.

Creutzberg, F., Morphology and dynamics of the instantaneous auroral oval, in *Magnetospheric Particles and Fields*, edited by B. M. McCormac, pp. 235-246, D. Reidel, Hingham, Mass., 1976.

Crooker, N. U., and R. L. McPherron, On the distinction between the auroral electrojet and the partial ring current systems, *J. Geophys. Res., 77*, 6886, 1972.

Deehr, C. S., J. D. Winningham, F. Yasuhara, and S.-I. Akasofu, Simultaneous observations of discrete and diffuse auroras by the Isis 2 satellite and airborne instruments, *J. Geophys. Res., 81*, 5527, 1976.

Dungey, J. W., Interplanetary magnetic field and the auroral zones, *Phys. Rev. Lett., 6*, 47, 1961.

Eather, R. H., The auroral oval—A reevaluation, *Rev. Geophys. Space Phys., 11*, 155, 1973.

Eather, R. H., and S. B. Mende, High-latitude particle precipitation and source regions in the magnetosphere, in *Magnetosphere-Ionosphere Interactions*, edited by K. Folkestad, p. 139, University of Oslo Press, Oslo, 1971.

Fairfield, D. H., and L. J. Cahill, Transition region magnetic field and polar magnetic disturbances, *J. Geophys. Res., 71*, 155, 1966.

Fairfield, D. H., and G. D. Mead, Magnetospheric mapping with a quantitative geomagnetic field model, *J. Geophys. Res., 80*, 535, 1975.

Feldstein, Y. I., On morphology of auroral and magnetic disturbances at high latitudes, *Geomagn. Aeron., 3*, 183, 1963.

Feldstein, Y. I., Peculiarities in the auroral distribution and magnetic disturbance distribution in high latitudes caused by the asymmetrical form of the magnetosphere, *Planet. Space Sci., 14*, 121, 1966.

Feldstein, Y. I., and G. V. Starkov, Dynamics of auroral belt and polar geomagnetic disturbances, *Planet. Space Sci., 15*, 209, 1967.

Frank, L. A., Relationship of the plasma sheet, ring current, trapping boundary, and plasmapause near the magnetic equator and local midnight, *J. Geophys. Res., 76*, 2265, 1971.

Freeman, J. W., *Kp* dependence of the plasma sheet boundary, *J. Geophys. Res., 79*, 4315, 1974.

Gonzalez, W. D., and F. S. Mozer, A quantitative model for the potential resulting from reconnection with an arbitrary interplanetary magnetic field, *J. Geophys. Res., 79*, 4186, 1974.

Heikkila, W. J., and J. D. Winningham, Penetration of magnetosheath plasma to low altitudes through the dayside magnetospheric clefts, *J. Geophys. Res., 76*, 883, 1971.

Heikkila, W. J., J. B. Smith, J. Tarstrup, and J. D. Winningham, The soft particle spectrometer in the ISIS-1 satellite, *Rev. Sci. Instrum., 41*, 1393, 1970.

Heppner, J. P., Electric field variations during substorms, *Planet. Space Sci., 20*, 1475, 1972.

Heppner, J. P., Empirical models of high-latitude electric fields, *J. Geophys. Res., 82*, 1115, 1977.

Hill, T. W., A three-dimensional model of magnetic merging at the magnetopause, *Radio Sci., 8*, 915, 1973.

Hirshberg, J., and D. S. Colburn, Interplanetary field and geomagnetic variations—A unified view, *Planet. Space Sci., 17*, 1183, 1969.

Hoffman, R. A., and J. L. Burch, Electron precipitation patterns and substorm morphology, *J. Geophys. Res., 78*, 2867, 1973.

Holzworth, R. H., and C.-I. Meng, Mathematical representation of the auroral oval, *Geophys. Res. Lett., 2*, 377, 1975.

Kamide, Y., Association of *DP* and *DR* fields with the interplanetary magnetic field variation, *J. Geophys. Res., 79*, 49, 1974.

Kamide, Y., and S.-I. Akasofu, Latitudinal cross section of the auroral electrojet and its relation to the interplanetary magnetic field polarity, *J. Geophys. Res., 79*, 3755, 1974.

Kamide, Y., and S.-I. Akasofu, The location of the field-aligned currents with respect to discrete auroral arcs, *J. Geophys. Res., 81*, 3999, 1976.

Kamide, Y., and N. Fukushima, Positive geomagnetic bays in evening high latitudes and their possible connection with partial ring current, *Rep. Ionos. Space Res. Jap., 26*, 79, 1972.

Kamide, Y., J. L. Burch, J. D. Winningham, and S.-I. Akasofu, Dependence of the latitude of the cleft on the interplanetary magnetic field and substorm activity, *J. Geophys. Res., 81*, 698, 1976.

Kan, J. R., and S.-I. Akasofu, A model of the open magnetosphere, *J. Geophys. Res., 79*, 1379, 1974.

Kavanagh, L. D., Jr., J. W. Freeman, Jr., and A. J. Chen, Plasma flow in the magnetosphere, *J. Geophys. Res., 73*, 5511, 1968.

Kivelson, M. G., Magnetospheric electric fields and their variation with geomagnetic activity, *Rev. Geophys. Space Phys., 14*, 189, 1976.

Kivelson, M. G., and D. J. Southwood, Approximation for the study of drift boundaries in the magnetosphere, *J. Geophys. Res., 80*, 3528, 1975.

Klumpar, D. M., J. R. Burrows, and M. D. Wilson, Simultaneous observations of field-aligned currents and particle fluxes in the postmidnight sector, *Geophys. Res. Lett., 3*, 395, 1976.

Lassen, K., On the classification of high-latitude auroras, *Geofys. Publ., 29*, 87, 1972.

Lassen, K., Relation of the plasma sheet to the nightside auroral oval, *J. Geophys. Res., 79*, 3857, 1974.

Lui, A. T. Y., and C. D. Anger, A uniform belt of diffuse auroral emission seen by the Isis-2 scanning auroral photometer, *Planet. Space Sci., 21*, 799, 1973.

Lui, A. T. Y., C. D. Anger, and S.-I. Akasofu, The equatorward boundary of the diffuse aurora and auroral substorms as seen by the Isis 2 auroral scanning photometer, *J. Geophys. Res., 80*, 3603, 1975.

Lui, A. T. Y., D. Venkatesan, C. D. Anger, S.-I. Akasofu, W. J. Heikkila, J. D. Winningham, and J. R. Burrows, Simultaneous observations of particle precipitations and auroral emissions by the Isis 2 satellite, *J. Geophys. Res., 82*, 2210, 1977.

Mauk, B. H., and C. E. McIlwain, Correlation of *Kp* with the substorm-injected plasma boundary, *J. Geophys. Res., 79*, 3193, 1974.

McPherron, R. L., C. T. Russell, and M. P. Aubry, Satellite studies of magnetospheric substorms on August 15, 1968, 9, Phenomenological model of substorms, *J. Geophys. Res., 78*, 3131, 1973.

Mead, G. D., and D. H. Fairfield, A quantitative magnetospheric model derived from spacecraft magnetometer data, *J. Geophys. Res., 80*, 523, 1975.

Montbriand, L. E., The proton aurora and auroral substorms, in *The Radiating Atmosphere*, edited by B. M. McCormac, p. 366, D. Reidel, Hingham, Mass., 1971.

Mozer, F. S., and P. Lucht, The average auroral zone electric field, *J. Geophys. Res., 79*, 1001, 1974.

Pike, C. P., and J. A. Whalen, Satellite observations of auroral substorms, *J. Geophys. Res., 79*, 985, 1974.

Schatten, K. H., and J. M. Wilcox, Response of the geomagnetic activity index *Kp* to the interplanetary magnetic field, *J. Geophys. Res., 72*, 5185, 1967.

Schield, M. A., J. W. Freeman, and A. J. Dessler, A source for field-aligned currents at auroral latitudes, *J. Geophys. Res., 74*, 247, 1969.

Snyder, A. L., and S.-I. Akasofu, Observations of the auroral oval by the Alaskan meridian chain of stations, *J. Geophys. Res., 77*, 3419, 1972.

Snyder, A. L., S.-I. Akasofu, and T. N. Davis, Auroral substorms observed from above the north polar region by a satellite, *J. Geophys. Res., 79*, 1393, 1974.

Sonnerup, B. U. Ö., Magnetopause reconnection rate, *J. Geophys. Res., 79*, 1546, 1974.

Starkov, G. V., Analytical representation of the equatorial boundary of the oval auroral zone, *Geomagn. Aeron., 9*, 614, 1969.

Stringer, W. J., and A. E. Belon, The morphology of the IQSY auroral oval, *J. Geophys. Res., 72*, 4415, 1967.

Sugiura, M., and D. J. Poros, Hourly values of equatorial *Dst* for the years 1957 to 1970, *GSFC Rep. X-645-71-278*, NASA Goddard Space Flight Center, Greenbelt, Md., 1971.

Sugiura, M., and D. J. Poros, Provisional hourly values of equatorial *Dst* for 1971, *GSFC Rep. X-645-72-200*, NASA Goddard Space Flight Center, Greenbelt, Md., 1972.

Vasyliunas, V. M., A survey of low-energy electrons in the evening sector of the magnetosphere with Ogo 1 and Ogo 3, *J. Geophys. Res.*, *73*, 2839, 1968.

Winningham, J. D., S.-I. Akasofu, F. Yasuhara, and W. J. Heikkila, Simultaneous observations of auroras from the south pole station and of precipitating electrons by Isis 1, *J. Geophys. Res.*, *78*, 6579, 1973.

Winningham, J. D., F. Yasuhara, S.-I. Akasofu, and W. J. Heikkila, The latitudinal morphology of 10-eV to 10-keV electron fluxes during magnetically quiet and disturbed times in the 2100–0300 MLT sector, *J. Geophys. Res.*, *80*, 3148, 1975.

Yasuhara, F., S.-I. Akasofu, J. D. Winningham, and W. J. Heikkila, The equatorward shift of the cleft during magnetospheric substorms as observed by Isis 1, *J. Geophys. Res.*, *78*, 7286, 1973.

Yasuhara, F., Y. Kamide, and S.-I. Akasofu, A modeling of the magnetospheric substorms, *Planet. Space Sci.*, *23*, 575, 1975.

Zmuda, A. J., and J. C. Armstrong, The diurnal flow pattern of field-aligned currents, *J. Geophys. Res.*, *79*, 4611, 1974.

(Received January 28, 1977;
accepted July 26, 1977.)

VOL. 83, NO. A12 JOURNAL OF GEOPHYSICAL RESEARCH DECEMBER 1, 1978

A Case Study of the Aurora, High-Latitude Ionosphere, and Particle Precipitation During Near-Steady State Conditions

J. D. WINNINGHAM

University of Texas at Dallas, Richardson, Texas 75080

C. D. ANGER

University of Calgary, Calgary, Alberta T2N 1N4

G. G. SHEPHERD

York University, Toronto, Ontario M3J 1P3

E. J. WEBER AND R. A. WAGNER

Air Force Geophysics Laboratory, Hanscom Air Force Base, Massachusetts 01730

An Isis 2 pass is singled out for a detailed examination of the particle fluxes, optical emissions, and ionospheric parameters observed during a quiescent period (late recovery) between two substorms. This pass was chosen because it was part of a coordinated data acquisition period between the Air Force Geophysics Laboratory (AFGL) Airborne Ionospheric Observatory, Isis 2, and DMSP (Defense Meteorological Satellite Program). As a result, both long-duration measurements (aircraft) and transient, snapshot (spacecraft) data are available. This allows, on a macroscopic level, the separation of space and time effects.

On the basis of the joint data set it was established that the latitudinal morphology observed by the satellite is basically spatial in nature. It is concluded that the observed particle fluxes are most easily understood in terms of precipitation from the quiet time plasma sheet without intervening acceleration. The observed optical emissions and ionospheric parameters are found to be in good qualitative and quantitative agreement (within experimental error) with the electron fluxes, although establishment of this point has required careful determination of the viewing direction of the optical instruments, removal of scattered light (albedo) from underlying cloud and snow, and consideration of the effects of photon-counting statistics on contour plots of the optical data.

INTRODUCTION

In a recent paper, *Winningham et al.* [1975] expanded upon the earlier electron flux morphology studies of *Hoffman and Burch* [1973] and *Frank and Ackerson* [1972]. *Winningham et al.* [1975] demonstrated that in the 2100–0300 dipole magnetic local time (MLT) sector, distinct and repeatable electron latitudinal distributions were observed as a function of substorm phase. Two regions, the boundary plasma sheet (BPS) and the central plasma sheet (CPS), were delineated by *Winningham et al.* [1975]. The BPS corresponds to the upper (lower) portion of the plasma sheet adjacent to the tail lobes, and the CPS the inner portion of the plasma sheet adjacent to the outer Van Allen belt. The BPS exhibits an extremely dynamic behavior as a function of substorm phase. The CPS, in comparison, changes very little, exhibiting mainly a slight spectral hardening and an equatorward shift followed by a poleward shift as the substorm proceeds. No detailed correlation with parameters other than magnetic field data was attempted by *Winningham et al.* [1975].

Kamide and Winningham [1977] studied in detail the dependence of the equatorial boundary of the CPS on the IMF B_z component and substorm phase (AE). It was determined that the IMF B_z component was the dominant influence on the CPS equatorial boundary with substorm activity playing a secondary role. The CPS lower boundary moved equatorward (poleward) as the IMF component decreased (increased). Substorm activity lowered the boundary no matter what the value of B_z was.

Deehr et al. [1976] compared photometric, all-sky, and particle data obtained concurrently by Isis 2 and the NASA 990 aircraft. In this paper it was shown that the CPS and BPS discussed in *Winningham et al.* [1975] correspond to the diffuse and discrete auroral regions, respectively. The period studied by *Deehr et al.* [1976] was an early recovery phase with the Isis satellite passing just to the east of the westward traveling surge.

In all the preceding papers, no concurrent auroral images or ionospheric data obtained by Isis 2 were examined. In the present paper an Isis 2 pass (orbit 3194, 0600 UT on December 9, 1971) is singled out for a detailed examination of the particle fluxes, optical emissions, and ionospheric parameters observed during a quiescent period (late recovery) between two substorms. This pass was chosen because it was part of a coordinated data acquisition period between the AFGL Airborne Ionospheric Observatory, Isis 2, and DMSP (Defense Meteorological Satellite Program). As a result, both long-duration measurements (aircraft) and transient, snapshot (spacecraft) data are available. This allows, on a macroscopic level, the separation of space and time effects.

Although these criteria were well satisfied, it was found that other factors limited the accuracy obtainable in a full-modeling calculation. In particular, all the plasma parameters are not available in the orbit-aligned mode used here; consequently, a detailed model analysis is not presented here but

Paper number 8A0779
0148-0227/78/128A-0779$01.00

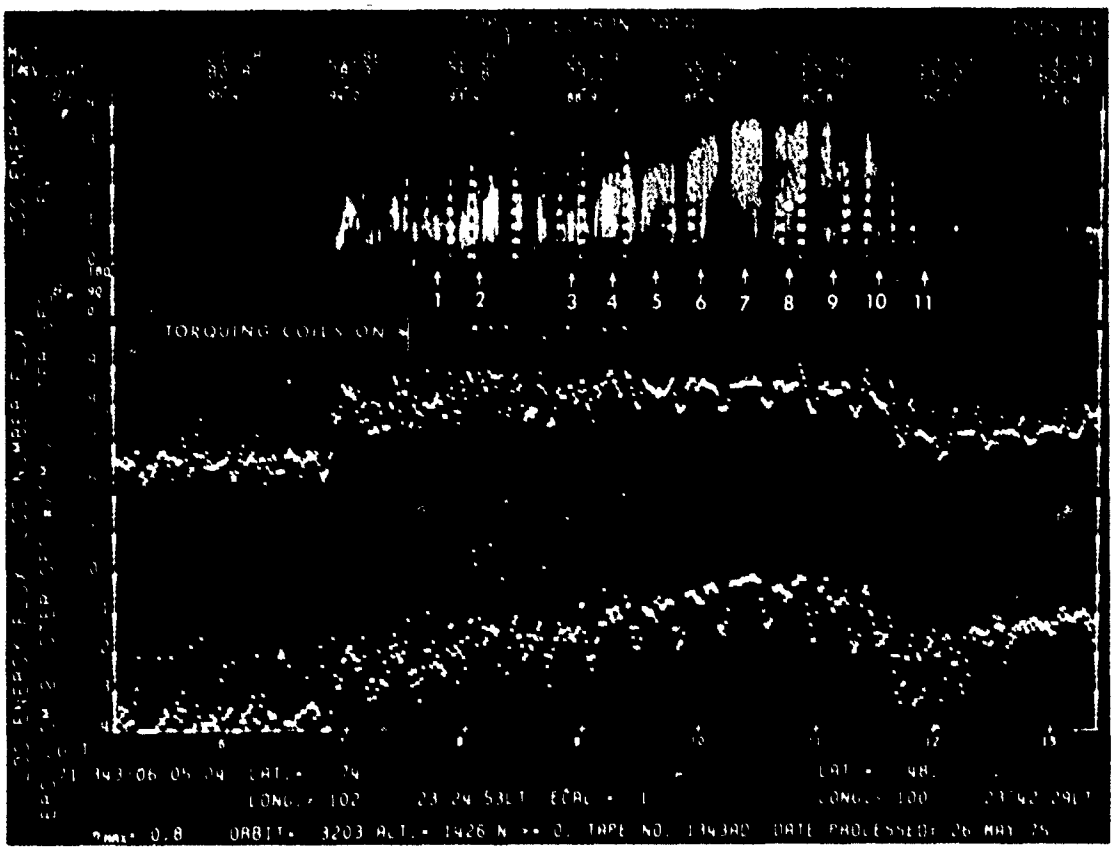

Fig 1a. Electron spectrograms for December 9, 1971. See *Winningham et al.* [1975] for a description of the spectrogram format.

will be the subject of later cartwheel studies. The semiquantitative comparisons available in this pictorial photometric mode nevertheless provide useful insights into the auroral process and lay the groundwork for precise optical-particle-plasma comparisons.

Observations

Particle Data. Figures 1*a* and 1*b* are energy-time spectrograms of the electron and proton fluxes observed by the soft particle spectrometer (SPS) on Isis 2 during the northern nightside portion of orbit 3194 on December 9, 1971. For a discussion of the spectrogram presentation, see *Winningham et al.* [1975]. From the beginning of the spectrogram at 0605:04 UT (invariant latitude Λ of 83.0, dipole magnetic local time (MLT) of 20.4 hours) to 0606:52 UT (Λ = 78.6°, MLT = 21.9 hours) a flux of low-intensity low-energy (<200 eV) electrons was observed (It should be noted that the magnetic attitude torquing coils were on until 0607:32 UT. As a result, the pitch angle given in the spectrogram is incorrect, and the electron spectrum below a few hundred electron volts is quantitatively incorrect This electron data can be used in a qualitative sense, however) The aforementioned low-energy electrons poleward of Λ = 78 6° have been identified by *Winningham and Heikkila* [1974] as being of probable magnetosheath origin That is, they are similar in spectral shape to magnetosheath electrons but are reduced in intensity by $\sim 10^{-2}$ Because of their uniformity and spatial extent (most of the polar cap), *Winningham and Heikkila* [1974] termed these fluxes polar rain. Within the sensitivity of the SPS, no proton fluxes were observed in conjunction with the electron polar rain.

Equatorward of 78.6°, a region of relatively uniform and more intense electron and proton flux was observed. Both particle species exhibited a hardening and intensification of their spectra as a function of decreasing latitude (see Figure 2). The maximum in the electron and proton energy flux was at $\Lambda \simeq 69.2°$ and $\Lambda \simeq 68.7°$, respectively. Equatorward of 69.2°, the electron spectrum became progressively weaker (see Figure 2), softer, and exhibited an increasingly trapped angular distribution. Below 68.7°, the proton fluxes rapidly decreased in intensity and isotropy. The sensible end of the electron and proton fluxes occurred at $\Lambda \simeq 65.9°$.

In Figure 2, representative electron spectra at minimum pitch angle are presented. The spectra are taken at the positions marked with arrows in Figure 1*a*. Spectra 1–7 demonstrate the spectral hardening with decreasing latitude, and spectra 8–10 the subsequent softening. Spectrum 11 is due to atmospheric conjugate photoelectrons. The most striking feature of each of these spectra is their basic shape, which varies between a power law and an exponential. No prominent 'monoenergetic' spectral peaks are observed. Comparison of spectra 1–3 in Figure 2*a* with spectrum 10 in Figure 2*c* shows a marked similarity of shape in the energy range greater than ~50 eV, even though these spectra are separated by 10° of invariant latitude (i.e., at the polar boundary of the BPS and the equatorial CPS boundary).

Data from several channels of the Isis 2 energetic particle

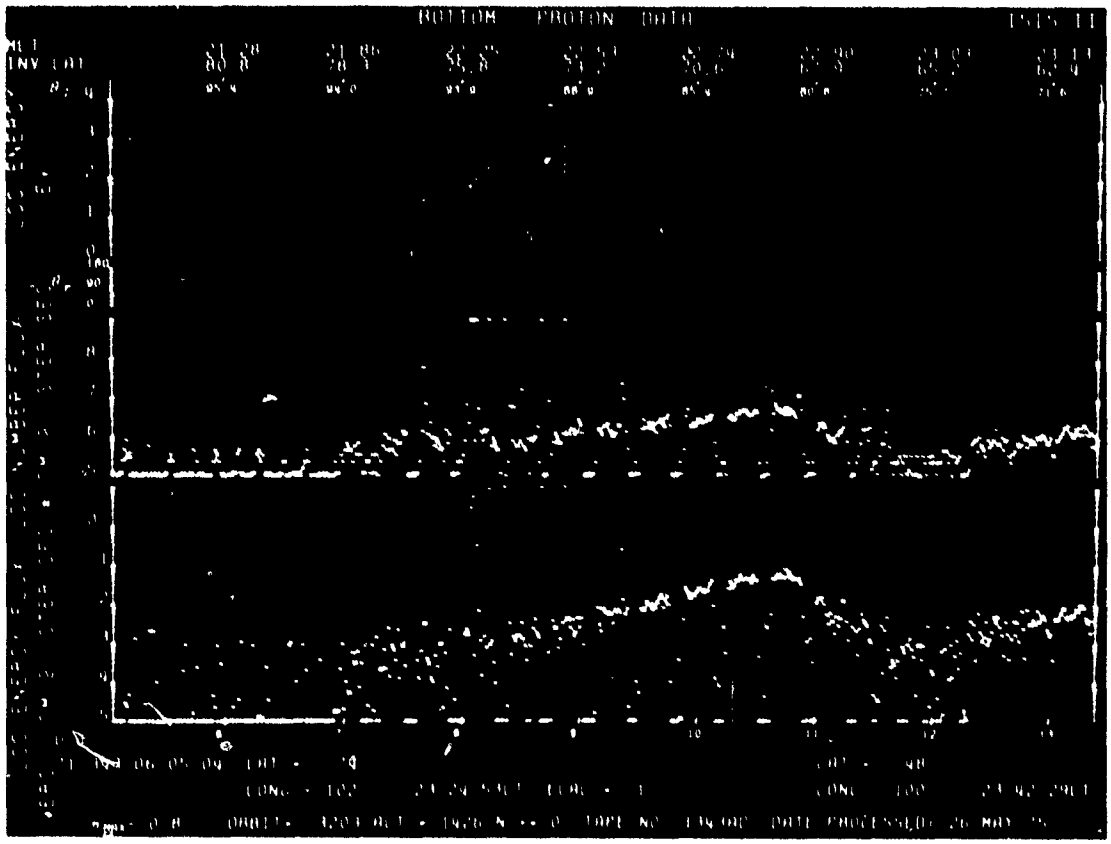

Fig. 1b. Proton spectrograms for December 9, 1971. See *Winningham et al.* [1975] for a description of the spectrogram format.

detector (EPD) [*Venkatarangan et al.*, 1975] indicate that the background boundary Λ_B [*McDiarmid and Wilson*, 1968] for electrons having energy of >40 keV was located at ~70.8°. In some works [*Frank and Ackerson*, 1972], Λ_B has been associated with the last closed field line. However, during this pass the low-energy (<20 keV) channels of the EPD exhibited evidence of an angular distribution peaked at 90° up to at least 76°. Above 76° the softer spectrum (Figure 2*a*) placed the flux below the EPD's energy range.

Magnetic Data Figure 3*a* is the II station *AE* index generated by the World Data Center A for Solar-Terrestrial Physics. (We recognize the limitations of this index, but it is the only one readily available) Examination of the *AE* index indicates pass 3194 (indicated by a bar) occurred subsequent to a small substorm starting at ~0307 UT and prior to a larger substorm beginning at 0847 UT.

Figure 3*b* gives the *H*, *D*, and *Z* components from Rostoker's chain of magnetometers in western Canada [*Kisabeth and Rostoker*, 1971]. Isis 2 paralleled the 101° west meridian during pass 3194, which placed it ~14° to the east of Rostoker's chain Inspection of Figure 3*b* reveals that the period of orbit 3194 was one of relative magnetic quiescence prior to the substorm commencing at 0847 UT Higher-resolution (×10) plots indicate that even low-level activity was absent

Interplanetary magnetic field data were available from Imp I, which was located in the evening sector magnetosheath, during orbit 3194 The magnetosheath IMF was southward (in *SM* coordinates) from 0525 to 0543 UT, northward from 0543 to 0604 UT, and slightly southward from 0604 to 0611 UT, after which time the field was northward. The 1-hour average IMF changed from northward to southward from 0600 to 0800 UT.

Ionospheric Data. Figures 4*a* and 4*b* give the local values and isodensity contours of electron density for orbit 3194. In Figure 4*a*, from Λ = 83° (0605:04 UT) to Λ = 78.6° (0606.48 UT) (the polar rain region), the local electron density was very low, 10^1 cm^{-3}, a value typical for the winter polar cap Owing to the sounder sweep period of 27 s, the next density profile after 78.6° was not obtained until Λ = 77.8° (0607 12 UT), or 20 s after Isis 2 entered the more intense particle flux region It can be seen that the local electron density had increased by a factor of 8.5 The local density was observed to increase further during the next sounder sweep. Structure was evident in the local density until Λ = 66.8° (0611.25 UT), after which time a steady decline to a minimum density at Λ = 62.8° (0612 52 UT) was observed Subsequent to the minimum, the density increased steadily until the plot was terminated

Figure 4*b* reveals that increases in density of varying degree were observed at all heights above F_2 max between 0606 48 and 0612 00 UT. As in the local density, fluctuations were observed until 0611.25 UT, after which time a relative minimum was observed. After the minimum a steady increase in density was observed at all heights It should be noted that the isodensity contours within the auroral region are derived by real height profiles which are magnetic field aligned (i e , the sounder wave is propagated along the field line)

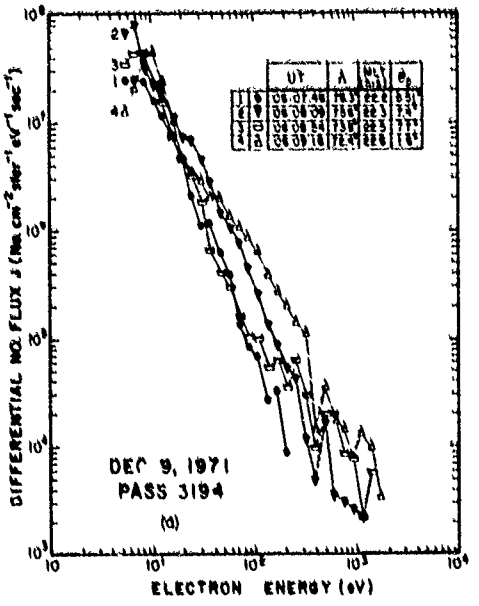

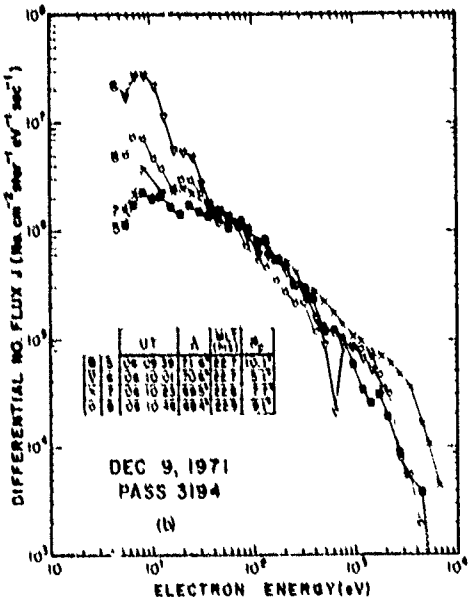

Fig. 2. Electron spectra at maximum pitch angles observed for each spin of Isis 2 orbit 1194.

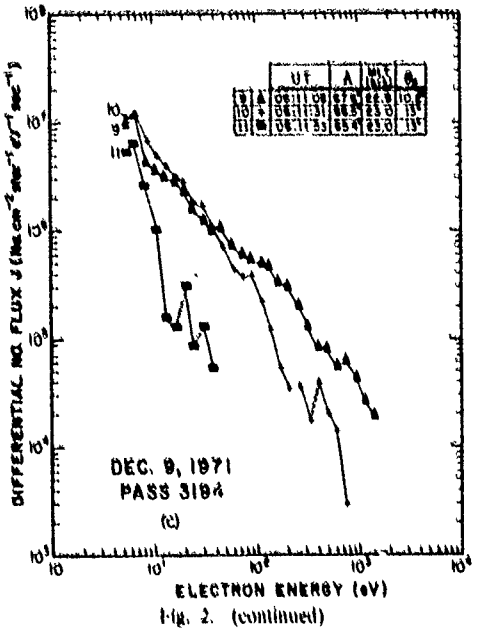

Fig. 2. (continued)

Examination of the local density measured by the Langmuir probe reveals essentially the same morphology as the sounder. The major difference between the two results is one of spatial temporal resolution, the Langmuir probe having much greater resolution. Both the Langmuir probe and the sounder indicate the region of intense particle fluxes to be coincident with a region of topside spread *F*, SUIZ [*Dyson and Winningham*, 1974]. Fine scale absolute density fluctuations as large as 10^4 cc^{-1} (relative fluctuations were as large as 30%) were observed by the Langmuir probe (L. H. Brace private communication, 1976) in a fixed bias mode of operation. The fluctuations ceased at 0612:00 UT, coincident with the end of auroral fluxes.

The satellite attitude was optimized for imaging by the auroral scanner during this pass. As a result, the attitude was less than ideal for the ion mass spectrometer and the retarding potential analyzer. However, these instruments indicated that the particle fluxes occurred within the light ion trough.

Optical Data. 'Images' of the nightside auroral oval on both sides of the spacecraft track were obtained by the optical instruments on Isis 2 [*Shepherd et al.*, 1973; *Anger et al.*, 1973] during this pass. The specific wavelengths covered were 3914 Å (N_2^+), 5577 Å, and 6300 Å O I. The data are presented as pictures on a geographic coordinate grid in Figure 5 (5577 Å and 3914 Å only) and as contour plots for all three wavelengths in Figure 6. The contoured 3914-Å and 5577-Å data are derived from the low-resolution pulse code modulation data that are electronically averaged from the frequency modulation-frequency modulation data used to construct the images of Figure 5.

The DMSP noon-midnight satellite and Isis 2 were in approximately the same local time plane during mid-December 1971, and telemetry was scheduled for passes that were close in UT. Figure 7 presents the DMSP auroral image of the northern nighttime sector at 0601 UT. Also shown are 3914-Å intensity contours measured by Isis 2 at 0609 UT and projected onto the DMSP picture at 100-km altitude. Isis was to the west of DMSP; however, owing to the higher altitude (1426 km) of Isis, its image encompasses nearly all of the area of the DMSP picture. Close coincidence is observed between the 3914 Å region in the Isis 2 image and the region of diffuse or continuous aurora seen in DMSP as a rather uniform belt of unstructured glow with a smooth equatorward boundary. It should be noted that the DMSP data are somewhat compromised by moonlight scattered by snow and clouds. Also, the dark area in the center of the DMSP image is an instrument artifact.

A broad region of diffuse aurora is evident in Figures 5–7 on both sides of local midnight (which is at approximately 267° longitude). In addition, a weak arc is present at higher latitudes extending to the east of the Isis 2 orbit (Figures 5 and 7). Its intensity is approximately 1 kR (3914) and 2 kR (5577). This arc represents the center of a much broader region in

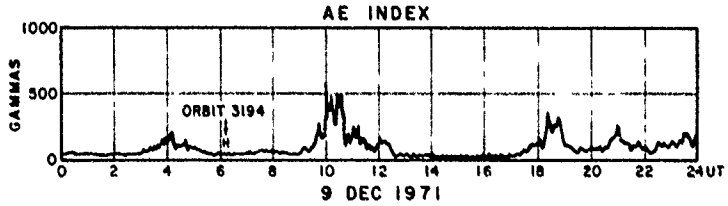

Fig. 3a. *AE* index for the period encompassing Isis 2 orbit 3194

which the 6300-Å intensity (figure 6*a*) is enhanced relative to its value in the diffuse aurora where the maximum 3914-Å and 5577-Å intensities (Figures 6*b* and 6*c*) occur. The ratio I(6300)/I(5577) has a value of about 1 in the vicinity of the arc but is well below 0.1 in the diffuse aurora. Figure 6*a* also reveals that the 6300-Å region is broader in latitude than for the other two lines at all local times shown in the figure.

Aircraft Data. During this coordinated data acquisition period the AFGL NKC-135 aircraft flew across northern Canada following a track designed to intersect several passes of the Isis 2 and DMSP satellites. At the time of this pass, the aircraft was traveling directly equatorward in corrected geomagnetic coordinates along the 2230 CG local time meridian. The objective was to make measurements of atmospheric ionization and luminosity resulting from the precipitating particles measured by Isis 2. Because of the relatively long time required by the aircraft to traverse the latitude region of particle precipitation (~2 hours from 75.3° to 67.6° CGL) compared with the satellite (a few minutes) we have chosen this period of low magnetic activity to make the comparison.

The aircraft flight track has been annotated onto Figures 6*a*-6*c* as a series of dots, with the dots 15 min apart in each figure. The direction of travel was (geographic) southwest, and the right-hand dot indicates the aircraft position at 0500 UT. The point of closest approach between aircraft and satellite was 0609 UT when Isis passed slightly to the west of the aircraft.

During this southbound flight leg, ionosonde returns indicated a region of particle-produced ionization at *E* layer heights (auroral *E*). *E* layer ionization could be determined in the aircraft ionograms from 0541 to 0700 UT and was collocated in space with the optical emissions originating primarily from *E* layer heights (3914 Å N_2^+ and 5577 Å O I) and with minimum I(6300 Å), I(3914 Å) ratios. This agreement is demonstrated in Figure 4, which shows the latitude profiles of the optical emissions, electron densities, and particle energy fluxes along the subsatellite track together with the measured *E* layer critical frequencies (f_0E_s).

Because of the good spatial agreement between optical, particle, and ionospheric parameters an attempt was made to

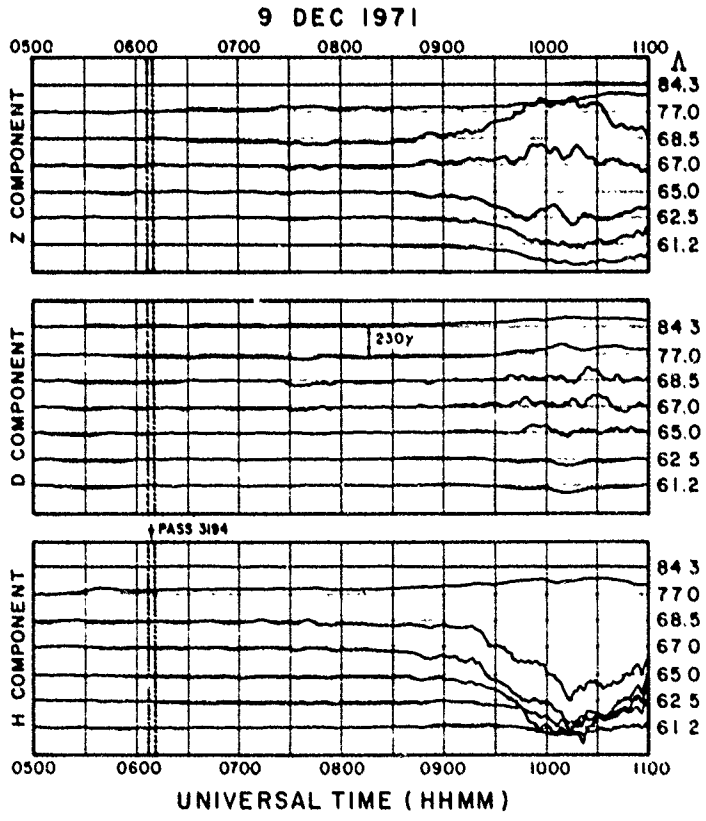

Fig. 3b. *H*, *D*, and *Z* traces from the Alberta magnetometer chain (courtesy of Gordon Rostoker)

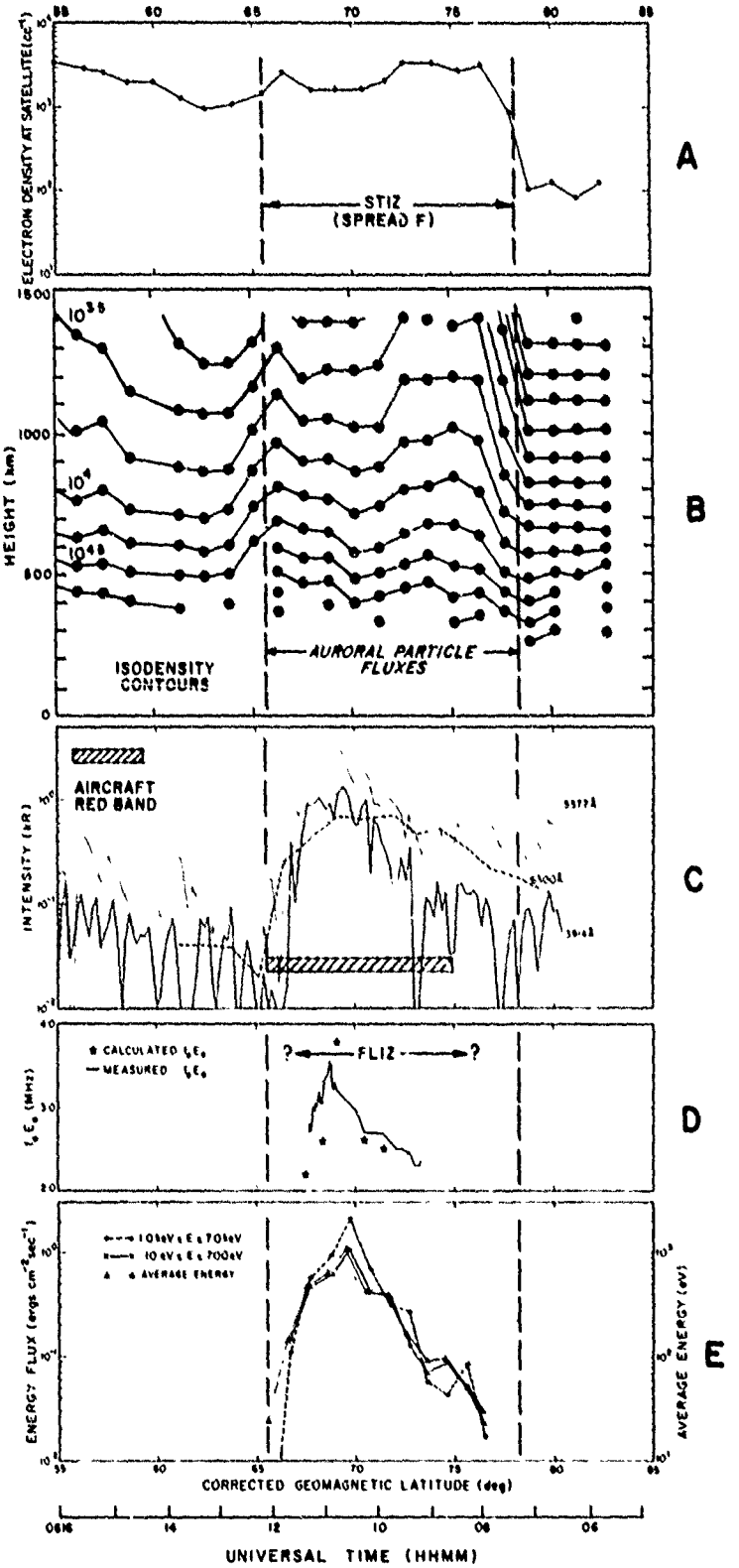

Fig. 4 Composite plot of (*a*) local electron density, (*b*) electron isodensity contours, (*c*) optical intensities observed at the foot of the field line connected to satellite, (*d*) calculated and measured f_0E_s, and (*e*) observed electron energy fluxes in two energy bands and average energy for electron spectra

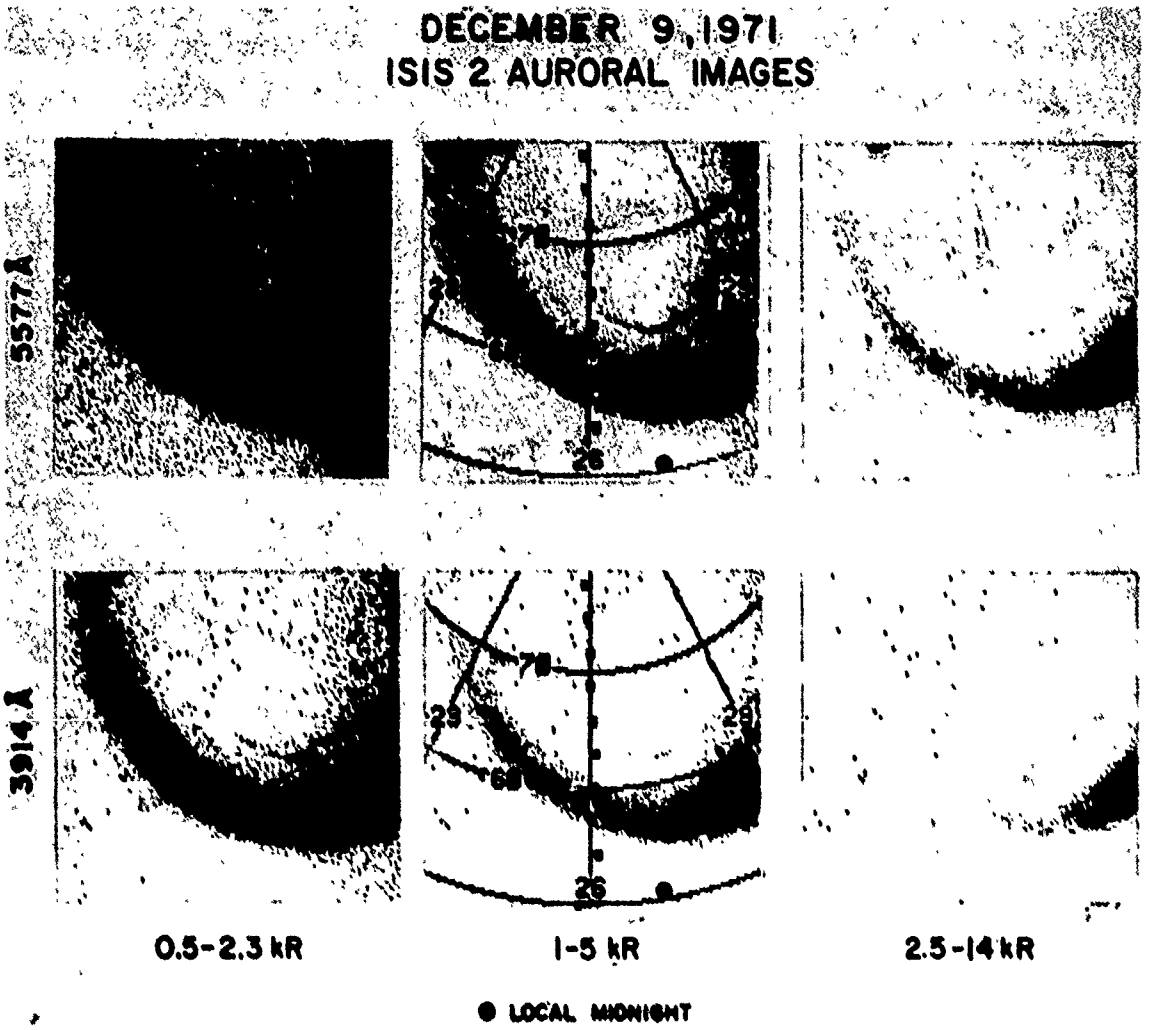

Fig. 5 Geographic projections of (*a*) 5577-Å and (*b*) 3914-Å data. The coordinate grids shown apply to all pictures, which differ only in the wavelength and range of intensities presented. The longitudes shown should be multiplied by 10. The pictures are in negative format, with intensities greater than the indicated range represented as black and those below as white. Intensities shown are observed oblique values, uncorrected for albedo. The magnetic subsatellite track is indicated by squares which correspond to 1-min intervals of spacecraft time starting at 0604 UT at the top of the pictures and going to 0612 at the bottom.

calculate the magnitude of the auroral E layer (f_0E_a) expected from the electron precipitation for comparison with the measured values. Protons contributed only about 10% to the total precipitated energy flux and were not considered to be a significant ionization source. The ionization production rates of *Rees* [1963], together with the electron spectra shown in Figures 2*a*–2*c*, were used to compute the total E layer ionization rate. Only electrons with $E > 700$ eV, which penetrate below 150 km [*Rees*, 1964], were included. Isotropy of the electron flux over the upper hemisphere was observed and was used in the calculation. Since the aircraft all sky camera photographs show only a weak steady glow and no discrete auroral forms [*Weber et al.*, 1977], the assumption of equilibrium during this period is reasonable, and thus steady state conditions were applied to arrive at electron density profiles. An effective recombination coefficient, α, of 3×10^{-7} cm^3 s^{-1} was used to represent electron losses during moderate auroral conditions [*Swider and Narcisi*, 1974]. The ambient nocturnal ionosphere was ignored, as this amounts to a critical frequency at E layer heights of 0.6 MHz [*King*, 1962] or, equivalently, to only about 10^{-3} of the ionization rate required to produce a 3-MHz auroral E layer.

The maximum value in each electron density height profile was converted to a plasma frequency and taken to be the layer critical frequency, the maximum frequency reflected by the layer. The measured and calculated values of f_0E_a are shown in Figure 4*d*. Comparison with the measured values shows reasonable agreement, especially at 71.5° latitude (0609 UT) at the point of closest aircraft satellite approach. From the comparison it is evident that small changes in the particle spatial morphology and possibly in intensity occurred during the aircraft southbound flight leg. The aircraft measurements show the peak value of f_0E_a shifted equatorward 1° compared with the satellite measurements. This slow equatorward shift of the continuous aurora and accompanying particle produced E layer during this period has been reported by *Whalen et al.*

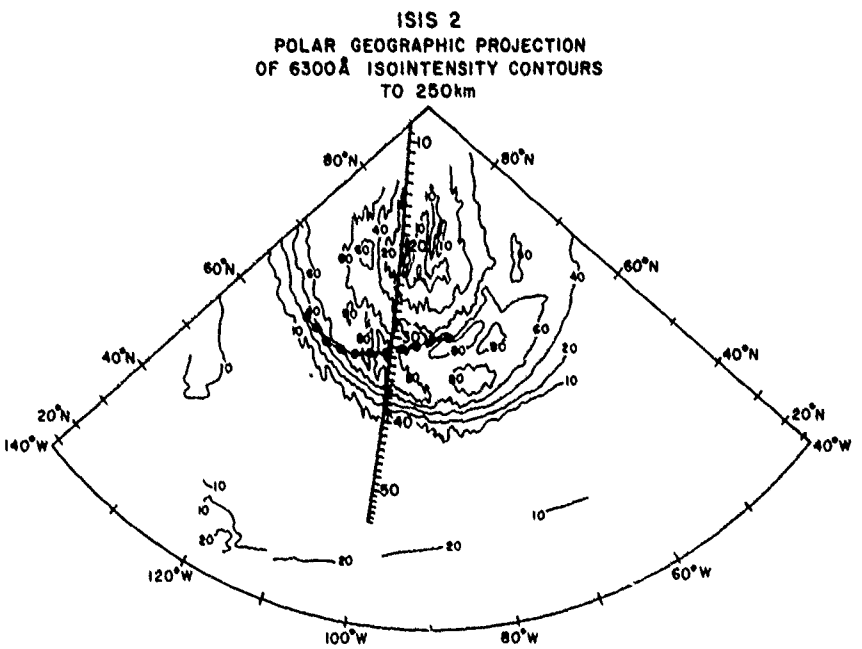

Fig. 6a. Isointensity contour plots of 6300-Å emissions for December 9, 1971. Contour labels are in units of 10 R

[1977]. Considering the time separation between aircraft and satellite measurements of 45 min in the poleward direction, with the data recorded simultaneously at 71.5°, and 51 min in the equatorward direction, E layer ionization and auroral emissions measured by aircraft and satellite compare favorably over a wide latitude range.

Because of the generally accepted proportionality between 3914-Å emission and ionization rate [*Vallance-Jones*, 1974] a comparison was made between the spatial intensity distribution of the 3914-Å emission and the magnitude and extent of the particle-produced auroral E layer. The E layer ionization was observed simultaneously by ionospheric sounders located

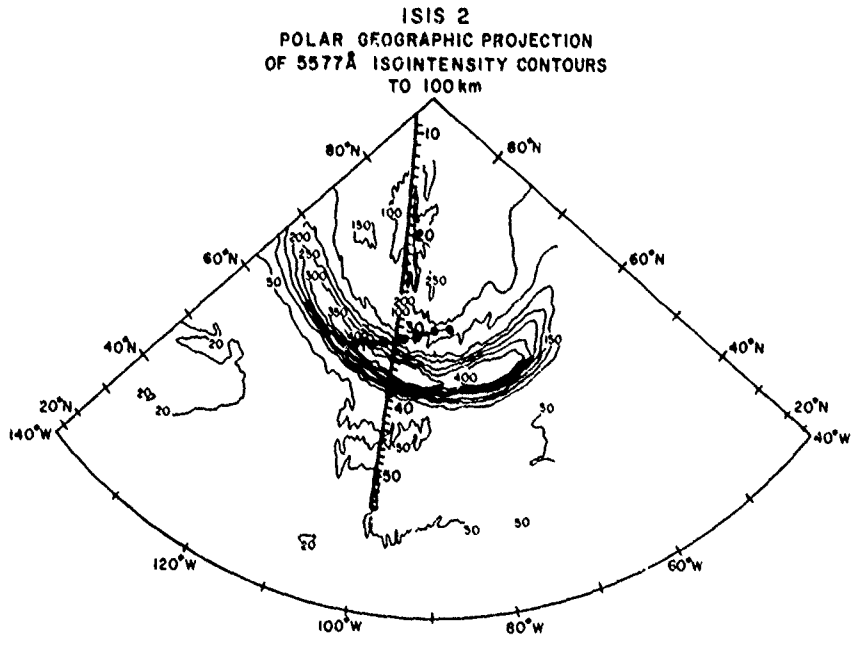

Fig. 6b. Same as Figure 6a except for 5577-Å emissions

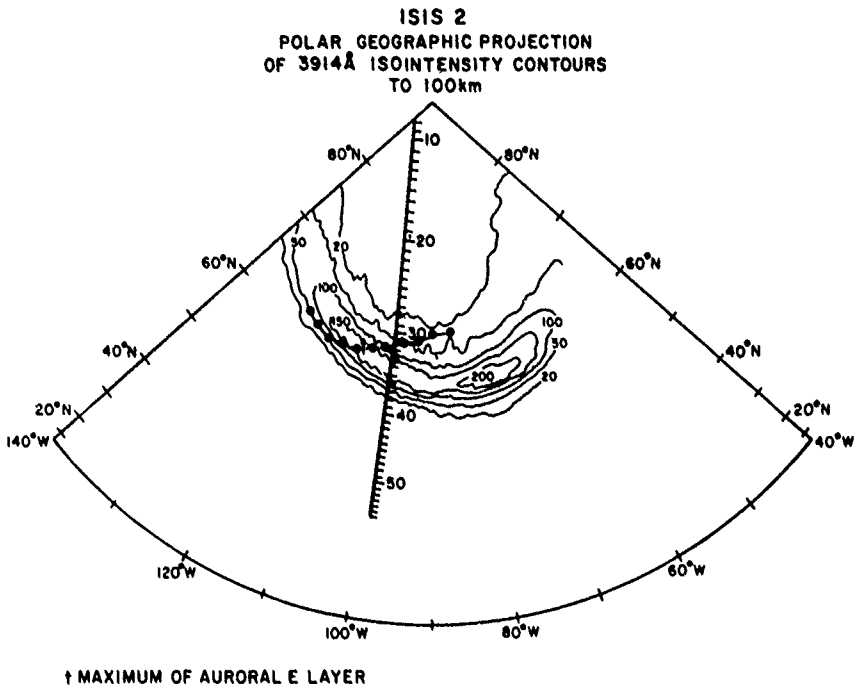

Fig. 6c. Same as Figure 6a except for 3914-Å emissions.

at the ground stations and aircraft shown in Figure 7. The 3914-Å intensity is proportional to the ion production rate and $(f_0E_a)^4$ is proportional to the recombination rate at the height of the maximum E layer electron density. Under steady state conditions these quantities will be equal.

As is seen in Figure 7, the 3914-A intensity at the location of the aircraft was 750 R. E layer critical frequencies measured by the airborne sounder were 2.7 MHz at 0604 UT and 2.7 MHz at 0615 UT, with $(f_0E)^4 = 53$. At Churchill's location, I(3914) = 1400 R, and at 0600 UT, Churchill recorded $f_0E_a = 3.15$ with $(f_0E)^4 = 98$. For both simultaneous measurements, the relation is

$$I(3914)(R) \sim 15(f_0E)^4 \quad (MHz)^4 \qquad (1)$$

Ground stations at Narssarssuaq and Godhavn are not covered by the 0600 UT Isis scan. However, if (1) were applied to the f_0E_a values of 2.1 MHz and 1.5 MHz measured at Narssarssuaq and Godhavn, the 3914-Å intensities would be 290 R and 76 R, respectively. Considering that the intensity contours are oval aligned, the contours may be extrapolated to place Narssarssuaq between the 200-R and 500-R contours of 3914-Å emission detected by Isis 2. Comparison of these independent measurements shows excellent agreement between the region of 3914-Å emission measured by Isis 2, the location of the continuous aurora measured by DMSP, and the magnitude and spatial extent of the particle-produced auroral E layer measured by ionospheric sounders.

The aircraft ionosonde and photometer also identified a region of enhanced F layer irregularities and 6300-Å auroral emission (see *Pike et al.* [1977] for a more complete discussion). Reference to Figures 4 and 6 reveals the observable region of F layer irregularities (FLIZ) and 6300-Å emission, as measured by the aircraft, to be within the region of soft particle precipitation and enhanced 6300-Å emission measured by the satellite. No quantitative results can be obtained from aircraft photometer owing to lack of reliable calibration data.

Comparison of Optical and Particle Data. The apparent quiescence and homogeneity of the aurora during this pass provides an almost ideal opportunity to compare particle and optical fluxes. The difference between times when the particle detectors sampled the precipitating fluxes and times when the optical instruments viewed the 100-km projection of these same magnetic field lines is also very favorable (10 s at high latitudes increasing to 45 s at the lower auroral latitudes). Since the intercomparison requires several steps, each of which involves significant potential sources of error, it seems worthwhile to describe the process in some detail.

First, extraction of the appropriate data from the two-dimensional optical images to form an optical profile which can be compared with the particle fluxes depends upon a precise knowledge of where the instrument was looking at any given time. This can be derived in a straightforward manner given the spacecraft position (which is well established), the orientation in space of the spacecraft spin axis, and spin rate, phase angle information which we derive ourselves from observed limb-crossing times. In a pass such as this where good 5577-Å airglow limb data are available, uncertainty in the spin axis coordinates normally represents the most significant source of error. In this case we have been able to use sightings of cities and stars together with the data from both limbs to correct the spin axis coordinates, resulting in a probable error in computed position of no more than 20 km.

As with other cases where detailed comparisons have been carried out under quiet conditions [*Lui et al.*, 1977], we observed an apparent discrepancy between the resulting optical and particle profiles, especially at the equatorward boundary. In particular, the particle flux declined to a very low level at a latitude (approximately 66.7°) where there was still considerable optical flux. Efforts to explain this excess in terms of protons or other particle fluxes outside the range of energies

Fig. 7. Auroral image (in positive format) obtained by DMSP on December 9, 1971, at 0600 U.T. The time delay between the image obtained by Isis 2 (Figure 5) and the DMSP data is 8 min. The contours are the 3914-Å contours in units of 10 R from Isis 2. The overlay coordinate system is corrected geomagnetic latitude and time.

measured by Isis are unconvincing. However, removal of the optical albedo contribution from underlying cloud, snow, and ice [*Hays and Anger*, 1978] has the effect of sharpening the optical profile and removing most of this discrepancy. A corrected optical profile was produced (Figure 4c) by assuming that albedo equals 0.7 and by using the iterative procedure described by Hays and Anger in which the effects of parallax and variable Van Rhyn factor are also taken into account. With appropriate allowances for statistical variations and the limited (once per spin) sampling rate of the particle detector the agreement between particle energy flux profile and the corrected 3914-Å optical profile appears quite good, although two regions remain where there is some remaining discrepancy: slightly below the equatorward boundary where both the 5577-Å and 3914-Å corrected profiles dip below the baseline values prevalent at lower latitudes and near 70° where the particle flux seems more sharply peaked than the optical. These apparent discrepancies will now be considered relative to possible east-west inhomogeneities in particle precipitation.

The albedo removal procedure applied in producing the corrected intensity profiles assumes east-west uniformity in the aurora. The large-scale validity of this assumption is apparent from an inspection of the pictures, but there remains the question of whether any small-scale structure might be distorting the computed profiles in ways that would make them unrepresentative. Small-scale structure could also affect the particle-optical comparison because the particle instrument samples a very confined region of space (essentially 1 gyro-

radius), while the optical detectors necessarily average over a larger region (10–50 km).

For these reasons we have examined the 5577-Å and 3914-Å data from a region extending about 100 km on either side of the spacecraft track. When relativity weak features are looked at with the maximum resolution (approximately 8 km) of the instrument, the effects of counting statistics become very pronounced leading to difficulties in distinguishing between real and purely statistical variations. This can be particularly deceptive in two-dimensional contouring where random clusterings of statistically high or low values can lead to very 'real'-looking variations, especially when the data have been smoothed. A discussion of this problem is given in the Appendix. There we are able to conclude that relatively small-scale auroral structure existed in the vicinity of the peak (giving rise to intensities of approximately 0.5–1 kR in excess of those to the east and west of the satellite track).

An overestimate of the average east-west intensity in the vicinity of the peak would also lead to an overestimate in the surface albedo intensity to be subtracted at a position just below the auroral boundary. The effect of such an error would be especially conspicuous at this location owing to the lack of any real aurora. An overestimate of 0.5 kR in the east-west average 3914-Å intensity over a 1° range in corrected geomagnetic latitude at 69° would be sufficient to explain the observed dip in the corrected profile. This is well within the realm of possibility and seems the most reasonable explanation of the dip.

Careful examination of the original pictures suggests that patchy east-west aligned arc segments are responsible for the observed intensity peak near 70° latitude. Small-scale variations of this sort (or time variations) could readily account for the discrepancy between optical and particle intensities in this region, since the optical intensities represent an average of a much larger region than that sampled by the particle detector.

Figures 8*a* and 8*b* present the corrected optical intensities at 3914 Å and 5577 Å as a function of electron energy flux in the local loss cone. The error bars in Figure 8 are representative of the calibration errors for the photometers and particle instrument. A least squares fit was made to the observed data (excluding point *e* which occurs in the region of observed east-west patchiness). The resulting relations have a slope of 950 ± 100 and 1700 ± 150 R erg^{-1} cm^{-2} s^{-1} at 3914 and 5577 Å, respectively.

The crosses in Figure 8 represent the values predicted by utilizing the results of *Rees and Luckey* [1974]. These values were derived as follows. The average energy for each loss cone energy flux measurement was derived and the appropriate 4278 Å, erg cm^2 s ratio was scaled from Figure 7 of Rees and Luckey. This value was then multiplied by 3.3 to derive the 3914-Å energy flux relationship. This ratio was multiplied by the observed energy flux resulting in the predicted 3914-Å intensities (crosses) in Figure 8*a*. The 5577-Å values (crosses in Figure 8*b*) were derived from the predicted 3914-Å flux and the ratio between 5577 Å and 4278 Å given by *Rees and Luckey* [1974]. No values could be derived for points *a*, *i*, *j*, *k*, and *l* because Rees and Luckey's relations are for $E > 300$ eV and the average energy for test points were <300 eV.

The predicted values are consistently lower than the experimentally determined ones. Some of this difference may be due to uncorrected background radiation. If the 300 R offset is subtracted from the 5577-Å experimental values, then reasonable agreement is observed. However, this same process does not bring the 3914-Å data into agreement. The experimental slope is much steeper than the predicted data, i.e., consistently more than is predicted. One possible reason for this is the low average energies observed (from 50 to 1000 eV). Most of the 3914-Å emissions would then come from >150 km and thus be sensitive to the neutral atmosphere model used. *Kasting and Hays* [1977] noted similar discrepancies when they utilized the Rees and Luckey predictions.

Residual 5577-Å intensities poleward and equatorward of the aurora are probably due to airglow. The higher level (400–500 R) inside the polar cap is remarkable but appears consistent with ground-based airglow measurements in this region [*Mullen et al.*, 1977], although their values are somewhat less intense than ours.

There is no point in attempting to model 6300-Å emissions at the present time, since the mechanisms underlying its production are still unclear. For example, a recent study by *Rees et al.* [1976] gave poor predictions of 6300-Å and 5577-Å emissions, as calculated from the primary precipitation particles. (A plot similar to the plots in Figures 8*a* and 8*b* was prepared, but no significant relationship could be derived.) Nevertheless, it is clear that one can use the $I(6300)/I(3914)$ ratio to estimate the average energy of the electrons [*Deehr et al.*, 1976], although the process should be regarded as empirical. The observed points of $I(6300) = I(3914)$ (Figure 4) correspond to the points where the soft and hard fluxes are equal and to the $E = 400$ eV (Figure 4). The poleward boundary of the region $I(3914) > I(6300)$ corresponds to higher F region electron densities. This region is narrower than the 'red band' defined by Pike in terms of half-intensity points, but if that definition is used, the spacecraft and ground-based data are consistent.

Discussion and Conclusions

If the data from Rostoker's chain of magnetometers and from the stations comprising the AE 11 index can be considered representative, the period surrounding Isis 2 orbit 3194 can be characterized as a period of relative magnetic quiescence. Figuratively speaking, it is the lull between storms. Data from the AFGL NKC-135 all-sky camera and scanning photometer provide evidence of quiet stable auroral conditions (see *Pike et al.* [1977] and *Weber et al.* [1977] for a more complete discussion of the aircraft data). In addition, the similarity of imaging data from Isis 2 and DMSP provide further support. We shall thus consider the data obtained by Isis 2 to be representative of a quasi-steady state environment.

On the basis of previous discussion, we view the variations in particle characteristics as essentially spatial. If decreasing invariant latitude is equated with decreasing geocentric distance in the equatorial plane, then the latitudinal patterns observed during orbit 3194 closely parallel the general quiet time geocentric pattern presented by *Frank* [1971]. That is, the average energy and energy flux first increase and then decrease as a function of decreasing geocentric distance (invariant latitude). Thus we conclude the fluxes observed during orbit 3194 to be of plasma sheet origin, the higher-latitude fluxes originating in the upper boundary plasma sheet and the lower-latitude portion in the central plasma sheet [see *Winningham et al.*, 1975].

Frank [1971] noted that in the premidnight hours the 'earthward edge of the plasma sheet is at 1–3 R_E beyond the plasmapause position in the premidnight period' [see *Frank*, 1971, Figure 8]. If the increase in electron density at the satellite beginning at approximately 0613 UT is interpreted as encompassing the equatorial plasmapause, then our results are in

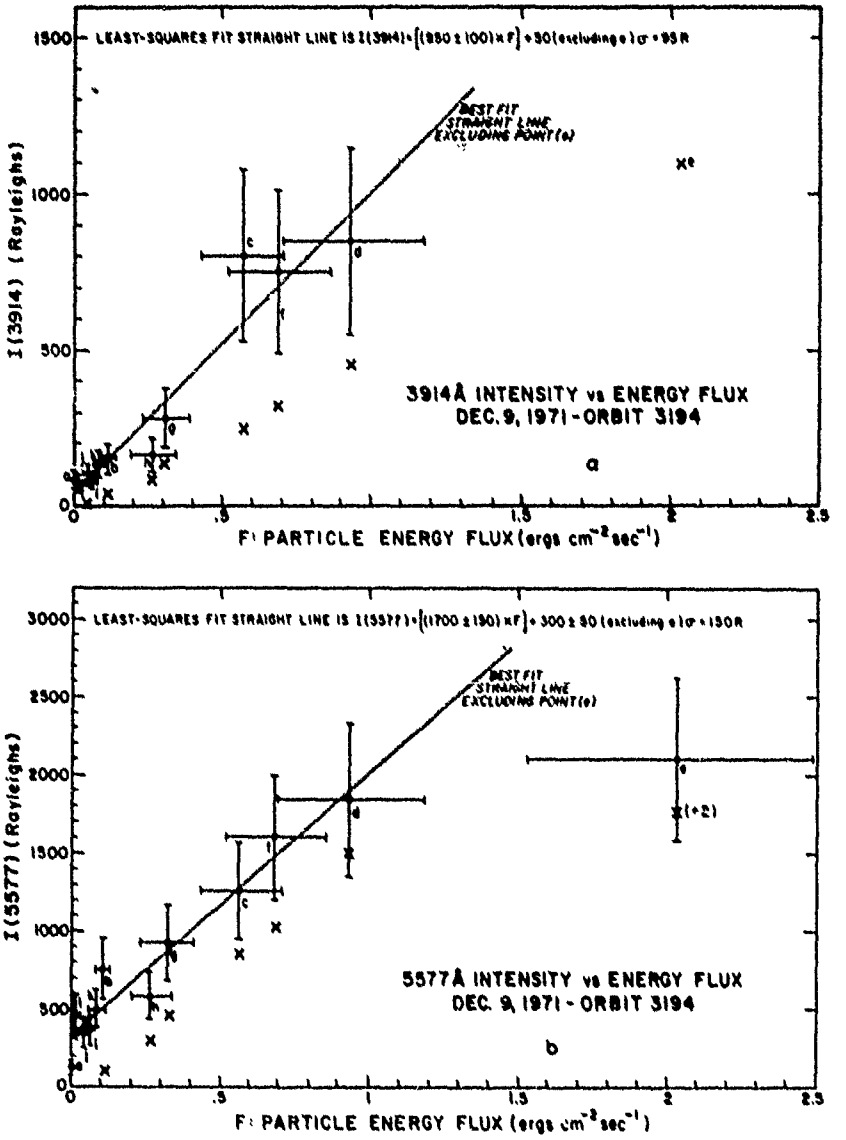

Fig. 8. Scatter plots for various auroral emissions versus total precipitated particle energy flux. Least squares fitted straight lines based on all data points except the one at the peak of the profile are shown also.

general agreement with those of *Frank* [1971]. Specifically, the edge of the low-altitude plasma sheet is located at $\Lambda \simeq 66°$, and the plasmapause is at $\Lambda < 62°$ (the exact value would depend on which definition one uses for the low-altitude plasmapause). Converting $\Delta\Lambda \geq 4°$ to ΔL gives 1.5 R_E, which is seen to lie within the 1–3 R_E found by *Frank* [1971].

Also *Frank* [1971] found that 'the trapping boundary for energetic electrons is usually observed coincident with or beyond the boundary of the earthward edge of the plasma sheet.' The '40-keV trapping boundary' defined by the Isis 2 EPD falls at $\Lambda \simeq 71°$, i.e., ~5° poleward of the inner edge of the low-altitude plasma sheet, in agreement with Frank. However, consideration of low-energy Isis 2 electron and proton fluxes show angular distributions peaked at 90° up to 76°. If such an angular distribution is taken as sufficient proof of closed field lines, then magnetic field lines are closed to at least 76°. Thus most of the low-altitude plasma sheet (possibly all) and by analogy the equatorial plasma sheet was on closed field lines during orbit 3194. Thus some caution should be used when interpreting the 40-keV boundary as the last closed field line. In the present case an erroneous conclusion would have been reached.

Comparison of the spectra in Figure 2 with published plasma sheet spectra [*Hones et al.*, 1971] reveals significant differences, especially at low energies. According to E. W. Hones (private communication, 1976) the majority of all plasma sheet spectra observed with the Vela satellites exhibit Maxwellian spectra. Only the portion of spectra 6, 7, and 8 (the spectra closest to the maximum in energy flux) above approximately 1 keV can be reasonably fitted by a Maxwellian distribution. In addition, the intensities of the low-altitude fluxes are larger than typical equatorial fluxes. Two possible conclusions come to mind. One is that there is no a priori reason to assume any relation between the auroral zone fluxes

and the equatorial plasma sheet. The second and more probable cause is the lack of detailed measurements inside and around the equatorial loss cone. This is the region of angular space where low-altitude fluxes must originate (in the absence of strong pitch angle scattering). *Hones* [1971] and more recently *McIlwain* [1975] have shown larger fluxes and different spectra inside the equatorial loss cone. Thus any firm conclusion concerning the agreement (or lack of it) between low- and high-altitude spectra must await more detailed measurements in the equatorial plasma sheet loss cone.

Along the magnetic subsatellite track the boundaries of the 'low-altitude plasma sheet' coincide with the topside poleward trough wall and the depleted polar cap. In addition, the low-altitude plasma sheet coincides with a region of enhanced electron density irregularities (spread *F*). This is not a terribly surprising result, since the observed particle fluxes represent one of the largest energy inputs into the darkened nightside ionosphere. If the relation between particle fluxes and optical emissions holds true for all local times observed by the Isis imaging system during orbit 3194, then similar topside ionospheric conditions could be reasonably expected at these locations. The same should hold true for bottomside ionospheric effects (i.e., E_s and FLIZ), and this conclusion has been verified for available ground-based sounders. This demonstrates

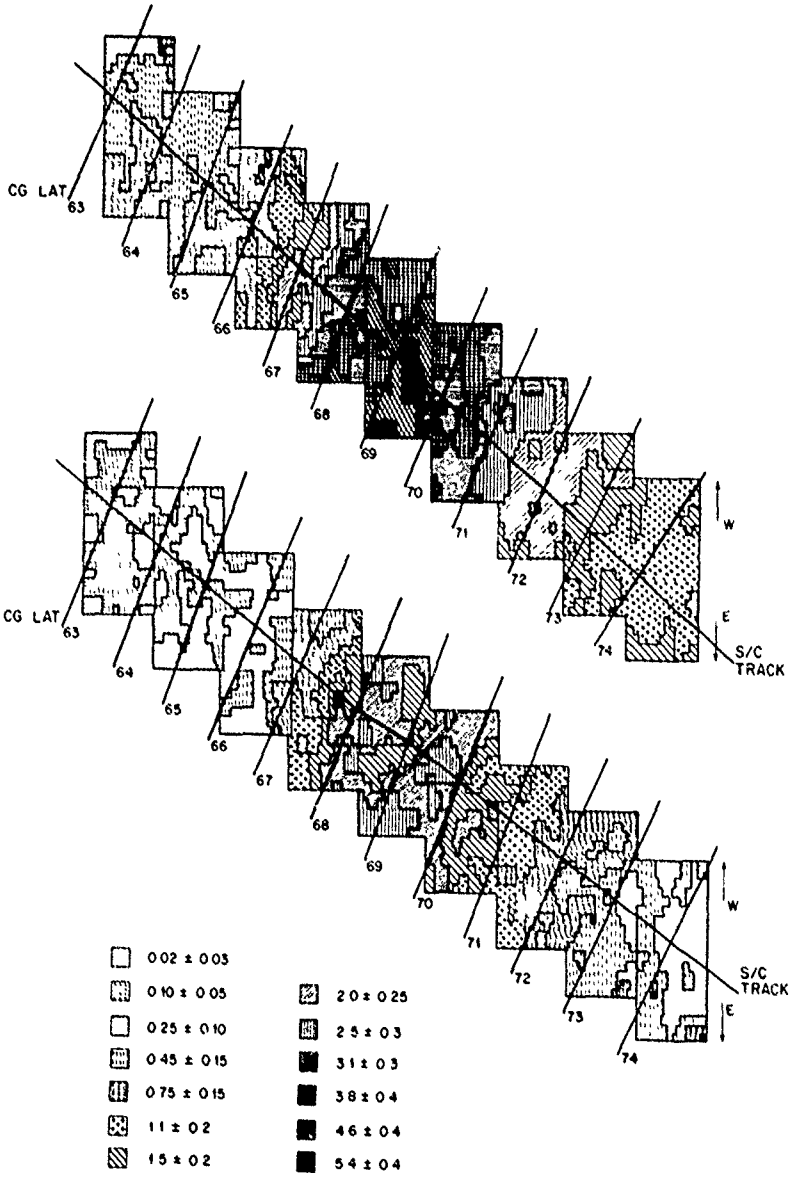

Fig. 9. A contour band plot of the (top) 5577-Å and (bottom) 3914-Å data along the spacecraft track and for about 80 km on each side. Lines of corrected geomagnetic latitude are also shown. The legend gives the intensity range in kilorayleighs of each band. The data from each spin are represented by a rectangle made up of 13 × 20 individual intensity values which have been smoothed in the manner described in the text. Data from nine successive spins were then joined to make a continuous map. East-west irregularities are attributable to counting statistics except in the 69° latitude range where both wavelengths show a consistent drop in intensity off the satellite track.

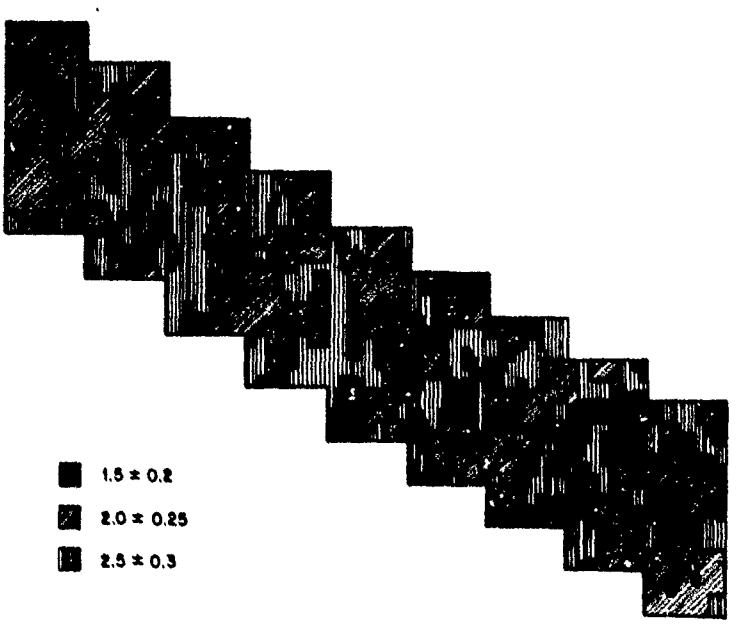

Fig. 10. A contour band plot of synthetic data processed and displayed the same as in Figure 8. Individual data values are derived from a constant intensity of 2.15 kR (10.8 counts) with superimposed counting statistical variations. The value of 2.15 kR (chosen to represent a typical case) is about 1σ removed from the center of one of the 3σ contour bands. Substantial variations are evident in the smoothed data. Such variation can be considered typical for data of any intensity where the same smoothing and relative contour bandwidth is used. They show the typical size and frequency of intrusions by adjacent bands due to statistical fluctuations alone and lead to the conclusion that most of the east-west irregularities in Figure 8 are attributable to counting statistics.

the power of 'geophysically calibrated' satellite auroral imaging systems, especially a high-altitude 'cinematography' system capable of viewing the complete auroral oval

As would be suspected from ground-based measurements, the region of low-energy electron fluxes corresponds to a region of enhanced red to green and red to blue ratios and *F* layer irregularities. In a like manner the more energetic electron spectra are associated with enhanced 5577-Å and 3914-Å photon fluxes and auroral *E* layers. These results provide support for active pursuit of 'intercalibrations' and intercomparison of satellite and ground-based (including aircraft) results to the mutual benefit of each type of measurement.

Comparison of Isis results with DMSP images supports the previously reported [*Mizera et al.*, 1975] preferential sensitivity of the DMSP system to higher-energy (greater than a few keV) electrons. Thus care should be taken in interpreting DMSP results, especially during quiet periods. Future auroral imaging systems should sample lines sensitive to low-energy fluxes.

The optical and particle data from this pass can be classified as being in 'reasonable' agreement once the effects of surface optical albedo and east-west nonuniformities in precipitation are taken into account. (Reasonable in this context is meant to imply as good as any current equivalent determination [i.e., *Kasting and Hays*, 1977].) Two-dimensional optical data of photometric quality are clearly required in carrying out such comparisons, along with great care in the interpretation of such data, even under what could be considered to be extremely quiet conditions. Dramatic variations in average particle energy (50–1000 eV) during this pass (which closely track the precipitated energy flux) show up prominently in the greater latitudinal width of the 6300-Å intensity profile relative to 5577 Å and 3914 Å and further illustrate the capabilities of optical remote sensing as a means of evaluating precipitating particle fluxes and energies over broad regions beneath a satellite.

APPENDIX: EVALUATION OF EFFECTS OF STATISTICAL VARIATIONS IN CONTOUR PLOTS

In developing a technique for presenting and interpreting data from the imaging system on Isis we have relied heavily on the use of synthetic data created by adding simulated counting statistical noise to a known two-dimensional profile (usually of constant intensity). The synthetic data are then processed and presented in the same way as the real data. When many different synthetic profiles based on the same 'real' profile were examined, we learned (somewhat to our dismay) what a large effect purely statistical variations can have on apparent contour shapes.

On the basis of this experience, we adopted the following procedure in preparing the two-dimensional intensity data. First, the data were smoothed by rows and columns by using a smoothing function of 0.25, 0.5, 0.25, and were then smoothed a second time by using the same procedure. Next they were grouped together in contour bands, each band comprising a 3σ range of intensities based on counting statistics, the reduction in σ due to smoothing being taken into account. The results for both 5577 Å and 3914 Å for the pass considered in this paper are shown in Figure 9. Most of the irregularities in the contour bands can be attributed to counting statistics, as is evidenced by Figure 10, which shows a comparable set of synthetic maps based on a uniform intensity (with statistical noise added). Data from successive spins have been joined together to give a continuous map. Examination of these and other synthetic maps leads one to conclude that the east-west variations in Figure 9 are no greater than those arising from the effects of

counting statistics alone except in the region between 69° and 70° CGL. Here east-west gradients become large and indicate that the spacecraft overflew a localized high plateau, with lower intensities on each side. Differences in the data near the peak may, in addition, imply temporal variations during the 10-s interval between samples at the two wavelengths.

Acknowledgments. The authors wish to thank L. H. Brace, J. R. Burrows, J. H. Hoffman, and J. H. Whitteker for furnishing their Isis data. The UTD portion of this work was supported by AFGL contract F 19628-76-C-0005 and NASA grants NGR44-004-150 and NGL44-004-130. The University of Calgary and York University work was supported by the National Research Council of Canada.

REFERENCES

Anger, C. D., T. Fancott, J. McNally, and H. S. Kerr, Isis-II scanning auroral photometer, *Appl. Opt., 12*, 1753, 1973.

Deehr, C. S., J. D. Winningham, F. Yasuhara, S.-I. Akasofu, Simultaneous observations of discrete and diffuse auroras by the Isis 2 satellite and airborne instruments, *J. Geophys. Res., 81*, 5527, 1976.

Dyson, P. L., and J. D. Winningham, Topside ionospheric spread *F* and particle precipitation in the dayside magnetospheric clefts, *J. Geophys. Res., 79*, 5219, 1974.

Frank, L. A., Relationship of the plasma sheet, ring current, trapping boundary, and plasmapause near the magnetic equator and local midnight, *J. Geophys. Res., 76*, 2265, 1971.

Frank, L. A., and K. L. Ackerson, Local time survey of plasma at low altitudes over the auroral zones, *J. Geophys. Res., 77*, 4116, 1972.

Hays, P. B., and C. D. Anger, The influence of ground scattering on satellite auroral observation, *Appl. Opt., 17*, 1898, 1978.

Hoffman, R. A., and J. L. Burch, Electron precipitation patterns and substorm morphology, *J. Geophys. Res., 78*, 2867, 1973.

Hones, E. W., Jr., J. R. Asbridge, S. J. Bame, and S. Singer, Energy spectra and angular distributions of particles in the plasma sheet and their comparison with rocket measurements over the auroral zone, *J. Geophys. Res., 76*, 63, 1971.

Kamide, Y., and J. D. Winningham, A statistical study of the instantaneous nightside auroral oval: The equatorward boundary of electron precipitation as observed by the Isis 1 and 2 satellites, *J. Geophys. Res., 82*, 5573, 1977.

Kasting, J. F., and P. B. Hays, A comparison between N_2^+ 4278-Å emission and electron flux in the auroral zone, *J. Geophys. Res., 82*, 3319, 1977.

King, G. A. M., *The Night-E Layer, Ionospheric Sporadic E*, edited by K. E. Smith and S. Matsushita, p. 219, Pergamon, New York, 1962.

Kisabeth, S. L., and G. Rostoker, Development of the polar electrojet during polar magnetic substorms, *J. Geophys. Res., 76*, 6815, 1971.

Lui, A. T. Y., D. Venkatesan, C. D. Anger, S.-I. Akasofu, W. J. Heikkila, J. D. Winningham, and J. R. Burrows, Simultaneous observations of particle precipitations and auroral emissions by the Isis 2 satellite in 19–24 MLT sector, *J. Geophys. Res., 82*, 2210, 1977.

Mizera, P. F., D. R. Croley, Jr., F. A. Morse, and A. L. Vampola, Electron fluxes and correlations with quiet time auroral arcs, *J. Geophys. Res., 80*, 2129, 1975.

McDiarmid, I. B., and M. D. Wilson, Dependence of the high-latitude electron ($E > 35$ kev) boundary on the orientation of the geomagnetic axis, *J. Geophys. Res., 73*, 7237, 1968.

McIlwain, E., Auroral electron beams near the magnetic equator, in *Physics of the Hot Plasma in the Magnetosphere*, edited by B. Hultqvist and L. Stenflo, p. 91, 1975.

Mullen, E. G., S. M. Silverman, and D. R. Korff, Nightglow (557.7 nm of O I) in the central polar cap, *Planet. Space Sci., 25*, 23, 1977.

Pike, C. P., J. A. Whalen, and J. Buchau, A 12-hour case study of auroral phenomena in the midnight local time sector: *F* layer and 6300-Å measurements, *J. Geophys. Res., 82*, 3547, 1977.

Rees, M. H., Auroral ionization and excitation by incident energetic electrons, *Planet. Space Sci., 11*, 1209, 1963.

Rees, M. H., Note on the penetration of energetic electrons into the earth's atmosphere, *Planet. Space Sci., 12*, 722, 1964.

Rees, M. H., and D. Luckey, Auroral electron energy derived from ratio of spectroscopic emissions, 1, Model computations, *J. Geophys. Res., 79*, 5181, 1974.

Rees, M. H., G. J. Romick, H. R. Anderson, and R. T. Casserly, Jr., Calculation of auroral emissions from measured electron precipitation: Comparison with observation, *J. Geophys. Res., 81*, 5091, 1976.

Shepherd, G., T. Fancott, J. McNally, and H. S. Kerr, Isis-II atomic oxygen red line photometer, *Appl. Opt., 12*, 1767, 1973.

Swider, W., and R. S. Narcisi, Ion composition in an IBC class II aurora, 2, Model, *J. Geophys. Res., 79*, 2849, 1974.

Vallance-Jones, A., *Aurora*, D. Reidel, Hingham, Mass., 1974.

Venkatarangan, P., J. R. Burrows, and I. B. McDiarmid, On the angular distributions of electrons in 'inverted V' substructures, *J. Geophys. Res., 80*, 66, 1975.

Weber, E. J., J. A. Whalen, R. A. Wagner, and J. Buchau, A 12-hour case study of auroral phenomena in the midnight sector: Electrojet and precipitating particle characteristics, *J. Geophys. Res., 82*, 3557, 1977.

Whalen, J. A., R. A. Wagner, and J. Buchau, A 12-hour case study of auroral phenomena in the midnight sector: Oval, polar cap, and continuous auroras, *J. Geophys. Res., 82*, 3529, 1977.

Winningham, J. D., and W. J. Heikkila, Polar cap auroral electron fluxes observed with Isis 1, *J. Geophys. Res., 79*, 949, 1974.

Winningham, J. D., F. Yasuhara, S.-I. Akasofu, and W. J. Heikkila, The latitudinal morphology of 10-eV to 10-keV electron fluxes during magnetically quiet and disturbed times in the 2100–0300 MLT sector, *J. Geophys. Res., 80*, 3148, 1975.

(Received September 2, 1977;
revised April 3, 1978;
accepted July 17, 1978.)

VOL. 81, NO. 31 JOURNAL OF GEOPHYSICAL RESEARCH NOVEMBER 1, 1976

Simultaneous Observations of Discrete and Diffuse Auroras by the Isis 2 Satellite and Airborne Instruments

CHARLES STERLING DEEHR

Geophysical Institute, University of Alaska, Fairbanks, Alaska 99701

J. DAVID WINNINGHAM

Center for Space Studies, University of Texas at Dallas, Richardson, Texas 75082

FUMIHIKO YASUHARA AND SYUN-ICHI AKASOFU

Geophysical Institute, University of Alaska, Fairbanks, Alaska 99701

All-sky camera and photometric data were obtained by airborne instrumentation as a function of latitude and time during the course of an auroral substorm. During the substorm recovery phase the Isis 2 satellite passed within 60 km of the aircraft zenith. The discrete and diffuse auroral regions were identified from the airborne all-sky camera data. Satellite and photometric observations of the corresponding incoming particles led to the following conclusions: (1) The diffuse and the discrete auroras seen in the all-sky camera data correspond to the two different particle precipitation regions observed from satellites and referred to as CPS and BPS, respectively (Winningham et al., 1975). (2) The diffuse auroral region is associated with high-energy stably trapped energetic electrons, and the discrete aurora is poleward of the stable electron trapping boundary. (3) The latitudinal distribution of characteristic particle energies does not change in a relative sense during the poleward expansion, but expands 'accordionlike.' (4) The height-integrated intensity ratio of the red (6300 Å) to green (5577 Å) emissions of atomic oxygen is a good indicator of the characteristic energy of the incoming particle spectrum.

INTRODUCTION

The auroral scanners aboard the Isis 2 and DMSP satellites have identified at least two types of auroras, the discrete and diffuse auroras [*Lui and Anger*, 1973; *Snyder et al.*, 1974; *Lui et al.*, 1975]. It is thus of great interest to examine the corresponding features in the pattern of precipitation of auroral particles. The precipitation patterns of auroral electrons along magnetic meridian lines have been studied by *Frank and Ackerson* [1971], *Hoffman and Burch* [1973], *Deehr et al.* [1973], and most recently by *Winningham et al.* [1975]. In general, the latitudinal profiles have suggested that one can distinguish at least two precipitation regions. Winningham et al. refer to these as the BPS (boundary plasma sheet) and CPS (central plasma sheet) regions, corresponding to the regions of discrete and diffuse auroras, respectively. The 'inverted V' structure [*Frank and Ackerson*, 1971] and 'lambda structures' [*Sharber and Heikkila*, 1972] are usually embedded in the BPS region.

In order to examine relationships between the precipitation pattern of auroral electrons and the two auroral regions a simultaneous observation, from above by the Isis 2 satellite and from below by the NASA 711 jet aircraft, was conducted over the Arctic Ocean on October 10, 1972. The purpose of this paper is to report some of the results of these observations.

OBSERVATIONAL CIRCUMSTANCES

Figure 1 shows both the satellite trajectory and the aircraft path, together with the *AU* and *AL* indices during the period of interest. Instead of projecting the satellite trajectory radially down to the earth's surface, it is projected along the geomagnetic field lines, to an altitude of 110 km, at which most of the precipitating electrons of the observed average energy are stopped. Over the Arctic Ocean, off Barrow, the aircraft headed first in the antiparallel direction to the expected Isis 2 trajectory (0857–1030 UT) and then flew parallel to the trajectory between 1030 and 1110 UT. The satellite passed nearest to the aircraft between 1104 and 1105 UT.

The aurora was very quiet until about 0930 UT and became quite active afterwards (see Figure 2). Several surges were observed between 0930 and 1010 UT, and an intense poleward motion began at about 1020 UT. At that time the aircraft was flying poleward, but the auroral motion overtook the aircraft at about 1023 UT and went far poleward of it by 1030 UT, at which time the aircraft turned equatorward. The satellite passed the nearest point to the aircraft when the aircraft was located approximately on the boundary between the diffuse and discrete auroral regions (70.0°N geographic latitude, 166.0°W geographic longitude). This can be seen more clearly in the all-sky photograph shown on the left-hand side of Figure 3.

In the all-sky photograph (Figure 3) we can easily distinguish two types of aurora, i.e., the brighter aurora poleward of the aircraft and the other less bright aurora, equatorward of it. Although almost no structure can be seen in the poleward aurora (because of the saturation of the film), some folds or wavy shapes are apparent near the western horizon, indicating rayed structure. Thus it is reasonable to identify the poleward aurora as a discrete aurora; in fact, it was the arc which advanced poleward at about 1020 UT. On the other hand, the equatorward aurora has a much more uniform and diffuse luminosity and could therefore be identified as a diffuse aurora.

The satellite traversed the auroral region between 1103 and 1107 UT, which was during the recovery phase of the substorm (a 200-γ negative bay at College, see Figure 1, bold line). The satellite path (again projected along the geomagnetic field lines to an altitude of 110 km) is plotted every 10 s from 1103:20 to 1106:00 UT on the all-sky photograph (Figure 3). The circled

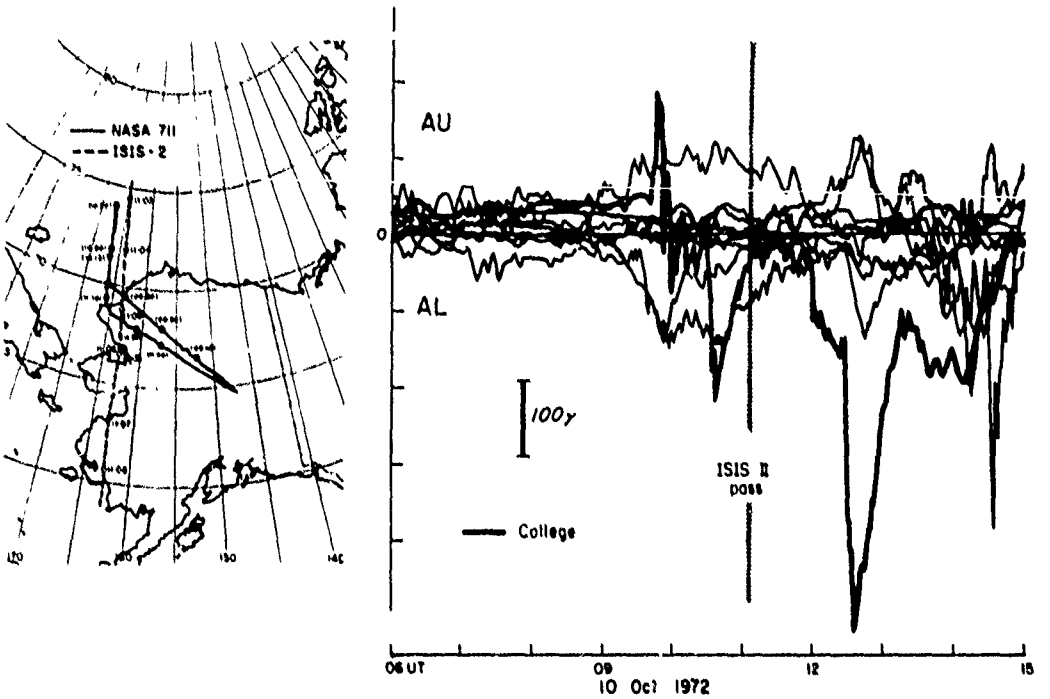

Fig. 1. A map of the Alaskan sector showing the route of the airplane (solid line) and that of the satellite (dashed line), labeled in universal time. Shown also are the *AU* and *AL* magnetic indices consisting of the envelope of auroral region *H* component magnetograms. The College magnetometer is shown as a heavier line.

dot indicates the point where the projected latitude of the satellite is 70.0°N, which is also the latitude of the zenith of the all-sky photograph. The longitudes of the zenith and the circled dot are different by approximately 60 km.

The soft particle spectrometer (SPS) spectrogram for this pass is shown on the right-hand side of Figure 3; for details of the spectrogram, see *Winningham et al.* [1975]. The satellite crossed the poleward edge of the auroral precipitation at 1103:31 UT and the equatorward edge at 1106:28 UT.

In the spectrogram we can also recognize two types of the particle precipitation, poleward and equatorward of approximately 70°N geographic latitude. The poleward precipitation shows a considerable structure and has an intense flux and higher average energy, while the equatorward one shows almost no structure (except for a very low energy burst around 1105:40 UT) and has a weaker flux and a lower average energy. Thus these two regions correspond to the BPS and CPS, respectively [*Winningham et al.*, 1975]. It can be seen that the aircraft was located near the boundary between the two precipitation regions during the satellite pass.

SATELLITE OBSERVATIONS

The low-energy (< 15 keV) electron data obtained by Isis 2 (see Figure 3) can be regarded as a 'snapshot' of the late substorm electron latitudinal profile. As mentioned in the previous section, two distinctively different regions can be recognized in the spectrogram. From 1103:23 UT (Λ = 70.8°) to 1104:32 UT (Λ = 67.6°) a band of structured intense electron flux was observed. At lower latitudes from 1104:32 to 1106:28 UT (Λ = 62.3°) a relatively uniform weaker electron flux was measured. In Figures 4*a*–4*d*, spectra representative of the structured region are presented, as is done for the diffuse precipitation in Figures 4*e*–4*h*.

The energy spectrum of auroral primary electrons can often be described by an equation of a Maxwellian type: $N(E)\,dE = N_0 E \exp(-E/\alpha)$ el cm^{-2} s^{-1} eV^{-1}, where α ($= kT_e$) is the 'characteristic energy,' or the energy at the peak of the distribution. As can be seen in Figures 4*e*–4*h*, the high-energy end of the spectrum in the diffuse auroral region is well described by a Maxwellian distribution, but the low-energy portion is best described by a power law. An exception to the low-energy power law was observed in spectrum 4*g*. This spectrum was taken from the low-energy burst observed in the spectrogram (Figure 3) at approximately 1105:30 UT. The low-energy burst cannot be described by a Maxwellian distribution either, the observed spectrum being narrower than a Maxwellian. This low-energy burst constitutes only a minor fraction of the total energy flux and thus does not contribute significantly to the auroral luminesity.

The characteristic energy of the electron spectra in the diffuse zone gradually increased from 0.9 keV as the invariant latitude decreased. A maximum of 1 keV was reached at ~1105:50 UT (Λ = 63.9°) after which time it gradually decreased to 0.6 keV (Figures 4*e*–4*h*). The power law portion (at low energies) of the observed spectra could be due to conjugate degraded primaries and secondaries.

The structured auroral region exhibits a variety of spectra, some of which are described by a Maxwellian curve (Figures 4*a* and 4*d*) and others which are not (Figures 4*b* and 4*c*). Spectrum 4*a* was obtained in the region just poleward of the intense bursts. Spectra 4*b* and 4*c* were obtained in the region of intense bursts and highest average energy. Spectrum 4*d* was observed just equatorward of the most intense bursts and is Maxwellian in shape except for the low-energy region, which is power law. Its characteristic energy (1.4 keV) is higher and its total energy input is greater than those observed in the diffuse

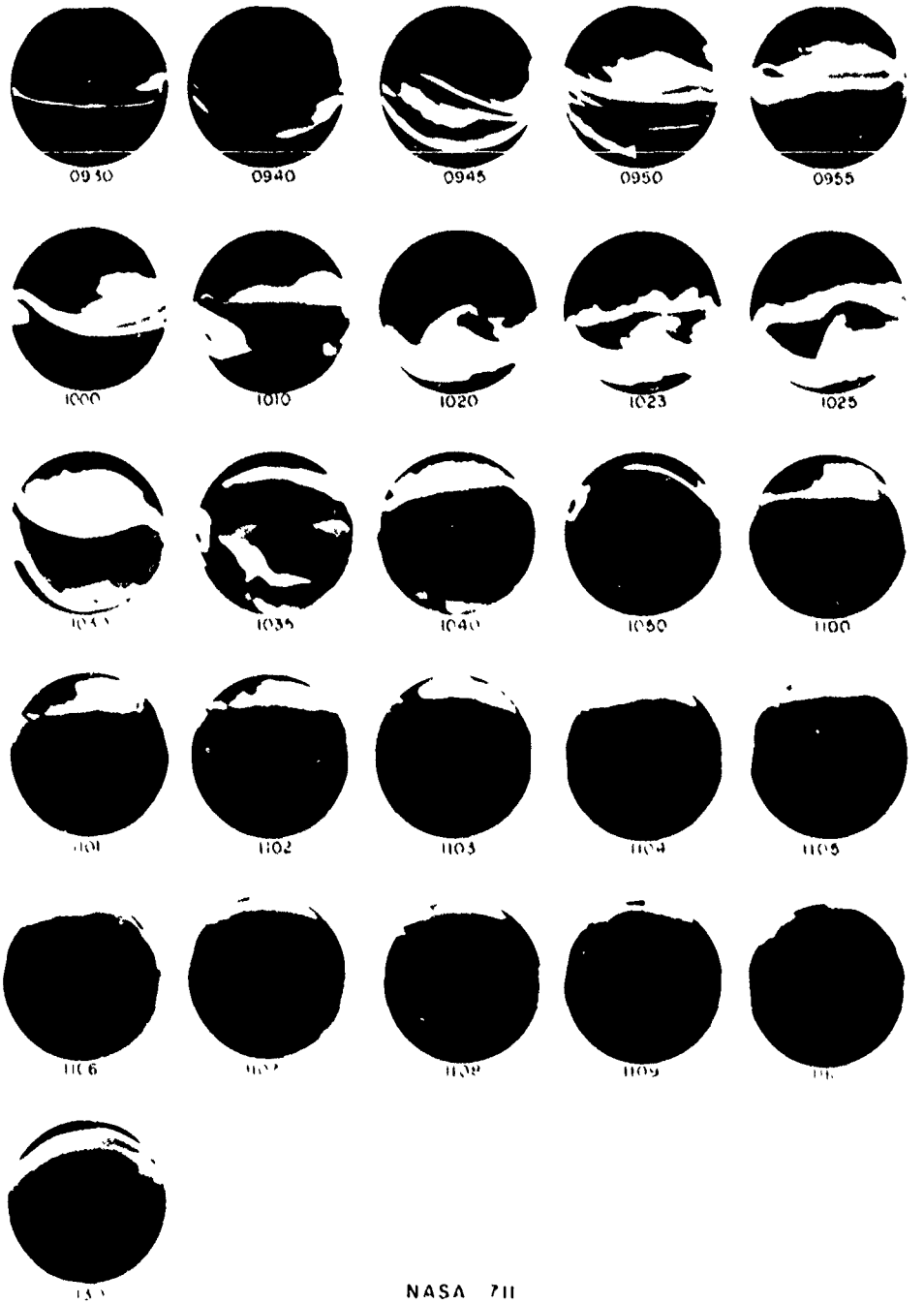

Fig. 2. A collection of all-sky camera photographs taken from the NASA 990 aircraft during the flight of October 10, 1972. The substorm begins over the aircraft at 0930 and expands poleward (up) with the aircraft until the aircraft turns equatorward at 1030, flying under the diffuse aurora to the end of the flight (geomagnetic north is up and east is to the right).

region (Figures 4*e*–4*h*).

The spectra shown in Figures 4*b* and 4*c* cannot be fitted with a Maxwellian distribution. These spectra can be better characterized as 'peaked' (or 'monoenergetic' if count rate were plotted). 'Peaks' in the spectra occur from 1 to 4 keV. Energy fluxes as large as 20 ergs cm^{-2} s^{-1} were observed. If isotropy is assumed, this flux would produce ~100 kR of 5577 Å, enough to saturate the all-sky film, as observed.

Data (courtesy of J. R. Burrows) from several channels of the energetic particle detector (EPD) are presented in Figure 3.

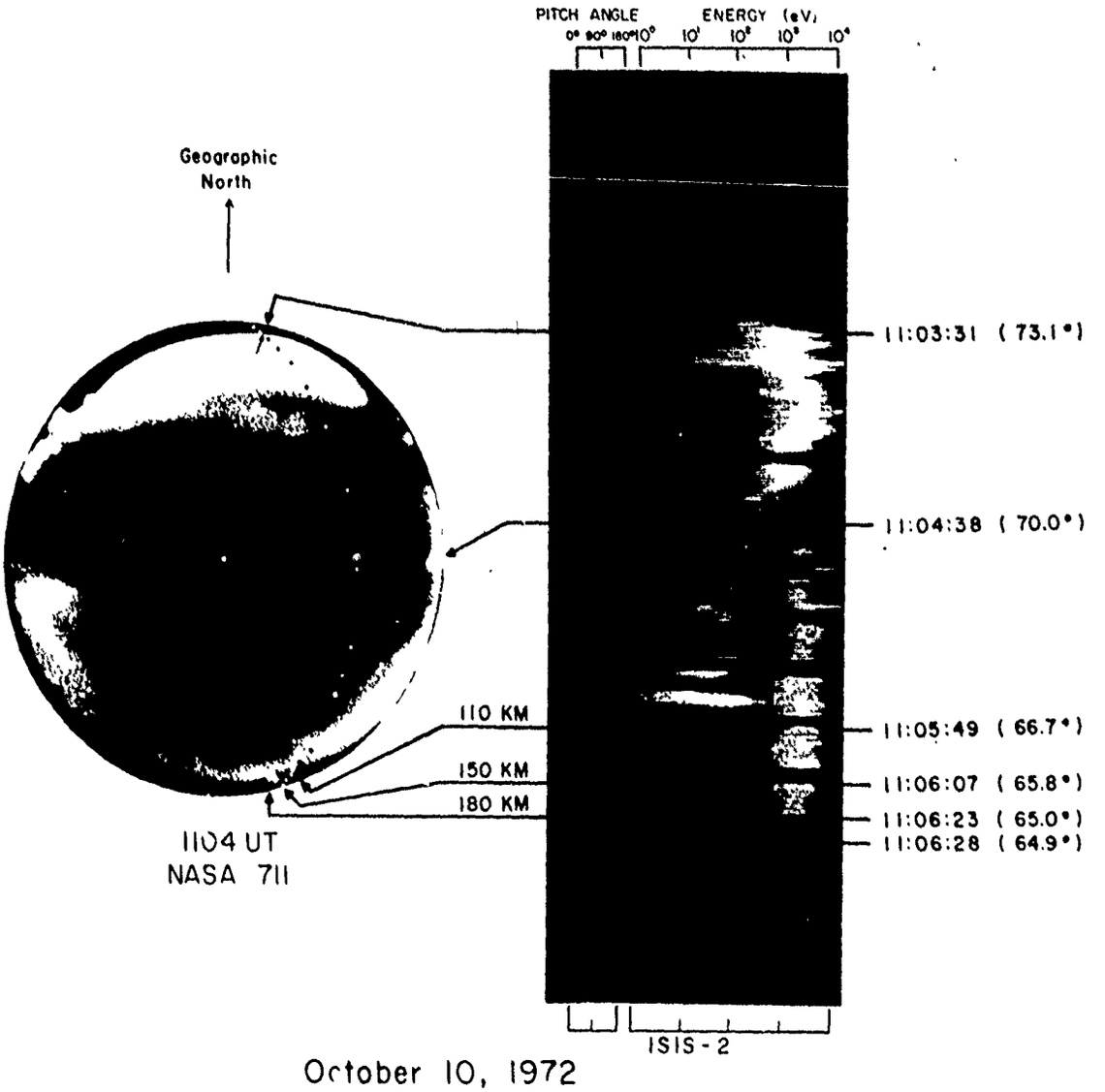

Fig. 3. An all-sky camera photograph corresponding to the closest time of passage of the satellite with the aircraft. The path of the satellite is projected downward along magnetic field lines to the 110-km altitude and shown as dots on the photograph. The times at which the satellite passes various points on the photograph are indicated by arrows, along with the assumed height of the aurora. The southern edge of the particle data corresponds to an auroral altitude of 150–180 km, which is consistent with the characteristic energy of the particles detected at the satellite (see text).

As in the lower-energy data, a change was observed in the EPD fluxes at approximately 1104:30 UT. Equatorward of this point a twice per spin modulated flux with deep minima in both hemispheres was observed. The >200-keV stable trapping boundary was located at this point (Figure 5*f*). Poleward of this boundary the energetic flux softened considerably (see Figures 5*a* and 5*b* for the ratios of the >22- to >40-keV and >40- to 60-keV fluxes) and became structured. It should be noted here that the 'softening' of the high-energy flux is reflected as an increase of the characteristic energy of the electrons measured with the SPS.

All-Sky Camera Observations

The intersection between the poleward edge of the auroral luminosity and the satellite trajectory projected to 110 km is indicated by a black arrow in Figure 3. (Hereafter the satellite location will be the projection to 110 km along the magnetic field.) It can be seen (Figure 3) that except for a very narrow (in latitude) region of soft (average energy less than 1 keV) particle precipitation, the poleward edge of the structured precipitation region coincides with the poleward boundary of the auroral luminosity, in spite of its large zenith angle (about 76°) in the all-sky photograph. The soft particles precipitating just poleward of the discrete aurora might have caused an appreciable luminosity. However, because the average energy is low (see Figure 4*a*), the height of this luminosity must have been higher than 110 km, so that it was likely to be located 'behind' the bright aurora.

If the heights of the equatorward edge of the diffuse aurora are assumed to be 110, 150, and 180 km, the equatorward

boundary of the diffuse aurora on the all-sky photograph can be compared in Figure 3 with that of the diffuse precipitation region on the spectrogram. The point of intersection between the equatorward edge of the auroral luminosity and the satellite path projected down to 110-, 150-, and 180-km heights is shown with the white arrow head, star mark, and triangle, respectively. If the height of the diffuse aurora is assumed to be 110 km, the particle and optical boundaries do not coincide (geographic latitude 66.7° from the all-sky photograph and 64.9° from the spectrogram), and thus the precipitation boundary is located at a lower latitude by approximately 2°. If the height is assumed to be 180 km, they almost coincide with each other (at approximately latitude 65.0°). The energy of electrons must have been near 600 eV to have caused a maximum ionization at 180-km altitude. Indeed, such a value is approximately that of the observed characteristic energy of the particles on the equatorward edge of the precipitation region (see Figure 4*b*).

Another effect which must be accounted for here is that the actual equatorward edge of the diffuse aurora must have been hidden by the lower-altitude part of the diffuse aurora. In fact, the equatorward edge of the diffuse aurora, determined by assuming a 110-km height, corresponds to the point of the highest average energy (approximately 2 keV) in the diffuse precipitation region (at 1105:49 UT; 66.7° geographic latitude, or see Figure 4*f*). As was mentioned earlier, the average energy of the particles gradually decreased equatorward of this point, and therefore the height of the luminosity must have increased (Figure 4*h*). These effects combine to produce the apparent discrepancy between the edges of the precipitation region and luminosity determined from an all-sky camera in the middle of this region.

The diffuse aurora observed by the satellite during this late substorm recovery was the result of the precipitation of Maxwellian electrons, most likely from the inner portion of the plasma sheet (CPS).

PHOTOMETRIC OBSERVATIONS

A 6-in. aperture birefringent filter photometer with a 5° full field of view directed toward the zenith was mounted on the aircraft. This photometer (described by *Deehr* [1969]) is of a type which continuously subtracts the observed background continuum emission signal from narrow discontinuities on the emission continuum. It is therefore most useful for observing the intensity of atomic emission lines, and for the present study these lines were the red and green lines of neutral atomic oxygen at 6300 and 5577 Å, respectively.

The usefulness of these auroral emission lines for determining the characteristic energy of the incoming particle population has been shown by several workers, most recently by *Rees and Luckey* [1974]. Both emissions originate from low, metastable energy levels of neutral atomic oxygen, but the lifetime of the 6300-Å line is considerably longer (110 versus 0.75 s), so this level is collisionally depopulated at a far greater rate at low auroral altitudes. Because both emissions are predominantly excited by secondary electrons whose energy spectrum is, in turn, determined by the characteristics of the incoming primary electrons and because the primary electrons are deposited in altitude inversely according to energy [cf. *Rees*, 1969], the ratio of the intensities of these two lines (6300 Å/5577 Å) is a good measure of the characteristic energy of the incoming primaries.

The intensity of the N_2^+ first negative group is directly related to 5577-Å emission [*Rees and Luckey*, 1974]. The 4278-Å N_2^+ emission may be a better measure of the total ionization than the green line, but it could not be used in the present study because the photometer is not linearly sensitive to emissions of spectral width greater than 6 Å.

Eather and Mende [1972] plotted 6300 Å/4278 Å versus 4278-Å emission as a measure of incoming particle energy for a number of similar aircraft excursions across the auroral zone and found that statistically the lower-energy particles and thus the resulting higher 6300 Å/4278 Å emission ratio were found on the poleward side of the nightside auroral precipitation zone [see also *Mende and Eather*, 1975]. However, this is not always the case, and at times lower characteristic energies could be found at lower latitudes and higher at higher latitudes. For example, the latitudinal distribution of characteristic energy may depend on substorm time [see *Winningham et al.*, 1975].

Figure 6 shows the observed intensity of 6300- and 5577-Å emissions along with the 6300 Å/5577 Å ratio as a function of time throughout the flight. Five areas of different auroral character are indicated in the figure according to Table 1.

The wide variations of the 6300 Å/5577 Å intensity ratio (Figure 6, area 2) are due mostly to viewing the upper and lower borders of moving discrete arcs, which is another indication of the dependence of this ratio on the altitude of the emitting region. The diffuse aurora (Figure 6, area 4), on the other hand, shows a remarkably steady relationship between the two emissions. Plotting the 6300 Å/5577-Å ratio as a function of the 5577-Å intensity (Figure 7) shows, as is generally known, that the brighter the aurora, the more energetic the incoming particles (see next paragraph). Thus all-sky camera pictures can, in general, be a good qualitative indicator of the characteristic energy of the incoming particles; the photometers can, however, provide a quantitative index of the incoming particle energy.

The intensity ratio predicted by *Rees and Luckey* [1974] is shown by solid lines in Figure 7. Because these curves are based on the predicted intensity of 4278-Å N_2^+ 1NG emission, a conversion to 5577-Å emission was made from Figure 4 of *Rees and Luckey*'s [1974] work. What is shown here is that the characteristic energy α of the incoming electrons varied between approximately 0.2 and 6 keV during the airplane flight. In terms of substorm events this may be summarized in the following way:

1. The initial poleward expanding arc is of low characteristic energy.
2. The bright, discrete poleward arcs immediately following the poleward expansion are associated with electrons of relatively high characteristic energy.
3. The diffuse aurora (after the poleward expansion) has a lower energy characteristic than the bright poleward expanding arc.

Implicit in this result is the support of the Rees and Luckey model for the particle-emission relationship. Indeed, the characteristic energies determined by the photometric data in Figure 7 for each type of aurora match very well the observed particle energy as listed in the last two columns of Table 1. Although the agreement is no better than the assumption that the intensity calibration (comparison with ground-based photometers) is within 50% and that the fluctuations are due to departure from total height integration of the emission.

As mentioned earlier, the particle data from the satellite pass shown in Figure 3 may be regarded as a late substorm snapshot of the latitudinal distribution of auroral precipitation as reconstructed from the photometric data. In other words, at

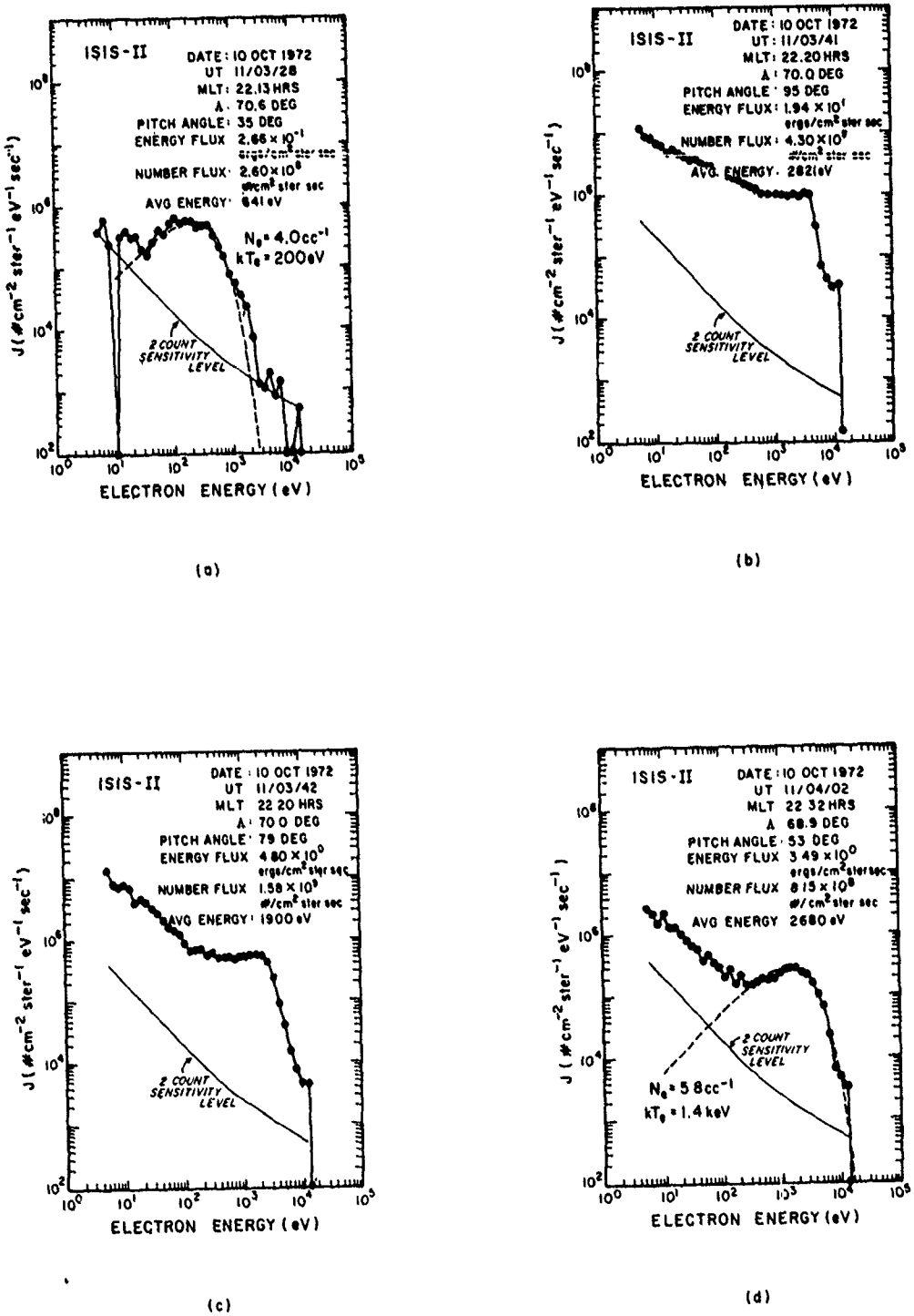

Fig. 4. Eight representative electron differential number flux spectra from the Isis 2 satellite pass 7073. The dots are actual data points, and the dashed lines are least square fits of Maxwellian energy distribution curves which are described by total number flux N_t and characteristic energy $\alpha(kT_e)$

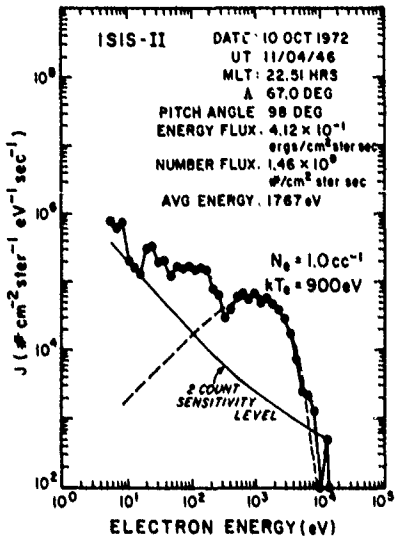

(e)

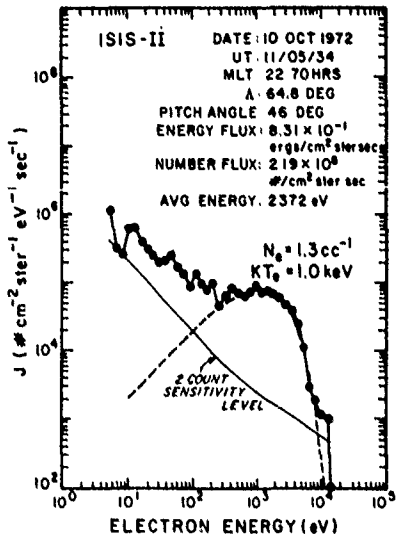

(f)

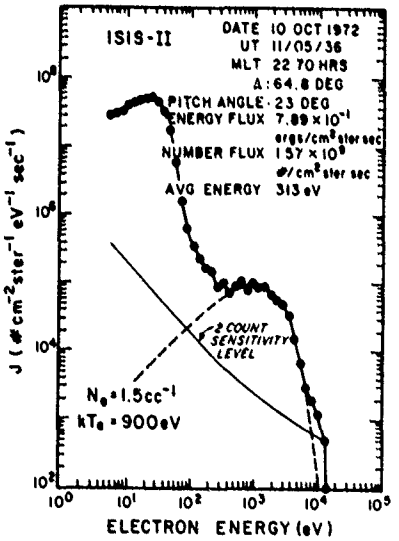

(g)

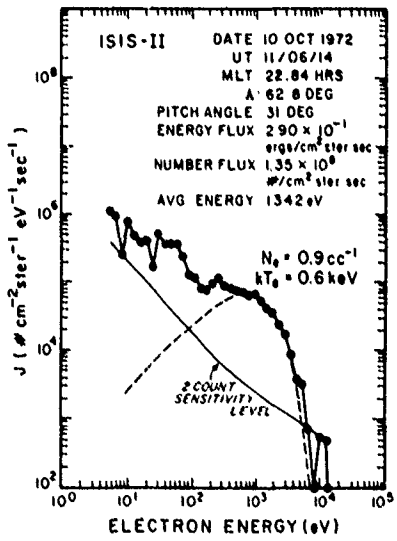

(h)

Fig. 4. (continued)

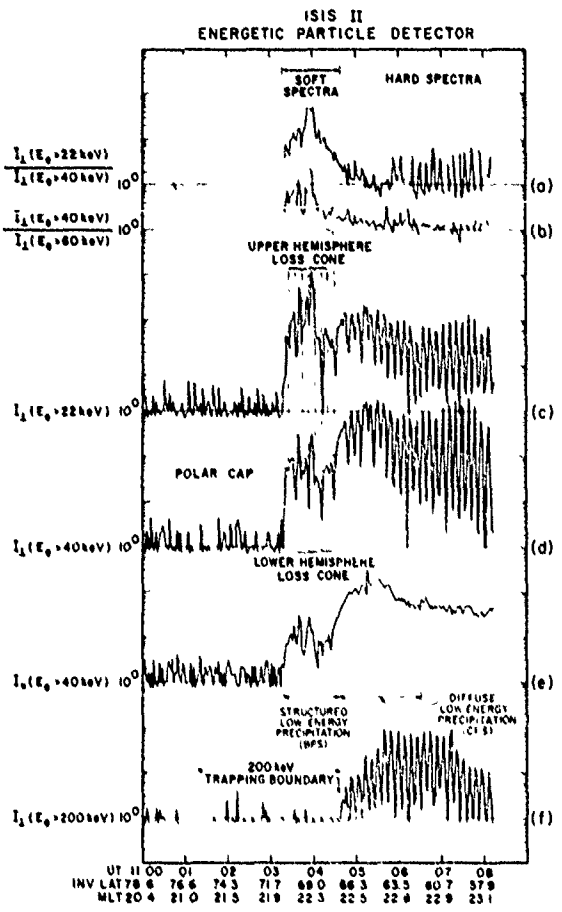

Fig. 5. Energetic particle detector (EPD) data from Isis 2 satellite pass 7073. Parallel and perpendicular markings refer to detector orientation with respect to satellite spin axis (courtesy of J. R. Burrows).

the time of the satellite pass late in the substorm, the latitudinal distribution of characteristic energy determined from the particle data was remarkably similar to that encountered during the course of the substorm from the aircraft according to the photometric observations. Thus the relative latitudinal distribution of particle energy remained roughly the same and appeared to expand accordionlike with the poleward expansion of the substorm. The only region in substorm space-time

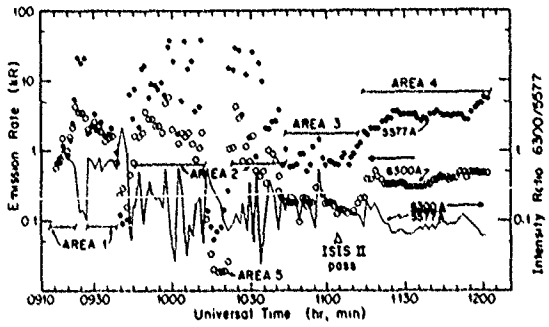

Fig. 6. The zenith intensity of the red (6300 Å) and green (5577 Å) lines of atomic oxygen are shown as open and solid circles, respectively, as a function of universal time during the NASA 990 aircraft flight of October 10, 1972. The intensity ratio is the solid line. The areas covering different auroral features are indicated and explained in Table 1.

not covered by this generalization is the early equatorward (diffuse) aurora (Figure 4*h*), which was equatorward of the airplane throughout the flight.

Another feature of interest is the appearance in Figures 3 and 4*d* of a large flux of low-energy electrons near 1105:36 UT. Although this spectrum indicates an increase of more than a factor of 10 in total number flux, the contribution to the total energy flux is almost nothing. The feature is therefore not visible on the all-sky camera photograph.

SUMMARY

All-sky camera and photometric data were obtained from a jet aircraft as a function of latitude during the course of an auroral substorm. Late in the substorm, near magnetic midnight, the Isis 2 satellite passed near the zenith of the aircraft on a north-south orbit. The position of the discrete and the diffuse auroral regions was determined from the all-sky camera data and compared to the particle data taken by the satellite. Additionally, the ratio of the red (6300 Å) and green (5577 Å) emission lines of atomic oxygen, as a measure of the incoming particle energy, was compared to the particle energy determined from the satellite and to the type of aurora seen on the all-sky camera.

The results of these intercomparisons are as follows:

1. The diffuse and the discrete auroras seen in the all-sky camera data correspond to the two different particle precipitation regions observed from satellites and referred to as CPS and BPS, respectively [*Winningham et al.*, 1975].

TABLE 1. Character of Aurora in the Five Areas Shown in Figure 6

Area	UT, hours	Latitude deg	Type of Aurora	Characteristic Energy	
				Isis 2	Figure 7
1	0915-0923	67	initial poleward expansion arc	200 eV (Fig. 4*a*)	200-600 eV
	0928-0938	68			
2	0923-0928	67.5	bright discrete poleward arcs	>2 keV (non-Maxwellian, see Figs. 4*b*, 4*c*)	<4 keV
	0945-1014	69-73			
	1020-1040	72.5-73			
3	1040-1110	73-69	between diffuse and discrete aurora	900 eV (Fig. 4*e*)	<1.6 keV
4	1115-1200	69-65	diffuse equatorward aurora	1 keV (Fig. 4*f*)	<2 keV
5	0930-0945	69	dark sky poleward of aurora		
	1015-1020	72-72.5			

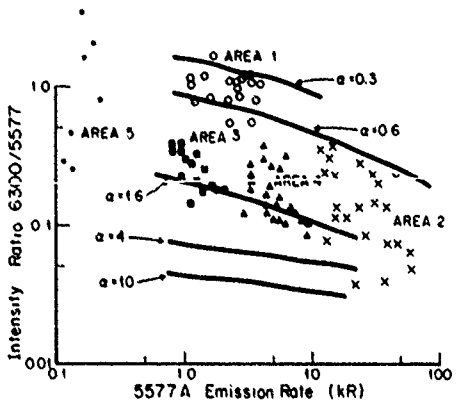

Fig. 7. The 6300 Å/5577 Å intensity ratio as a function of the 5577-Å emission rate. The solid lines indicate the values predicted by *Rees and Luckey* [1974]. The data points are separated according to the areas defined in Figure 6 and Table 1.

2. The diffuse auroral region is associated with stably trapped energetic particles, and the discrete aurora is poleward of the stable trapping boundary.

3. The latitudinal distribution of characteristic particle energies does not change in a relative sense during the poleward expansion but expands accordionlike.

4. The height-integrated intensity ratio of the red (6300 Å) to green (5577 Å) emissions of atomic oxygen is a good indicator of the characteristic energy of the incoming particle spectrum.

Acknowledgments. The UTD portion of this work was supported by NASA grants NGR44-004-150 and NSG 4085 and U.S. Air Force contracts F19628-75-C-0032 and F19628-76-C-0005. The University of Alaska portion was supported by NSF grant ATM74-23832A01 and NASA grant NGR02-001-093.

The Editor thanks I. B. McDiarmid for his assistance in evaluating this paper.

REFERENCES

Deehr, C. S., The twilight enhancement of the auroral and nebular lines of neutral atomic oxygen, *Ann. Geophys.*, *25*, 881, 1969.

Deehr, C. S., A. Egeland, K. Aarsnes, R. Amundsen, H. R. Lindalen, F. Søraas, P. Stanning, H. Borg, G. Gustafsson, L.-A. Holmgren, W. Riedler, P. A. Smith, G. R. Thomas, and R. Jaeschke, Particle and auroral observations from the Esro 1/Aurorae satellite, *J. Atmos. Terr. Phys.*, *35*, 1979-2011, 1973.

Eather, R. H., and S. B. Mende, High latitude particle precipitation and source regions in the magnetosphere, in *Magnetosphere-Ionosphere Interactions*, edited by K. Folkestad, Scandinavian University Books, Oslo, Norway, 1972.

Frank, L. A., and K. L. Ackerson, Observations of charged particle precipitation in the auroral zone, *J. Geophys. Res.*, *76*, 3612, 1971.

Hoffman, R. A., and J. L. Burch, Electron precipitation patterns and substorm morphology, *J. Geophys. Res.*, *78*, 2867, 1973.

Lui, A. T. Y., and C. D. Anger, A uniform belt of diffuse auroral emission seen by the Isis-2 scanning photometer, *Planet. Space Sci.*, *21*, 799, 1973.

Lui, A. T. Y., C. D. Anger, D. Venkatesan, W. Sawchuck, and S.-I. Akasofu, The topology of the auroral oval as seen by the Isis 2 scanning auroral photometer, *J. Geophys. Res.*, *80*, 1795, 1975.

Mende, S. B., and R. H. Eather, Spectroscopic determination of the characteristics of precipitating auroral particles, *J. Geophys. Res.*, *80*, 3211, 1975.

Rees, M. H., Effects of low energy electron precipitation on the upper atmosphere, in *The Polar Ionosphere and Magnetospheric Processes*, edited by G. Skovli, Gordon and Breach, New York, 1969.

Rees, M. H., and D. Luckey, Auroral electron energy derived from ratio of spectroscopic emissions, 1, Model computations, *J. Geophys. Res.*, *79*, 5181, 1974.

Sharber, J. R., and W. J. Heikkila, Fermi acceleration of auroral particles, *J. Geophys. Res.*, *77*, 3397, 1972.

Snyder, A. L., S.-I. Akasofu, and T. N. Davis, Auroral substorms observed from above the north polar region by a satellite, *J. Geophys. Res.*, *79*, 1393, 1974.

Winningham, J. D., F. Yasuhara, S.-I. Akasofu, and W. J. Heikkila, The latitudinal morphology of 10-eV to 10-keV electron fluxes during magnetically quiet and disturbed times in the 2100-0300 MLT sector, *J. Geophys. Res.*, *72*, 3148, 1975.

(Received February 18, 1976;
accepted July 28, 1976.)

VOL. 82, NO. 35 JOURNAL OF GEOPHYSICAL RESEARCH DECEMBER 1, 1977

Dependence of Substorm Occurrence Probability on the Interplanetary Magnetic Field and on the Size of the Auroral Oval

Y. KAMIDE,[1,2] P. D. PERREAULT,[3] S.-I. AKASOFU,[4] AND J. D. WINNINGHAM[5]

The dependence of substorm occurrence probability on the north-south component B_z of the interplanetary magnetic field (IMF) and on the size of the auroral oval is examined on the basis of two independent data sets (Isis 1 and 2 low-energy electron data and all-sky camera data from the Alaska meridian). The occurrence of substorms is identified by the electron precipitation pattern (Isis data), the auroral features in the Alaskan sector, and available ground magnetic records. The substorm occurrence frequency increases as the oval expands and as the B_z component of the IMF decreases. It increases from approximately 25% to 100% for B_z values of the IMF ranging from +7 to −5 nT; here B_z values are averaged for 1 hour preceding the time of satellite passage and the onset of substorms observed by the all-sky cameras. The occurrence probability of quiet times increases with an increasing value of the northward IMF. It is interesting to note that there are almost no periods without substorms when the IMF has a large southward component, but substorms do occur even when the IMF has a large northward component. Since there is a close relationship between the direction of the IMF and the size of the auroral oval, our finding that the occurrence frequency of substorms increases with the expansion of the auroral oval suggests that the substorm probability may be related to the amount of energy stored in the magnetotail.

INTRODUCTION

A large number of ground-based and spacecraft observations of plasma parameters and electric and magnetic fields have been used in constructing a working model of magnetospheric substorms [*Akasofu*, 1968; *McPherron et al.*, 1973a; *Akasofu and Kan*, 1973; *Mozer*, 1973]. In particular, during the last several years, one of the most important subjects in magnetospheric physics has been the role of the north-south component (B_z) of the interplanetary magnetic field (IMF) on substorm processes (see review papers by *Burch* [1974] and *Nishida* [1975]). It has been noted that the auroral oval, along which polar substorms occur, responds to the IMF; it expands equatorward and contracts poleward during periods of southward and northward IMF, respectively [e.g., *Akasofu et al.*, 1973; *Winningham et al.*, 1975; *Holzworth and Meng*, 1975; *Kamide and Winningham*, 1977]. However, we are still far from even a first approximation of the cause of substorms [*Vasyliunas and Wolf*, 1973; *Burch and Hoffman*, 1974; *Vasyliunas*, 1976].

It was about a decade ago when substorms observed along the classical auroral zone were found to be associated with a southward turning of the IMF [e.g., *Fairfield and Cahill*, 1966; *Rostoker and Fälthammar*, 1967]. This finding has also been claimed to be statistically confirmed by *Arnoldy* [1971] and *Foster et al.* [1971]. Subsequently, however, *Nishida* [1971] has shown a few cases of substorms occurring during the northward directed IMF. *Akasofu et al.* [1973] have shown, by using all-sky camera data along a meridian chain of observatories, that substorms are quite frequently observed along the contracted auroral oval during periods of the northward IMF. Thus they have concluded that there is no single IMF signature, such as its southward turning, that is consistently related to the substorm onset. Recently, it has been reported by *Kamide and Akasofu* [1974] and *Kamide et al.* [1975] that there is no qualitative distinction between the 'normal' and 'contracted oval' substorms in terms of typical auroral and geomagnetic disturbance features (i.e., a breakup, westward traveling surges, and negative bays) but that the energy released during a substorm associated with the southward IMF is greater than that released during a substorm associated with the northward IMF. *Lui et al.* [1976] have shown that there is no basic difference between these substorms except for the intensity and extent of the area covered by active auroras and electrojets.

There is one important problem which is crucial in seeking substorm generation mechanisms: Does substorm occurrence probability depend on the B_z component of the IMF (or equivalently on the size of the oval)? If the occurrence frequency has a strong dependence on the IMF direction (or the size of the auroral oval), one might be able to speculate that the occurrence frequency of substorms is closely related to the amount of energy stored in the magnetotail, since there is a definite relationship between the IMF B_z and the magnetic energy stored in the magnetotail [e.g., *Siscoe and Crooker*, 1974; *Gonzalez and Mozer*, 1974; *Akasofu*, 1975]. If, on the contrary, the occurrence probability has no such dependence, substorms may be regarded as a random process. This dependence has been difficult to examine because of the lack of continuous observational data on the entire polar region.

Lui et al. [1975] have shown, using auroral scanning photometer imagery from 58 Isis 2 satellite passes, that the substorm 'seeing' probability decreases as the auroral oval size decreases. They then suggested that although the seeing probability is not the same as the occurrence probability, there is the possibility that the latter decreases as the auroral oval contracts poleward.

In this paper an attempt is made to show that there is a definite dependence of substorm occurrence frequency on the north-south component of the IMF and on the size of the auroral oval on the basis of two independent data sets: Isis satellite electron spectrograms and all-sky camera records along the Alaska meridian.

[1]Cooperative Institute for Research in Environmental Sciences, University of Colorado, NOAA, Boulder, Colorado 80302
[2]On leave of absence from the Kyoto Industrial University, Kyoto 603, Japan
[3]Radio Physics Laboratory, Stanford Research Institute, Menlo Park, California 94025
[4]Geophysical Institute, University of Alaska, Fairbanks, Alaska 99701
[5]Center for Space Sciences, University of Texas at Dallas, Richardson, Texas 75080

Paper number 7A0765

ISIS SATELLITE DATA

Analysis Procedure

In the first data set we determine the size of the auroral oval from 351 Isis 1 and 2 satellite electron spectrograms. Details of the Isis soft particle spectrometer can be found in works by *Heikkila et al.* [1970], *Heikkila and Winningham* [1971], and *Winningham et al.* [1973]. For details of the format of electron spectrograms, see the works by *Winningham et al.* [1975] and *Lui et al.* [1977]. We define the equatorward boundary of the auroral oval by the equatorward edge of >100-eV electron precipitation at low altitude (<3500 km). The accuracy of the boundary determination is approximately 0.1° in latitude. The equatorward boundary of the diffuse precipitation is a more convenient parameter with which to express the size of the auroral oval than the position of discrete auroras [*Lui et al.*, 1975; *Kamide and Winningham*, 1977]. It should be noted, however, that the auroral breakup, the first indication of the substorm onset, generally occurs along the equatorward boundary of the belt of discrete auroras or near the poleward edge of the diffuse aurora [*Akasofu*, 1974]; thus the onset of auroral substorms occurs systematically at higher latitudes than are indicated in this paper.

The 351 satellite passes had to meet the following criteria for the purpose of our study: passes occurred during dark hours, IMF data were available, and *Dst* was small (in order to eliminate the possible influence of large storms). The observations were grouped into only two periods, quiet and substorm, since it was not possible from available information to assign, without ambiguity, the phase and the magnitude of substorms for each satellite pass. This grouping was made primarily by examining the presence of a sharp increase of the *AE* index and of structured discrete auroral precipitation; the typical pattern of the spectrogram corresponding to quiet and substorm times was given by *Winningham et al.* [1975]. We also carefully checked individual magnetograms whenever it was necessary. For 46 cases, however, it was impossible to determine the character of the disturbances, i.e., they were either substorms or merely minor fluctuations. These cases are identified as 'uncertain' in Table 1.

TABLE 1. Summary of Conditions During the 351 Isis Passes Used in This Analysis

Condition	Percent of Passes
Magnetic local time	
<2100	9.3
2100-2300	31.1
2300-0100	32.2
0100-0300	25.1
>0300	2.3
Interplanetary magnetic field	
Northward ($Bz > 0$)	48.1
Southward ($Bz < 0$)	51.9
Toward sector ($By > 0$)	50.7
Away sector ($By < 0$)	49.3
Season	
Summer	63.5
Winter	36.5
Substorm activity	
Quiet time	38.5
Substorm in progress	48.4
Uncertain	13.1

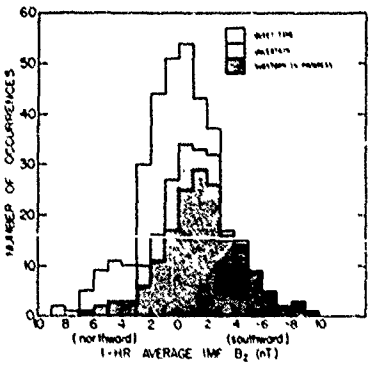

Fig. 1. Histogram showing the distribution of the north-south component (Bz) of the interplanetary magnetic field (IMF) in the data sample from 351 Isis satellite passes. Distributions for substorm and quiet times are distinguished by different symbols. Bz value represents the average value for a 1-hour period preceding the time of the satellite passage over the auroral region.

In order to express systematically IMF conditions we have used Bz values (data from Explorer 33, Explorer 35, Imp 5, and Imp 6) in solar magnetospheric coordinates averaged for 1 hour preceding the time of the Isis passage over the equatorward boundary of the auroral oval. We also have taken into account the transit time for the IMF signal to the magnetopause (at $\lambda = 10\ R_A$) by assuming the solar wind speed to be 400 km/s.

Uniformity of Data

The choice of the 351 passes was based solely on data availability. However, before we proceed with any analysis, it is important to examine factors which might influence the substorm probability owing to the nonuniformity of the data sampling. Factors which could seriously affect the results are uneven sampling in magnetic local time (MLT), IMF conditions, season, and substorm activity. Table 1 summarizes the conditions under which all 351 Isis traverses occurred. The observations appear to be distributed quite uniformly in local time in the dark sector; thus the present data set allows us to make a statistical study on the longitudinal extent and variability of substorms. The IMF conditions do not seem biased; the data are symmetrically distributed with respect to $Bz = 0$ as seen in Figure 1. It is also noted that the IMF data acquisition over heliographic latitude was carried out quite uniformly about the equator [cf. *Coleman and Rosenberg*, 1971]. A somewhat uneven distribution can be found in terms of season, but this would not pose a serious problem. Since the satellite orbital characteristics dictated that we take our data from two different seasons (summer and winter), the data set cannot be used to examine the dependence, if any, on a wide range of dipole tilt angles, from −35° to +35°. However, as was shown by *Kamide and Winningham* [1977], the uneven sampling over the tilt angle could bias the results only slightly.

There are some complications involved in determining substorm activity. In some cases, although substorm signatures were observed at a midnight magnetic observatory, the Isis spectrograms did not reflect a typical substorm pattern, a result indicating that the substorm-activated region did not reach the Isis local time. The category 'substorm in progress' in Table 1 includes such cases. This category also includes the opposite cases in which we found typical substorm precipitation patterns without any indication of geomagnetic activity.

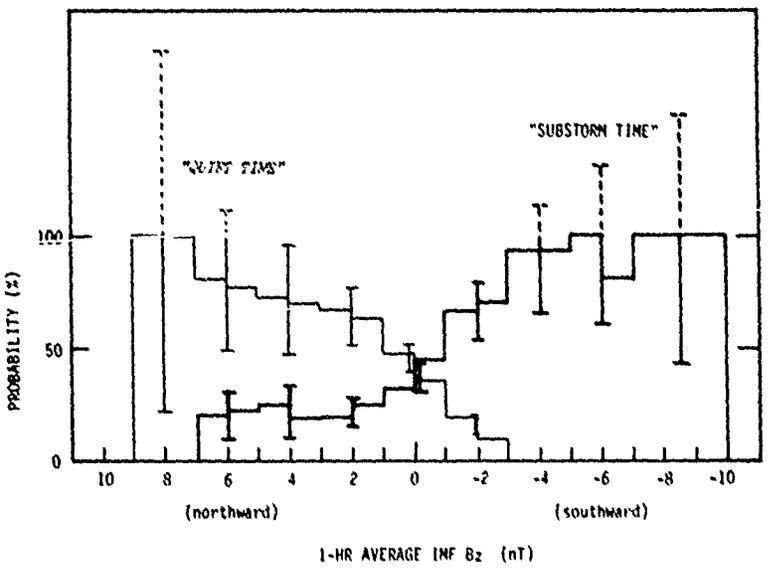

Fig. 2. Probability of substorm time (represented by the heavy line) and quiet time (represented by the light line) as a function of the Bz value of the IMF

In such cases we interpreted that contracted oval substorms were in progress, but we could not identify the corresponding signatures, owing to the poor coverage of ground observatories. In the category 'uncertain,' we have included the cases in which no discrete precipitation was found, but some minor magnetic fluctuations were found in high-latitude magnetograms. The category 'quiet time' was defined as cases in which no substorm signature was noticed in any available data set but may include some substorm cases which were beyond the 'field of view' of both the Isis latitudinal scan and the ground observatory network.

Results

Figure 1 presents a histogram of the distribution of all the samples in terms of the Bz component of the IMF with differentiation for different substorm categories. When all 351 cases are considered, it is striking that the resulting histogram is similar to a Gaussian distribution with the peak value being around $Bz = 0$. In contrast, the distribution of substorm samples alone is shifted toward the southward IMF by about 2 nT, and the peak for quiet cases is shifted toward the northward IMF.

In Figure 2 we show the frequency (probability of observing substorms and quiet times) as a function of the IMF Bz, together with the corresponding uncertainty as indicated. The probability P (in percent) was computed as

$$P = S/T \times 100$$

where S is the number of substorm events in every 1-nT interval of Bz and T is the total number of the samples in the same Bz interval. For every 2-nT interval of Bz the uncertainty ΔP was determined from

$$\Delta P\ (\%) = P \times [1/(S)^{1/2} + 1/(T)^{1/2}]\ (2)^{1/2}$$

and $\pm\Delta P$ is also given in Figure 2. Note that since the Isis data are available only at approximately 2-hour intervals, the 'substorm probability' presented here could more accurately be called the probability of substorm observation by a low-energy electron detector on a polar-orbiting satellite.

Two points are worth noting in Figures 1 and 2. First, the substorm probability defined above increases as Bz decreases; however, this increase does not occur in a simple way. In the range $Bz > 2$ nT the probability is almost constant at 20–30%. It then increases monotonically for greater southward IMF, and if the magnitude of the southward Bz is larger than 5 nT, the substorm probability becomes essentially 100%. Second, the probability of observing quiet times increases with an increase of Bz. However, it does not reach 100% until Bz becomes about 7 nT. In other words, substorms can often occur even during northward IMF periods, whereas quiet times are seldom observed during southward IMF periods. Some indications of substorm activity are almost always present during periods of the southward IMF. The increase of the uncertainty with the increase of the IMF magnitude is simply due to the insufficient number of cases in such ranges provided by the present data set. However, geomagnetic activity is very high when the magnitude of the southward IMF is very large, say, $Bz < -10$ nT [*Perreault*, 1974; *Russell et al.*, 1974], and it is extremely quiet when the northward Bz is very large. It should be noted that although our statistics could not extend the substorm probability curve beyond $Bz = 7$ nT simply because of an insufficient number of samples, it is most likely that the probability curve will decrease gradually with further increase of Bz. It should eventually reach zero near $Bz = 10$ nT.

Figure 3 shows histograms of the latitudinal distribution of the equatorward boundary of the >100-eV electron precipitation determined from the Isis spectrograms for different local times. The oval location tends to shift equatorward with advancing local time. This is in agreement with what the auroral oval of *Feldstein and Starkov* [1967] predicts. Note that the occurrence frequency of the auroral oval as a function of latitude agrees well with the results of *Liu et al.* [1975], who examined the occurrence of the optical auroral oval along the midnight meridian. Since different parameters were measured

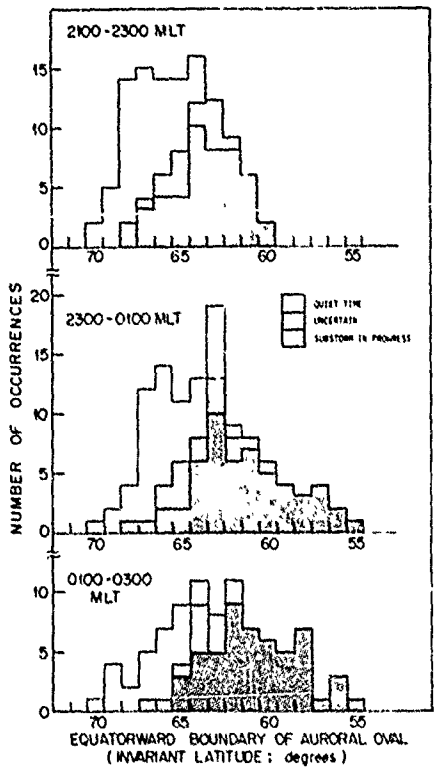

Fig. 3. Histogram showing the distribution of the invariant latitude of the equatorward boundary of the nightside auroral oval at three different local time sectors. Distributions for substorm and quiet times are distinguished by different symbols.

(see *Kamide and Winningham* [1977] for a detailed discussion), our data extend somewhat more toward lower latitudes than theirs.

Since the size of the auroral oval is closely related to the *Bz* component of the IMF [e.g., *Holzworth and Meng*, 1975; *Kamide and Winningham*, 1977], substorm probability as a function of oval location (in latitude) is expected to correlate well with substorm probability as a function of the IMF. The tendency of higher substorm frequency in lower latitudes can be seen in Figure 3 at all local time sectors. The probability of observing substorms along the expanded oval (e.g., <62° invariant latitude) is essentially 100%.

We must be careful in discussing the probability of substorm occurrence on the basis of the seeing probability obtained from the polar-orbiting satellite data with a 2-hour orbital period. Although our original data are not seriously biased by uneven sampling of the IMF conditions, it would not be correct to state unconditionally that there is a high probability of substorm occurrence when the IMF is directed southward, and vice versa. Along these lines, three factors need to be considered. None of these factors is necessarily conclusive per se, but when they are combined, we conclude with a high degree of confidence that an IMF and a latitudinal dependence of substorm occurrence probability does exist.

1. From an extensive examination of electron and proton auroras, *Montbriand* [1971] concluded that auroral substorms occurring during periods of low geomagnetic activity tend to recover faster than those during more active periods. *Kamide and Akasofu* [1974] have shown statistically that weak substorms, in terms of the total electrojet current (perhaps corresponding to Montbriand's low geomagnetic activity), occur along the contracted auroral oval during northward IMF periods. Thus it is likely that substorms occurring at higher latitudes recover faster than ones occurring in the normal auroral zone or along the expanded oval. Since substorms can take place anywhere between >70° and <60° in invariant latitude [*Kamide and Akasofu*, 1974], one may introduce a 'weight function' over latitude (or the IMF) in compensating the difference of lifetime of substorms. If this could be done properly, one might be able to convert the substorm seeing probability to the 'occurrence' probability. However, even if it is assumed that there is a difference in the weight function by a factor of 2 between the contracted oval substorms and expanded oval substorms, or equivalently between the northward and southward IMF [see *Montbriand*, 1971, Figure 1], the converted occurrence probability would not significantly change our results shown in Figures 2 and 3. That is, there is the minimum size of the auroral oval (and the corresponding large magnitude of the northward IMF) along which a substorm is never generated, and there is some size of the oval (and the corresponding southward IMF *Bz* value) along which substorm features are almost always present.

2. In terms of the longitudinal extent of the substorm-activated area seen in the auroral scanning photometer data, *Lui et al.* [1975] classified auroral substorms into two types: confined and widespread. Particle data taken from a narrow band along the trajectory of a polar-orbiting satellite might fail to detect some substorms which occur only within a limited longitudinal extent near midnight. That is to say, the satellite trajectory would sometimes fall outside the substorm region even if we have identified substorm activity by other means. If this effect were indeed serious, we would have a significantly different result in the substorm seeing probability between midnight and earlier (or later) local time hours. However, at least within the local time sectors we examined (2100–0300 MLT), there is no marked difference in terms of the percentage of substorm cases over latitude (see Figure 3).

3. It may well be that some of the cases which were identified as uncertain or quiet time in fact occurred during weak substorms. The latitudinal pattern of the auroral electrons could be different than that of the 'normal' substorms. However, the cases we determine as substorm in progress can never be quiet times. If there were no latitudinal dependence of the substorm occurrence probability, then the seeing probability would be 100% everywhere. This cannot be the case, since it is unlikely that there was always substorm activity or that all the 351 randomly selected satellite passes occurred during periods of substorm in progress.

On the basis of these considerations it may be concluded that there is indeed a latitudinal and IMF dependence of the substorm occurrence frequency.

AURORAL SUBSTORMS ALONG THE ALASKA MERIDIAN

In this section we provide further support for the conclusion concerning substorm probability, reached in the previous section, on the basis of a statistical examination of a different data set, viz., 63 substorms observed in auroral photographs from the Alaska meridian chain of all-sky cameras. *Akasofu et al.* [1973] claimed that most previous studies of substorm occurrence were based on an examination of geomagnetic records and thus suffered seriously from an inevitable inaccuracy in timing and substorm identification. By the use of the auroral breakup and the subsequent poleward motion of an auroral

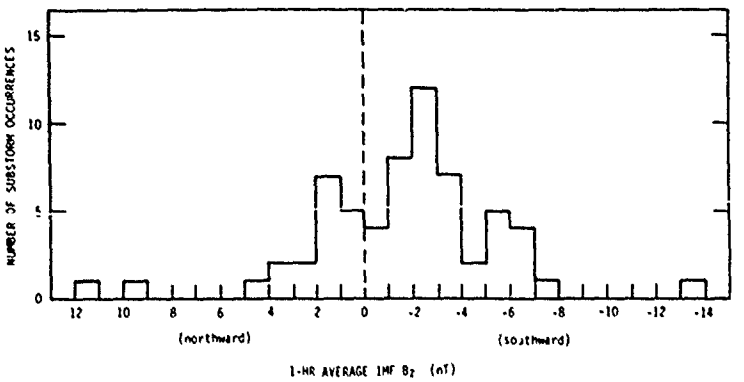

Fig. 4 Histogram showing the distribution of the north-south component of the IMF in the sample of 63 auroral substorms obtained from the all-sky camera data along the Alaska meridian.

arc in the midnight sector [*Akasofu*, 1964] we can determine the onset time $T = 0$ with an accuracy of ±2 min, as well as the latitude at which the first indication of the substorm onset occurs. Unlike the data from a polar-orbiting satellite, the all-sky camera records are available on a continuous basis, although they provide data only in a limited longitudinal span.

Akasofu et al [1973] have found that auroral substorms are quite common even when the *Bz* component of the IMF is positive, a finding implying that there is little or no dependence of substorm occurrence probability on the IMF orientation. However, two important questions remain unanswered. First, they examined the IMF data in solar ecliptic coordinates only at approximate onset time, whereas it may have been more appropriate to use an integrated IMF value in solar magnetospheric coordinates over a certain period, say, 1 hour, rather than an instantaneous value. Second, their 'quite common' is not quantitatively clear. Thus it is important to find the substorm occurrence frequency as functions of IMF values and latitude of the auroral breakup.

The basic data set we will use in this section is essentially the same as the 54 auroral substorms examined by *Akasofu et al.* [1973], in which 10 substorms were presented as examples. Here we increase the number of substorm samples to 63 which are distributed in late evening and midnight hours between 2140 and 0140 MLT. Those substorms were identified from all-sky camera data at College (invariant latitude, 64.9°), Fort Yukon (66.8°), Inuvik (71.0°), Bar I (70.8°), and Sachs Harbor (76.2°). The corresponding IMF data from Imp 3, Imp 5, Explorer 33, Explorer 35, and Heos 1 were also examined. To be consistent with the previous test, an average of the *Bz* component for 1 hour preceding each onset time was calculated in solar magnetospheric coordinates. We have identified substorms in the interval of 1966–1970, when all-sky camera records from at least two stations were available. The data availability at each station is limited by several factors such as mechanical problems, local weather, full moon, and data quality. Nevertheless, our data samples are not seriously biased in the sense that a single all-sky camera can identify accurately the location of a substorm onset which occurs within at least ±3° latitude. All 63 substorm events were taken from periods when the latitudinal range from 61° to 70° was completely monitored by the all-sky camera network.

Figure 4 shows the distribution of all the samples as a function of the IMF *Bz* component. It is noted that the peak of the occurrence in this particular data set is not located at $Bz = 0$ but is shifted a few nanoteslas toward the negative *Bz*, indicating, as expected, that more substorms tend to be found during southward IMF periods. This feature is in agreement with the distribution of the hatched area of Figure 1, although the dependence of the number of substorm cases on the IMF in Figure 4 is not very clear in comparison with Figure 1. We believe that the uneven slope is simply due to the insufficient data set used in constructing Figure 4. A somewhat peculiar feature in Figure 4 is that two substorms are identified in the high-*Bz* range, whereas no substorm was found in the *Bz* range to be greater than 7 nT in the set of the 351 Isis scans. However, these two events occurred under unusual states of the IMF; in both cases, $|B| \approx 14$ nT. In fact, these substorms were observed during the initial and recovery phases of magnetic storms, although the corresponding *Dst* magnitude was not very large (−7 and −35 nT, respectively).

In Figure 5 we show the distribution of the same data samples over invariant latitude, which indicates the location of the auroral arc that showed the first indication of the breakup. In most cases the breakup occurred along the southernmost arc of a preexisting group of discrete arcs. The latitudinal distribution of all auroral arcs during quiet and substorm

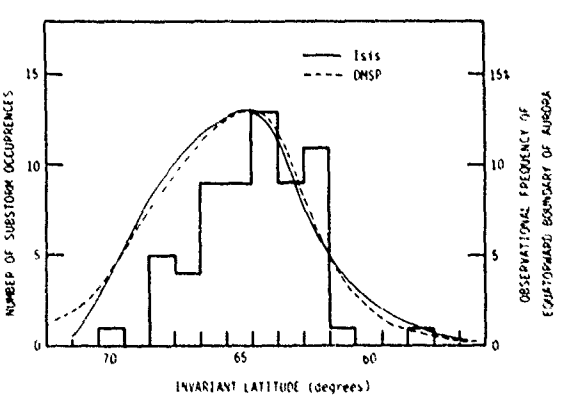

Fig. 5 Histogram showing the distribution of invariant latitude of 63 auroral breakups. The dashed curve represents the occurrence frequency of the southernmost discrete auroral arcs at midnight for all cases including substorm and quiet times obtained from DMSP satellite observations (B. S. Dandekar, personal communication, 1977). The distribution of the equatorward boundary of the auroral oval obtained from Isis satellite observations is also indicated by the solid curve (transferred from Figure 3 by shifting 1° poleward).

periods is shown by two curves in Figure 5. The dashed curve represents the observational frequencies of the southernmost auroral arc near midnight at the corresponding latitude, which were obtained from more than 7000 northern hemisphere arcs seen in the DMSP satellite imagery (B. S. Dandekar, personal communication, 1977). Note that since the location was determined from randomly selected satellite passes, some of them occurred during substorms and some occurred during quiet periods. The solid line was transferred from our Figure 3 (2300–0100 MLT) by smoothing the uneven distribution and by shifting it poleward by 1°. The shift was made on the basis of the fact that in the Isis data we identified the equatorward boundary of the diffuse auroral precipitation which can usually be found 0.5°–2° equatorward of the southernmost discrete arc [e.g., *Winningham et al.*, 1975]. These two curves agree surprisingly well with each other, the agreement substantiating our assumption that these curves represent reasonably well the occurrence frequency of all discrete auroral arcs over invariant latitude.

Comparing the distribution of 'all' arcs including quiet time arcs with those of arcs associated only with substorms, we find that there is a significant departure of the substorm time auroral distribution from the distribution of all arcs for latitudes greater than 65°. On the other hand, the substorm auroral distribution does not deviate systematically from the all arc distribution below 64° latitude. These features indicate that only a part of higher-latitude arcs indicates the initial sign of the breakup (about 50% at 67°), whereas there is a high probability of substorm features if the aurora moves equatorward below 64°. Note that there was no all-sky camera station south of College (64.9°), so that we missed some substorms occurring below 61°.

Discussion

In this paper the dependence of substorm occurrence probability on the direction of the IMF and on the size of the auroral oval was investigated. The occurrence probability was based on the substorm seeing probability, which was obtained statistically from the two independent data sets: the latitudinal electron precipitation pattern observed by the Isis satellites and the auroral breakup observed by all-sky cameras at the Alaska meridian. Since the real occurrence probability can only be determined from continuous monitoring of the entire polar region, any set of measurements made by a polar-orbiting satellite with a 2-hour orbital period and by a network of ground observatories only for limited periods must be carefully examined. The statistics of the measurements might be influenced by uneven sampling in the IMF and invariant latitude in conjunction with substorm activity. Further, it was not possible to deduce a smoothed probability over the IMF and latitude because of an insufficient volume of data. However, the conclusions derived from this study are still valid, since there are some consistent characteristics in the two separate sets. In addition, some features in our data are very similar to those in a fairly large volume of other data, such as the location of auroral arcs determined by B. S. Dandekar (personal communication, 1977) from over 7000 DMSP satellite passes. Thus we believe that an increase in the number of data samples would only decrease the magnitude of uncertainty and produce relatively minor quantitative changes in the substorm occurrence probability.

Subject to these provisions, we have reached the important conclusion that the substorm occurrence frequency has a strong dependence on the north-south component of the IMF and on the size of the auroral oval (i.e., the size of the polar cap). This dependence on the oval size is not unexpected, since the auroral oval size is a measure of magnetic flux in the magnetotail, and thus an increase in the amount of the magnetotail energy should result in an increase of substorm probability. Therefore on combining the results obtained in the present study with earlier results by *Kamide and Akasofu* [1974] it appears that both the intensity and the occurrence frequency increase with the expansion of the auroral oval.

During the last several years, one of the most important topics in magnetospheric physics has been the role of the north-south component of the IMF on substorm processes. *Dungey*'s [1961] suggestion that the southward directed IMF plays a crucial role in generating magnetospheric substorms has been claimed to have been confirmed by a number of studies [e.g., *Fairfield and Cahill*, 1966; *Rostoker et al.*, 1972; *Arnoldy*, 1971]. However, most of these studies were based solely on an examination of ground-based magnetic records from standard auroral zone observatories (or geomagnetic activity indices) and the north-south component of the IMF. *Akasofu et al.* [1971] showed that fairly intense substorms often occur beyond the field of view of standard observatories. From these two observations it was not difficult to infer that when the IMF is directed northward, substorms could take place along the contracted auroral oval during quiet (in terms of available magnetic activity indices) periods and thus out of the range of the normally used auroral zone observatories. In fact, this inference was shown to be correct by *Akasofu et al.* [1973], who indicated that there is no single IMF signature (such as the southward turning) that can be consistently related to the substorm onset. Then *Kamide* [1974] showed that substorms associated with the northward IMF are less intense in terms of the total electrojet current and the corresponding mid-latitude magnetic perturbations than substorms associated with the southward IMF.

McPherron et al. [1973*b*] have suggested that one should distinguish these weak substorms occurring during northward IMF periods by calling them 'localized' substorms. Thus the normal substorms along the standard auroral zone would have a strong association with the southward directed IMF. As was mentioned earlier, such localized substorms do not differ from the normal substorms in their characteristics. First, in the vicinity of the auroral breakup every substorm feature, such as the poleward expansion, the westward traveling surge, Pi 2 pulsations, and a sharp onset of negative H component excursion, is observed during both localized and normal substorms. Second, statistically, there is no distinct line to draw between the localized and normal substorms in terms of electrojet and mid-latitude magnetic response [*Kamide and Akasofu*, 1974]. The auroral breakup can occur anywhere between >60° and <70° geomagnetic latitude, depending chiefly upon the IMF condition prior to a particular substorm event. Third, the localized substorms can occur isolated from the normal subsequent substorm, although it has been argued that they are often found in the 'growth phase' prior to a normal substorm.

Akasofu [1975] has suggested that the quantity defined by

$$S = \int_0^t (\Phi_D - \Phi_N)\, dt$$

has a fundamental importance in substorm processes, where Φ_D and Φ_N denote the production rate of open field lines along the dayside neutral line and of closed field lines along the nightside neutral line, respectively. S is equal to the amount of

an excess magnetic flux at a time t reckoned from the time when the *Bz* component of the IMF begins to decrease after a prolonged period of a large positive IMF *Bz*. Indeed, *Akasofu and Kamide* [1976] have shown that the electrojet energy for each substorm has a close relation to the IMF state which controls the amount of S. *Akasofu* [1975] noted that substorms occur so long as $S > 0$ regardless of the sign of the *Bz* component of the IMF. This agrees well with our statistical results presented in this paper; the substorms can be observed at any value of the IMF and the size of the oval, except for the value corresponding to the state $S = 0$. Thus it may well be that the situation $S = 0$ corresponds to the 'ground' state [*Bratenahl et al.*, 1976] in which a substorm never occurs. The work of *Akasofu and Kamide* [1976] has implied that the minimum size of the auroral oval is located near 72° geomagnetic latitude at midnight.

Our statistical results somewhat restrict our options in seeking generation mechanisms for magnetospheric substorms. Our results indicate that substorms do not occur with an equal probability for different values of the IMF *Bz* component or for different sizes of the auroral oval. Since the magnetospheric substorm can be considered as a process by which the magnetosphere tends to remove sporadically the excess energy in the magnetotail, the results obtained in this paper indicate that the substorm occurrence probability is closely related to the amount of energy stored in the magnetotail. This conclusion implies that the triggering mechanism has something to do with an increase in the stored energy. It is interesting to note that once a substorm has begun, the process does not always continue until all the available free energy is depleted. Some mechanisms tend to suppress further development of the substorm [*Atkinson*, 1966]. In such a case the energy released during the substorm does not reach a maximum intensity commensurate with the size of the auroral oval. It is highly probable that a subsequent substorm could occur to release the remaining energy [*Kamide et al.*, 1977].

Finally, it may be noted that although the use of a different length of time (say, 30 min, 45 min, or 1.5 hours) to obtain the average of the IMF has not been found to alter the essentials of our results, time variations of the IMF in individual substorm occurrences could be more important than the average *Bz* values.

Acknowledgments The authors would like to thank B. S. Dandekar for providing his unpublished results concerning the auroral distribution. They are grateful to T. Lui and S. Matsushita for reviewing an earlier version of this manuscript. The University of Alaska portion of this work was supported in part by the National Science Foundation, Atmospheric Science Section, grant ATM74-23832, and in part by Air Force Geophysics Laboratory (AFGL) contract F19628-76-C-074. The University of Texas at Dallas portion was supported by AFGL contract F19628-76-C-005 and NASA grants NGL44-004-130 and NGR44-004-150. One of the authors (Y.K.) would like to thank the High Altitude Observatory of the National Center for Atmospheric Research, under whose aegis portions of this paper were completed.

The Editor thanks A. Nishida and G. Rostoker for their assistance in evaluating this paper.

REFERENCES

Akasofu, S.-I., The development of the auroral substorm, *Planet. Space Sci.*, *12*, 273, 1964.

Akasofu, S.-I., *Polar and Magnetospheric Substorms*, 222 pp., Springer, New York, 1968.

Akasofu, S.-I., A study of auroral displays photographed from the DMSP-2 satellite and the Alaska meridian chain of stations, *Space Sci. Rev.*, *16*, 617, 1974.

Akasofu, S.-I., The roles of the north-south component of the interplanetary magnetic field on large-scale auroral dynamics observed by the DMSP satellite, *Planet. Space Sci.*, *23*, 1349, 1975.

Akasofu, S.-I., and Y. Kamide, Substorm energy, *Planet. Space Sci.*, *24*, 223, 1976.

Akasofu, S.-I., and J. R. Kan, Some new thoughts on magnetospheric substorms, *Radio Sci.*, *8*, 1049, 1973.

Akasofu, S.-I., C. R. Wilson, L. Snyder, and P. D. Perreault, Results from a meridian chain of observatories in the Alaskan sector, *Planet. Space Sci.*, *19*, 477, 1971.

Akasofu, S.-I., P. D. Perreault, F. Yasuhara, and C.-I. Meng, Auroral substorms and the interplanetary magnetic field, *J. Geophys. Res.*, *78*, 7490, 1973.

Arnoldy, R. L., A signature for substorms in the interplanetary medium, *J. Geophys. Res.*, *76*, 5189, 1971.

Atkinson, G., A theory of polar substorms, *J. Geophys. Res.*, *71*, 5157, 1966.

Bratenahl, A., P. J. Baum, and T. Yeh, On the ground state of the magnetosphere (abstract), *Eos Trans. AGU*, *57*, 994.

Burch, J. L., Observations of interactions between interplanetary and geomagnetic fields, *Rev. Geophys. Space Phys.*, *12*, 363, 1974.

Burch, J. L., and R. A. Hoffman, AGU/NASA topical conference on electrodynamics of substorms and magnetic storms, *Eos Trans. AGU*, *55*, 971, 1974.

Coleman, P. J., Jr., and R. L. Rosenberg, North-south component of the interplanetary magnetic field, *J. Geophys. Res.*, *76*, 2917, 1971.

Dungey, J. W., Interplanetary magnetic field and the auroral zone, *Phys. Rev. Lett.*, *6*, 47, 1961.

Fairfield, D. H., and L. J. Cahill, Jr., Transition region magnetic field and polar magnetic disturbances, *J. Geophys. Res.*, *71*, 155, 1966.

Feldstein, Y. I., and G. V. Starkov, Dynamics of auroral belt and polar geomagnetic disturbances, *Planet. Space Sci.*, *15*, 209, 1967.

Foster, J. C., D. H. Fairfield, K. W. Ogilvie, and T. J. Rosenberg, Relationship of interplanetary parameters and occurrence of magnetospheric substorms, *J. Geophys. Res.*, *76*, 6971, 1971.

Gonzalez, W. D., and F. S. Mozer, A quantitative model for the potential resulting from reconnection with an arbitrary interplanetary magnetic field, *J. Geophys. Res.*, *79*, 4186, 1974.

Heikkila, W. J., and J. D. Winningham, Penetration of magnetosheath plasma to low altitudes through the dayside magnetospheric clefts, *J. Geophys. Res.*, *76*, 883, 1971.

Heikkila, W. J., J. B. Smith, J. Tarstrup, and J. D. Winningham, The soft particle spectrometer in the Isis-1 satellite, *Rev. Sci. Instrum.*, *41*, 1393, 1970.

Holzworth, R. H., and C.-I. Meng, Mathematical representation of the auroral oval, *Geophys. Res. Lett.*, *2*, 377, 1975.

Kamide, Y., Association of *DP* and *DR* fields with the interplanetary magnetic field variation, *J. Geophys. Res.*, *79*, 49, 1974.

Kamide, Y., and S.-I. Akasofu, Latitudinal cross section of the auroral electrojet and its relation to the interplanetary magnetic field polarity, *J. Geophys. Res.*, *79*, 3755, 1974.

Kamide, Y., and J. D. Winningham, A statistical study of the 'instantaneous' nightside auroral oval: The equatorward boundary of electron precipitation as observed by the Isis 1 and 2 satellites, *J. Geophys. Res.*, *82*, this issue, 1977.

Kamide, Y., S.-I. Akasofu, S. E. DeForest, and J. L. Kisabeth, Weak and intense substorms, *Planet. Space Sci.*, *23*, 579, 1975.

Kamide, Y., S.-I. Akasofu, and E. P. Rieger, Coexistence of two substorms in the midnight sector, *J. Geophys. Res.*, *82*, 1620, 1977.

Lui, A. T. Y., C. D. Anger, and S.-I. Akasofu, The equatorward boundary of the diffuse aurora and auroral substorms as seen by the Isis 2 auroral scanning photometer, *J. Geophys. Res.*, *80*, 3603, 1975.

Lui, A. T. Y., S.-I. Akasofu, E. W. Hones, Jr., S. J. Bame, and C. E. McIlwain, Observation of the plasma sheet during a contracted oval substorm in a prolonged quiet period, *J. Geophys. Res.*, *81*, 1415, 1976.

Lui, A. T. Y., D. Venkatesan, C. D. Anger, S.-I. Akasofu, W. J. Heikkila, J. D. Winningham, and J. R. Burrows, Simultaneous observations of particle precipitations and auroral emissions by the Isis 2 satellite in the 1900–2400 M.L.T. sector, *J. Geophys. Res.*, *82*, 2210, 1977.

McPherron, R. L., C. T. Russell, and M. P. Aubry, Satellite studies of magnetospheric substorms on August 15, 1968: A phenomenological model for substorms, *J. Geophys. Res.*, *78*, 3131, 1973*a*.

McPherron, R. L., C. T. Russell, M. G. Kivelson, and P. J. Coleman, Jr., Substorms in space: The correlation between ground and satellite observations of the magnetic field, *Radio Sci.*, *8*, 1059, 1973*b*.

Montbriand, L. E., The proton aurora and auroral substorms, in *The*

Radiating Atmosphere, edited by B. M. McCormac, p. 366, D. Reidel, Hingham, Mass., 1971.

Mozer, F. S., On the relationship between the growth and expansion phases of substorms and magnetospheric convection, *J. Geophys. Res.*, *78*, 1719, 1973.

Nishida, A., Interplanetary origin of electric fields in the magnetosphere, *Cosmic Electrodynamics*, *2*, 350, 1971.

Nishida, A., Interplanetary field effect on the magnetosphere, *Space Sci. Rev.*, *17*, 353, 1975.

Perreault, P. D., On the relationship between interplanetary magnetic fields and magnetospheric storms and substorms, Ph.D. thesis, Univ. of Alaska, Fairbanks, 1974.

Rostoker, G., and C.-G. Fälthammar, Relationship between changes in the interplanetary magnetic field and variations in the magnetic field at the earth's surface, *J. Geophys. Res.*, *72*, 5853, 1967.

Rostoker, G., H.-L. Lam, and W. D. Hume, Response time of the magnetosphere to the interplanetary electric field, *Can. J. Phys.*, *50*, 544, 1972.

Russell, C. T., R. L. McPherron, and R. K. Burton, On the cause of geomagnetic storms, *J. Geophys. Res.*, *79*, 1105, 1974.

Siscoe, G., and N. Crooker, A theoretical relation between *Dst* and the solar wind merging electric field, *Geophys. Res. Lett.*, *1*, 17, 1974.

Vasyliunas, V. M., An overview of magnetospheric dynamics, in *Magnetospheric Particles and Fields*, edited by B. M. McCormac, p. 99, D. Reidel, Hingham, Mass., 1976.

Vasyliunas, V. M., and R. A. Wolf, Magnetospheric substorms: Some problems and controversies, *Rev. Geophys. Space Phys.*, *11*, 181, 1973.

Winningham, J. D., S.-I. Akasofu, F. Yasuhara, and W. J. Heikkila, Simultaneous observations of auroras from the south pole station and of precipitating electrons by Isis 1, *J. Geophys. Res.*, *78*, 6579, 1973.

Winningham, J. D., F. Yasuhara, S.-I. Akasofu, and W. J. Heikkila, The latitudinal morphology of 10-eV to 10-keV electron fluxes during magnetically quiet and disturbed times in the 2100–0300 MLT sector, *J. Geophys. Res.*, *80*, 3148, 1975.

(Received June 20, 1977;
accepted August 11, 1977.)

VOL. 82, NO. 32 JOURNAL OF GEOPHYSICAL RESEARCH NOVEMBER 1, 1977

The Development of Auroral and Geomagnetic Substorm Activity After a Southward Turning of the Interplanetary Magnetic Field Following Several Hours of Magnetic Calm

KNUD LASSEN

Geophysics Section II, Danish Meteorological Institute, Copenhagen, Denmark 2100

J. R. SHARBER

Department of Physics and Space Sciences, Florida Institute of Technology Melbourne, Florida 32901

J. D. WINNINGHAM

Center for Space Sciences, University of Texas at Dallas, Richardson, Texas 75080

A comprehensive study of growth phase and substorm activity following a period of magnetic calm has been conducted through a network of all-sky camera stations, auroral zone magnetic observatories, and particle detectors aboard the Isis 1 satellite. We have carefully documented the observations with the following results. The preexpansive phase arc which extended at least from 17 to 05 MLT was responsible for an energy input rate of $\simeq 3 \times 10^{-}$ ergs/s before breakup An equatorward drift of this arc of 6 km/min, observed only in the evening sector, remained until after the expansive phase, when its motion stopped abruptly at the time of the maximum poleward displacement of the arcs. Electrons responsible for the prebreakup arc had energies of ≃1–5 keV. Protons of ≃4-keV energy were measured equatorward of the electron arc. During the expansive phase, symmetrically traveling disturbances were observed propagating eastward in the evening sector and westward in the morning sector. The propagation stopped for 1–2 min at the time of maximum expansion and then continued, thus suggesting a momentary variation in the rate of convection. Equivalent currents consistent with observed magnetic perturbations represented approximately the same *DPZ* (twin vortex) pattern before the expansive phase as during it, however, although the magnitude of the currents was greater during the expansive phase, the dominant feature during this phase was an intense westward auroral electrojet The camera observations of diffuse cloudlike aurora showed an injection of ≃40-keV electrons during the expansive phase along the auroral oval between midnight and 0400 corrected geomagnetic time Movement of the cloud indicated an eastward gradient drift of the electron population.

INTRODUCTION

On the basis of data from an extensive body of all-sky camera documentation and polar magnetograms, *Akasofu* [1964] outlined the substorm sequence Although his initial description has been modified slightly [*Akasofu*, 1968; *Montbriand*, 1971], it remains essentially correct in ordering the observed geophysical phenomena into a consistent picture. Since that time an enormous effort has gone into further documenting substorm-related phenomena and into establishing the cause of the onset of the substorm expansive phase (see review by *Rostoker* [1972]). Whereas in Akasofu's description the substorm sequence is initiated by the sudden breakup of an auroral arc accompanied by a steep decrease of the horizontal component of the magnetic field, it was claimed by *McPherron* [1970] that the complete substorm sequence includes a disturbance period which he denoted the substorm growth phase. According to his statement, intervals of magnetic calm may be followed by significant deviations of the horizontal component of the magnetic field prior to the start of the expansion phase of a magnetospheric substorm.

Since McPherron's suggestion that a growth phase exists, several authors [*Iijima and Nagata*, 1972, *McPherron et al.*, 1973, *Kokubun and Iijima*, 1975] (and others) have contributed to the study of the phenomenon by giving more detailed descriptions of the signatures which are observed to be characteristic of that situation. The authors appear to agree in the opinion that the onset of an isolated substorm is preceded by a growth phase, which is closely related to the north-to-south change of the interplanetary magnetic field (IMF), following it with a delay of 10–20 min. The signatures of this growth phase observed on the ground are the following: a gradual decrease in H, the horizontal magnetogram, at auroral zone stations before its sharp drop; a gradual decrease in H at low latitudes (especially in the evening-midnight sector); the growth of a polar equivalent current of the twin vortex mode (especially in the polar cap); and the equatorward motion of auroras [*Kokubun and Iijima*, 1975].

In opposition to the above mentioned view, *Akasofu et al.* [1973] have suggested that the changes in the magnetic field characteristic of the growth phase have limited significance, since these changes do not themselves result in the onset of the expansive phase They suggested instead that the mechanism which triggers the expansive phase is an internal one, largely independent of external factors related to convection such as the southward turning of the interplanetary magnetic field In continuation of this suggestion, *Akasofu* [1975] has demonstrated that the southward turning of the B_z component and the subsequent chain of processes, proposed by *McPherron et al.* [1973], do not have any significance in causing the expansive phase Substorms are frequently being triggered in direct relation to such a chain of processes, in which the 'growth phase' of the substorm may then appear as part of the

Paper number 7A0679

TABLE 1. Stations Used in This Study

Station	Symbol	Geographic Latitude, deg	Geographic Longitude, deg	Corrected Geomagnetic Latitude, °N	Observation
Alert	AT	82.5	295.5	86	M
Thule	TH	77.5	290.8	86	A, M
Resolute Bay	RB	74.7	265.2	84	M
Godhavn	GO	69.2	306.5	77.5	A, M
Ny Aalesund		78 9	11 9	75.5	A
Søndre Strømfjord	SS	67.0	309.2	75.5	A
Baker Lake	BL	64 3	264.0	75	M
Heiss Island	BT	80.6	58.5	74.5	M
Fort Churchill	FC	58.8	265 9	71	A
Narssarssuaq	NAR	61.2	314.6	68	A, M
Great Whale River	GW	55.3	282.2	68	A, M
Dixon Island	DI	73.5	80.4	67 5	M
Tromsø	TR	69.7	18 9	66.5	A, M
Reykjavik	RY	64.2	338.3	66	M
Tixi Bay	TI	71.6	129.0	65	M
Murmansk	MM	69.0	33.1	64.5	S, M
Kiruna	KI	67.8	20 4	64.5	M
College	CO	64.9	212.2	64 5	M
Meanook	ME	54.6	245 6	64	M
Wellen	WE	66.2	190.2	60	M
Lerwick	LE	60.1	358 8	59	M
Bangui	BA	4.4	18.6	5	M
M'Bour	MB	14.6	343 0	21	M
San Juan	SJ	18.1	293.8	30	M
Fredericksburg	FR	38 2	282.6	50	M
Tucson	TU	32.2	249 2	40	M
Honolulu	HO	21 3	202 0	21	M

complete substorm picture. However, they may as well be released at a later stage, after the end of the B_z negative interval, as long as the area of the polar cap is greater than a certain minimum value, namely, the area after a prolonged period of large positive B_z. Once the polar cap has achieved this minimum value, no substorm can be released until a new southward turning of the IMF has initiated erosion of field lines on the dayside of the magnetosphere with the accompanying features of increasing convection, observable from ground-based observatories.

No matter whether the growth phase is an integral part of the substorm phenomenon, as proposed by McPherron, or more likely an independent B_z negative, increased convection phenomenon in accordance with the statements of Akasofu, there is still a need for further detailed study of the development of the geomagnetic and auroral activity observed after the southward turning of the IMF.

On February 25, 1969, the Isis 1 satellite happened to pass over the premidnight sector of the auroral oval during a geophysical situation which appears to have been identical with the substorm growth phase defined by McPherron The event followed a period of low substorm activity, characterized by values of AE less than 200 γ during the 34 hours before the substorm and less than 60 γ during the last 6 hours By combining the satellite particle measurements with ground-based observations we have been able to report in the following a careful documentation of the development of the auroral and magnetic activity through the growth phase and the subsequent substorm onset and expansion phase as well as of the particle precipitation preceding the substorm onset Our observations give a detailed picture of the gradual development of auroral and geomagnetic activity which follows the southward turning of the interplanetary magnetic field and which, in this particular event, is completed by the onset of a substorm with remarkable poleward expansion.

DATA SOURCES

In our study we made use of ground-based observations made during the event at the stations listed in Table 1, together with particle measurements from the Isis 1 satellite and magnetic field measurements from the satellites Explorer 35 and Heos 1. The ground-based observations are auroral all-sky photographs (A in column 6 of Table 1), spectrograms (S in column 6), and geomagnetic records (M in column 6)

The interplanetary magnetic field was measured by the satellites Explorer 35 in the evening quadrant ($(X, Y, Z)_{SE}$ = (−8, +63, −61) R_E) and Heos 1 in the forenoon quadrant ($(X, Y, Z)_{GSM}$ = (11, −31, 14) R_E). Both satellites appear to have been outside the shock front. None of the records was complete, thus detailed results from Heos 1 are missing during 0000-0300 UT, but hourly averages do exist for this interval [*Kmg*, 1975] Similarities of gross features of the B_z variation at the two satellites indicate a time lag between them of about 30 min. From the position of the satellites it is estimated then that the B_z variations at the front of the magnetopause occur 15-17 min earlier than those at Heos 1. Hence the B_z variations observed at Heos 1 have been referenced to the front of the magnetosphere by a shift of 15 min toward earlier hours In Figure 1 they have been shown together with magnetic records from the stations Tromsø, Reykjavik, Narssarssuaq, Great Whale River, and Fort Churchill, which were all situated in the 18-04 magnetic time sector of the auroral zone In the figure the stations are ordered from east to west Each arrow represents 200 γ The magnetic H records from a number of mid- and low-latitude stations are shown in Figure 2 The stations are ordered from east to west, with the most easterly

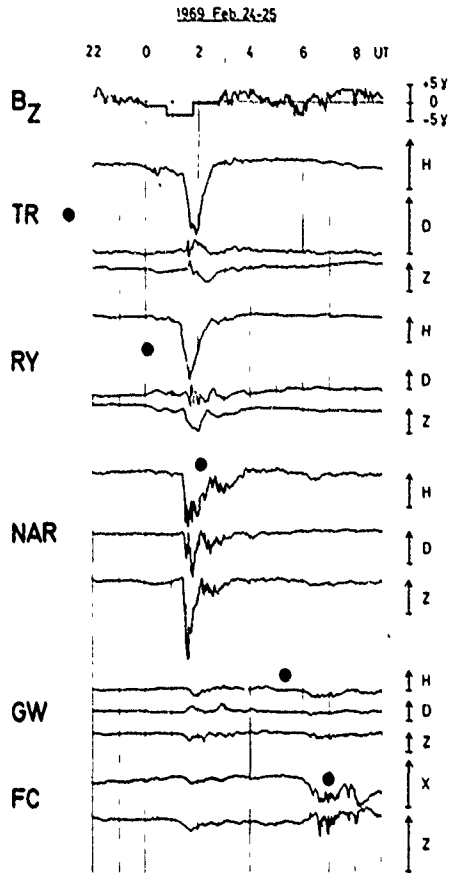

Fig. 1. Normal magnetograms from the auroral zone stations Tromsø, Reykjavik Narssarssuaq, Great Whale River, and Fort Churchill, February 24-25, 1969. Each arrow represents a variation of 200 γ. The dots indicate station geomagnetic midnight. Top curve: B_z (vertical GSM coordinate) as measured at Heos 1, referenced to the front of the magnetosphere by a shift of 15 min toward earlier hours.

one (Bangui) at the top of the figure. Each arrow in the figure represents 20 γ.

At the time of the substorm the nightside of the auroral zone was situated between western Siberia in the east and Northwest Territories in the west, with the magnetic midnight meridian crossing the Iceland-Greenland area. Conditions were not ideal for auroral observations. The moon was in its third quarter; the Soviet cameras, Reykjavik, Kiruna, and several stations in Greenland were not in operation because of bad weather, and most of the remaining stations had some cloud cover early in the evening. Nevertheless, eight well-distributed cameras were available for a study of the development of the auroral display in the course of the night (Table 1 and Figure 3). At each of the stations the sky was photographed with one exposure per minute except at Tromsø, where three exposures per minute were taken. The photographs have been used as a basis for the description of the distribution of the aurora; a selected series has been transformed to synoptic maps in geographical coordinates, shown here as Figures 4*a* and 4*b*. In projecting the auroral forms on the maps a mean height of 110–120 km has been assumed for the lower border of the arcs and bands.

MAGNETIC OBSERVATIONS

The IMF had been directed northward for several hours when the decrease of B_z began between 2200 and 2300 UT. Because of the oscillatory character of the change it is difficult to determine the exact hour when B_z went negative; after 2345–2350, B_z was definitely negative. The first departure from several hours of magnetic quiet was observed at approximately the same time, i.e., at 2345–0015 at the auroral zone stations situated near and shortly after magnetic midnight (Figures 1 and 5). The departure is seen as a gradual decrease of H, but D and Z are also affected. In the evening sector, Great Whale and Fort Churchill were little influenced by the disturbance before 0100 UT (Figures 1 and 6). At the low-latitude stations situated in the evening sector a gradual decrease of H set in between 0000 and 0030 UT and continued until the expansive phase onset at 0130. The onset is recognized as a sudden decrease of H in Figure 1. In Figure 2 it appears as the onset of a positive bay in the midnight sector and of a negative bay of comparable magnitude in the evening-afternoon sector. The transition takes place near the longitude of San Juan. At San Juan a flat depression is observed from shortly after midnight to 0300 UT, with only a small negative perturbation to be seen in connection with the expansion phase of the substorm. The gradual decrease of H at mid- and low-latitude stations as well as the flat depression observed at San Juan may be caused by an increase of a cross-tail or ring current system, which becomes detectable in the records about ½ hour after the change of sign of B_z.

The magnetic signatures of this event are in agreement with the description given by *McPherron* [1970]. Following a decrease of B_z to negative values a growth phase of about 1½-hour duration is observed, characterized by a gradual decrease of H at low latitudes and by a contemporary change of the magnetic elements at auroral latitudes in the direction in which they are subsequently changed by the substorm. The growth phase is superseded by the expansion phase initiated by the sharp onset at about 0130.

Before the end of the recovery phase of this substorm a new onset is noticed at 0210–0215 at the low-latitude stations, especially at Bangui and M'Bour. In the auroral zone the magnetic bay is most clearly recorded at Narssarssuaq; at Tromsø the onset is recognized as an abrupt change of the slope in H. The magnetic activity from this double substorm dies away by about 0400 UT. After 2 hours calm a new moderate substorm is observed in the midnight sector (Fort

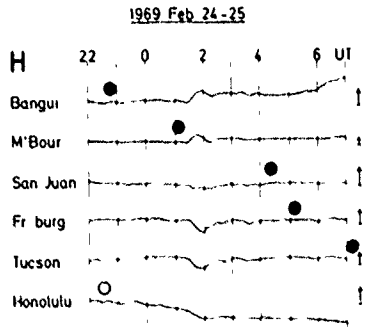

Fig. 2. Horizontal variation at low- and mid-latitude stations, February 24-25, 1969. Length of arrows is 20 γ. The dots indicate station midnight, the open circle at Honolulu indicates noon.

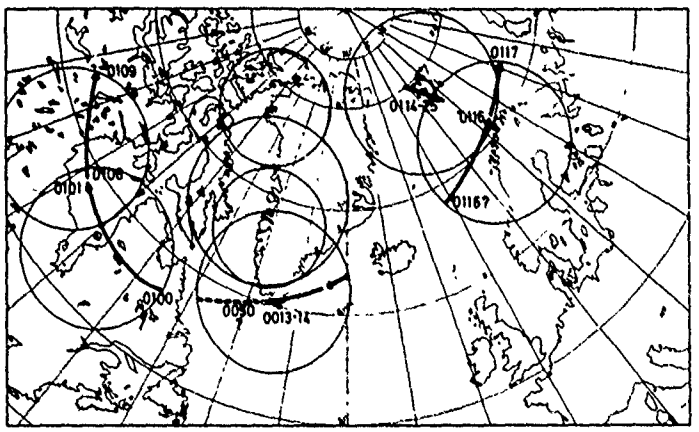

Fig. 3. Development of presubstorm arc, February 25, 1969. The times indicated are UT Circles represent the fields of view of camera stations (A) of Table 1.

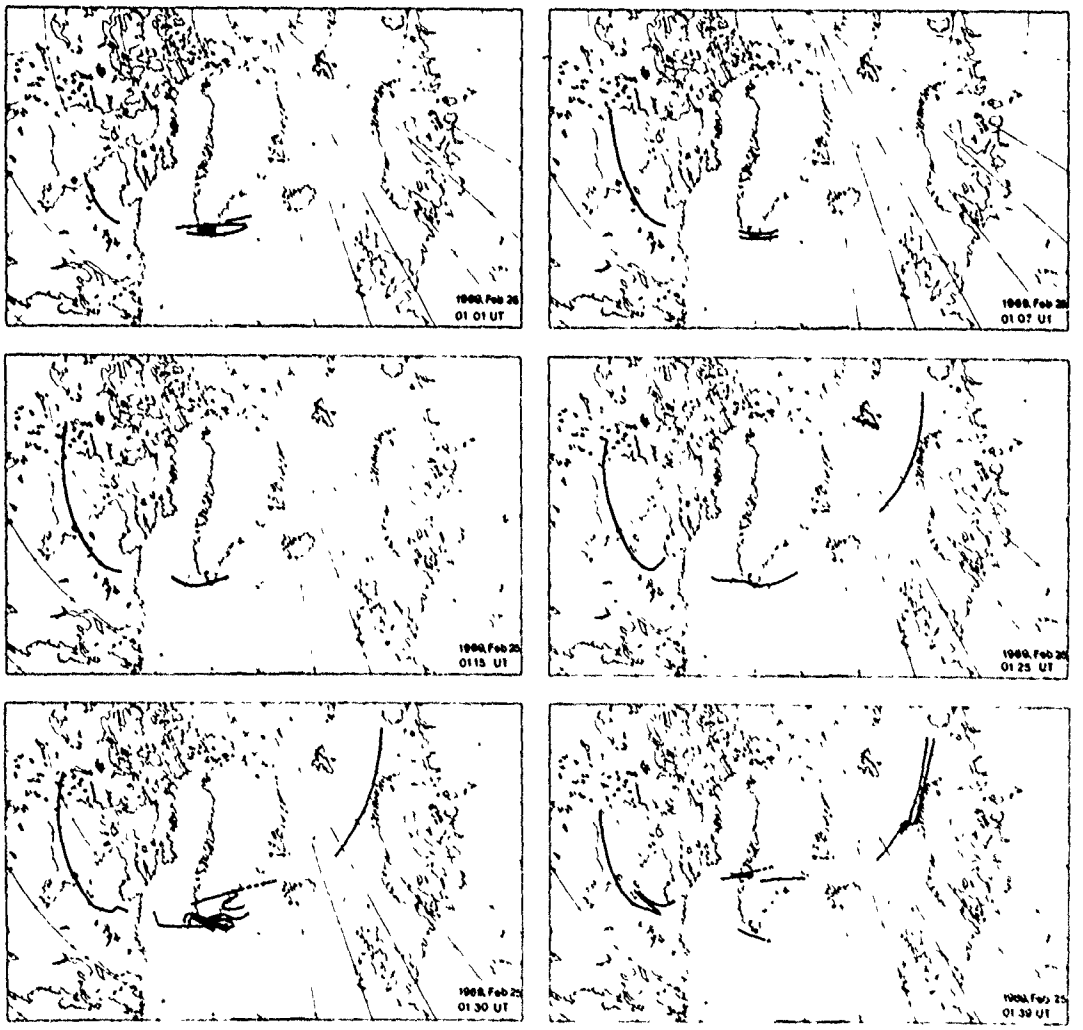

Fig. 4a Development of auroral display, February 25, 1969 Growth phase and poleward expansion

Churchill, Figure 1). We shall comment further on the onset of this substorm in a later section.

We have used the ground magnetometer data in the construction of equivalent current vectors to represent the current distribution before and after breakup at 0130 UT. This enables a comparison of the current system during the growth phase with that during the time of maximum expansion. We have taken the time of the satellite crossing of the arc (0115 UT) as a time during which we would consider the growth phase to be well in progress. The equivalent current vectors which could produce the magnetic perturbations at a number of polar cap and auroral zone stations at the time of the crossing have been drawn in a corrected geomagnetic latitude/time diagram in Figure 7. Also shown are the equivalent current vectors derived from the same stations during the time of maximum disturbance of the event. The maximum magnetic disturbance was measured during the 20 min immediately following the poleward expansion; the situation at 0150 UT has been chosen for construction of the current vectors. The quiet level for both graphs has been defined as the level which immediately preceded the onset of the event, i.e., during 2200–2400 UT. The equivalent current system during the growth phase is similar to the system corresponding to $B_z < -1\ \gamma$ in the winter months (*DPZ* system) as constructed by *Friis-Christensen and Wilhjelm* [1975]. In this system, which is believed to depict the magnetic field produced by field-aligned current sheets in the auroral oval and by a Hall current maintained by the electric field between the sheets, the disturbance vectors over the polar cap are of the same order of magnitude as those in the postmidnight auroral oval. In Friis-Christensen and Wilhjelm's paper (their Figure 5) the equivalent vectors are approximately 2 times the magnitude of those found here, in accordance with the fact that their parameter $\bar{B}_z$ (the 2-hour average of the actual and preceding hour) is numerically greater in their data than in ours.

Following a further decrease of B_z the equivalent currents during the maximum disturbance at 0150 UT are more intense than those at 0115 by a factor of 2, thus being comparable to the average currents of Figure 5 of *Friis-Christensen and Wilhjelm* [1975]. Superimposed on the *DPZ* system we find at

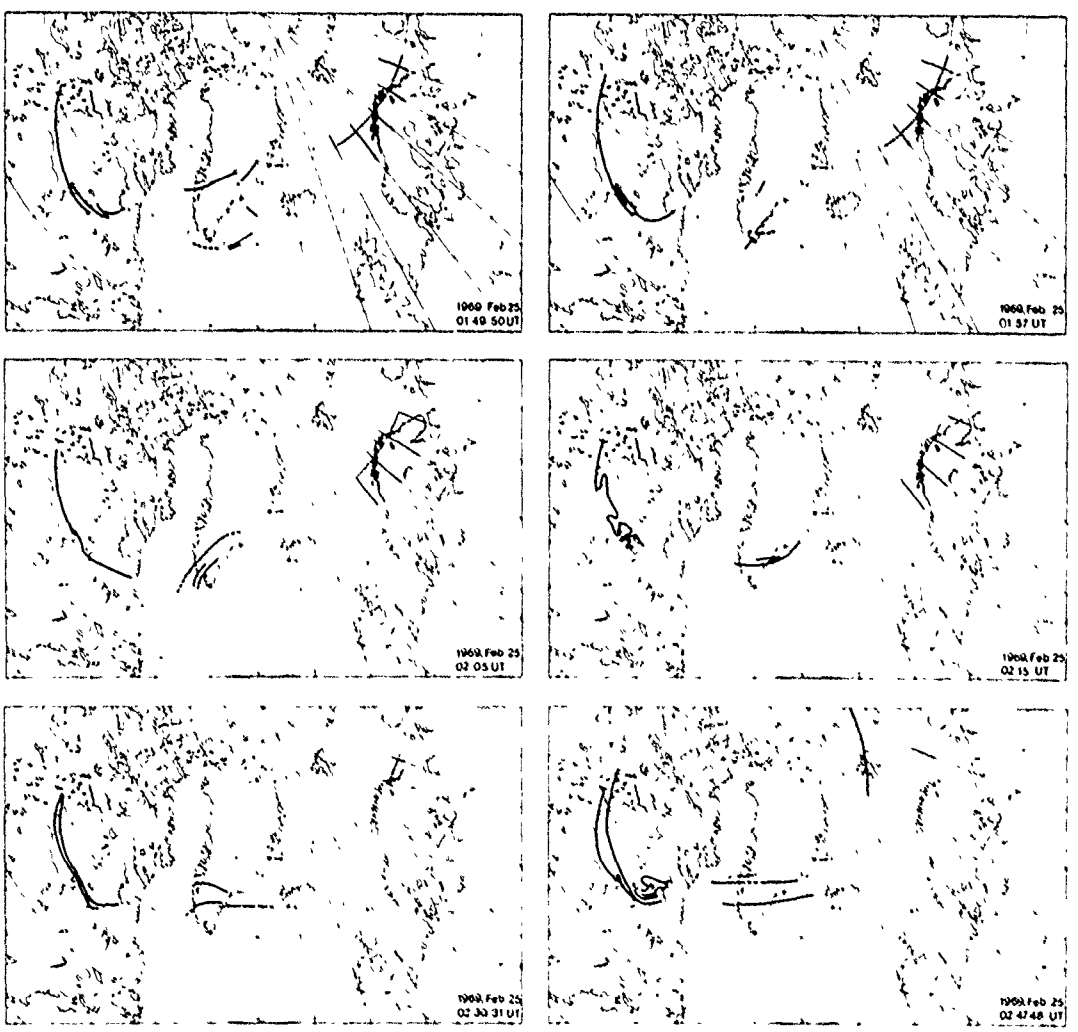

Fig. 4b. Development of auroral display, February 25, 1969. Recovery and second (minor) substorm.

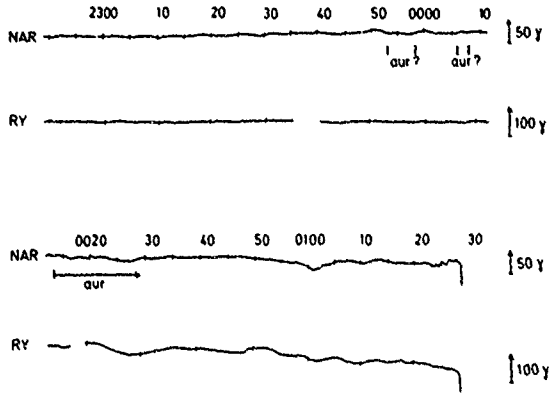

Fig. 5. Rapid run magnetograms showing the horizontal component at Narssarssuaq and Reykjavik, February 24-25, 1969 The gradual depression prior to abrupt onset of the magnetic substorm is clearly displayed.

0150 UT an intense westward auroral electrojet. Thus although the current systems during growth (B_s negative) and expansive phase are identical in most respects, they differ by the presence during the expansive phase of the intense westward auroral electrojet. A similar statement has been given earlier by *Iijima and Nagata* [1968]. The dominant role of the westward electrojet after breakup is in agreement with the substorm model of *McPherron et al.* [1973], according to which the breakup is associated with the sudden increase of the westward electrojet.

AURORAL OBSERVATIONS

The course of the auroral substorm near magnetic midnight can be summarized by reference to Figure 8. The figure presents, in negative, a sequence of all-sky photographs from Narssarssuaq. The breakup occurred at 0128 UT, corrected geomagnetic midnight at the station. The poleward expansion ended at about 0137; after this time the oval part of the bulge was gradually replaced by a diffuse veil, leaving the discrete forms in the polar front of the bulge only. The auroras returned from the north, and by 0213 a new expansion was in progress to the west of the station, giving rise to increased intensity in the withdrawing bands. After the second expansion, auroral arcs remained at about 71° corrected geomagnetic latitude until a new substorm onset occurred near 0600 UT. It follows from the magnetic and auroral observations presented above that the period studied may be divided into two time intervals with rather different types of activity, the prebreakup interval following the calm period at about 0045 and the postbreakup (expansion and early recovery) interval which started at about 0130 UT. In the following sections we present and discuss in more detail ground-based observations made during the event at the stations listed in Table 1, for the two intervals separately. Observations of drift of auroral arcs and surges which were made within both intervals, spanning the time of breakup, are presented in a special section, as are also the particle measurements from the Isis 1 satellite

PREBREAKUP INTERVAL

Buildup of Activity

The first observation of auroral light before the breakup was made near the midnight meridian at Narssarssuaq station Although it is difficult to be certain because of the presence of moonlight and a few clouds, a faint arc stretching from the northeastern horizon up to about 10° elevation is possibly seen in the frames taken at 2353, 2358, and later at 0006-0008 UT. From the time of 0013-0014 an auroral band was definitely present and extended from the northeast horizon to the zenith. The band persisted as a single homogeneous arc until at 0050 the intensity increased gradually, beginning at the eastern horizon. Folds shaped like a narrow westward traveling surge moved from the horizon toward the zenith and combined with the original arc at 0100 to form a row of multiple arcs of moderate intensity. A few minutes later a new 'surge' was seen low in the northeast for about 5 min. The intensity increases and the westward movement of folds were accompanied by a negative bay in H with an amplitude of 20 γ in Narssarssuaq and Reykjavik (Figure 5).

Apparently as a continuation of the formation of parallel arcs over Narssarssuaq, the arc developed to the west, becoming first detectable within the Great Whale field of view at 0100 UT, at the eastern horizon of Fort Churchill at 0106, and crossing the sky to the northwestern horizon at 0109 (Figure 3). At Narssarssuaq, after a few minutes of intensity decrease, a sharp arc developed from the horizon in the southwest and extended to the eastern horizon. During the same time the display was developing toward the east. It was observed from Tromsø through a light cloud cover at 0116 UT as a homogeneous arc reaching from the western horizon toward the northeastern horizon; at 0117 it stretched from horizon to horizon. The arc could have been present in lower intensity before 0116, so that the observation might indicate an increase in intensity in an already existing aurora. Certainly, by 0125 UT the arc system extended at least from a geographic longitude of 100°W to 45°E (17.5-05.5 MLT) with sufficient intensity for easy camera observation of the luminosity.

At about 0115 UT a poleward turning of the arc was observed in low elevation at the eastern horizon of Great Whale (Figure 18). The arc was first observed at Great Whale at 0100. Between this time and 0115 the arc resembled that of Figure 18 without the poleward turning at the extreme east. The exact minute at which the distortion sets in is difficult to determine, because the region is insufficiently covered by the cameras. For the same reason it is impossible to judge whether the arc is continuous, thus forming either a poleward bulge or a spiral in this area, or discontinuous, forming a sun-aligned arc as a signature of increased convection (a short polar cap band becomes visible at approximately the same time over Spitsbergen (Figure 3)). In the following we refer to this part of the display as 'the poleward extension.' Further signatures of the formation of the poleward extension may also have been the temporary increase in the intensity of the western part of the arc as observed from Narssarssuaq during the interval 0113-0116 as well as the onset of small irregular pulsations with periods of several minutes in the Great Whale magnetogram (Figure 6). The disturbance set in between 0110 and 0115, probably about 0112, and continued as a gradual de-

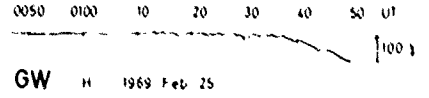

Fig. 6. Rapid run magnetogram of the horizontal component at Great Whale River, February 25, 1969. Note the small-scale perturbations during formation and approach of westward traveling surge

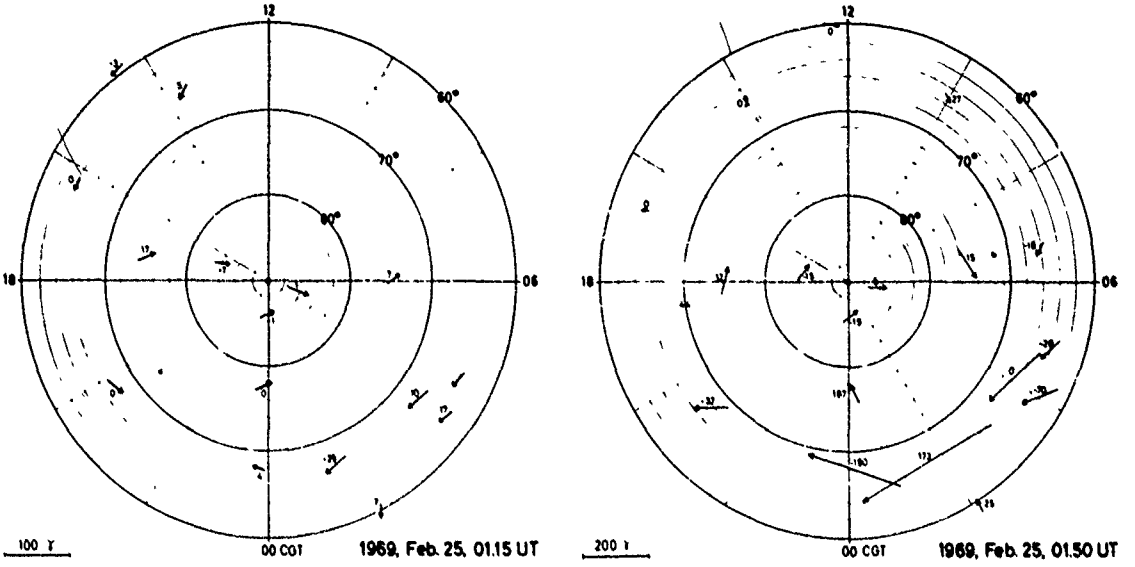

Fig. 7. Equivalent current vectors during prebreakup (growth) phase (0115 UT, left) and maximum of expansive phase (0150, right) of substorm on February 25, 1969. Numbers beside arrows indicate vertical magnetic perturbation in gammas. Note the different scale in the two diagrams.

crease of 100 γ as the westward traveling surge reached the station at about 0139.

Following the formation of the poleward extension the intensity again increased from the east in the southern arc (which at this time was the only one visible) over Narssarssuaq, the lower border became irregular, and the intensity increased from the west along the arc to meet the easterly increase near the meridian. Here the arc formed a sharp kink at 0125, and lateral movements were observed between 0125 and 0127. The intensity increase from the region of the poleward extension to the west of the station was accompanied by an obvious though small decrease in H (Figure 5). The actual breakup began at 0128–0129 very near Narssarssuaq as parallel arcs were formed along the northern border of the original arc. The abrupt onset of the magnetic perturbation in H occurred at 0128 in the Reykjavik magnetograms and less than ½ min later at Narssarssuaq (Figure 5).

Interpretation of Observations

The magnetic and auroral observations may be summarized as follows. Within minutes to tens of minutes after the shift of sign in B_z, precipitation of auroral particles is observed in the auroral oval close to magnetic midnight. The latitude of the oval is 68°. A gradual deviation of the magnetic elements at auroral zone stations is initiated at the same time, indicating the presence of a *DPZ* (convection) current system, and signatures of increased cross-tail or ring currents are seen in the records of H at low-latitude stations. The observations indicate an increasing convection set up by the negative value of B_z. A minor disturbance (double bay) at about 0020 is visible in stations from the polar cap to low latitude. This is probably a *DP*2 disturbance [*Nishida*, 1968], which may indicate irregularities in the convection rate. The increase in auroral intensity at 0050 followed by a narrow westward traveling surge and a development toward morning and evening of the quiet arc is consistent with the description of a confined substorm given by *Lui et al.* [1975]. In their example the magnetic effect of the substorm was about 20 γ. The decrease of H in our 0050–0110 event is approximately 20 γ and shows the signatures of a confined substorm. This disturbance is immediately followed by changes in the auroral pattern which could be associated with the convection pattern, i.e., a poleward turn of the arc before midnight and a polar cap aurora in the morning. The observations from the last 10 min before breakup give the impression of increasing convection and precipitation accompanied by increasing instability of the arcs, which finally result in the breakup and expansion.

EXPANSION AND EARLY RECOVERY

The rapid poleward expansion, initiated by the breakup, was completed by 0137 as the breakup arcs covered the entire area from a few degrees south of Narssarssuaq to Søndre Strømfjord (Figures 8 and 9). Simultaneously with this expansion the southernmost arcs moved equatorward with decreasing intensity; at the end of the poleward expansion, all discrete forms except those at the highest latitudes dissolved, and an equatorward broadening of a diffuse veil took place, which soon covered most of the sky. At the same time the discrete forms at the poleward edge of the display began a slow equatorward retreat.

The westward border of the region of poleward extension between Canada and Greenland appears to have remained relatively stationary during the expansive phase. However, as the expansion proceeded, a narrow zonal 'fiord' did develop in the low-latitude part of this westward extension. The formation of this fiord is evident in Figure 4*a* in the 0130 UT frame between 60° and 70° west longitude. The Great Whale photographs show that it developed into a small loop which became more and more elongated toward the west, eventually opening, thus forming two bands a few degrees north of the original band. These bands, shown in the 0139–0157 UT frames of Figures 4*a* and 4*b*, reached the Great Whale meridian at about 0141 but did not continue into the Fort Churchill field of view. The development of the western loop was accompanied by a

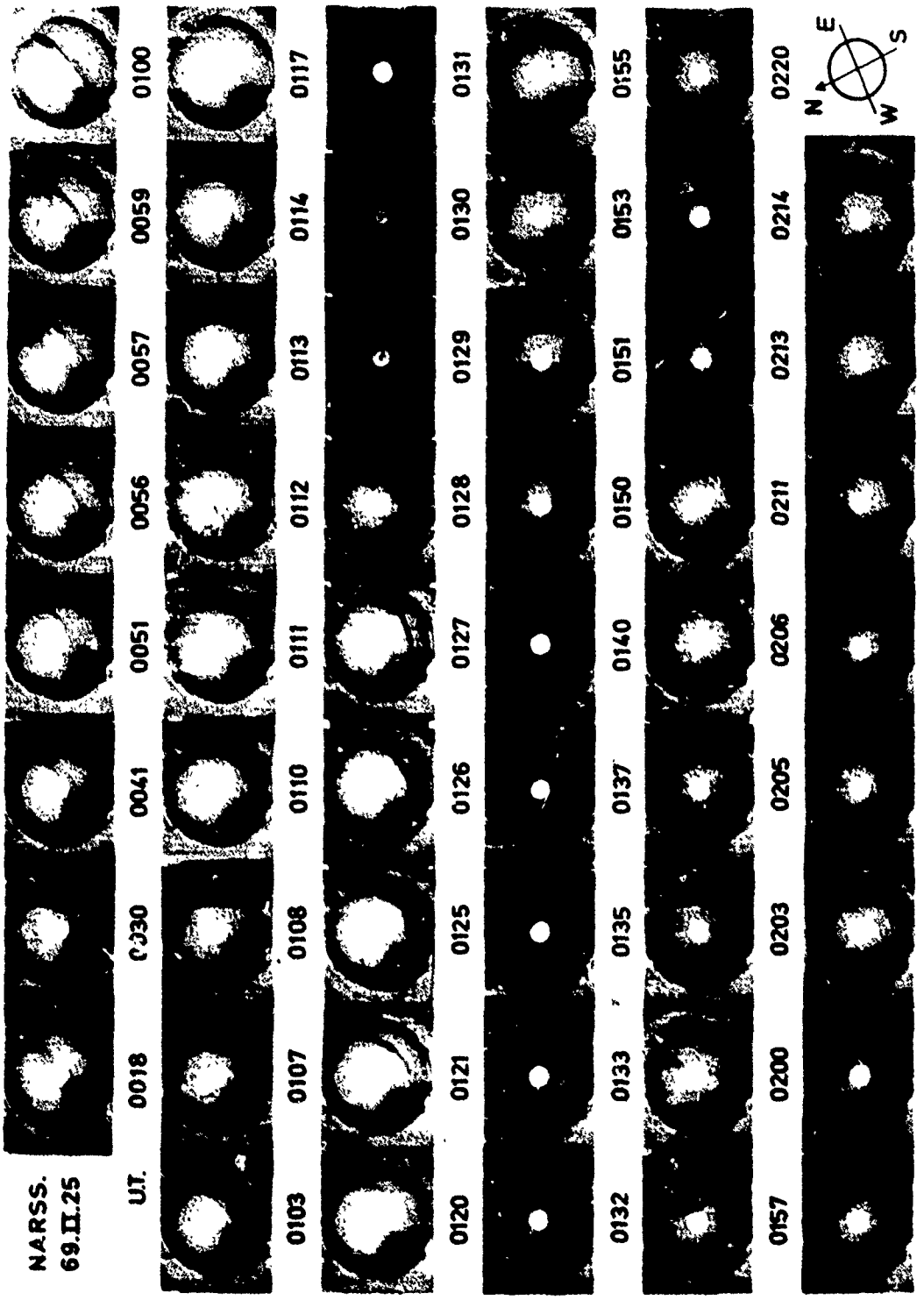

Fig. 8. All-sky camera photographs from Narssarssuaq, February 25, 1969

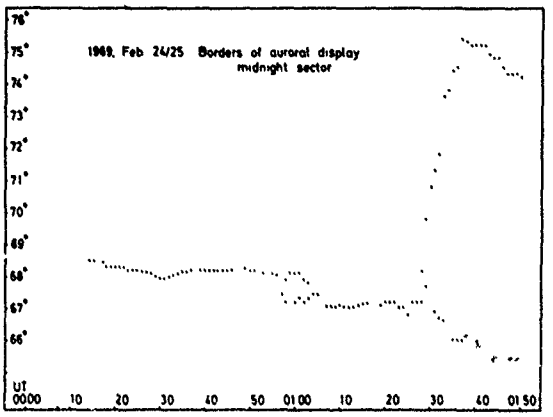

Fig. 9. Position in corrected geomagnetic latitude of the auroral arcs at Narssarssuaq. During the growth phase the position is indicated by the open dots. The positions of the northernmost and southernmost arcs during expansion are shown by the solid dots. The hatched area is more or less filled by discrete and diffuse auroras. The dense hatching indicates the equatorward border of the diffuse veil.

gradual decrease in H at Great Whale (Figure 6). Thus the loop behaved like the westward traveling surge as described by *Akasofu* [1968] with the exception that the westward border of the poleward expanding bulge did not move toward the west together with the surge but remained stationary on the evening side of the poleward extension of the arcs. In a single snapshot of the auroral display taken in the interval 0139–0157 UT the loop would have been interpreted as multiple discrete auroral arcs linked with the western limit of the poleward expanding bulge. A DMSP satellite photograph showing just this situation on November 24, 1971, has been published by *Pike and Whalen* [1974]. Our study, based on all-sky camera data, demonstrates how such multiple arcs may develop from a loop on the western border of the poleward expanding bulge.

The propagation toward the morning sector of the disturbance associated with the breakup and expansion phase may be observed from Tromsø, which was situated 4 hours after geomagnetic midnight. A sequence of all-sky photographs illustrating the development of the display at this station is presented in Figure 10. The intensity of the arc immediately to the north of Tromsø began to increase at 0130. Two minutes later a parallel arc of lower intensity became visible on the equatorward edge of the original one and slowly increased in intensity. At about 0137 the two arcs were dislocated equatorward, and after 0139, diffuse auroras with bandlike structure appeared on the equatorward side of the arcs. The movement of the original arc, which seemed to constitute the poleward edge of the display, as well as the movement of the boundaries of the diffuse aurora, has been plotted in Figure 11. This figure also shows the distribution of auroral light along the meridian as recorded by the spectral camera C-180-S at Loparskaya in the Murmansk area. Auroral data are not available before 0130 because of snow, but after this hour, spectrograms of 10-min exposure time were recorded. A comparison of the two plots in Figure 11 shows good agreement between the stations with regard to the latitudinal shift, but a time lag of 10 ± 5 min is observed between the equatorward shifts. Apparently, the low-latitude diffuse area propagated eastward with an approximate velocity of 1° min (or 50 km/min). On the assumption that the diffuse cloudlike aurora was produced by electrons which had become trapped on near-earth field lines during the breakup and expansion process in the magnetosphere, their energy may be estimated by using a formula deduced by *Sletten et al.* [1971] from a paper by *Hamlin et al.* [1961]. The formula, which gives an expression for the drift period of nonrelativistic electrons mirroring close to the atmosphere, may be written $T(s) = 4 \times 10^4 (LE)^{-1}$, where T is the azimuthal drift period in seconds, E is the energy in keV of the trapped electrons, and L is the McIlwain shell parameter. L is approximately 6, and the stations are separated by 12°. The observed time lag of 10 ± 5 min gives an estimated particle energy of $E = 37 \pm 10$ keV ($\simeq$40 keV). If we assume that the electrons became trapped on near-earth field lines ($L \simeq 6$) no earlier than at the breakup, then they would have drifted along this shell for no more than 10 min before arriving at Tromsø. This places the eastern limit of the trapping region only about 10° to the west of Tromsø, i.e., between Iceland and Scandinavia.

The observations from Narssarssuaq (Figure 9) indicate that the first possible incidence of auroral particles at $L = 6$ takes place at 0133–0134, about 4 min before the effect at Tromsø. Thus it seems probable that the diffuse low-latitude aurora is formed practically without time delay all along the auroral oval from midnight to shortly before 0400 geomagnetic time, with a delay at later local times which may be explained by the assumption of energetic electrons drifting in the geomagnetic field.

The diffuse cloudy auroras over northern Scandinavia began to withdraw gradually toward the auroral zone at about 0200 UT. During the withdrawal the luminosity concentrated into a few diffuse bands. At 0215–0220 the southern border was near Tromsø, and at 0230 the display was no longer detectable in the all-sky photographs. Thus the poleward retreat of the equatorward boundary matches well the recovery of the horizontal field at Tromsø (Figure 1).

OBSERVATION OF AURORAL DRIFT

Equatorward Shift of the Oval in the Evening Sector

From the first occurrence of auroral light a gradual equatorward drift of the arc was observed in the evening sector. The position of the arc observed in the early evening at Fort Churchill (19 geomagnetic time) and at Great Whale (21 geomagnetic time) is shown in Figure 12. The figure shows the drifts to be similar at the two stations with a steadier drift occurring at Fort Churchill. The irregularities at Great Whale centered at 0122 and 0130 depict the passage of two large wavelike structures, the first of which was a forerunner to the small surge that is easily detectable in the photographs of 0121–0123 (Figure 13).

The equatorward shift of the arc was measured to be 3°/hour and therefore cannot be attributed solely to the natural shift of the position of the auroral oval in the course of the evening. The change in the latitude of the Feldstein oval (Q = 3) at 20 MLT is approximately 1°/hour equatorward, from which we can infer an equatorward drift in the position of the arc relative to the oval of 2°/hour or about 4 km/min. This observation agrees with results reported by *Starkov and Feldstein* [1971] that auroral forms generally drift equatorward during an hour or so prior to the expansive phase of a substorm, but it should be noted that in our observations the equatorward drift was found only in the evening part of the oval. Neither at midnight nor in the morning sector could a similar drift be found.

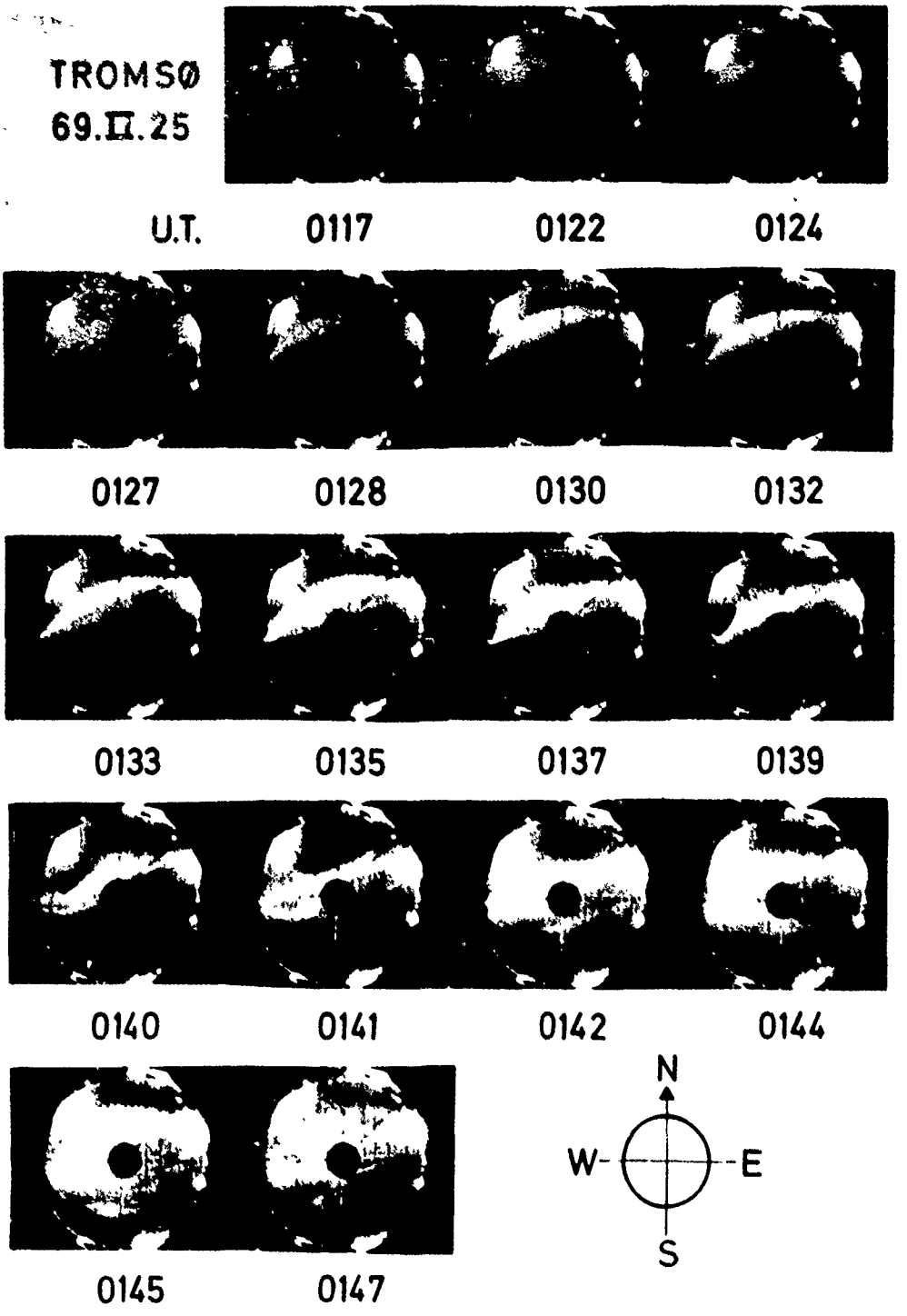

Fig. 10. All-sky camera photos from Tromsø, February 25, 1969.

It is of particular interest to note that the equatorward drift continued through the growth and expansion phases but stopped at the two evening stations a few minutes before the poleward expansion ended. This was also a few minutes before the narrow westward traveling surge arrived at Great Whale. If we make the tentative assumption that the equatorward drift of the arc results from a westward ionospheric field (see, for example, *Kelley et al.* [1971], *Mozer* [1971]), the magnitude of this field, given by $v = (E \times B)/B^2$, is 4 mV/m westward. Our observations show that this field was present during the growth phase and most of the expansion phase and then suddenly disappeared.

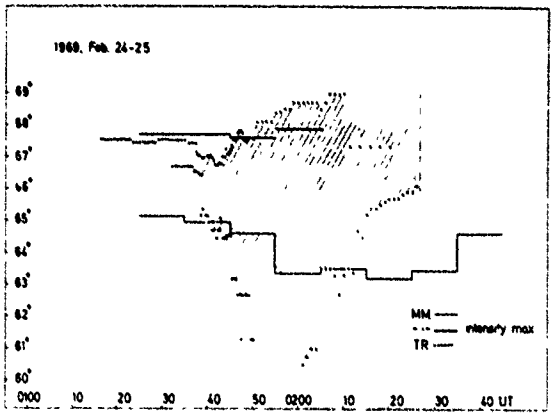

Fig. 11. Broadening of auroral display at Tromsø (dots) and Murmansk (line segments), based on all-sky camera (TR) and spectrograph (MM). The intensity maximum in the spectrographic record is indicated by a narrow double line. In the spectrogram the poleward boundary could not be determined with sufficient accuracy. After 0225, observations were not possible at Tromsø because of cloudiness.

Symmetrically Traveling Disturbances

In the morning sector the equatorward broadening was initiated by the passage of an eastward traveling, small but distinct bulge in the main arcs. The movement of the bulge can be followed in Figure 10. A closer inspection of the figure shows that the arc was dislocated slightly equatorward on both sides of the bulge. The combined effect of this dislocation and the bulge produces the depression of the northern arc at 0135–0145 shown in Figure 11. The projection on the ground of the arc system which clearly shows the bulge is presented in Figure 14. More detailed measurements of the eastward shift of the position of the bulge are given in Figure 15. Note that the ordinate in the figure gives the distance of the maximum deviation in the bulge along the arc from an arbitrary zero meridian, measured in degrees of geomagnetic longitude.

At Great Whale a disturbance similar in shape to but of smaller dimension than a westward traveling surge was seen to move from the vicinity of the great poleward bulge between Canada and Greenland toward the west. As is shown in the photographic sequence of Figure 13, the surge was first detected at 0120; at 0125 it appears to have reached the Great Whale meridian, but at this time it was difficult to distinguish because of the presence of a great number of small-scale folds along the arc. At 0131–0132 the band was again more regular, with a single bulge in the western end, quite similar to the disturbance present near Tromsø at the same time. The westward movement of this bulge and that of the bulge originally approaching Great Whale from the east (presumably the same form) are plotted in Figure 15 and labeled GW. As it approached the western horizon at Great Whale, it became observable in low elevation from Fort Churchill, and the motion measurements taken from the Fort Churchill photographs are plotted in the same figure (labeled FC). A few minutes later the Fort Churchill camera stopped operation for 4 min, enough time for the bulge to become rather poorly defined. But the few observations made at Fort Churchill before the break follow the trend in the Great Whale plot. The displacement in longitude results from the uncertainty in selecting the same point on the aurora from the two stations. At any rate, the observations from these two stations show that a small bulge moved westward across the Great Whale field of view and into the Fort Churchill field of view during the time interval 0120–0139. Between 0134 and 0142 the eastward drift of a similar bulge near Tromsø was measured. The two surges appeared to have about the same drift speed; in the time interval 0135–0138, when the Tromsø measurements were most accurate, the eastward drift speed was 2.2° ± 0.3° geomagnetic longitude per minute, while the westward drift speed of the bulge near Great Whale was measured to be 2.0° ± 0.5° geomagnetic longitude per minute. The bulge at Tromsø drifted close to the 107° geomagnetic longitude meridian, and the one at Great Whale drifted near the 357° meridian. Thus during this short interval the two bulges were of similar shape and were observed to drift symmetrically in relation to the geomagnetic midnight meridian (≃50° geomagnetic longitude).

The western irregularity became visible in the Great Whale field of view a few minutes after the formation of the poleward extension between Canada and Greenland. The drift velocity of this and accompanying irregularities along the arc was relatively constant or slightly decreasing until 0134–0135, when an increase in the velocity occurred. Unfortunately, data are not available to show whether the drift stopped at 0139–0140, as is the case with the eastern irregularity, although the shape of the drift curve of Figure 15 does indicate this possibility. At Tromsø the drift stopped completely for about 2 min at 0139–0140, after which it continued with the same velocity as before. If the symmetric drift of the two irregularities is more than a coincidence, it can perhaps be thought of as an effect associated with changes in the convection and thus in the polar cap electric field during the expansion.

SATELLITE PARTICLE OBSERVATIONS

At 0115 UT the Isis 1 satellite passed over the arc at a position 10.3° east of Great Whale. The electron spectrogram of the southbound pass is presented in Figure 16, where the electrons associated with the visual arc appear distinctly at an invariant latitude of about 68° and a magnetic local time of 20.8 hours. Immediately poleward of this precipitation is a restricted region containing electrons of energies in the 100- to 250-eV range. Equatorward of the auroral precipitation the spectrogram shows photoelectrons of energy between ≃10 eV and ≃60 eV, coming down the field lines from sunlit magnetically conjugate points.

The electron differential number spectrum measured near

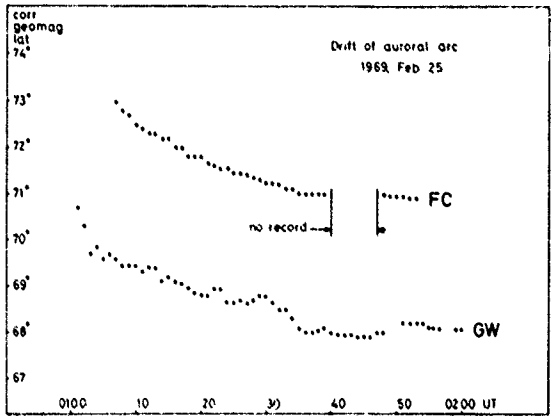

Fig. 12. Equatorward drift of auroral arc in the evening sector. (Top curve) Fort Churchill (19 MLT) (Bottom curve) Great Whale River (21 MLT).

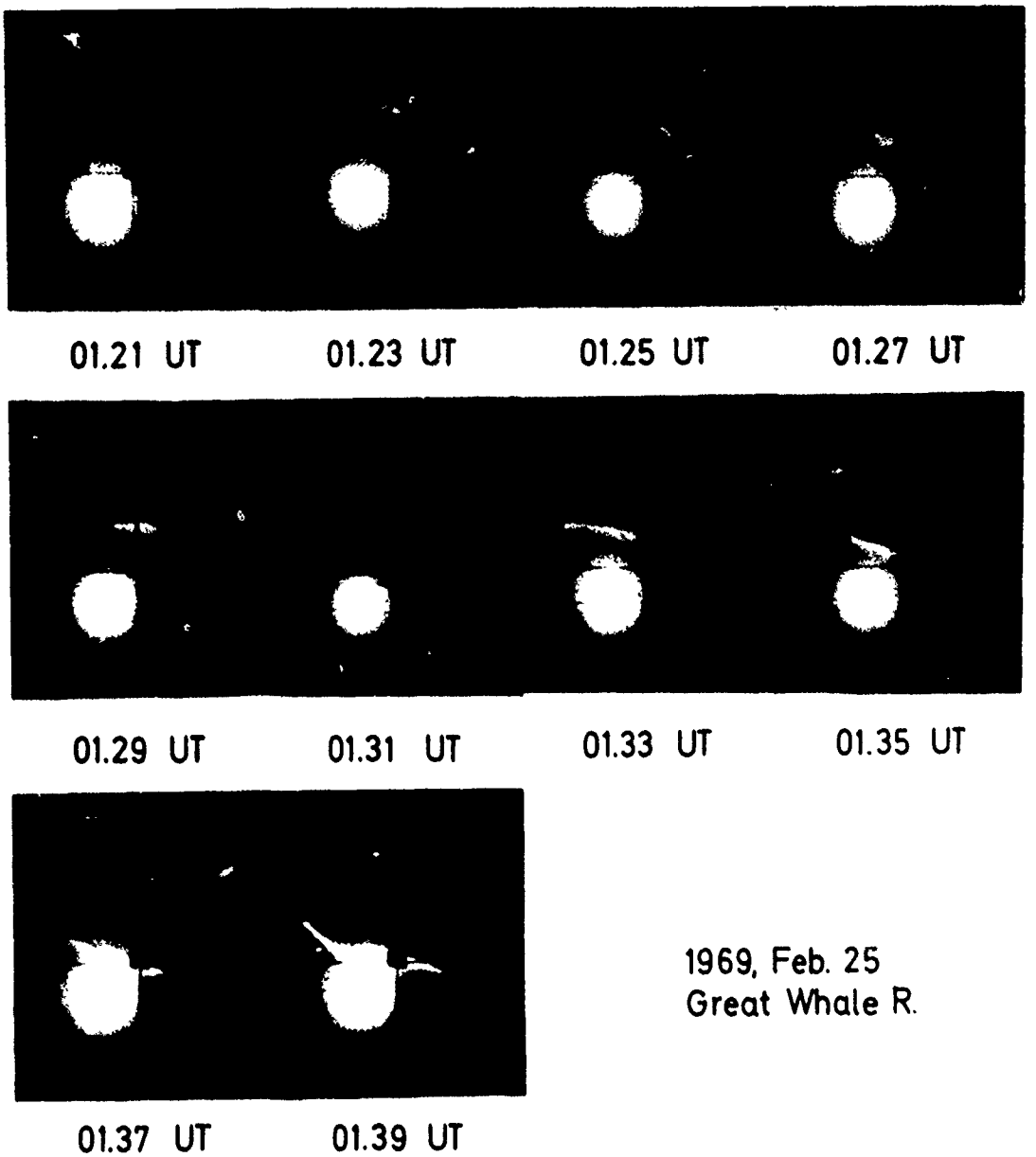

Fig. 13. All sky photographs from Great Whale River, February 25, 1969, showing westward movement of irregularities in the auroral arc.

the center of the region of precipitation is shown in Figure 17. This spectrum, labeled dN/dE, is characteristic of nightside auroral precipitation showing a rather steep negative slope at low energies and the typical auroral peak, in this case at 1.3 keV. The total energy in the spectrum (in the range 10 eV to 11.6 keV) is 4.3 ergs cm^{-2} s^{-1} sr^{-1}. Assuming an isotropic electron distribution, this energy flux corresponds to a brightness of 20 kR of light at 5577 Å [*Dalgarno et al.*, 1965]. Examination of individual spectra indicates that the peak in the electron spectrum increases and then decreases as the arc is crossed. Such a latitudinal morphology has been referred to as an 'inverted V' structure by *Frank and Ackerson* [1971] and is a common feature associated with many auroral arcs.

The enlarged photograph of Figure 18 shows the arc as it was observed from the Great Whale River Observatory at 0115 UT. The small white circle near the right edge of the photograph marks the point at which the geomagnetic field line, through which the satellite passed at the time the maximum energy flux was detected (0114:56), intersects the height of maximum auroral luminosity. As is shown by the 'energy flux' curve of Figure 17, most of the energy was carried at >3 keV, which places the height of maximum luminosity at about 120 km [*Rees*, 1969].

The soft particle spectrometer also provided a measurement of protons in the range of energies 10 eV to 11.6 keV. Within this energy range, protons were observed to precipitate over a

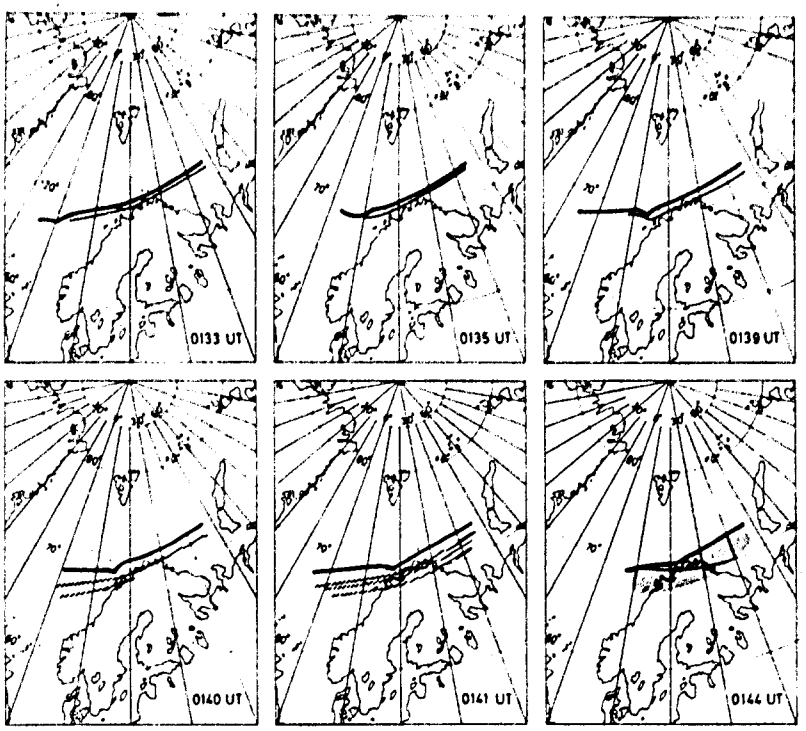

Fig. 14. Maps showing eastward movement of surge in the morning sector, as observed from Tromsø.

region extending from an invariant latitude of 67.4°–66.6°. The proton energy flux profile is plotted in Figure 19, which clearly demonstrates that the proton precipitation occurred equatorward of the electron precipitation associated with the visual arc. The energy associated with the protons over this range of invariant latitude averaged 3.0×10^{-2} erg/cm² s sr. Because of low count rates it was not possible to measure a proton spectrum, but the average proton energy appeared to be near 4 keV.

Since the satellite crossed the region of particle precipitation before the time of maximum disturbance, it is possible to estimate energy input into the auroral ionosphere before the onset of the expansive phase. Figure 19 shows the electron energy flux profile measured as the satellite passed over the arc. A directional intensity of 0.2 erg/cm² s sr corresponds to 1 kR of light at 5577 Å, which is near the visibility threshold above the background light of the night sky. As the figure indicates, an electron flux in excess of this value was detected for four consecutive spectral sweeps or for 8 s. The satellite horizontal speed was 7 km/s, so that at the satellite altitude of 620 km the 'arc width' was 56 km. Integrating across the arc, the rate of energy input per unit length of the arc was 5×10^7 ergs/s cm. The prebreakup arc was observed by cameras from west of Fort Churchill to east of Tromsø and most likely

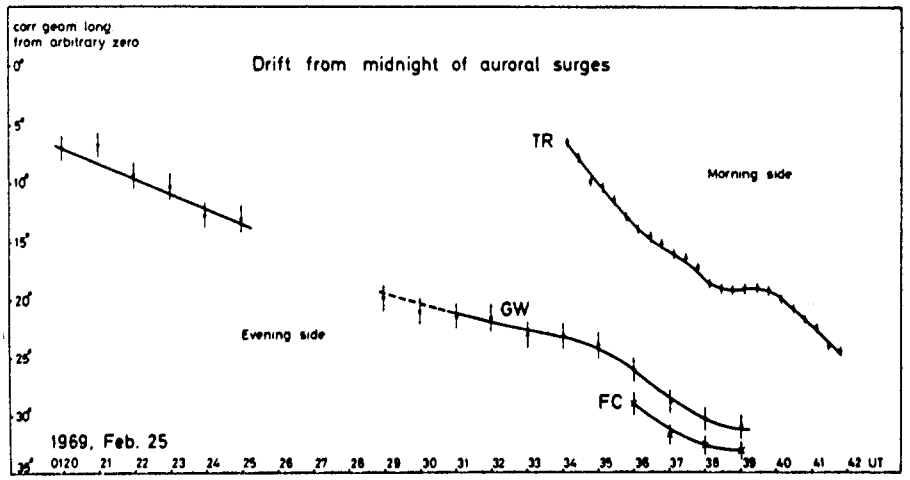

Fig. 15. Drift from midnight of auroral surges. The drift seen at Great Whale and Fort Churchill is westward; that at Tromsø is eastward.

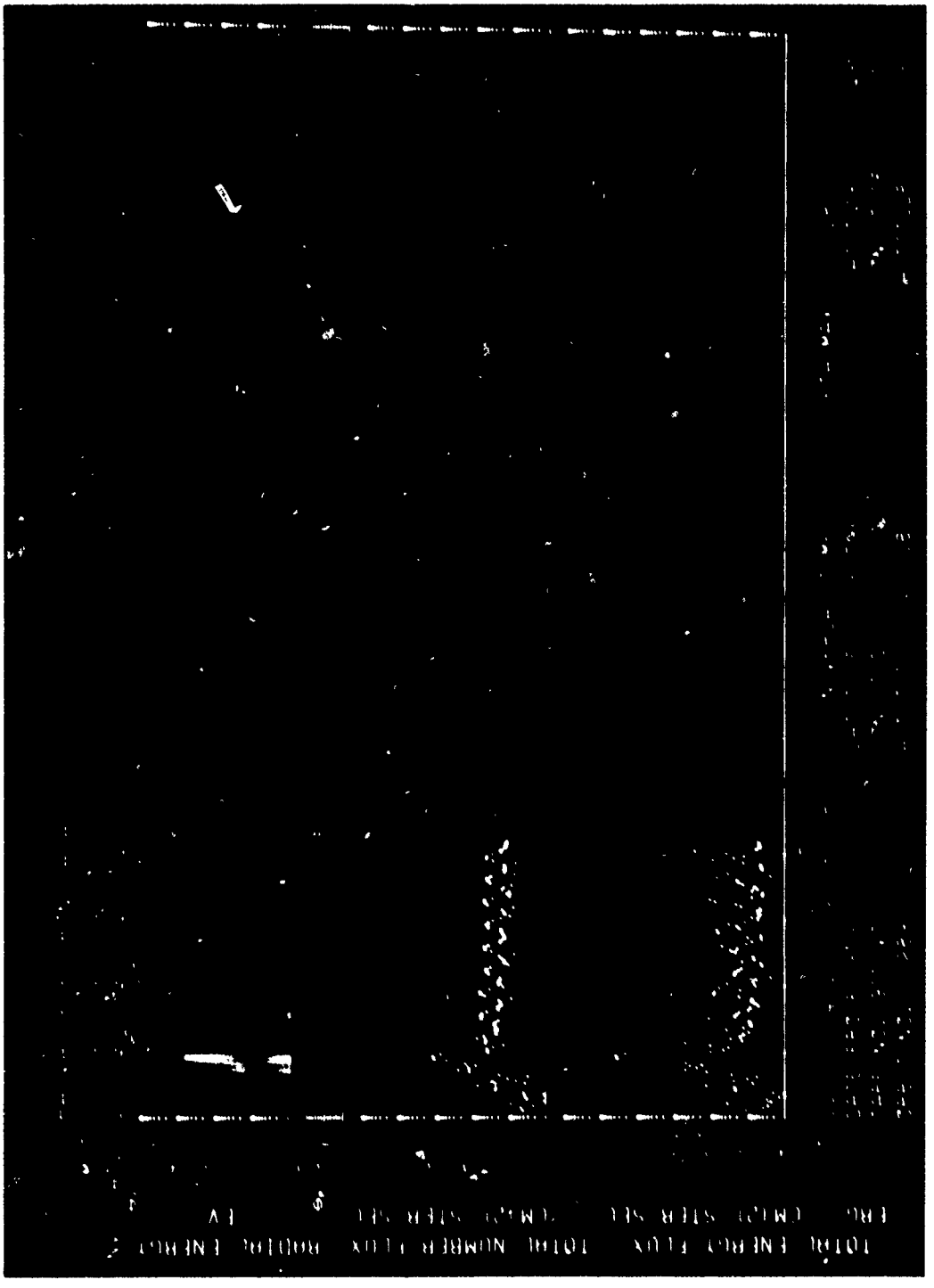

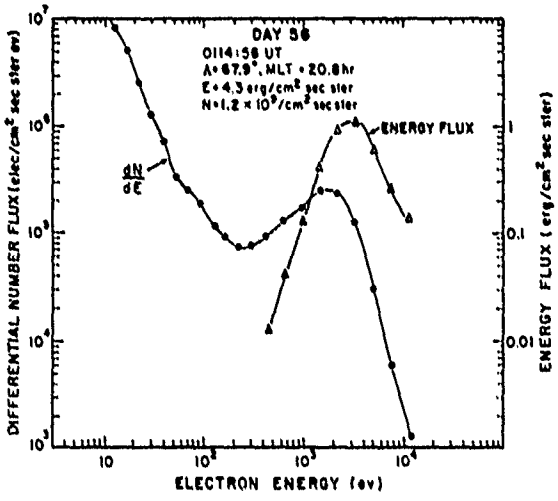

Fig. 17. Electron differential number spectrum (dN/dE) and energy flux measured by the Isis 1 soft particle spectrometer at 0114:56 UT on February 25, 1969.

extended much further in both directions. A length of 7×10^8 km approximates this distance, and with this assumption the total energy input rate was 3.5×10^{16} ergs/s. The arc was visible for at least ½ hour before breakup; therefore an energy of 7×10^{19} ergs was deposited into the auroral atmosphere by the electrons before breakup. The protons in the region equatorward of the arc carried considerably less energy than the electrons, a feature not unusual in auroral events. The ratio of the energy of the protons equatorward of the arc to that of electrons within the arc was 1.6×10^{-2}.

The question of whether or not auroral arcs always occur on closed magnetic field lines continues to be a matter for determination. We have attempted such a determination for the arc observed on February 25 by making use of the S-50 detector of the Isis 1 energetic particle experiment (compliments of J. R. Burrows, National Research Council, Ottawa, Canada). This detector responds to electrons of energy >40 keV and offers the advantage of a large geometric factor of 4×10^{-2} cm² sr. Figure 20 shows the S-50 flux plotted against universal time and invariant latitude, where the counts have been averaged over pitch angle in order to compare the trapped particle flux outside the 63° loss cone with the downcoming ($\alpha < 63°$) and upcoming ($\alpha > 117°$) fluxes. At latitudes below about 68° the trapped flux exceeds the precipitated flux, indicating a closed field line configuration. From the figure it is not possible to tell exactly where the angular distribution changed, but it must have been between 67.9° and 68.4°. *Fritz* [1970] would identify this location as $\Lambda_{1,0}$, a boundary defined to be the lowest latitude at which isotropy occurs for electrons of $E > 35$ keV. We note that on the nightside this boundary always occurs at a latitude lower than the Λ_b of *McDiarmid and Burrows* [1968], which is the lowest latitude at which counts fall to cosmic ray background and which is interpreted by them as the high-latitude limit of closed field lines. In the present case, Λ_b was above latitude 71.2°, the highest latitude tracked on this pass. Thus we can state that the electron arc is associated with or lies below the boundary between open and closed field lines and that the proton arc clearly lies on closed magnetic field lines

Discussion

Growth Phase

It has been shown that the substorm under study here, which followed a period of magnetic calm, appears to have been preceded by an interval before breakup with activity corresponding to the growth phase defined by *McPherron* [1970]. The gradual development of the activity starts shortly after the southward turning of the interplanetary magnetic field; the magnetic deflections at auroral latitudes as well as at middle and low latitudes, the auroral activity, the westward magnetospheric electric field deduced from the auroral drift, and the precipitation of auroral particles measured by the satellite all support McPherron's suggestion that the start of the substorm growth phase indicates either a commencement or a gradual enhancement of magnetospheric convection. The observation of symmetrically drifting auroral surges during growth and expansion phases as well as of auroral patterns similar to part of the convection pattern may give further support to this idea. In the present case we are apparently concerned with a situation in which increased convection initiated by a negative B_z is terminated by several substorms: first a very small confined substorm and then two greater substorms with clear breakup and poleward expansions which are not separated from each other but which seem to belong to the same disturbance event.

The very small substorm occurred at about 0100 UT approximately ½ hour before the expansion phase of the major substorm. It was characterized by a small westward traveling surge and a small magnetic bay of $\simeq 20\,\gamma$ and therefore fits the description of a weak substorm along a contracted oval as concluded from ground-based observations [*Montbriand*, 1971] and DMSP 2 imaging [*Akasofu*, 1974*b*]. The southward turning of the IMF preceded even this event by more than an hour, and the first departure from magnetic quiet was observed at auroral zone as well as low-latitude stations about 1

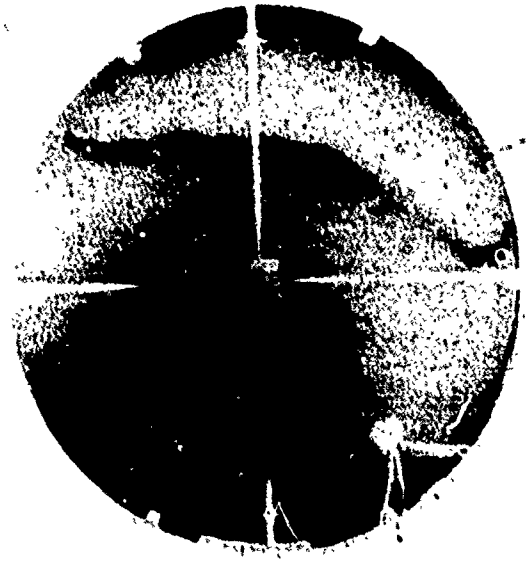

Fig. 18. All-sky photograph taken at Great Whale River Observatory at 0115 UT on February 25, 1969. The small white circle designates the field line intersection point at 120 km

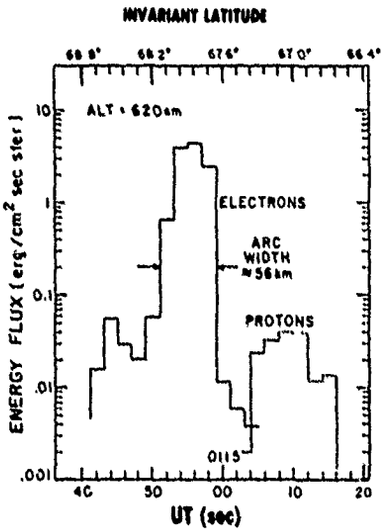

Fig. 19. Electron and proton energy flux latitudinal profiles. The proton precipitation lies distinctly equatorward of the electron precipitation associated with the visual arc. Minute 15 of hour 01 is labeled as 0115 and begins at the 00 mark on the abscissa.

hour before the appearance of the small substorm. Accordingly, we take the view that this substorm may also have resulted from the southward turning of the IMF and represented a small release of energy before the much greater release at 0130.

As in the main event under study, the 0600 substorm which appears at Fort Churchill and Great Whale River was preceded by a short interval of activity, which is similar to the growth phase of the 0130 substorm: following the recovery of substorm activity at 0400, quiet arcs were situated near 71° corrected geomagnetic latitude. Near 0525, B_z went negative (Figure 1). At 0525–0530 the arcs became more intense (Figure 21); at 0541 an arc was broadening from the midnight sector into the Fort Churchill field of view. At 0603 a bright arc was suddenly observed at about 68°; at 0606–0610, internal activity was seen in the arc; at 0608–0610 it developed toward the east across the Great Whale zenith; and at 0616 a moderate poleward expansion began. The development of the auroral display has its counterpart in the magnetic record from Fort Churchill (Figure 1). Also, the low-latitude stations near midnight (Fredericksburg and Tucson, Figure 2) show features of increasing cross-tail current between 0540 and substorm onset at about 0600. Thus although the observational data are more limited at this substorm, we see features very much like those described above, beginning with the negative turning of B_z and ending with the poleward expansion about 50 min later. The poleward expansion does not reach as high a latitude as in the 0130 substorm; the product of B_z and time from southward turning to breakup is also less in the 0600 substorm [*Arnoldy*, 1971].

Our observations do not determine whether the expansive phase trigger mechanism is internal or external. We can only point to our observations that the southward turning of the IMF was followed by clear signatures of increased magnetospheric convection: *DPZ* equivalent current systems of gradually (though not monotonically) increasing intensity, signatures of an increasing cross-tail and/or ring current, precipitation of auroral particles in an increasing longitudinal sector of the midnight auroral oval, and finally a poleward curvature of arcs in the premidnight area that resembles the drift pattern in the polar cap. Minor signatures of instability or activity are followed by the sharp breakup.

It is apparent from the observations presented here as well as from observations of *Subbarao and Rostoker* [1973], *Hones et al.* [1973], *Akasofu et al.* [1973], *Rossberg* [1974], and *Aka-*

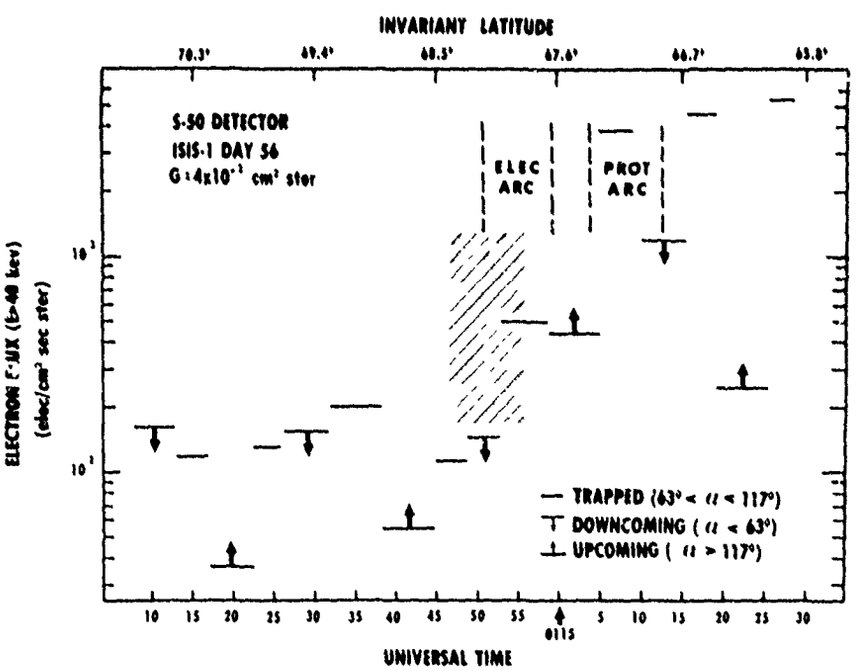

Fig. 20. High-energy electron fluxes averaged over pitch angle. The low-latitude limit of the position of the boundary between open and closed field lines lies between invariant latitudes 67.9° and 68.4°, indicated by hatching. The arrow on the abscissa labeled 0115 indicates the beginning of minute 15 of hour 01 (UT).

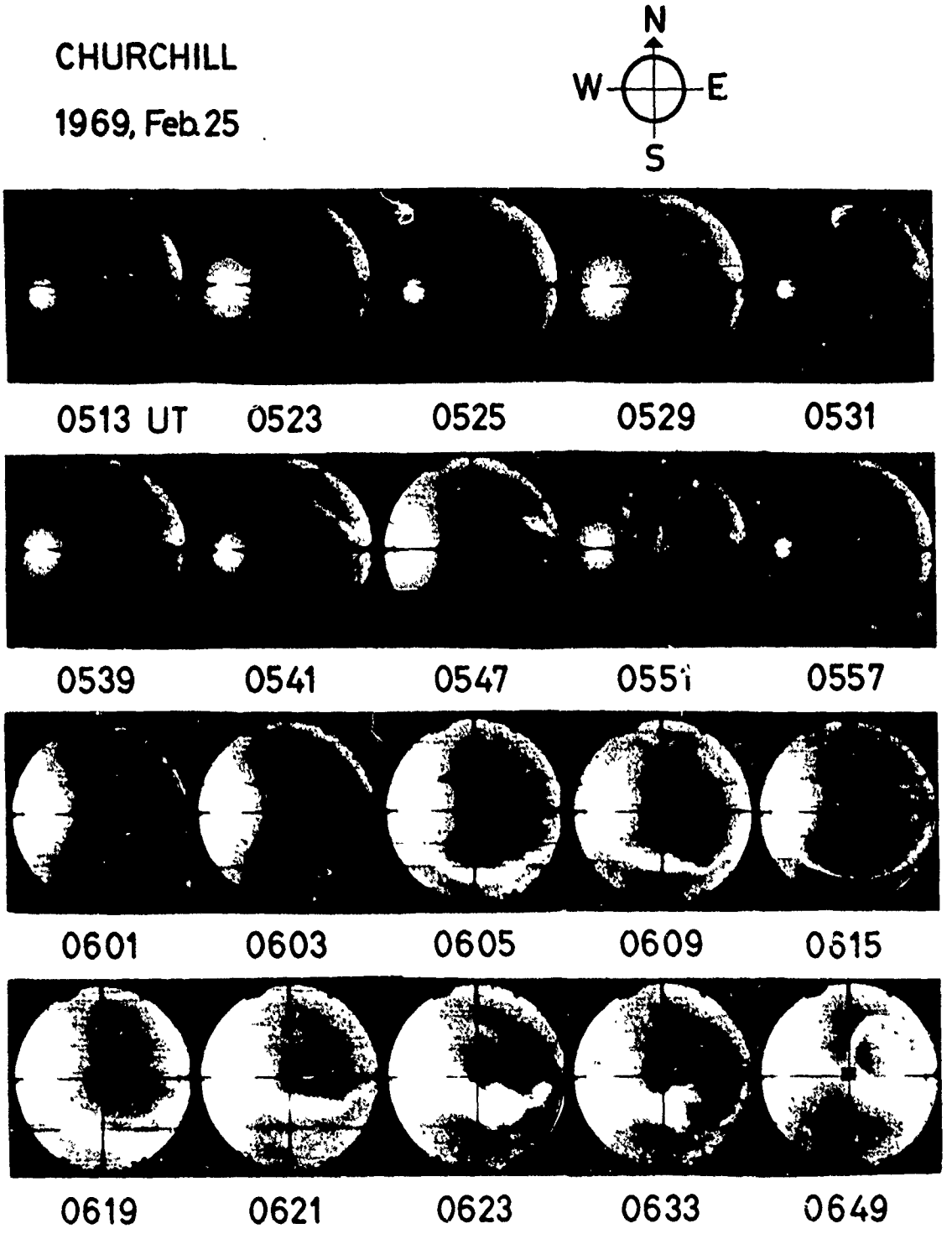

Fig. 21. All-sky photographs from Fort Churchill, February 25, 1969, showing auroral activity during the prebreakup (growth) phase and beginning of expansion phase of the later substorm

sofu [1975] that some substorms have a gradual and easily defined growth or development phase, while others do not. Obviously, there is no clear one-to-one relation between the growth phenomenon and the substorm. It is in agreement with current substorm theories that a B_z-negative-caused magnetospheric convection, if it is continued for a sufficiently long period, may result in substorm activity, as in the case studied here. However, the evidence discussed above seems to argue against the use of the term growth phase when it is applied with the same weight as the term 'expansive phase' in describ-

ing a definite phase of every substorm. The term may, however, be suitable in describing a magnetospheric situation which may lead to the triggering of a substorm.

Ionospheric Electric Fields

In a study of the ionospheric electric field by means of balloon-borne detectors, *Mozer* [1971] found a regular behavior of the electric field in the auroral zone. Averaging over 19 substorms, he found that about 1 hour before the onset of the expansive phase the westward component of the electric field increased from zero and reached a maximum value at the time of breakup. The field remained at this level throughout the expansion phase and then began a return toward zero. The southward component remained at a zero level until it suddenly increased at the onset of the expansion. Our observation that the equatorward drift of the auroral arc appears during the growth phase, continues through the expansive phase, and then suddenly stops is in agreement with Mozer's observation of the duration of the positive excursion of the westward component of the electric field. Our observation of the limitation of the equatorward drift to the evening side of the substorm center appears, however, to be new. It is not obvious from Mozer's balloon measurements. His conclusions are based on average values without information about the location of the balloons in relation to the substorm.

Particle Precipitation and Relationship to the Magnetosphere

The particle precipitation associated with this auroral display has been studied both by direct measurement and by observation of the drift of cloudlike auroral forms. Most of the electrons responsible for the luminosity in the premidnight sector before breakup possessed energies of 1–5 keV. The cloudlike form observed drifting from Tromsø to Murmansk was produced by electrons of ≈40-keV energy. This energy determination, based on the assumption that the electrons were gradient drifting, is in agreement with the photographic observations of *Stormer* [1955], which give a mean height of 94 km for ordinary cloudlike auroras over Norway. The ionization production maximum for 40-keV electrons has been calculated by *Rees* [1963] to be 92 km. Our observations of diffuse aurora indicate that such electrons appeared nearly simultaneously all along the oval from midnight to shortly before 0400 geomagnetic time and that the drift of the cloudlike aurora east of Tromsø is consistent with gradient drift of 40-keV electrons at auroral latitudes.

This observation agrees well with the model for precipitation into the auroral zone of electrons in the >30-keV range presented by *Sletten et al.* [1971] on the basis of observations by several authors (see their list of references). In their model, electrons within the loss cone are precipitated in an elongated region following the auroral oval from geomagnetic midnight toward dawn. Electrons with other pitch angles drift eastward, following the L shells from this source region, and are gradually precipitated by pitch angle scattering or other mechanisms. This drifting electron population may be responsible for the mantle aurora [*Hoffman and Burch*, 1973].

Thus our observations support a mechanism which would inject 40-keV electrons into the auroral oval during the expansive phase of the substorm. The observation by the Vela satellites [*Hones et al.*, 1973] of an enhancement in the $E > 45$-keV electron flux at the time of rapid thinning of the plasma sheet at the satellite suggests that these electrons may be of the same population as that responsible for the production of the diffuse cloudlike auroras which appear at auroral latitudes during breakup.

Our present Isis 1 electron observations made before auroral breakup agree well with the growth phase morphological pattern of *Hoffman and Burch* [1973]. The term growth phase was defined by them as the time between the southward turning of the IMF and the appearance of auroral breakup. The studies of *Akasofu et al.* [1973] and *Akasofu* [1974a] would have categorized the present observation as the 'plasma sheet quiet arc' of a 'growth phase pattern.' *Winningham et al.* [1975], using Isis 1 and 2 particle data, have amplified the patterns of *Hoffman and Burch* [1973] but do not include a pattern representing a preexpansive phase, IMF south condition (since this condition does not always initiate a complete substorm sequence). They do state, however, that an observation of the kind we report would be categorized as representing their 'boundary plasma sheet' (BPS) region during a period for which the IMF is directed southward (see their Figure 19). This BPS region is always located poleward of the region of diffuse aurora and often contains discrete arcs.

As we have illustrated in Figure 19, the highest fluxes of protons of about 4-keV energy were measured within a region equatorward of the electron arc. A similar latitudinal profile, characteristic of the premidnight hours, has been obtained statistically with airborne [*Eather and Mende*, 1971] and ground-based [*Fukunishi*, 1975] Hβ observations. The study of *Fukunishi* [1975] clearly places the belt of proton precipitation equatorward of discrete auroral arcs during times which he defines as the 'quiet' phase and the 'prebreakup' phase. Our particle observations show that the separation can occur on an instantaneous basis, a fact which must be included in any theory which seeks to explain the global development of an auroral substorm. Isis 1 crossed the arc at a local time of 20.5 hours and a magnetic local time of 20.8 hours. We also note that apparent separation between the region of maximum proton precipitation and the region of maximum electron precipitation (the arc) does not completely exclude protons from the electron precipitation region, it only excludes protons within the energy range 10 eV to 11.6 keV and above an energy flux level of $\approx 10^{-3}$ erg/cm^2 s sr.

The observed protons were most likely associated with the quiet time ring current, which, according to the San Juan magnetogram of Figure 2, intensified as the substorm sequence continued. The greatly reduced proton flux at the position of the arc before breakup implies either (1) an upward field-aligned electric field at the auroral arc or (2) that the mechanism which energizes electrons and protons does not precipitate the protons efficiently. Only when the proton population of the near-earth plasma sheet reaches a critical intensity are protons precipitated by resonant wave-particle interactions as suggested by *Kennel and Petschek* [1966]. Adiabatic compression operates on protons on closed field lines in the tail region, but the dominant mechanism is betatron or transverse energization which operates on the transverse component of the proton motion. Our observation, using the high-energy electron data, that the boundary between open and closed field lines lies at a latitude at least as high as 67.9° insures that the protons we observed were on closed magnetic lines.

SUMMARY AND CONCLUSIONS

A comprehensive study of the major substorm of February 25, 1969, at 0130 UT and several weak substorms before and after this event has resulted in the following observations.

1. The preexpansive phase auroral arc extended approxi-

mately along the auroral oval from 17.5 to 05.5 MLT and was responsible for an energy input rate of $\simeq 3 \times 10^{10}$ ergs/s before the breakup.

2. In the evening sector, from the earliest observation of auroral light, an equatorward drift of 6 km/min was observed; this drift was present only in the evening sector and ceased after the onset of the expansive phase at the time of maximum poleward displacement of the breakup arcs.

3. In the evening-midnight sector the increase in the intensity of the preexpansive phase arc accompanied the increase in the deviation of the horizontal magnetogram component.

4. The equivalent currents obtained from the observed magnetic deflections were of the *DPZ* type (twin vortex mode) before the onset of the expansive phase. After the onset the *DPZ* currents were more intense by a factor of 2, but the dominating current during this period was an intense westward auroral electrojet.

5. During the expansive phase, symmetrically traveling disturbances were observed propagating eastward and westward away from the midnight sector. The propagation stopped for 1–2 min at the time of maximum poleward expansion and then continued (at least in the morning side) with the original velocity.

6. Electrons in the 1- to 5-keV range were measured by satellite over the preexpansion phase arc. They were observed near and probably within the low-latitude limit of the boundary between open and closed field lines.

7. Protons of $\simeq$4-keV energy were measured equatorward of the electron arc; their intensity was 1.6×10^{-2} that of the electrons within the arc, and they were definitely on closed field lines.

8. An injection of $\simeq$40-keV electrons as determined from the observations of diffuse cloudlike aurora occurred during the expansive phase. At times later than 04 MLT the cloudlike aurora associated with the 40-keV electron population was observed to drift eastward toward later morning hours.

The major substorm at 0130 UT and a smaller substorm at 0600 UT show growth phase features in their visual and magnetic signatures. However, other investigations show that many substorms have occurred for which there is no classic growth pattern and also that some growth phase patterns do not always result in a complete substorm sequence [*Kokubun et al.*, 1977]. Accordingly, we emphasize the usefulness of the growth phase concept in describing a magnetospheric condition which is initiated by a southward turning of the IMF but stress that in general it should not be expected to bear a one-to-one correspondence with the substorm expansive phase.

Acknowledgments. We are indebted to H. Derblom, Ionosfaerobservatoriet, Uppsala, S. I. Isaev, Polar Institute, Apatity, Murmansk, M. J. Neale, National Research Council (NRC), Canada, J. Sommer, World Data Center A, Copenhagen, and O. Holt, Nordlysobservatoriet, Tromsø, for placing copies of records at our disposal. We also wish to thank J. R. Burrows and M. Wilson, NRC, Canada, for providing the energetic particle data from Isis 1, P. Hedgecock, Imperial College, London, for magnetometer data from Heos 1, and J. Frazier of the University of Texas at Dallas (UTD) and I. Kaufman of the Florida Institute of Technology for technical assistance. The UTD portion of the work was supported by NASA contract NGR 44-004-150 and by Air Force contracts AFCRL F 19628-75-C-0032 and AFCRL F 19628-76-R-0009. We also gratefully acknowledge research funds provided by the Danish Meteorological Institute and by the Florida Institute of Technology.

REFERENCES

Akasofu, S.-I., The development of the auroral substorm, *Planet. Space Sci.*, *12*, 273, 1964.

Akasofu, S.-I., Auroral substorm and associated magnetic disturbances, in *Polar and Magnetospheric Substorms*, D. Reidel, Hingham, Mass., 1968.

Akasofu, S.-I., The aurora and magnetosphere, The Chapman memorial lecture, *Planet. Space Sci.*, *22*, 895, 1974*a*.

Akasofu, S.-I., A study of auroral displays as photographed from the DMSP-2 satellite and from the Alaska meridian chain of stations, *Space Sci. Rev.*, *16*, 617, 1974*b*.

Akasofu, S.-I., The roles of the north-south component of the interplanetary magnetic field on large-scale auroral dynamics observed by the DMSP satellite, *Planet. Space Sci.*, *23*, 1349, 1975.

Akasofu, S.-I., P. D. Perreault, and F. Yasuhara, Auroral substorms and the interplanetary magnetic field, *J. Geophys. Res.*, *78*, 7490, 1973.

Arnoldy, R. L., Signature in the interplanetary medium for substorms, *J. Geophys. Res.*, *76*, 5189, 1971.

Dalgarno, A., I. D. Latimer, and J. W. McConkey, Corpuscular bombardment and N_2^+ radiation, *Planet. Space Sci.*, *13*, 1008, 1965.

Eather, R. H., and S. B. Mende, Airborne observations of auroral precipitation patterns, *J. Geophys. Res.*, *76*, 1746, 1971.

Feldstein, Y. I., Auroras and associated phenomena, in *Solar-Terrestrial Physics*, edited by E. R. Dyer, p. 152, D. Reidel, Hingham, Mass., 1972.

Frank, L. A., and K. L. Ackerson, Observations of charged particle precipitation into the auroral zone, *J. Geophys. Res.*, *76*, 3612, 1971.

Friis-Christensen, E., and J. Wilhjelm, Polar cap currents for different directions of the interplanetary magnetic field in the *y-z* plane, *J. Geophys. Res.*, *80*, 1248, 1975.

Fritz, T. A., Study of the high-latitude, outer-zone boundary region for $\geq$40-keV electrons with satellite Injun 3, *J. Geophys. Res.*, *75*, 5387, 1970.

Fukunishi, H., Dynamic relationship between proton and electron auroral substorms, *J. Geophys. Res.*, *80*, 553, 1975.

Hamlin, D. A., R. Karplus, R. C. Vik, and K. M. Watson, Mirror and azimuthal drift frequencies for geomagnetically trapped particles, *J. Geophys. Res.*, *66*, 1, 1961.

Hoffman, R. A., and J. L. Burch, Electron precipitation patterns of substorm morphology, *J. Geophys. Res.*, *78*, 2867, 1973.

Hones, E. W., Jr., J. R. Asbridge, S. J. Bame, and S. Singer, Substorm variations of the magnetotail plasma sheet from $X_{SM} \simeq -6\ R_E$ to $X_{SM} \simeq -60\ R_E$, *J. Geophys. Res.*, *78*, 109, 1973.

Iijima, T., and T. Nagata, Consitution of polar magnetic disturbances, *Rep. Ionos. Space Res. Jap.*, *22*, 1, 1968.

Iijima, T., and T. Nagata, Signatures for substorm development of the growth phase and expansion phase, *Planet. Space Sci.*, *20*, 1095, 1972.

Kelley, M. C., J. A. Starr, and F. S. Mozer, Relationship between magnetospheric electric fields and the motion of auroral forms, *J. Geophys. Res.*, *76*, 5269, 1971.

Kennel, C. F., and H. E. Petschek, Limit on stably trapped particle fluxes, *J. Geophys. Res.*, *71*, 1, 1966.

King, J. H., Interplanetary magnetic field data book, report, NASA, April 1975.

Kokubun, S., and T. Iijima, Time-sequence of polar magnetic substorms, *Planet. Space Sci.*, *23*, 1483, 1975.

Kokubun, S., R. L. McPherron, and C. T. Russell, Triggering of substorm by solar wind discontinuities, *J. Geophys. Res.*, *82*, 74, 1977.

Lui, A. T. Y., C. D. Anger, and S.-I. Akasofu, The equatorward boundary of the diffuse aurora and auroral substorms as seen by the Isis 2 auroral scanning photometer, *J. Geophys. Res.*, *80*, 3603, 1975.

McDiarmid, I. B., and J. R. Burrows, Local time asymmetries in the high-latitude boundary of the outer radiation zone for different electron energies, *Can. J. Phys.*, *46*, 49, 1968.

McPherron, R. L., Growth phase of magnetospheric substorms, *J. Geophys. Res.*, *75*, 5592, 1970.

McPherron, R. L., C. T. Russell, and M. P. Aubry, Satellite studies of magnetospheric substorms on August 15, 1968, 9, Phenomenological model for substorms, *J. Geophys. Res.*, *78*, 3131, 1973.

Montbriand, L. E., Proton aurora and auroral substorm, in *The Radiating Atmosphere*, edited by B. M. McCormac, p. 366, D. Reidel, Hingham, Mass., 1971.

Mozer, F. S., Origin and effects of electric fields during isolated magnetospheric substorms, *J. Geophys. Res.*, *76*, 7595, 1971.

Nishida, A., Geomagnetic *DP2* fluctuations and associated magnetospheric phenomena, *J. Geophys. Res.*, *73*, 1795, 1968.

Pike, C. P., and J. A. Whalen, Satellite observations of auroral sub-

storms, *J. Geophys. Res.*, *79*, 985, 1974.
Rees, M. H., Auroral ionization and excitation by incident energetic electrons, *Planet. Space Sci.*, *11*, 1209, 1963.
Rees, M. H., Auroral electrons, *Space Sci. Rev.*, *10*, 413, 1969.
Rossberg, L., Remarks on the growth phase of substorms, in *Magnetospheric Physics*, edited by B. M. McCormac, p. 367, D. Reidel, Hingham, Mass., 1974.
Rostoker, G., Polar magnetic substorms, *Rev. Geophys. Space Phys.*, *10*, 157, 1972.
Sletten, A., J. Stadsnes, and H. Trefall, Auroral-zone x-ray events and their relation to polar magnetic substorms, *J. Atmos. Terr. Phys.*, *33*, 589, 1971.
Starkov, G. V., and Ya. I. Feldstein, Substorms in auroras, *Geomagn. Aeron.*, *11*, 478, 1971.
Stormer, C., *The Polar Aurora*, p. 108, Oxford University Press, New York, 1955.
Subbarao, S., and G. Rostoker, Relationship of southward drifting auroral arcs to the magnetospheric electric field and substorm activity, *J. Geophys. Res.*, *78*, 1100, 1973.
Winningham, J. D., F. Hasuhara, S.-I. Akasofu, and W. J. Heikkila, The latitudinal morphology of 10-eV to 10-keV electron fluxes during magnetically quiet and disturbed times in the 2100–0300 MLT sector, *J. Geophys. Res.*, *80*, 3148, 1975.

(Received February 18, 1976;
accepted July 18, 1977.)

VOL. 81, NO. 34 JOURNAL OF GEOPHYSICAL RESEARCH DECEMBER 1, 1976

The Topside Magnetospheric Cleft Ionosphere Observed From the Isis 2 Spacecraft

G. G. SHEPHERD,[1] J. H. WHITTEKER,[2] J. D. WINNINGHAM,[3] J. H. HOFFMAN,[3] E. J. MAIER,[4] L. H. BRACE,[4] J. R. BURROWS,[5] AND L. L. COGGER[6]

Data from the Isis 2 spacecraft for five orbits in November 1971 are examined in detail. The spacecraft was then in cartwheel configuration, permitting detailed angular and spectral measurements of charged particle fluxes ($E > 5$ eV), local ion densities and temperatures, local electron densities and temperatures, F region peak electron densities, and 6300- and 5577-Å emissions accurately located at the field line foot. In the November 9 and 10 orbits, highly structured regions of electron flux having average energies of ~0.7 and ~0.2 keV are observed. The O^+ density at the 1400-km spacecraft altitude generally reflects the electron precipitation, disappearing rapidly at the poleward boundary with He^+ becoming dominant in the polar cap. Throughout this region of enhanced O^+ densities, strong polar wind flows of H^+ are observed. The electron densities obtained with the topside sounder are sometimes higher than the ion densities; this is in part due to the structured nature of the cleft region, but other indirect plasma processes may also be involved. The ion temperature is about 2000°K inside the cleft and rises to about 5000°K at the poleward cleft boundary. The F region peak density shows some structure but no uniquely identifiable cleft response, and the optical emissions generally show a multiple peaked structure, normally with the lowest red/green ratio in the equatorward components. The November 17 and 18 orbits differ in that the electron spectrum precipitation energies are closer to 100 eV, are less structured, and are displaced to higher invariant latitude. The O^+ densities are higher, while the light ions are little changed, and O^+ is observed poleward of the precipitation region, implying strong convection perpendicular to the auroral oval. The optical red/green ratio is higher for these orbits. A tentative explanation for the different behavior is the passage of a sector boundary between these two dates with the interplanetary field direction changing from 'away' to 'toward.'

INTRODUCTION

The existence of dayside aurora and the continuity of the auroral oval have been known for some time [*Feldstein*, 1963]. Studies of the polar cap ionosphere had revealed topside density enhancements attributable to particle energy input on the earth's dayside [*Nishida*, 1967; *Sato and Colin*, 1969]. But the recognition of the magnetospheric dayside cusps [*Heikkila and Winningham*, 1971; *Frank and Ackerson*, 1971] or cleft [*Heikkila*, 1972] came about through the observation of magnetosheathlike plasma at low altitudes and high latitudes on the earth's dayside. Subsequently, many manifestations of this dayside energy source have been identified and studied [*Vasyliunas*, 1974]. Pronounced ionospheric characteristics are elevated electron temperature [*Brace and Miller*, 1974] and F region irregularities [*Dyson and Winningham*, 1974; *Ahmed and Sagalyn*, 1973]. *Whalen and Pike* [1973] related the F region irregularity zone to the occurrence of 6300-Å emission, a direct indicator of incident low-energy electrons.

The role of the cleft as an ionization source for the polar cap is a topic of current study; *Knudsen* [1974] discussed the plausibility of this in terms of the convection pattern in the polar cap. But a more recent study [*Knudsen et al.*, 1975] suggests that the ionospheric residence time in the cleft is too short to provide a significant effect. *Whitteker* [1976] has given a detailed review and thorough discussion of ionospheric cleft effects.

The Isis 2 spacecraft offers an opportunity to measure the cleft particle fluxes and ionospheric response at 1400 km as well as topside electron density profiles and F region peak densities. The optical emissions at 6300, 5577, and 3914 Å can also be detected with the on-board photometers. This paper reports upon a detailed and coordinated set of observations for a few orbits in November 1971. This period was chosen because the orbit then had a suitable local time, the spacecraft was in cartwheel configuration for good measurements of local parameters, and the polar cap was reasonably dark for optical viewing.

DATA ACQUISITION

A brief description of the instruments and a list of relevant references has been given by *Shepherd et al.* [1973]. For this study a period of cartwheel configuration was chosen (spin axis perpendicular to the orbit plane) in order to obtain the best ion data. In this mode a complete scan about the velocity vector is obtained once every spin (roughly 18 s). In addition, a complete pitch angle scan is obtained with the particle detectors.

As will be seen in the data, there is considerable fine structure present in the local plasma. For this reason, caution should be exercised in comparing the results from experiments which nominally measure the same parameter. For example, both the ion mass spectrometer (IMS) and the retarding potential analyzer (RPA) measure ion density, but since the sensors are located about 90° apart on the spacecraft, the 'simultaneous' samples analyzed are separated by about 5 s in time and 35 km in space. For one instrument the data points are separated by about 125 km. Thus what sometimes appears to be a discrepancy in the density profile observations along the spacecraft track is simply a measure of the fine-scale structure of the ambient medium. This is to be contrasted with the local density determinations provided by the sounder, which, it is estimated, represent a measurement over a scale size of

[1] Centre for Research in Experimental Space Science, York University, Toronto, Ontario, Canada
[2] Communications Research Centre, Ottawa, Ontario, Canada
[3] Center for Space Sciences, University of Texas at Dallas, Richardson, Texas 75082
[4] Goddard Space Flight Center, Greenbelt, Maryland 20771
[5] Herzberg Astrophysical Institute, National Research Council, Ottawa, Ontario Canada
[6] Physics Department, University of Calgary, Calgary, Alberta, Canada

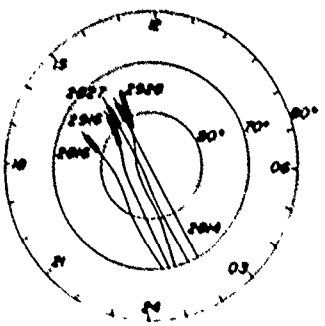

Fig. 1. Invariant polar projection, showing the spacecraft tracks labeled by orbit number, for the orbits used in this study. The regions of cleft precipitation are shown by the thickened traces.

about 1 km and which are obtained alternately at intervals of 100 and 300 km. A further complication is that the existence of sufficiently rapid local variation (which often occurs) precludes the reduction of the RPA current-voltage curves to determine the ambient ion temperature. This lack of continuous (once per spacecraft rotation) ion temperature data should be considered in interpreting temperature differences in the various regions.

The two-dimensional mapping capability for the optical data is not available, since the scanning occurs repeatedly along the spacecraft track. The consequent high redundancy of the data is used here to minimize the delay time between the acquisition of the optical data and the direct measurements made at the spacecraft on the field line connected to the emitting region. This is achieved simply by selecting optical data from the single spin giving the minimum time delay for the center of the cleft region. It was also possible to inspect adjacent spins to confirm that temporal variations were not significant. The individual optical data points are obtained at 45 Hz for the auroral scanning photometer (ASP) and 30 Hz for the red line photometer (RLP), and though they are converted to equivalent spacecraft time for the plots shown, each is obtained in roughly 1 s of viewing time, so that it is an instantaneous pattern that is presented.

DATA PRESENTATION

Figure 1 is a polar plot in invariant coordinates, showing the paths of the Isis 2 spacecraft for the passes used in this study. The extent of the cleft precipitation for each orbit is shown by the thickened portion along each path. The magnetic times for the cleft crossings vary within a range of a few hours following local magnetic noon.

Orbit 2816

Figure 2 shows a composite of the results obtained from orbit 2816 on November 9, 1971, at 0947 UT. The top frame shows the soft particle spectrometer (SPS) electron data in the format described by *Heikkila and Winningham* [1971]. The magnetic local time and invariant latitude are shown along the top of this frame, and the invariant latitude is hand lettered below for clarity. The second frame is from the 150-eV electron channel of the energetic particle detector (EPD) experiment. It will be seen later that the cleft electron energies are sometimes sufficiently low to be entirely below the threshold of this detector, comparison of this channel with the SPS data thus gives a very sensitive indication of energy spectral changes. In this particular orbit the EPD channel has four flux peaks. The most equatorward one near 76.3° invariant is the broadest and is at the poleward limit of a keV flux continuum that starts at 74.6°. The SPS shows its maximum energy flux centered at 0.7 keV in this feature. The three more poleward peaks extending to 78° are narrower and more discrete, and the SPS shows that their average energy softens toward 0.2 keV with increasing latitude. The keV flux may be characteristic of 16.5 hours magnetic local time, which is rather far into the afternoon to be classified as a cleft pass. No protons were observed, which is also characteristic of the late afternoon sector. The other orbits to be shown will be presented in order of increasing proximity to local magnetic noon.

The next frame, labeled SDR (sounder), shows the local electron density obtained at 1400 km by the topside sounder. It is sharply peaked in its latitude distribution, not at the center of the cleft precipitation but at its poleward edge, 1° of latitude away. The density enhancement in the vicinity of the cleft is about a factor of 3. The next lower frame, labeled IMS, contains the ion mass spectrometer local ion densities, showing a marked O^+ response over the entire region of energetic electron energy input. Since the IMS has been intercalibrated against the SDR, the differences between the two are unexpected. Closer examination of individual data points shows that the single high point in the SDR local density was taken close to an EPD (and SPS) flux peak, while the closest IMS point was in the trough between two electron flux peaks. This point will be discussed later. The O^+ density drops sharply at the poleward cleft boundary, beyond which He^+ becomes the dominant ion, with several times the density of H^+. Throughout this region (the polar cap) the O^+ is virtually absent, and below the threshold of the IMS, a few ions per cubic centimeter. The thickened base line of this frame indicates the region where polar wind flows of H^+ ions are observed by the IMS to be greater than 1 km/s. The flow is seen to occur throughout the O^+ enhancement region. The next lower frame (SDR) shows the electron densities measured at the F region peak and indicates variations of the order of 50% in the region of the cleft energy source.

The bottom frame contains the optical emission rates for the 6300- and 5577-Å lines, obtained from a single spin as described earlier. Multiple peaks are evident, superimposed on a background that rises in the equatorward direction in response to local twilight. The most equatorward peak is strongest, at 76.3° invariant. In it the 5577-Å intensity exceeds that at 6300 Å, and this corresponds well to the equatorward flux peak with average energy near 0.7 keV. The adjacent poleward peak has roughly equal 5577-Å and 6300-Å intensities and seems to correspond to the narrow pair of electron flux peaks at 77.0° invariant, which are unresolved in this viewing geometry. A weak peak, still further poleward at 77.8° invariant, corresponds to the very narrow 0.2-keV flux seen there. These multiple features appear to be auroral arcs, which are characteristic of the late afternoon sector [*Shepherd et al.*, 1976].

Orbit 2827

This pass occurred November 10, 1971, at 0638 UT and a local magnetic time of 14.5 hours, the composite data are shown in Figure 3. As in orbit 2816, there is a lower-latitude keV flux continuum from 75.0° to 78.2° invariant, while the discrete features extend as far as 79.6° (Note the SPS data absence due to command sequencing near 77.4°.) The more poleward region of precipitation is characterized by narrow discrete fluxes having average energies of $\gtrsim$0.2 keV, the two most poleward features having energies below the EPD thresh-

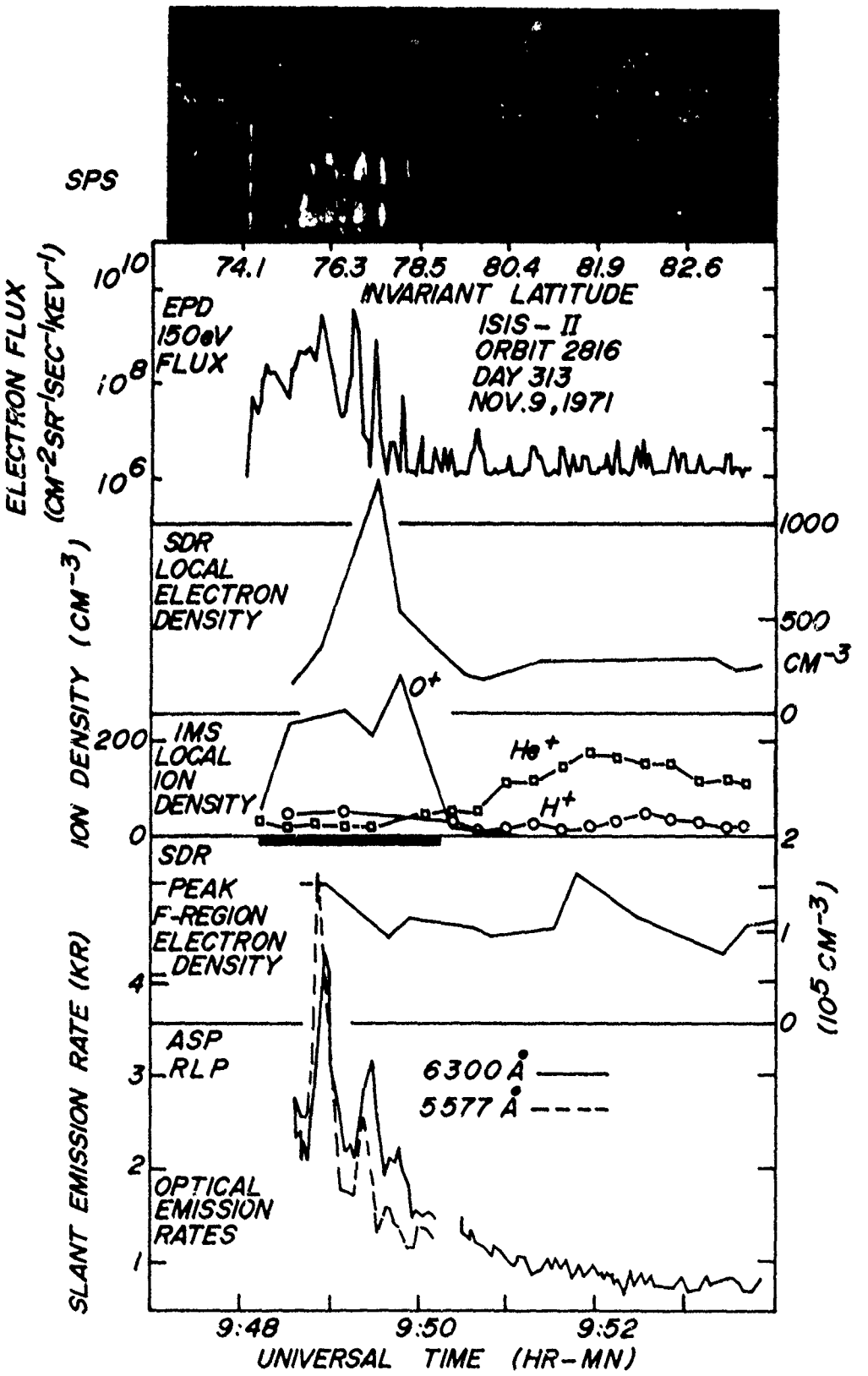

Fig. 2 Collected Isis 2 data for orbit 2816, November 9, 1971, at 16.5 hours MLT. The universal time shown at the bottom is the time at which the spacecraft crossed the field line to which all data relate, and the spacecraft invariant latitude is shown at the top. The top frame is an SPS electron spectrogram where the vertical direction is energy and the trace density indicates flux. The vertical bars extending over the whole energy range are sun pulses in the instrument. Successive frames downward show data from the EPD 150-eV channel, SDR local electron density, IMS, ion composition and regions of H^+ flow being indicated by the thick base line, SDR-measured F region peak density, RLP 6300-Å measurements, and ASP 5577-Å data.

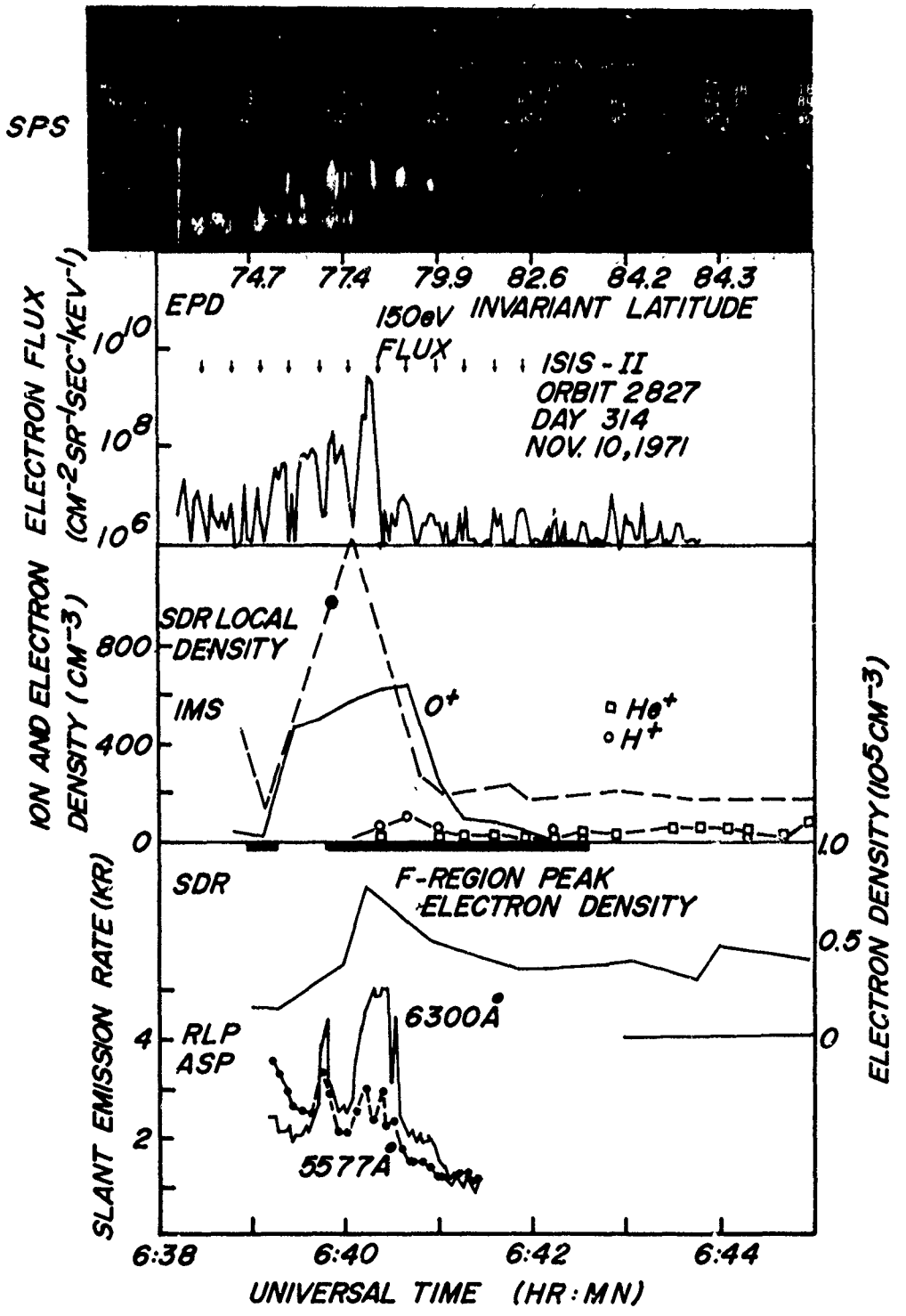

Fig. 3. Collected Isis 2 data for orbit 2827, November 10, 1971, at 14.5 hours MLT. The sequence of short arrows indicates the times at which the EPD and SPS were looking down the field line. The caption of Figure 2 applies to this figure also.

old. Both the SPS and the EPD fluxes show periodic minima at about 18-s intervals due to scanning through the atmospheric loss cone; the times of downward viewing are shown by the series of short vertical arrows in the figure. The small EPD flux peaks poleward of 78.2° invariant arise from sunlight, and these 'sun pulses' are manifested in the SPS spectrogram as weak vertical bars. A weak proton flux (not shown) ended at 0640:45, at about the same time as the termination of the electron flux.

Again in this pass the SDR local density has an isolated peak density about twice that shown by the IMS for which the O^+ density is again relatively uniform across the precipitation region. The solid circle (the only point not visible as a discontinuity in slope in the straight line connection of discrete points used here) on the dashed curve just prior to the SDR peak is a second consistent high-density point, suggesting that the explanation offered before of a chance high flux coincidence may be inadequate. In a stream of 5×10^9 electrons cm^{-2} s^{-1} of 100-eV energy the number density is about 10^6 el cm^{-3}. This is only 1 order of magnitude below the ambient densities, and the ionospheric response to this charge input may involve electric fields and waves that affect the electron and ion measurements differently. In addition, the SDR samples a 1-km region around the spacecraft and is therefore much more likely than the IMS to be within sampling range of one of the discrete flux regions.

As in the previous example, the O^+ drops sharply at the poleward boundary, with a slight tail extending to 83.0° invariant in this case, beyond which He^+ becomes the dominant ion. The H^+ flow shows a slight break near its equatorward edge. The *F* region peak density has a significant response to the largest EPD peak, which also coincides with the peaking of a broad optical emission having a red/green ratio of about 4. There is a narrow equatorward flux peak with a red/green ratio of 2.5 that coincides with the 0.7-keV flux peak at 77.1° invariant. The 6300-Å emission is the stronger of the two at all latitudes, and this reddening may be attributed to closer proximity to magnetic noon.

Orbit 2814

The data from this orbit, shown in Figure 4, were taken two orbits prior to that of Figure 2, November 9, 1971, at 0600 UT with a magnetic local time of 14.1 hours. There is a keV flux continuum present from 76.0° to 79.0° invariant, with intense flux bursts at 79.4°, 78.9°, and 79.6° invariant extending in energy from 0.1 to 1 keV. Equatorward of these bursts there are several others centered near 0.1 keV and one very narrow intense flux at 77.6° having energies from 5 to 100 eV, evident only in the SPS spectrogram. A weak proton flux ended at 0603:00 UT. Both the SDR density and the IMS O^+ density show a double-peaked response to these distinct regions of ≃1-keV precipitation (there is an SPS data absence near the equatorward peak), and the absolute density values agree as well. This shows that the differences between the electron and ion densities seen in other orbits do not arise from a consistent error such as in calibration. It is also appropriate to note here that these apparent differences between electron and ion densities do not occur at lower latitudes; they are a polar cap phenomenon

For this orbit, RPA densities and temperatures were also available and are shown. Apart from the region near 79.0° these densities generally agree with the SDR densities, but the temperature results are surprising at first sight, showing values below 2000°K in the region of energy input and nearly 5000°K in a narrow region just at the poleward cleft boundary. But a numerical model of topside dynamics (J. H. Whitteker, unpublished manuscript, 1976) accounts for this behavior as adiabatic heating of the ions when the poleward convecting topside ionosphere collapses as a result of the drop in electron temperature when the convecting plasma leaves the region of precipitation. Further in the polar cap, high values of about 3500°K are observed. The RPA also indicated the presence of wavelike plasma structures from 0601:20 to 0603:11 UT (the region of precipitation) and again at 0606:35 (in the polar cap region of high ion temperature). In the IMS data, He^+ again becomes dominant poleward of the cleft, although O^+ reappears in the ion temperature enhancement at 0606. Again, the H^+ flows follow the O^+ enhancement region.

The *F* region peak densities show a curious weak depression in the cleft region. There are again two well-defined optical peaks, the equatorward one being more intense, at 2.5 kR of 6300-Å emission. Unlike the two preceding orbits, it has the higher optical red/green ratio and appears to correspond to the very narrow intense SPS feature at 77.6° mentioned earlier, which occurred when the SPS was sampling pitch angles, θ_p, in the downcoming (precipitating) loss cone. The poleward feature appears to correspond to the unresolved features at 78.2° and 78.7°.

Orbit 2928

These data, obtained November 18, 1971, at 0600 UT and shown in Figure 5, are dramatically different from the preceding examples. They are taken closer to magnetic noon, at 13.8 hours, which may be a partial explanation. The flux measured by the SPS is less structured and spreads over a broader region, while the absence of any significant EPD response shows that the energies involved are much lower. The weak proton flux terminates at 0602:30, at the same location as the electrons. There is a rising base line level in the 5-eV threshold level that makes the electron energy appear higher than it actually is in the poleward region. The SDR local density peaks at the poleward boundary, with much larger densities present, about 4000 cm^{-3} compared to typically 800 cm^{-3} in the previous examples. The precipitating energy flux does not have instantaneous values exceeding those of previous orbits, about 1 erg cm^{-2} sr^{-1} s^{-1}. The O^+ response is similar to the SDR response, rising gradually through the cleft region and dropping abruptly at the poleward boundary, well beyond the region of maximum energy input. The He^+ and H^+ densities (multiplied by 10 on the plot) are not much affected by this substantial increase in O^+, except that H^+ now exceeds He^+, and the light ions are not dominant in the polar cap. The H^+ flows are found throughout the region with the maximum velocities at the poleward side, where the O^+ concentration is lowest. The *F* region densities may be affected by the energy input, though one cannot be certain. The optical responses are dramatic, with a feeble 5577-Å response in contrast with a 6300-Å emission rate of about 4 kR above background. One can still imagine a double-peaked structure with no green component at all in the poleward peak and only a weak one in the equatorward features. The region of bright 6300-Å emission has sharply defined boundaries, at 74.7° and 79.0° invariant, with an extension into the polar cap not seen on earlier passes. The red/green ratio measured above background appears to be about 8. All of this is consistent with a dramatic softening of the total energy input, producing a large increase in 6300-Å emission and much enhanced O^+ densities at the spacecraft

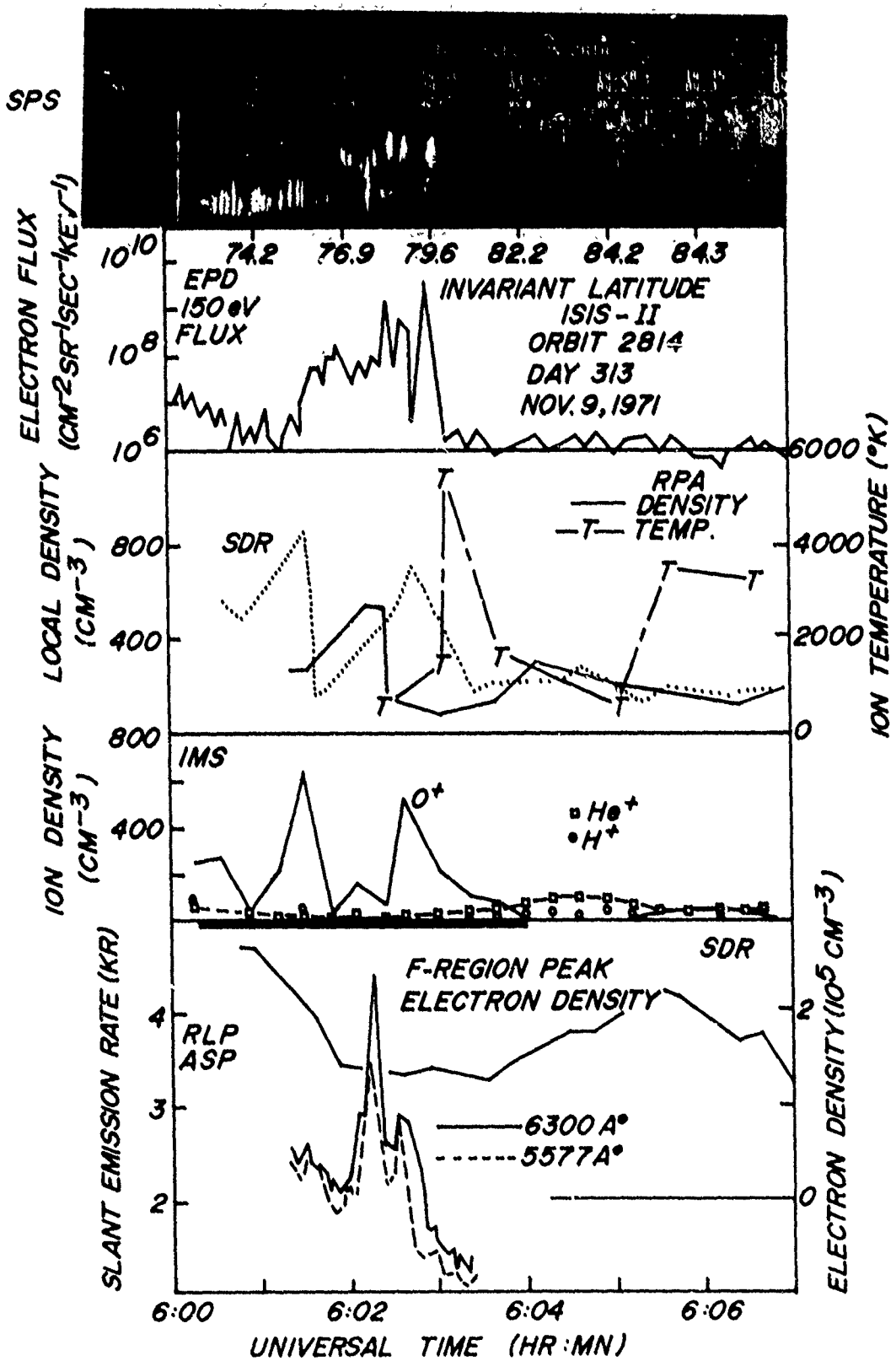

Fig. 4. Collected Isis 2 data for orbit 2814, November 9, 1971, at 14 hours MLT. The caption of Figure 2 applies, except that a frame of RPA data is added. The symbol *T* connected by a broken line indicates ion temperature, the solid curve indicates RPA total ion density, which is compared with the SDR local electron density

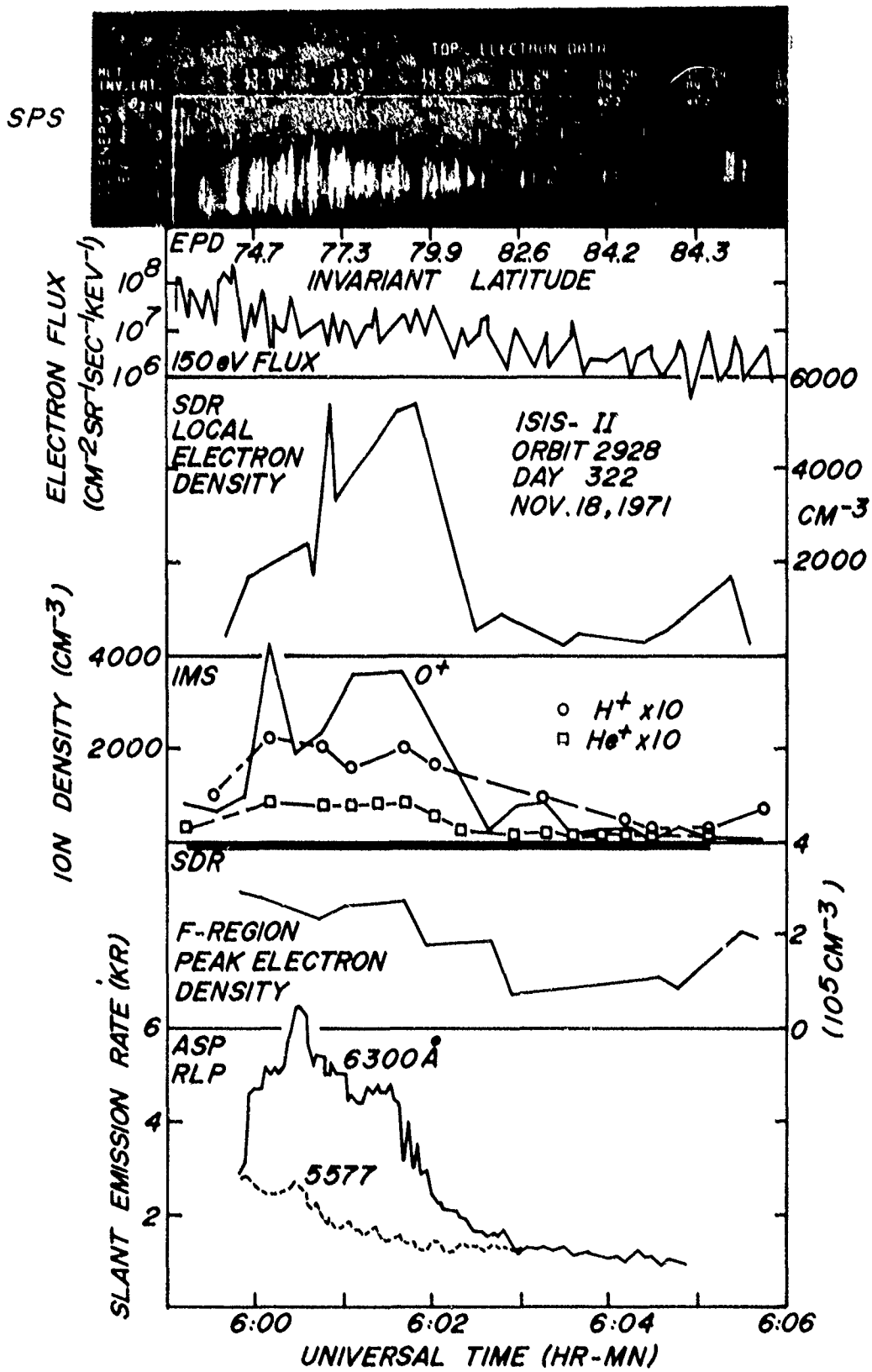

Fig. 5. Collected Isis 2 data for orbit 2928, November 18, 1971, at 13.8 hours MLT. The caption of Figure 2 applies; further data for this orbit are shown in Figure 6.

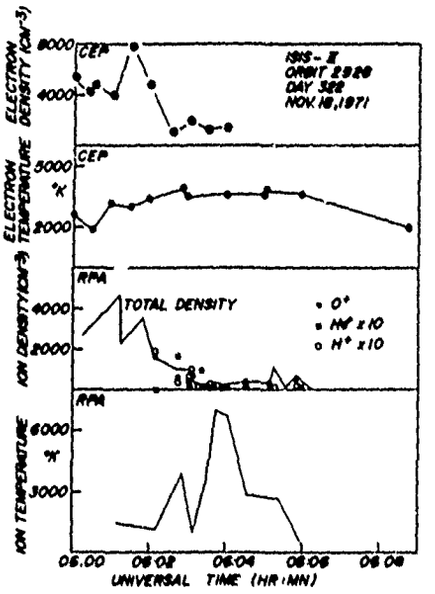

Fig. 6. Further Isis 2 data from orbit 2928 (see Figure 5 also) containing CEP measurements of electron density and temperature, compared with RPA ion densities and temperatures.

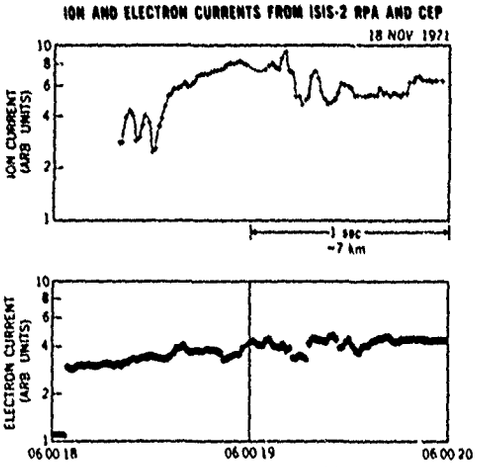

Fig. 7. Ion and electron currents measured by the Isis 2 RPA and CEP for 2 s at 0600:18 UT on November 18, 1971, showing the small-scale structure present in the plasma. The current to the CEP (primarily electrons) is measured with the sweep voltage held constant at +4 V with respect to the spacecraft. Current to the RPA (primarily ions) is measured with the retarding voltage sweeping at a rate very slow compared to the scale times of the structure detected.

The electron densities at the spacecraft are sufficiently high to permit electron temperature values to be obtained with the cylindrical electrostatic probe (CEP). This was not possible in the orbits previously shown because the spacecraft was in sunlight (producing photoelectrons) and the ionosphere was dark, yielding low densities. The results are shown in Figure 6, along with those obtained from the RPA. Both the RPA and the CEP show a sharp response in plasma density about at 0601 UT, at the center of the region of energy input. The RPA densities are in accord with those obtained from the SDR and the IMS, and apart from one high point at 0601:40, with the CEP densities as well. The SDR electron density peaks at the same location as does the CEP-measured electron density, though at a lower absolute value. The electron temperature shows little variation poleward of the cleft, at about 3500°K, while the ion temperature shows a pronounced rise, to 7000°K, poleward of the cleft, as seen before in orbit 2814 and explained as adiabatic collapse heating.

Fine structure in the plasma density is present sporadically during this pass. An example of the wavelike structure is shown in Figure 7, which shows 2 s of data obtained simultaneously by the CEP and by the RPA. The lower curve is the current to the cylindrical probe when it was held at a constant +4-V potential with respect to the spacecraft. The upper curve is the ion current observation from the RPA when the sweep voltage change was not causing a significant change in the magnitude of the current. Some of the fine-scale structure is present in the same phase relationship in the two signals. This implies a modulation of the local plasma density (both ions and electrons) in both space and time. Note that some of the fine structure in the electron data has extremely sharp boundaries, appearing as discontinuities in the current, whereas the corresponding boundaries in the ion data are often not so sharp. The RPA instrument time response is adequate to follow the current changes as shown in the electron data. Thus the differences are real and presumably arise from the ionospheric response to the precipitating electrons, as conjectured for the apparent differences in SDR and IMS densities. The fractional changes in density for the two species are noticeably different, the fluctuations in the ion current being larger than the corresponding fluctuation in the electron current. This may be a further indication that the ion plasma was the driven, or excited, component receiving its stimulus from the energetic electrons present in the region. A more complete survey of the small-scale structures in the cleft region will be the subject of a separate study.

Orbit 2916

This orbit, at 15.0 hours magnetic time, is shown here because it has characteristics similar to those of orbit 2928, even though its magnetic time is similar to the times of the first three orbits presented. It was acquired on November 17, 1971, at 0717 UT, and the data are shown in Figure 8. The SPS shows a fairly compact region with energies below 300 eV and with little prominent structure. There is a weak EPD response to ~79° invariant and only sun pulses thereafter. The weak proton flux ends at 0718:20 UT somewhat before the electron flux disappears. The SDR local density again is peaked near the poleward boundary and trails off far into the polar cap, to 83.3° invariant. The O^+ peak from the IMS is also sharply peaked with a density of about half that of the sounder. In a fashion not inconsistent with the SDR densities the O^+ density shows a smaller but significant (300 ions cm^{-3}) level up to 83.3° invariant as well, substantially poleward of the poleward boundary of precipitation. The characteristic rise of He^+ does not occur until this point is reached. The H^+ flows are found again throughout the region of O^+ enhancement. The *F* region density shows a pronounced cleft response in the same location as the local electron density peak. The 6300-Å optical emission shows four distinct regions that can be identified with SPS flux regions, the equatorward component at 2.5 kR being the most intense. The spike of 5577-Å emission cannot be associated with a flux feature and appears to be transient.

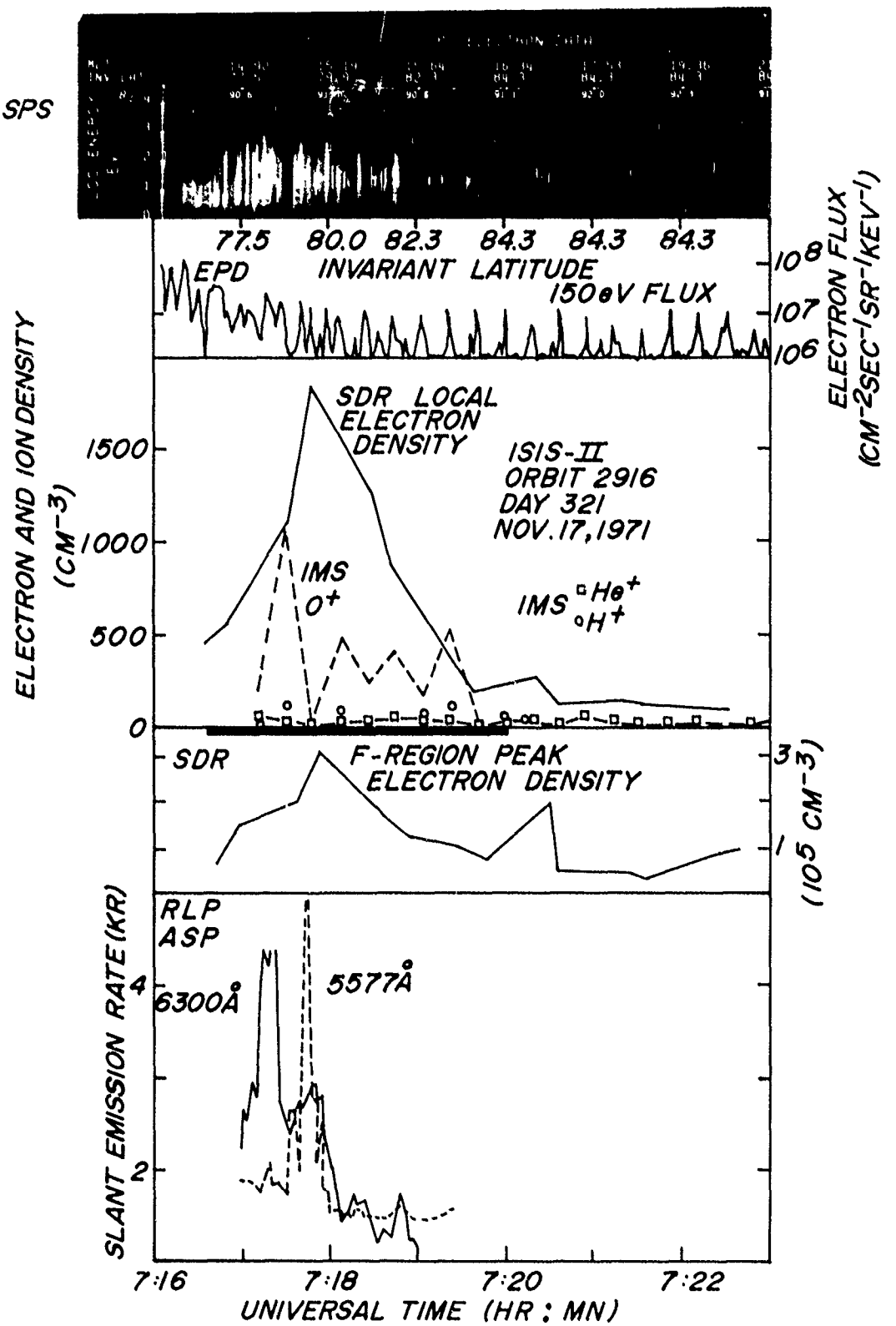

Fig. 8 Collected Isis 2 data for orbit 2916, November 17, 1971, at 15.0 hours MLT. The caption of Figure 2 is applicable

DISCUSSION

All of the data shown here were obtained by relatively low levels of geophysical activity, from orbit 2916 (Kp = 0o) to 2928 (Kp = 2−), the other three having Kp values of 1−. The AE values order the orbits differently, from 2916 (AE = 20) to 2816 (AE = 79). However, for orbit 2928 (AE = 45) the AE value was 261 some 2 hours earlier, so some of the distinct characteristics of the pass may result from earlier substorm activity.

From the interplanetary magnetic field (IMF) data provided by *King* [1975] and *Fairfield and Ness* [1974] one finds that the interplanetary field turned from toward to away at 14 hours on November 8 and has remained so until late on November 10, which includes the first three orbits presented, 2816, 2827, and 2814. The following towards sector continued until November 22, which includes the last two orbits, 2928 and 2916. There are some data gaps in the intervals described, so the boundary crossings identified do not meet the criteria of *Wilcox et al.* [1975], but provided no rapid changes occurred, the identifications given here should be valid.

Thus the pronounced differences between the characteristics of the two groups of orbits and the consistency within each group suggest that the IMF influences the pattern of the cleft precipitation and the behavior of the cleft ionosphere. For the toward orbits the electron precipitation is of lower energy, exhibits less latitudinal structure extended over a broader region, and is located at a higher invariant latitude, extending poleward of 80°. (For orbit 2915, not described here, the flux extends to 83° invariant.) The data analyzed here are rather limited for such generalized conclusions, but *Titheridge* [1976] analyzed a very large body of topside ionosphere data and concluded that during toward sectors the cleft response is located at higher latitudes and is broader than during away sectors. For the away orbits described here the electron precipitation is confined to a narrow latitude region, is highly structured, and contains distinct regions of keV fluxes and 0.2-keV electrons. In two of the three cases the 0.2-keV precipitation was seen as narrow discrete flux regions on the poleward side of the keV precipitation, but in the other case a single intense 5- to 100-eV flux region appeared near the center of the keV flux region.

We consider now the differences in ionospheric behavior. For the away orbits the O^+ density measured at 1400 km closely follows the electron precipitation, showing its rapid upward diffusion above the region of production; it is also a region of strong upward H^+ polar wind flow. It may be that these cleft-associated flows are related to those observed in the plasma mantle [*Rosenbauer et al.*, 1975]. The O^+ disappears rapidly at the poleward boundary, implying the absence of poleward convection, or more likely, convective flow parallel to the cleft, the existence of which has been shown by *Heelis et al.* [1976] and by *Jeffries et al.* [1975]. In orbit 2814 the rise in ion temperature immediately at the poleward boundary supports this idea of minimal convection perpendicular to the oval. The appearance of He^+ as the dominant ion in the polar cap is consistent with the lack of polar wind flow observed there for these orbits. This may be characteristic of the winter polar cap. For the toward orbits the O^+ is clearly seen well poleward of the region of precipitation, consistent with a strong convective flow perpendicular to the oval. The rise in ion temperature also occurs considerably poleward of the precipitation region.

Another possibility is that the convective effects described are determined solely by proximity to local magnetic noon. This does not appear to be the case, because the times of 13.8 and 15.0 hours for the toward orbits overlap those of the away orbits at 14.1, 14.5, and 16.5 hours. On the other hand, if the effect of the IMF were to shift the convective pattern in local time, then a shift of about 1 hour would remove the overlap. This is consistent with the behavior described by *Heppner* [1972], where a dusk-to-dawn IMF (equivalent to toward) shifted the convective flow toward the afternoon side in the northern hemisphere. *Heelis et al.* [1976] have extended Heppner's one-dimensional dawn-dusk measurements by obtaining from the AE-C satellite two-dimensional ion flows near the cleft. They also find a tendency for the flow within the polar cap to be preferentially directed to either the morning side or the evening side in the five cases that they examined.

CONCLUSIONS

1. The electron energy spectrum varies dramatically over the latitude range of the cleft, with distinct components near 0.7 keV and 0.2 keV. The 0.7-keV components tend to be on the equatorward side, with narrow discrete 0.2-keV flux regions at the poleward boundary, but the 0.2-keV discrete regions can also be contained within the region of more energetic precipitation. The above pattern was observed during an IMF away sector, in which the region of cleft precipitation was also more confined in latitude and was below 80° invariant. During a toward sector the precipitating electrons were all close to 0.1 keV and formed a less structured pattern that was broader in latitude and extended poleward of 80° invariant.

2. The proton input is not a significant energy source for the ionospheric characteristics described here.

3. At 1400 km the O^+ density is enhanced to a few hundred ions per cubic centimeter over the region of cleft precipitation, and for an away sector it falls sharply at the poleward boundary. For a toward sector the O^+ was observed inside the polar cap, well beyond the region of electron energy input. These differences are attributed to convective flows parallel to and perpendicular to the auroral oval.

4. For some data points the electron densities measured by the topside sounder are a factor of 2 or 3 larger than the O^+ densities measured nearby. This may be due to the pronounced structure in the electron fluxes and the consequent ionospheric response to the charge input combined with the larger sampling volume of the sounder. In the one case of very high ionospheric densities the electron and ion densities were in agreement. The same ionospheric response may be responsible for the plasma waves detected by the RPA and CEP.

5. Throughout the region of cleft O^+ enhancement, polar wind flows of H^+ exceeding 1 km/s are observed. These terminate at the poleward cleft boundary, where the O^+ vanishes and He^+ becomes the dominant polar cap ion at 1400 km, about three times more abundant than H^+.

6. The ion temperature rises at the poleward cleft boundary when the perpendicular convective flow is weak and rises well beyond the boundary when the flow is rapid.

7. The 5577-Å and 6300-Å emissions are good indicators of the keV and eV fluxes, respectively. Frequently, a characteristic double hump structure is evident, the poleward one corresponding to the 0.2-keV electrons and the equatorward one having a red/green ratio nearer unity. But one optical peak can correspond to more than one electron flux peak, and additional weaker optical peaks are also observed. For the toward sector, with strong 0.1-keV fluxes, the red/green ratio reached a value of 8.

8. The F region peak density showed little response to the

cleft energy source, but in some cases a factor of 2 enhancement was discernible.

Acknowledgments. The authors are grateful to D. Boulding, spacecraft controller at the Communications Research Centre, Ottawa, and C. Freeman, data processing engineer at the Goddard Space Flight Center, for their part in acquiring and processing the data used here. This work is sponsored jointly by the Canadian Department of Communications and the National Aeronautics and Space Administration; direct support of some investigations is provided by the National Research Council of Canada. The University of Texas at Dallas portion of this work was supported by NASA grants NSG 5085 and 5087 and Air Force Geophysics Laboratory contract F19628-76-C-005.

The Editor thanks J. E. Titheridge for his assistance in evaluating this paper.

REFERENCES

Ahmed, M., and R. C. Sagalyn, Thermal positive ions in the dayside polar cusp measured on the Isis-1 satellite, *Space Res., 13*, 541, 1973.

Brace, L. H., and N. J. Miller, Ionospheric heating in the cleft (abstract), *Eos Trans. AGU, 55*, 69, 1974.

Dyson, P. L., and J. D. Winningham, Topside ionospheric spread *F* and particle precipitation in the dayside magnetospheric clefts, *J. Geophys. Res., 79*, 5219, 1974.

Fairfield, D. H., and N. F. Ness, Interplanetary sector structure: 1970–1972, *J. Geophys. Res., 79*, 5089, 1974.

Feldstein, Y. I., Some problems concerning the morphology of aurora and magnetic disturbances at high latitudes, *Geomagn. Aeron., 3*, 183, 1963.

Frank, L. A., and K. L. Ackerson, Observations of charged particle precipitation into the auroral zone, *J. Geophys. Res., 76*, 3612, 1971.

Heelis, R. A., W. B. Hanson, and J. L. Burch, Ion convection velocity reversals in the dayside cleft, *J. Geophys. Res., 81*, 3803, 1976.

Heikkila, W. J., The morphology of auroral particle precipitation, *Space Res., 12*, 1343, 1972.

Heikkila, W. J., and D. J. Winningham, Penetration of magnetosheath plasma to low altitudes through the dayside magnetospheric cusps, *J. Geophys. Res., 76*, 883, 1971.

Heppner, J. P., Polar cap electric field distributions related to the interplanetary magnetic field direction, *J. Geophys. Res., 77*, 4877, 1972.

Jeffries, R. A., W. H. Roach, E. W. Hones, E. M. Wescott, H. C. Stenbaek-Nielsen, T. N. Davis, and J. D. Winningham, Two barium plasma injections into the northern magnetospheric cleft, *Geophys. Res. Lett., 2*, 285, 1975.

King, J. H., Interplanetary magnetic field data 1963–74, *Rep. UAG-46*, World Data Center A for Solar-Terr. Phys., Boulder, Colo., 1975.

Knudsen, W. C., Magnetospheric convection and the high-latitude F_2 ionosphere, *J. Geophys. Res., 79*, 1046, 1974.

Knudsen, W. C., P. M. Banks, J. D. Winningham, and D. M. Klumpar, Theoretical modelling of the convecting F_2 ionosphere at high latitudes, paper presented at Sixteenth IUGG General Assembly, Grenoble, France, 1975.

Nishida, A., Average structure and storm time change of the polar topside ionosphere at sunspot minimum, *J. Geophys. Res., 72*, 6051, 1967.

Rosenbauer, H., H. Grünwaldt, M. D. Montgomery, G. Paschmann, and N. Sckopke, Heos 2 plasma observations in the distant polar magnetosphere: The plasma mantle, *J. Geophys. Res., 80*, 2723, 1975.

Sato, T., and L. Colin, Morphology of electron concentration at a height of 1000 km at polar latitudes, *J. Geophys. Res., 74*, 2193, 1969.

Shepherd, G. G., C. D. Anger, L. H. Brace, J. R. Burrows, W. J. Heikkila, J. Hoffman, E. J. Maier, and J. H. Whitteker, An observation of polar aurora and airglow from the Isis-2 spacecraft, *Planet. Space Sci., 21*, 819, 1973.

Shepherd, G. G., F. W. Thirkettle, and C. D. Anger, A topside optical view of the dayside cleft region, *Planet. Space Sci.*, in press, 1976.

Titheridge, J. E., Ionospheric heating beneath the magnetospheric cleft, *J. Geophys. Res., 81*, 3221, 1976.

Vasyliunas, V. M., Magnetospheric cleft symposium, *Eos Trans. AGU, 55*, 60, 1974.

Whalen, J. A., and C. P. Pike, *F* layer and 6300-Å measurements in the day sector of the auroral oval, *J. Geophys. Res., 78*, 3848, 1973.

Whitteker, J. H., The magnetospheric cleft—Ionospheric effects, *J. Geophys. Res., 81*, 1279, 1976.

Wilcox, J. M., L. Svalgaard, and P. C. Hedgecock, Comparison of inferred and observed interplanetary magnetic field polarities, 1970–1972, *J. Geophys. Res., 80*, 3685, 1975.

(Received May 27, 1976;
accepted July 28, 1976.)

VOL. 82, NO. 13 JOURNAL OF GEOPHYSICAL RESEARCH MAY 1, 1977

ROCKET-BORNE MEASUREMENTS OF THE DAYSIDE CLEFT PLASMA: THE TORDO EXPERIMENTS

J. D. Winningham,[1] T. W. Speiser,[2] E. W. Hones, Jr.,[3] R. A. Jeffries,[3] W. H. Roach,[3] D. S. Evans,[4] and H. C. Stenbaek-Nielsen[5]

Abstract. Results are presented from low-energy plasma analyzers (12 eV to 12 keV) carried on two rockets launched into the dayside cleft during January 1975. We conclude that (1) atmospheric interaction becomes important for <1-keV electrons at approximately 250 km, (2) characteristics of particles in 'inverted V's' observed in the afternoon cleft are consistent with their interpretation as being due to parallel electric field acceleration from a constant source population, and (3) magnetospheric 'energetic' (>2 keV) electrons intermingle with 'magnetosheathlike' plasma in the cleft.

Introduction

The past two years have marked a dramatic upsurge in sounding rocket launches into the low-altitude cleft region. Prior to 1974 only four instrumented rocket payloads [Maynard and Johnstone, 1974; Ledley and Farthing, 1974] and one thermite barium release [Mikkelsen and Jorgensen, 1974] had been launched into or in the vicinity of the cleft. The instrumented payloads were launched from Hall Beach, Northwest Territories (Λ= 79.7°), on March 15, 18, 19, and 22, 1971, and the barium release from Sondre Stromfjord, Greenland (Λ= 74.5°), on December 10, 1972.

In contrast, from June 1974 to November 1975, 15 rockets were fired in the cleft region from launch sites at Cape Parry, Northwest Territories, Canada, and Sondre Stromfjord, Greenland. Ungstrup et al. [1975a] reported results from two rockets launched from Greenland in July 1974; these payloads were more comprehensive than their predecessors as they included particle spectrometers, dc electric and magnetic probes, and thermal plasma sensors. During December 1974 through January 1975, two major campaigns, totaling 11 rockets, were executed in Canada (Cape Parry, Northwest Territories, Λ = 74.5°) and Greenland (Sondre Stromfjord). These launchings included extensive plasma and field instrumentation, optical sensors, shaped charge barium injections, and lithium releases [Haerendel, 1975; Torbet et al., 1975; Ungstrup et al., 1975b; Temerin et al., 1975; Shepherd et al., 1975, 1976; Winningham et al., 1975a; Wescott et al., 1975; Stenbaek-Nielsen et al., 1975; Jeffries et al., 1975; Torbet and Carlson, 1975].

Another series consisting of two rocket launches was completed during November 1975 at Cape Parry. These vehicles included particle detectors, barium lined shaped charges, plasma drift detectors, and energetic particle sensors.

In this paper we will present results from the soft particle spectrometer (SPS) [Heikkila et al., 1970] instruments carried as an environmental monitor on Tordo Uno and Dos. The Tordo Uno and Dos programs were designed by the Los Alamos Scientific Laboratory and the University of Alaska Geophysical Institute, and the rockets were launched from Cape Parry by the Sandia Laboratories on January 6 and 11, 1975, 2349:02 and 0025:02 UT, respectively.

Instrumentation

The primary objective of the Tordo campaign was the injection of barium ions into the low-altitude cleft (initial results from the shaped charge barium releases are described in the paper by Jeffries et al. [1975]). In addition to the shaped charge, a low-energy (12 eV to 12 keV) plasma analyzer (SPS) similar to the one on the Isis 1 and 2 satellites [Heikkila et al., 1970] was carried as a monitor to locate the detonation point relative to the cleft. For proper barium injection payloads were actively stabilized in relation to the local magnetic field, the result being a unique SPS pitch angle of 45°. The SPS concurrently measured the differential energy spectrum of both electrons and positive ions in 15 logarithmically spaced steps from 12 eV to 12 keV every 3.2 s. In addition, there was a sixteenth step at zero energy to monitor the background count rate. Each energy level was held for 0.2 s, and the count rate was sampled eight times during this period. Multiple sampling was employed in order to evaluate possible temporal/spatial aliasing occurring during the 3.2 s required to complete a stepping sequence.

The energy band pass of the SPS was set at 32% (being a divergent electrostatic lens, the SPS resolution is determined by a field stop), and the geometric factor (not including the energy band pass) was 8.6×10^{-4} cm^2 sr. In order to match the energy band passes at full width at half maximum (FWHM), 22 logarithmically

[1]Center for Space Sciences, University of Texas at Dallas, Richardson, Texas 75080.
[2]Department of Astro-Geophysics and Cooperative Institute for Research in Environmental Sciences, University of Colorado, Boulder, Colorado 80302.
[3]Los Alamos Scientific Laboratory, Los Alamos, New Mexico 87545.
[4]Space Environment Laboratory, National Oceanic and Atmospheric Administration, Boulder, Colorado 80302.
[5]Geophysical Institute, University of Alaska, Fairbanks, Alaska 99701.

Paper number 6A0955.

spaced steps would be required instead of the 15 used on these flights.

The energy-analyzed particles were detected by 14-stage RCA discrete dynode electron multipliers [Bunting, et al., 1972], and the subsequent pulses were amplified by high gain bandwidth amplifiers [Smith, 1972]. Postacceleration was employed to increase the detection efficiency of the multipliers at low energies. The pulse train from each amplifier was $\log_2$ compressed and stored for subsequent telemetry to the ground.

Magnetic Conditions

Tordo Uno was launched on January 6, 1975, at 2349:02 UT (approximately 1330 magnetic local time). The Kp value for the 3-hour period including the flight was 6+ and for the following period was 6-. Figure 1a gives AU and AL for the 6-hour period bracketing the Tordo Uno flight. It should be noted that the AE index shown is based on the standard 11 auroral zone stations plus data from an additional 8 stations in Greenland (courtesy of T. S. Jorgensen) and Scandanavia (courtesy of R. S. Pellinen). Inspection of Figure 1a indicates that the magnetosphere was in an extreme state of agitation during this 6-hour period. During the flight, AE was as large as 750γ. Solar wind magnetic field data were not available for this period.

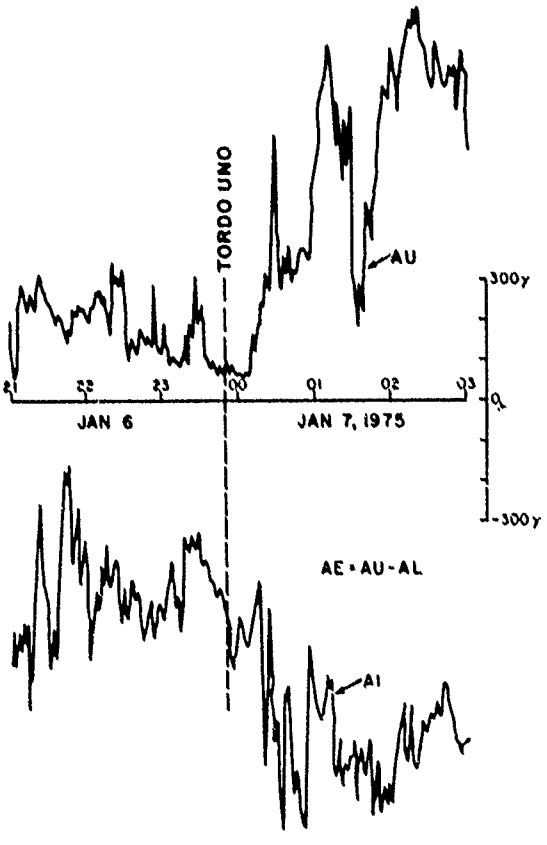

Fig. 1a. AU and AL indices for January 6, 1975. The auroral index is constructed of the standard 11 auroral zone stations plus an additional 8 stations on the nightside in Greenland and Scandanavia.

Tordo Dos was launched on January 11, 1975, at 0025:02 UT (approximately 1400 magnetic local time). The two days encompassing the Tordo Dos flight were relatively quiet; January 10 was a Q day and January 11 was a QQ day. The Kp value for the last 3-hours of January 10 was 1+, and for the first 3-hours of January 11 the Kp value was 2. Examination of Figure 1b shows that magnetic activity was weaker and more representative of classical substorm morphology during the 6-hour period bracketing Tordo Dos than during Tordo Uno. The flight of Tordo Dos occurred during the recovery phase of a small high-latitude substorm (maximum AE = 250γ).

Interplanetary magnetic field data from Imp 8 were available during the Tordo Dos flight and are presented in Figure 2. The IMF went southward at 2216 UT on January 10 and remained southward or close to zero until 0102 on January 11, when it became positive again. A more detailed description of the motion of the cleft and its relation to the IMF during January 10 and 11 can be found in the work of Stiles et al. [1977].

Experimental Results

Tordo Uno. As was mentioned in the previous section, Tordo Uno was launched during a period of prolonged magnetic activity. Examination of the bottomside sounder records from Cape Parry and Sachs Harbour (see Jeffries et al. [1975] and Stiles et al. [1977] for a more complete description) indicated that the equatorward edge of the cleft was south of Cape Parry. The general characteristics of the ionograms indicated precipitation of particles at both Parry and Sachs. As a result of the above considerations a decision was made to launch westward in order to avoid possible exiting the precipitation region northward into the polar cap. Figure 3 shows the projection of the rocket trajectory to 100 km along the earth's magnetic field. From Figure 3 it can be seen that the rocket traveled from approximately 75° to 76.4° invariant latitude.

A synoptic view of the electron data from Tordo Uno is presented in the energy-time spectrogram format in Figure 4. This format is essentially the same as that used for Isis 1 and 2 spectrograms [see Winningham et al., 1975b], with the addition of the altitude profile (solid line) to the energy flux panel and the launch universal date and time at top left. The Z axis (grey scale) of the spectrogram (top panel) has been scaled to give the count per 11.11 ms instead of the actual acumulation period. This was done in order to have the same relationship, between count/accumulation period and grey scale, as that in the Isis 1 and 2 spectrograms.

One of the most striking features observed in the electron spectrogram is the absence of major spatial/temporal structure. This was not the case for Tordo Dos, as will be seen in the following section. Throughout the Tordo Uno flight the count/accumulation period (differential energy flux) maximized at approximately 100-200 eV.

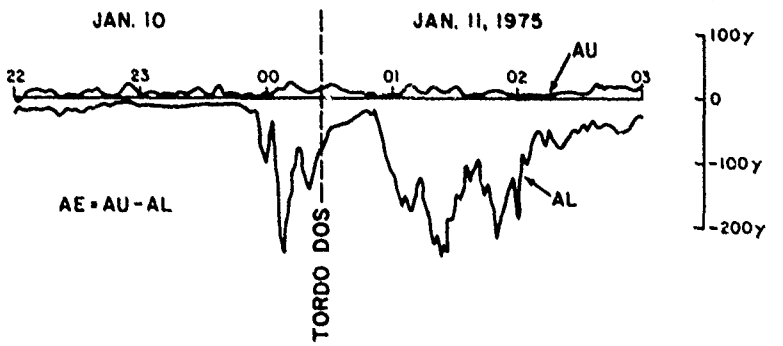

Fig. 1b. Same as Figure 1a but for January 11, 1975.

A 6300-Å scanning photometer belonging to G. G. Shepherd, York University, and an all-sky camera were operated at Sachs Harbour during the Tordo campaign. The photometer indicated a uniform glow of about 300 R, increasing to 1 k R toward the south of Cape Parry during the flight of Tordo Uno. Also the all-sky camera data showed a lack of any discrete aurora.

A more quantitative presentation of the data is given in Figures 5, 6, and 7. Figure 5 presents electron differential flux versus altitude, Figure 6 a representative electron spectrum near apogee, and Figure 7 differential flux versus time. Inspection of Figure 5 and 7 reveals, as did inspection of Figure 4, the absence of dramatic acceleration events (see Figure 8 for comparison).

Throughout the flight the electron spectrum can be divided into two relatively distinct regions, above and below approximately 2 keV. Below 2 keV the spectrum appears to be comprised of a low-energy 'primary' plus 'secondary' population, the primary portion of the spectrum being broader than a Maxwellian curve. For reference, a Maxwellian curve has been included in Figure 6 and has been normalized to the 87-eV experimental point (most of the spectra around apogee exhibit a relative maximum at 87 eV). Also included in Figure 6 are representative near-concurrent plasma mantle and magnetosheath spectra measured by Hawkeye (courtesy of L. A. Frank). The Hawkeye data will be considered again in the discussion section.

The electron spectrum above 2 keV was statistically poor but well above the noise level. Typical counting rates were less than 100/s. The spectrum presented in Figure 6 is an average of 26 spectra (83.2 s) beginning at 2350:36.8 and ending at 2352:00 UT. The deviation of each individual spectrum from the average was minor. This high-energy portion of the electron spectra increased and decreased throughout the flight (see Figure 7a) independently of the lower energy population.

Examination of Figures 5a and 5b reveals a sharp increase of flux with altitude between 180 and 250 km. This altitude related variation was energy dependent, lower energies displaying the largest increase with increasing altitude. Above 250 km (2350:56 UT) the dependence was mainly spatial and/or temporal, not altitudinal. From 2350:56 to 2353:26.4 UT there was a steady increase in the electron flux at energies between 87 and 1021 eV that was energy independent (Figure 7). At 2353:26.4 UT an abrupt increase in magnitude was observed in all energy channels below 1021 eV. The only spectral change occurring was a slight enhancement in the lowest energy channel (12 eV). At 2354:30.4 UT an abrupt decrease was observed, after which time the flux remained at values close to the preincrease level except for three narrow bursts.

At energies below 87 eV an initial flux increase with altitude was also observed. However, at later times the flux profiles were not identical to those at higher energies discussed earlier. The initial slow increase was observed in the 52.8-eV channel but not in the 30.8-, 18.9-, and 11.7-eV channels. The 30.8-eV sample exhibited a relatively flat profile with altitude prior to the increase. At 18.9 and 11.7 eV a relative maximum was observed, the 18.9-eV sample leading the 11.7-eV sample in either space or time (2351:30 and 2352:00 UT, respectively). As in the higher energy channels, an abrupt increase and decrease in flux was observed after 2353:26.4 UT.

Throughout the flight positive ion fluxes were weak. At apogee the peak ion flux occurred in the few hundred electron volt range with flux levels of approximately 10^{3} cm^{-2} sr^{-1} s^{-1}.

Tordo Dos. Ionosonde returns obtained prior to launch indicated that the cleft was poleward of Cape Parry and close to, but poleward of, Sachs Harbour. (The ionosonde returns for this day are described in detail by Stiles et al. [1977].) The decision had been reached that Tordo Dos would be launched across the equatorward boundary of the cleft. In order to accomplish this goal the launch azimuth was set as close to magnetic north as range safety requirements would allow (Figure 3).

From high voltage turnon at 0020:27.6 UT (180 km) to 0028:13.2 UT (390 km), downcoming

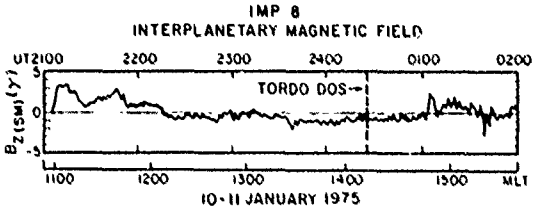

Fig. 2. Interplanetary magnetic field Z component (solar magnetospheric) from Imp 8 for January 10-11, 1975.

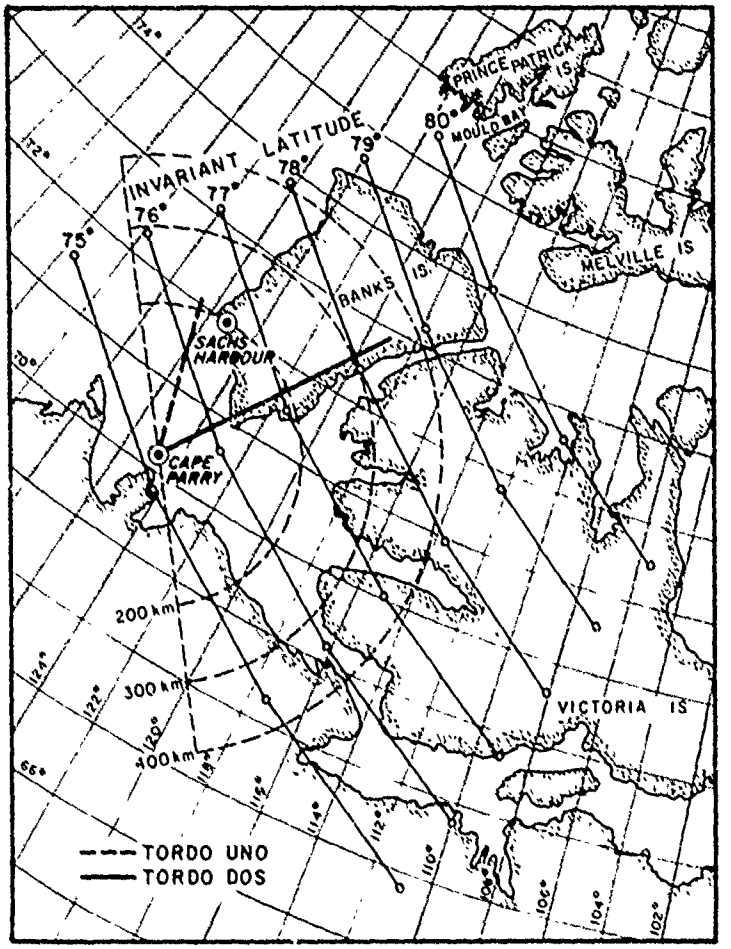

Fig. 3. Tordo Uno and Dos trajectories projected to 100 km along the earth's magnetic field.

atmospheric photoelectrons and very weak high-energy electrons were observed (Figure 8). A maximum in the photoelectron flux was observed between approximately 300 and 340 km. Mantas and Bowhill [1975] predict a maximum in the downcoming photoelectron flux at approximately 290 km for a 90° solar zenith angle. Our peak was above this altitude, but the zenith angle (100°) was also larger. In addition, electron density fluctuations, causing the observed spread F, would result in fluctuations in the atmospheric photoelectron flux and a smearing of the altitudinal profile (G. P. Mantas, private communication, 1976).

Examination of the SPS data indicates that the cleft equatorward boundary was crossed at 0028:13.2 UT at an invariant latitude of 76.4° (Figure 9). From 0028:13.2 to 0029:10.8 UT the electron spectrum peaked at approximately 100-200 eV and varied in magnitude. The spectral shape is similar to shapes reported in the literature for the cleft [Winningham and Heikkila, 1974]. Subsequent to this time, two 'inverted V's' were observed, one centered at 0029:26.8 and the other at 00:31 UT. Morphologically, inverted V's are regions in energy-time spectrograms where the maximum count rate (region of maximum darkness or lightness, depending of film polarity) moves first to higher energy then to lower energy with advancing time, producing an inverted V shape. Between the two inverted V's the electron spectra were either peaked in the 100- to 200-eV range or were due to atmospheric photoelectrons.

Inspection of each electron spectrum during passage through the inverted V's indicated that on a gross scale the peak in the electron distribution function (particles cm^{-2} sr^{-1} eV^{-1} s^{-1}) was increasing and then decreasing in both energy and magnitude. In addition, several relative maxima were observed (see Figure 12). The spectrum in Figure 10a was obtained just prior to the first 'energized' spectrum in the second inverted V. It is well fitted by a Maxwellian distribution (dashed curved) with a 'temperature' of 1.7×10^6 °K and a density of 0.5 cm^{-3} (assuming isotropy). The solid circles represent a correction for atmospheric photoelectrons utilizing the spectrum measured at 0030:11.6 UT. Spectra in Figure 10b are representative of the peaked distributions in the second inverted V.

All-sky camera data were obtained from Sachs Harbour, which at the time of Tordo Dos had just

Fig. 4. Electron energy-time spectrogram for Tordo Uno.

entered astronomical twilight (12° solar depression angle). In the all-sky camera data, faint auroras are visible toward the north, and their positions are plotted in Figure 9 together with those of the two inverted V events observed by the rocket particle detectors and cleft returns deduced from the ionosonde data. All the data shown have been mapped to an altitude of 160 km. The height of 160 km used for calculating the position of the auroras was selected on the basis of the energy spectra (Figure 8) and luminosity profiles derived by Rees [1963].

As can be seen in Figure 9, auroras were observed only in the vicinity of the second inverted V event. No auroral form associated with the first event could be discerned in the data. This at first appeared strange considering the very similar energies and energy fluxes in the two events. As will be discussed below, the explanation is to be found in a combination of viewing angles from Sachs Harbour and the latitudinal width of the two precipitation events.

From Figure 8 we find a characteristic energy in the two events of 1 keV and an energy flux of about 1 erg/cm² s sr or 3 ergs/cm² s (assuming isotropy). For a 1-keV characteristic energy, Rees and Luckey [1974], calculate a column emission rate of 0.16 kR/erg/cm² s in 4278 Å and a corresponding emission rate ratio 5577/4278 Å of 6. Thus the estimated brightness of the form, if overhead, would be 3 x 0.16 x 6 = 3 kR in 5577Å. The forms are not overhead but are off to the northeast at an elevation angle of about 45° and 35°, respectively, and the SPS data (Figure 8) indicate the latitudinal width of the precipitation in the second event to be 3 times that of the first. Romick and Belon [1967] have calculated the brightness of an aurora for various values of width, position relative to the observer, and height luminosity profile. They find that the brightness of an arc 0.3° wide at an elevation angle of 35° (very similar to the values for the second inverted V event) would be 0.35 of the overhead value. Further, they find that auroras well away from the zenith have a brightness roughly proportional to their thickness, all other things being equal. With these corrections for aspect and width applied the auroras associated with the two inverted V events would appear with a brightness of 0.3 and 1 kR with respect to an observer at Sachs Harbour.

Under ideal conditions the 35-mm f 1.2 all-sky camera used at Sachs Harbour can resolve forms of slightly less than 1 kR in 5577 Å [Romick and Brown, 1971]. Thus the aurora associated with the first inverted V event (0.3 kR) should not be visible in the all-sky data even under ideal conditions, and given the twilight condition during the experiment, the aurora (1 kR) associated with the second inverted V should only be marginally detectable, which is in good agreement with the actual data.

It should be noted that the 6300-Å photometer

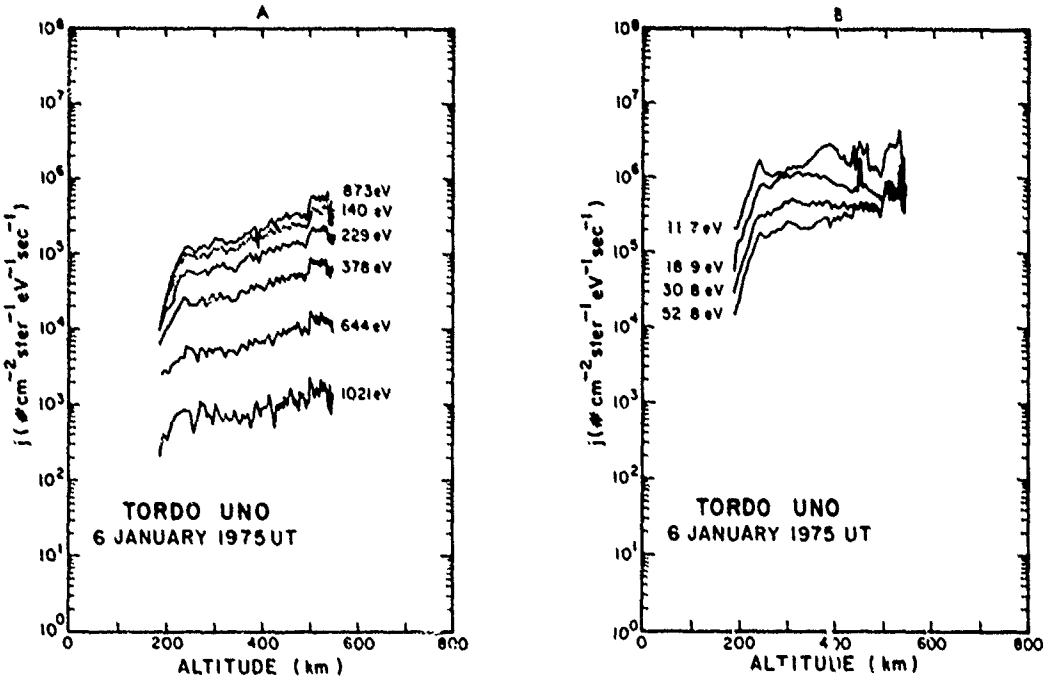

Fig. 5. Differential number flux versus altitude for Tordo Uno.

observed, in addition to the auroral form also detected by the all-sky camera, a faint arc just north of Sachs Harbour at an invariant latitude of 76.4°. The photometer was scanning geographic north-south and thus was pointing away from the rocket trajectory, and it is uncertain what relevance these measurements have to the observations along the rocket trajectory.

A strong oblique E layer return is seen in the Cape Parry ionograms, and several returns are also seen in the Sachs Harbour ionograms. By assuming that the returns come from ionospheric structures aligned along constant magnetic latitude a triangulation can be made to determine the location of the irregularity. By triangulating on the strongest oblique E layer return its position was found to lie within the region of the second inverted V event as shown in Figure 9.

From Figure 9 it can be seen that the cleft as measured by the SPS was indeed poleward of Sachs Harbour by a few tenths of a degree. The position of the cleft as determined by the SPS (76.4°) is coincident with the aforementioned weak red arc even though they are separated by approximately 4° of longitude.

As in Tordo Uno, the proton fluxes were very weak. It should be noted that the SPS as used in Tordo Uno and Dec was approximately 20 times more sensitive than were the Isis SPS's. (The main increase in sensitivity is due to the increased accumulation period.)

Discussion and Conclusions

The exact location of the Tordo Uno measurements relative to the cleft boundaries is difficult to establish. Only one detail can be stated with certainty, that is, Tordo Uno was poleward of the equatorward boundary of the cleft. Comparison of Tordo Uno positive ion fluxes with Isis results indicate a position in the poleward portion of the cleft. This conclusion is based on two characteristics of the positive ions, namely, their low intensity and low average energy. Typical results from Isis show the hardest and most intense fluxes at the equatorward edge of the cleft with a subsequent poleward softening and decrease in intensity.

Another possible interpretation of the results would be that the observed electrons are polar rain electrons [Winningham and Heikkila, 1974]. However, several facts argue against this interpretation. The observed density of the primary electrons is as high as approximately 5 cm^{-3}. Winningham and Heikkila's [1974] results show the polar rain fluxes to be only a few percent of the cleft fluxes. If these densities were measured in the polar cap, cleft densities would be >100 cm^{-3} and by inference, magnetosheath densities would be at least as large. Such cleft densities are rarely observed. An even more telling argument comes from concurrent measurements of solar wind densities by Imp 7 (courtesy of W. C. Feldman) and magnetosheath densities by Hawkeye (Figure 6) (courtesy of L. A. Frank). Both were approximately 10 cm^{-3} during the period of Tordo Uno.

Comparison with the Hawkeye results (Figure 6) indicates a factor of approximately 2 decrease in density between the magnetosheath and the poleward portion of the cleft. The results of Akasofu et al. [1973] demonstrate that the poleward portion of the cleft maps to the inner edge of the magnetospheric boundary layer (see their Figure 11). Additionally Akasofu et al. show the boundary layer

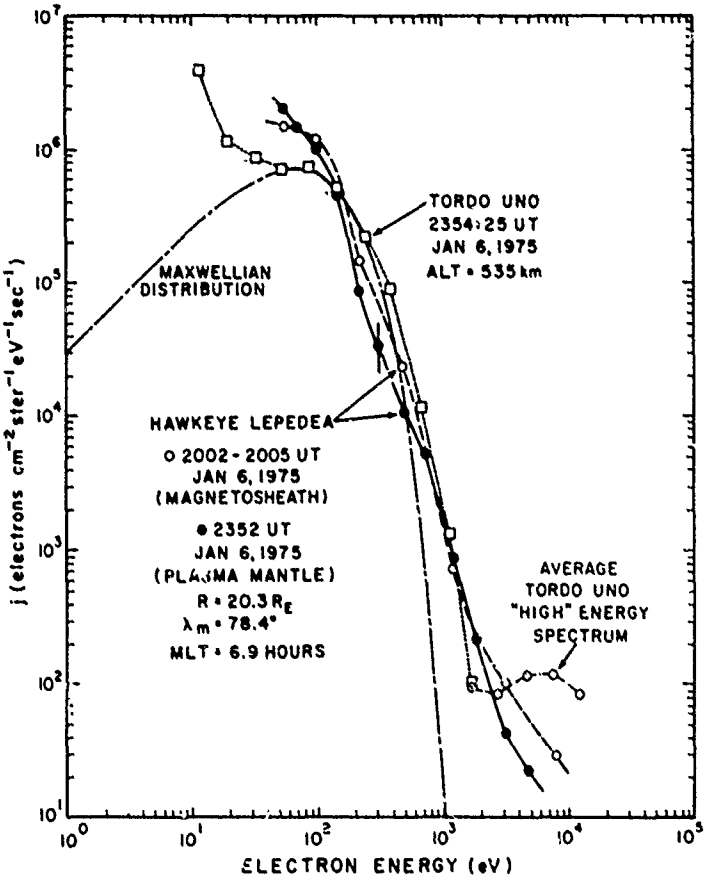

Fig. 6. Electron spectra from Tordo Uno and Hawkeye for January 6, 1975.

densities to be less than or equal to the magnetosheath density and to decrease with increasing inward penetration of the boundary layer. Thus the most consistent interpretation of the results places Tordo Uno in the poleward portion of the cleft.

The 'high-energy' portion of the electron spectrum observed by Tordo but not by Hawkeye in Figure 6 can be attributed to an internal magnetospheric source, i.e., drifting energetic electrons from the nightside. Recent papers by McDiarmid et al. [1976] and Haerendel and Paschmann [1975] have shown that trapped energetic electrons are observed concurrently with entry layer and cleft plasma. Eastman et al. [1976] find that electron spectra in the boundary layer develop high-energy (few keV) tails with increasing inward penetration of the boundary layer and have associated these to leakage of magnetospheric plasma into the boundary layer. In the present case, Tordo Uno sampled only inside the loss cone, and thus nothing can be said concerning the pitch angle distribution. Spectrally, the electrons are similar to low-altitude polar satellite measurements in the same region [Winningham, 1972].

The initial energy-dependent increase in electron flux with altitude (<250 km) is due to the interaction of the primary beam [Banks et al., 1974, Figure 16] with the atmosphere. Above this altitude, spatial and/or temporal changes predominate. In summary, Tordo Uno and the associated barium jet were launched into the poleward portion of the afternoon cleft which contained unenergized magnetosheathlike electrons. With reference to the work by Jeffries et al. [1975], Figure 3 shows the path of the barium plasma leaving the vicinity of Tordo Uno to be essentially directly antisolar across the polar cap into the nightside auroral zone.

By comparison, we know the position of Tordo Dos vis-à-vis the cleft equatorward boundary relatively well. Tordo Dos was launched equatorward of the cleft, crossed its equatorward boundary, and encountered two inverted V's in the cleft prior to barium injection. In assuming the cleft boundary to be zonal (i.e., parallel to magnetic latitude) over the short longitude span traversed and to be fixed for the duration of the Tordo Dos flight, barium injection occurred approximately 1.9° into the cleft. The latter assumption is supported by concurrent results from the sounders.

The electron precipitation observed in Tordo Dos was dramatically different from Tordo Uno. 'Monoenergetic' peaks were observed (Figure 10b) in the electron spectra, and the energy of these peaks varied systematically, i.e., the inverted V's. Such behavior has been attributed to

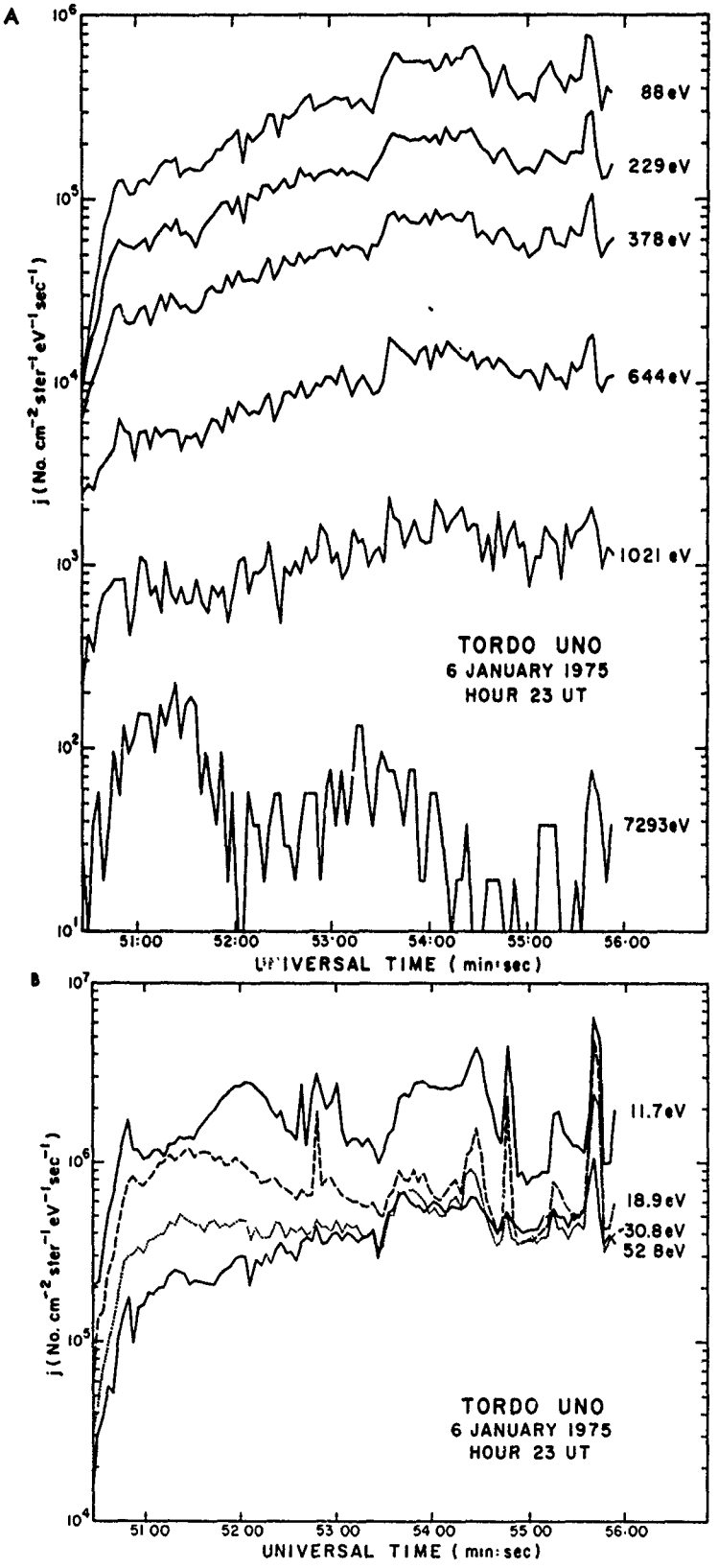

Fig. 7. Differential energy flux versus time (distance) for Tordo Uno.

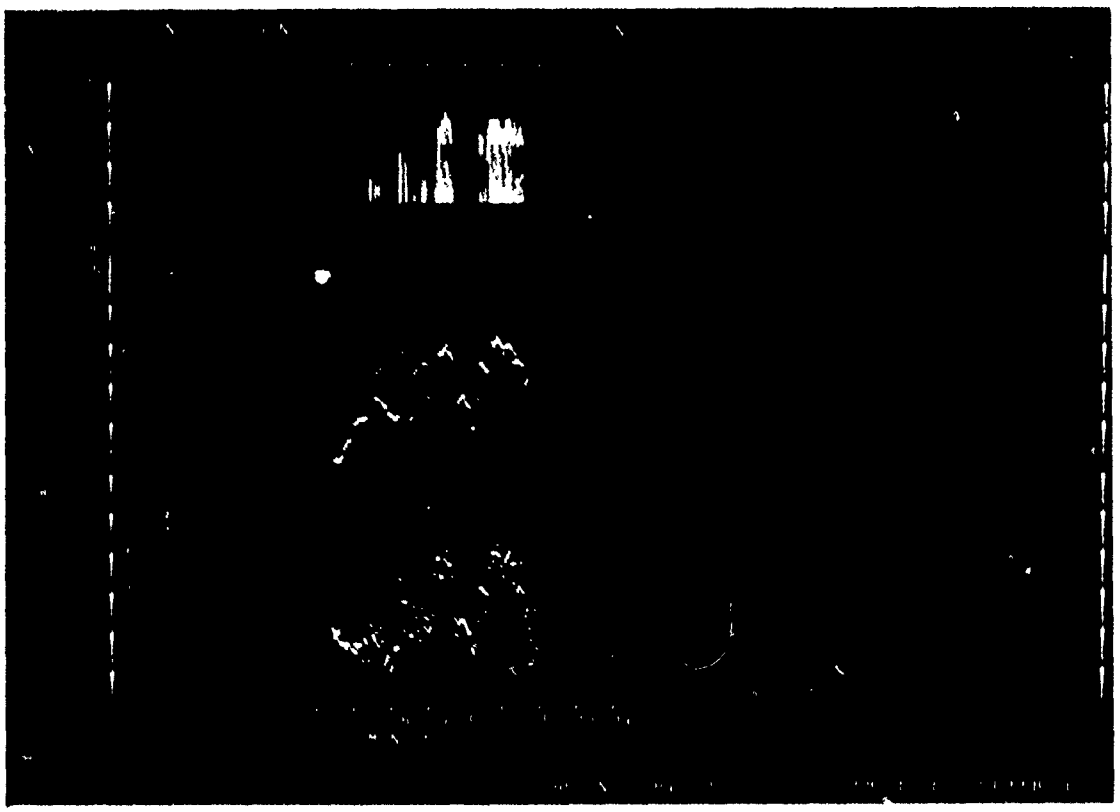

Fig. 8. Electron energy-time spectrogram for Tordo Dos.

acceleration by an electric field parallel to the earth's magnetic field [Burch et al., 1976, and references therein]. To investigate this possibility, the numerical model of Evans [1974] was applied to the data. It should be noted that the experimental data are inadequate in pitch angle and spectral resolution to prove or or disprove uniquely any theory; only consistency can be shown.

With the aforementioned reservations in mind the experimental spectra are easily derivable from Evans' model. An example of a spectrum from the second inverted V is given in Figure 11. A least squares Maxwellian fit is made to the high-energy tail of the observed fluxes, and the temperature of the assumed Maxwellian plasma at the top of the accelerator is determined as indicated on the figure. The probable error from the least squares fit is also indicated. The initial Maxwellian is allowed to fall through a potential drop V_o, producing a jetted beam at the bottom of the accelerator. The beam then produces backscattered and secondary electrons upon interaction with the atmosphere. those upgoing electrons with energies less than eV_o are reflected by the parallel electric field and would be observed by the instrument as low energy downgoing particles. The Maxwellian fit together with a choice of V_o fixes the density n of the assumed Maxwellian plasma. The accelerating potential is then varied, producing the solid curve at low energies in Figure 11, until a 'best fit' to the data is obtained. Thus for this model the only free parameters which we vary are V_o and the B Ratio, the ratio of magnetic field strengths at the accelerator exit and at the top of the atmosphere.

For the backscatter calculations we used the electron impact ionization cross section for atomic oxygen from Banks et al. [1974] (see also Opal et al. [1971]). Use of the cross section for N_2 would increase the low-energy fluxes by about 12% at about 100 eV.

Figure 12 presents the results of these calculations for the second inverted V. All points except the first and last are derived or 'fitted' quantities. This first point (denoted by a circle) corresponds to the 'nonaccelarated' spectrum (Figure 10a) encountered just prior to the second inverted V (see Figure 12). The last point (also denoted by a circle) is from a temperature fit only at that point. It can be seen that even though the potential varied dramatically, the density (assuming source isotropy) and the temperature were constant within one standard deviation. In addition, the 'nonaccelerated' density and temperature lie within the same bounds.

Note that the nonaccelerated values are local quantities and the derived quantities refer to the input of the 'linear accelerator,' as described above. Thus the inverted V has as its source population a Maxwellian with a density of 0.87 ± 0.25 cm^{-3} and a temperature of 117 ± 24 eV.

If all the assumptions in Evans' model are valid in this case, the approximate position of the exit of the accelerator can be determined

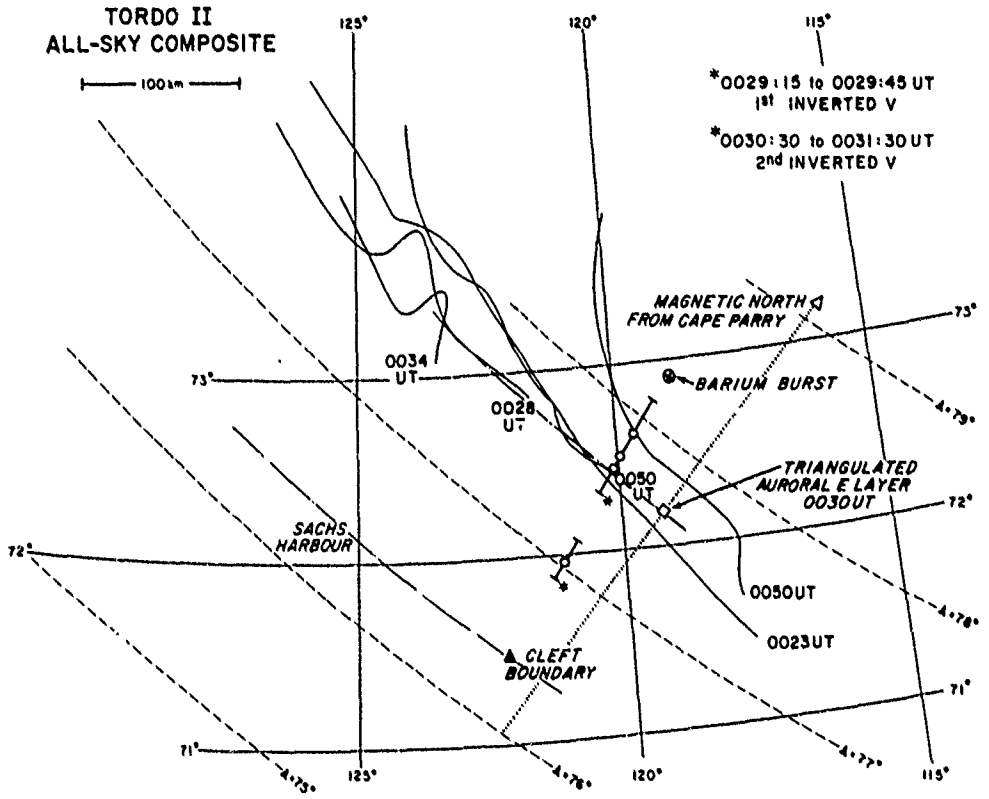

Fig. 9. Schematic of geographic location of observed auroral arcs, inverted V events, barium release, and returns observed by the ionosondes. All positions have been reduced to the 160-km altitude level.

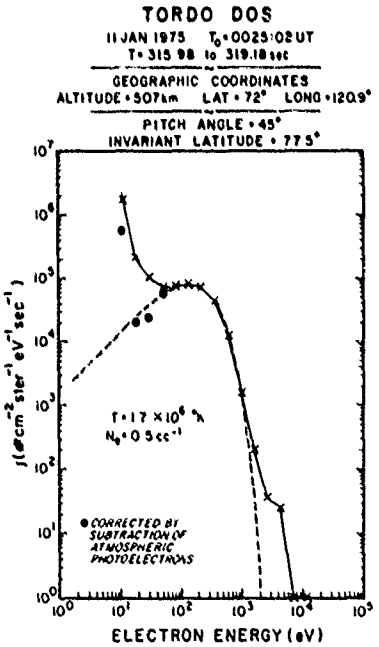

Fig. 10a. Electron spectrum obtained prior to entry into second inverted V observed by Tordo Dos.

from the B Ratio. The derived value of 12.5 gives an approximate lower limit of 1R_E above Tordo or 2 R_E geocentric. This value is consistent with the lower limit value obtained by assuming that the collimation cone had expanded just enough to include the measured pitch angle.

Our results are in basic agreement with those of Burch et al. [1976] except for one feature. Burch et al. pointed out that in all the cleft inverted V's they observed the characteristic energy (temperature) went up as the acceleration potential increased. They interpreted this as a heating as well as an acceleration of the source population. The results as shown in Figure 12 indicate that no statistically important heating occurred for this second inverted V event on Tordo Dos. However, some remarks on the nature of the high energy tail are in order. We found that with few exceptions the more high energy data points we included in the least squares routine, the hotter the temperature of the plasma. Thus the high energy tail in the inverted V event is non-Maxwellian. Since the potential is chosen primarily to find a fit to the lower energy portion of the spectrum and since this depends mostly on the fluxes near the peak of the beam, we used only two or three data points near the beam maximum to determine the temperature for the results shown in Figure 12 (for example, in Figure 11, fluxes at energies of 634.4, 1033, and 1655 eV). In addition, data

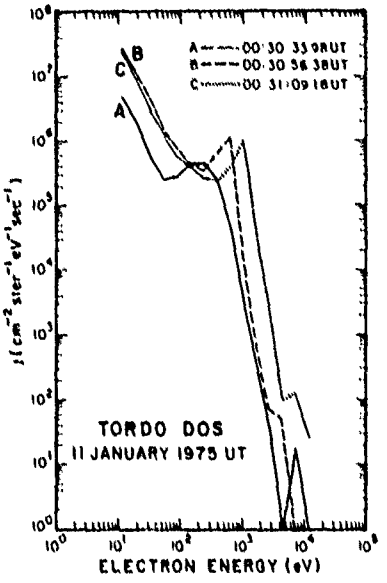

Fig. 10b. Representative electron spectra obtained in second inverted V observed by Tordo Dos.

points at the lower intensity levels are experimentally less well determined.

To test this apparent disagreement with Burch et al., we ran new 'fits' using the criterion that we would use all data in the tail with flux values greater than 10^3 cm^{-2} s^{-1} sr^{-1} eV^{-1}. By using this criterion, only 8 of the 23 cases are changed. (In one case, at t= 0030:30, the temperature went from 54 to 127 eV, but we could no longer find a reasonable 'fit' to the spectrum.) The temperatures of these eight cases did come out higher than before, necessitating reduced values for V_o in some cases, with a general trend of temperature and V_o proportionality. Linear regression analysis in this case yields a temperature of $0.06\ V_o + 102$ eV, but the correlation is not high (correlation coefficient is 0.35).

It therefore appears that our analysis is consistent with no apparent heating of the plasma at energies near the beam maximum, but some heating at higher energies proportional to V_o cannot be ruled out. It is equally possible that the non-Maxwellian nature of the tail is a feature of the original plasma (see Figure 10a).

Burch et al. [1976] reported the cleft inverted V's to be in a region of antisunward convection. No convection measurements were available at the position of the Tordo Dos inverted V's. However, the barium streak was released approximately 7 km poleward of the second inverted V and drifted antisunward at approximately constant magnetic latitude [Jeffries et al., 1975, Figure 3].

In conclusion, Tordo Dos crossed the equatorward boundary of the cleft, traversed approximately 1.9^o of its extent, and encountered two inverted V's. The inverted V's

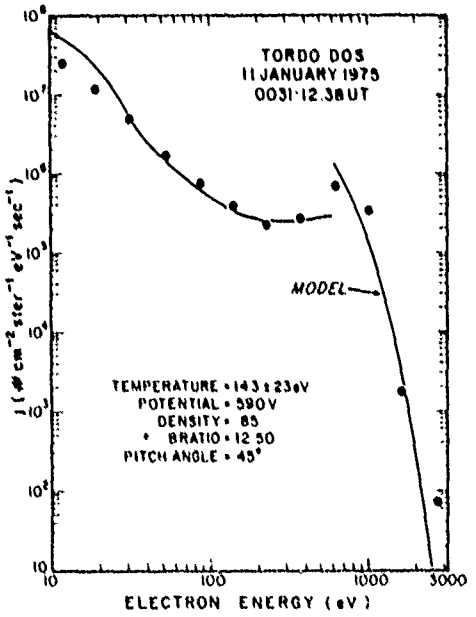

Fig. 11. Experimental and modeled electron spectrum for second inverted V in Tordo Dos data. Model spectrum generated by using the numerical model of Evans [1974].

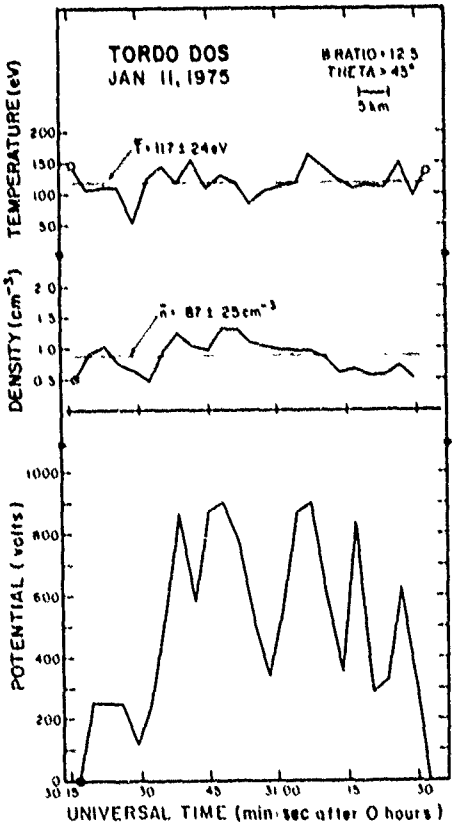

Fig. 12. Density and temperature derived from Evans' [1974] model for source spectrum of second inverted V observed by Tordo Dos and the necessary potential drop. See text.

can be well modeled by the model of Evans [1974] by utilizing a constant source temperature and density and a varying potential. A 'best guess' places the accelerator at a minimum geocentric distance of 2 R_E. The barium injected just subsequent to the second inverted V drifted essentially parallel to the cleft (i.e., at approximately constant magnetic latitude) and antisunward as opposed to the perpendicular and antisunward motion of Tordo Uno. The cloud motion and its dynamics will be detailed in a subsequent paper.

Acknowledgments. The UTD portion of this work was supported by ERDA contracts P/O KH-69046-1 and LC5-83449-1, Air Force Geophysics Laboratory contract F19628-76-C-005, and the National Aeronautics and Space Administration grant NGR 44-004-124. The support of the Geophysical Institute was supported by NASA contract NGR 02-001-087. One of us (T.W.S.) would like to thank the Space Environment Laboratory, NOAA, Boulder, Colorado, for support, computer time, and technical assistance. Thanks go to Harold Fishbine, C. R. Thompson, Jack Frazier, and Lou Wadel, whose technical efforts made the present paper possible.

The Editor thanks I. B. McDiarmid and I. S. Mikkelsen for their assistance in evaluating this paper.

References

Akasofu, S.-I., E. W. Hones, Jr., S. J. Bame, J. R. Asbridge, and A. T. Y. Lui, Magnetotail and boundary layer plasmas at a geocentric distance of approximately 18 RE: Vela 5 and 6 observations, J. Geophys. Res., 78, 7527, 1973.

Banks, P. M., C. R. Chappell, and A. F. Nagy, A new model for the interaction of auroral electrons with the atmosphere: Spectral degradation, backscatter, optical emission, and ionization, J. Geophys. Res., 79, 1459, 1974.

Bunting, W. D., Jr., J. Tarstrup, and W. J. Heikkila, Detection efficiency of electron multipliers for low-energy electrons, J. Appl. Phys., 43, 1585, 1972.

Burch, J. L., S. A. Fields, W. B. Hanson, R. A. Heelis, R. A. Hoffman, and R. W. Janetzke, Characteristics of auroral electron acceleration regions observed by Atmosphere Explorer C, J. Geophys. Res., 81, 2223, 1976.

Eastman, T. E., E. W. Hones, Jr., S. J. Bame, and J. R. Asbridge, The magnetospheric boundary layer: Site of plasma, momentum and energy transfer from the magnetosheath into the magnetosphere, Geophys. Res. Lett., 3, 685, 1976.

Evans, D. S., Precipitating electron fluxes formed by a magnetic field aligned potential difference, J. Geophys. Res., 79, 2853, 1974.

Haerendel, G., Exploration of the polar cusp by an international rocket campaign (abstract), Eos Trans. AGU, 56, 430, 1975.

Haerendel, G., and G. Paschmann, Entry of solar wind plasma into the magnetosphere, in Physics of the Hot Plasma in the Magnetosphere, edited by B. Hultqvist and L. Stenflo, pp. 23-43, Plenum, New York, 1975.

Heikkila, W. J., J. B. Smith, J. Tarstrup, and J. D. Winningham, The soft particle spectrometer in the Isis-1 satellite, Rev. Sci. Instrum., 41, 1393, 1970.

Jeffries, R. A., W. H. Roach, E. W. Hones, Jr., E. M. Wescott, H. C. Stenbaek-Nielsen, T. N. Davis, and J. D. Winningham, Two barium plasma injections into the northern magnetospheric cleft, Geophys. Res. Lett., 2, 185, 1975.

Ledley, B. G., and W. H. Farthing, Field-aligned current observations in the polar cusp ionosphere, J. Geophys. Res., 79, 3124, 1974.

Mantas, G. P., and S. A. Bowhill, Calculated photoelectron pitch angle and energy spectra, Planet. Space Sci., 23, 355, 1975.

Maynard, N. C., and A. D. Johnstone, High-latitude dayside electric field and particle measurements, J. Geophys. Res., 79, 3111, 1974.

McDiarmid, I. B., J. R. Burrows, and E. E. Budzinski, Particle properties in the dayside cleft, J. Geophys. Res., 81, 221, 1976.

Mikkelsen, I. S., and T. S. Jorgensen, Electric fields in the cleft region observed by Ba^+ clouds (abstract), Eos Trans. AGU, 55, 70, 1974.

Opal, C. B., W. K. Peterson, and E. C. Beatty, Measurement of secondary electron spectra produced by electron impact ionization of a number of simple gases, J. Chem. Phys., 55, 4100, 1971.

Rees, M. H., Auroral ionization and excitation by incident energetic electrons, Planet. Space Sci., 11, 1209-1218, 1963.

Rees, M. H., and D. Luckey, Auroral electron energy derived from ratio of spectroscopic emissions, 1, Model computations, J. Geophys. Res., 79, 5181-5185, 1974.

Romick, G. J., and A. E. Belon, The spatial variation of auroral luminosity, 1, The behavior of synthetic model auroras, Planet. Space Sci., 15, 475-493, 1967.

Romick, G. J., and N. B. Brown, Midday auroral observations in the oval, cusp region, and polar cap, J. Geophys. Res., 76, 8420-8424, 1971.

Shepherd, G. G., F. Creutzberg, B. Delana, J. C. Gerard, and D. J. McEwen, Rocket launch into dayside cleft aurora from Cape Parry, N. W. T., Dec. 6, 1974 (Abstract), Eos Trans. AGU, 56, 431, 1975.

Shepherd, G. G., J. F. Pieau, F. Creutzberg, A. G. McNamara, J. C. Gerard, D. J. McEwen, B. Delana, and J. H. Whitteker, Rocket and ground-based measurements of the dayside magnetospheric cleft from Cape Parry, N. W. T., Geophys. Res. Lett., 3, 69, 1976.

Smith, J. B., An amplifier for electron multiplier pulse counting amplicications, Rev. Sci. Instrum., 43, 488, 1972.

Stenbaek-Nielsen, H. C., E. W. Hones, Jr., and J. D. Winningham, Plasma convection and electric fields in the quiet time magnetospheric cleft from the Tordo Dos experiment (abstract), Eos Trans. AGU, 56, 432, 1975.

Stiles, G. S., E. W. Hones, Jr., J. D. Winningham, R. P. Lepping, and B. J. Delana,

Ionosonde observations of the northern magnetospheric cleft during December 1974 and January 1975, J. Geophys. Res., 82, 67, 1977.

Temerin, M., C. W. Carlson, F. S. Mozer, and M. C. Kelly, Rocket measurements of polar cusp electric fields and plasma density (abstract), Eos Trans. AGU, 56, 430, 1975.

Torbet, R. B., and C. W. Carlson, Impulsive ion injection into the polar cap, paper presented at Summer Advanced Study School, Magnetospheric Particles and Fields, Def. Nucl. Agency, Lockheed Palo Alto Res. Lab., and Off. of Nav. Res., Graz, Austria, 1975.

Torbet, R. B., K. A. Anderson, and C. W. Carlson, Observations of low and medium energy particles in the polar cusp (abstract), Eos Trans. AGU, 56, 430, 1975.

Ungstrup, E., A. Bahnsen, J. K. Olesen, F. Primdahl, F. Spangslev, W. J. Heikkila, D. M. Klumpar, J. D. Winningham, U. Fahleson, C.-G. Falthammar, and A. Pedersen, Geophys. Res. Lett., 2, 345, 1975.

Ungstrup, E., A. Bahnsen, J. K. Olesen, F. Primdahl, F. Spangslev, W. J. Heikkila, D. M. Klumpar, J. D. Winningham, U. Fahleson, C.-G. Falthammar, and A. Pedersen, Particle, field, and plasma observations in the low altitude prenoon cleft (abstract), Eos Trans. AGU, 56, 430, 1975b.

Wescott, E. M., H. C. Stenbaek-Nielsen, T. N. Davis, R. A. Jeffries, W. H. Roach, and E. W. Hones, Jr., Anti-solar polar cap convection and magnetic field configuration observations from the disturbed time Tordo Uno magnetospheric cleft injection experiment (abstract), Eos Trans. AGU, 56, 432, 1975.

Winningham, J. D., Characteristics of magnetosheath plasma observed at low-altitudes in the dayside magnetospheric cusps, in Earth's Magnetospheric Processes, edited by B. M. McCormac, pp. 68-80, D. Reidel, Dordrecht, Netherlands, 1972.

Winningham, J. D., and W. J. Heikkila, Polar cap auroral electron fluxes observed with Isis 1, J. Geophys. Res., 79, 949, 1974.

Winningham, J. D., R. A. Jeffries, E. W. Hones, Jr., and T. N. Davis, Cleft particle observations in conjunction with barium shaped charge releases (abstract), Eos Trans. AGU, 56, 432, 1975a.

Winningham, J. D., F. Yasuhara, S.-I. Akasofu, and W. J. Heikkila, The latitudinal morphology of 10-eV to 10-keV electron fluxes during magnetically quiet and disturbed times in the 2100-0300 MLT sector, J. Geophys. Res., 80, 3148, 1975b.

(Received October 4, 1976;
accepted December 13, 1976.)

VOL. 82, NO. 29 JOURNAL OF GEOPHYSICAL RESEARCH OCTOBER 1, 1977

Numerical Model of the Convecting F_2 Ionosphere at High Latitudes

W. C. KNUDSEN

Lockheed Palo Alto Research Laboratory, Palo Alto, California 94304

P. M. BANKS

Utah State University, Logan, Utah 84322

J. D. WINNINGHAM AND D. M. KLUMPAR

University of Texas at Dallas, Richardson, Texas 75080

Time-dependent behavior of tubes of F layer plasma is computed for tubes carried around several flow paths in the polar region. The flow paths are those proposed previously by Knudsen (1974). Ionization sources include direct and scattered solar photons and measured fluxes of precipitating energetic electrons. Computed electron concentrations are compared with measured concentrations from topside sounder data obtained in the same satellite pass as the energetic electron flux data. The following conclusions are drawn: The proposed convection pattern produces a tongue of F layer plasma over the polar cap with electron concentrations consistent with the measured concentrations. Had the F layer been assumed to be nonconvecting over the polar cap, the computed concentrations would have been a factor of 10 too small. Rapid convection of plasma across the cleft prevents significant increase in N_mF_2 at the cleft. Rapid convection must exist through the intense nightside auroral energetic particle precipitation zones, or a compensating electron loss mechanism must develop to prevent the buildup of an ionization ridge. A mid-latitude trough is formed by the proposed convection pattern with only normal F layer recombination processes operating. The low concentration in the trough is maintained by scattered solar EUV photons. The trough predicted by the numerical model is not observed in the topside sounder data.

INTRODUCTION

In a previous paper, *Knudsen* [1974] presented a model for the convection field of the high-latitude F layer and evaluated semiquantitatively the expected time-dependent behavior of a tube of F layer plasma carried around the polar regions by the field. The proposed field appeared to explain many of the high-latitude F layer anomalies. The purpose of the present paper is to present the initial results of a more detailed numerical study of the behavior of the high-latitude F layer. Tubes of ionization are subjected to time-dependent ionization rates from both solar photons and precipitating energetic electrons as the tubes follow the convection field proposed in the previous paper, and the time-dependent response of the plasma within the tube is computed.

NUMERICAL MODEL

The time-dependent behavior of the plasma within a magnetic flux tube was computed with a numerical code developed by *Schunk and Walker* [1973]. The code solves the coupled momentum and continuity equations for NO^+, O_2^+, and O^+ ions in the E and F regions. Minor changes were made in the code to permit the addition of ionization rates resulting from energetic electron fluxes and also from solar EUV scattered into the nightside of the ionosphere. The code was also modified to permit the base of the flux tube to change in latitude and longitude with elapsed time in a prescribed manner.

The code does not solve the energy balance equation, and consequently, it is necessary to specify T_e and T_i. For this study we have set both T_e and T_i equal to the neutral gas temperature T_n. Heating of the thermal electron gas by fluxes of soft electrons with energies of a few tens of electron volts is thus neglected, and the enhancement of electron concentrations at altitudes above approximately 400 km in response to electron heating will not be reproduced in the model.

The variations of the neutral constituents N_2, O_2, and O with latitude and local time were derived from the model atmosphere of *Jacchia* [1971] for winter (solar declination, $-23°$) and medium solar activity ($F_{10.7} = 130 \times 10^{-22}$ W m^{-2} Hz^{-1}). The NO density was the same as that used by *Schunk and Walker* [1973].

The numerical solution was obtained over the altitude range 120–500 km. The upper altitude limit was set at 500 km to ensure proper convergence of the solution for reasonably sized time steps. The fluxes of NO^+ and O_2^+ were set equal to zero at the upper boundary. To simulate the loss of O^+ through operation of the polar wind, the upward velocity of O^+ ions at the 500-km boundary was assumed to be constant at 10 m s^{-1}. At the lower boundary the O_2^+ and NO^+ concentrations were arbitrarily set to 10^5 cm^{-3}. Also at this boundary the O^+ density was assumed to be in chemical equilibrium and was set equal to

$$[O^+] = \frac{P(O^+)}{k_1[N_2] + k_2[O_2]}$$

where $[O^+]$, $[N_2]$, and $[O_2]$ are the appropriate densities and $P(O^+)$ the ion production rate of O^+; k_1 and k_2 are reaction rates defined by *Schunk and Walker* [1973]. The concentrations of NO^+ and O_2^+ near the lower boundary are governed primarily by chemical reaction rates, so that their concentrations a short distance above the lower boundary are insensitive to the arbitrarily assigned values.

The gyrofrequency of the ions is comparable to or less than their collision frequency at and below an altitude of approximately 180 km. The ions do not 'follow' the flux tubes below this altitude. We may expect therefore that the model results

Paper number 7A0474.

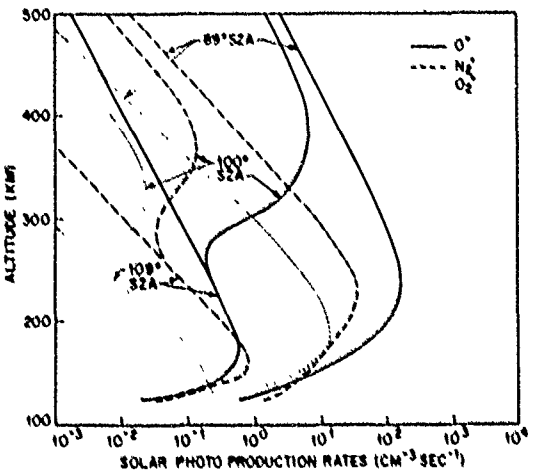

Fig. 1. Production rates of O^+, N_2^+, and O_2^+ by solar photons at three SZA's computed by the numerical model. Those at 109° SZA represent background rates from scattered photons

below 180 km will be in error at the E and F_1 altitudes near boundaries separating regions of different ion production rates.

The vertical drift which may be imparted to the plasma by the electric field causing the convection of the plasma and also by neutral winds has been neglected in this first model. Vertical drift was felt to be a second-order effect which could be studied after first-order effects were clarified. Some discussion of the expected drift is given by *Knudsen* [1974].

The displacement of the magnetic pole from the geographic pole imparts a universal time dependence into the high-latitude F layer concentration, which is to be the subject of a future study. For the present study we assume that the magnetic and geographic axes are collinear.

The ionization sources included in the model are solar EUV photons, both direct and scattered, and precipitating electrons. The method of calculating the direct photo-ionization rates for N_2, O_2, and O is described by *Schunk and Walker* [1973]. We are interested in the high-latitude F layer during winter in the present study and have calculated the Chapman grazing incidence function using 23° for the solar declination angle. To simulate the ionization rates from scattered EUV, the ionization rates from direct photons were added to background ionization rates produced by scattered photons. The background ionization rates were computed with the same code that was used for the direct ionization rates with the following changes. The solar zenith angle was set to zero, and the photon fluxes in the 11 spectrum intervals suggested by *Hinteregger et al.* [1965] were set to zero except for the wavelength intervals 1027–911 Å, 630–460 Å, and 370–280 Å. The fluxes in these intervals were set at 1×10^9, 1×10^9, and 1×10^8 photons cm^{-2} s^{-1}, respectively, and correspond to H Lyman β, He I 485 Å, and He Lyman α [*Chen and Harris*, 1971]. The total photoionization rates from both the direct and the scattered photons for three solar zenith angles (SZA's) are given in Figure 1. Those for a SZA of 109° are effectively the background rates with no contribution from the direct rates.

Ionization rates from precipitating electrons were computed by using energy distribution functions measured by the soft particle spectrometer (SPS) on the Isis 2 satellite. The energy time spectrograms over the northern polar cap on December 15 (day 349, orbit 3278), 1971, are shown in Figures 2 and 3. The satellite crossed the northern polar cap from approximately 1200 MLT (magnetic local time) to 2300 MLT (Figures 2 and 3). Spectra at times labeled 1–11 were selected as being representative and were used in computing the ionization rates produced by the electrons. The locations of the satellite at the times at which the spectra were recorded are shown in Figure 7. The electron precipitation was assumed to be uniform in local time for approximately 3 hours on either side of the satellite track in both the dayside cleft region and the nightside auroral region. Auroral oval emission data in 5577 Å and 3914 Å recorded on the Isis 2 satellite [*Lui and Anger*, 1973] indicate that on the nightside of the oval the precipitation was, in fact, more intense in the premidnight sector than in the postmidnight sector.

The data from the satellite pass shown represent a quiet period. The AE index was below 100 γ for 28 hours prior to the pass except for two short excursions. Sixteen hours prior to the pass the AE index went as high as 300 γ during a 2-hour period, and approximately 3 hours before the pass it rose to approximately 150 γ for a 2-hour period.

The proton number and energy fluxes over the polar region for the pass shown were 2 orders of magnitude lower than the corresponding electron fluxes and have been neglected as an important source of ionization.

Electron spectra for several pitch angles in the downgoing hemisphere at each of the 11 regions enumerated in Figures 2 and 3 have been analyzed and used to derive the spectra illustrated in Figures 4 and 5. The precipitating flux was reasonably uniform with pitch angle, and the spectra shown are considered representative of the spectra observed at each region. The SPS on Isis 2 measures electron flux down to 5 eV. For the purpose of computing ionization rates from these fluxes we have arbitrarily extended the measured 10-eV fluxes to 1 eV at a constant level. Since the numerical code used for computing thermal plasma behavior does not balance energy and since electrons with less than 10-eV energy produce no significant ionization, this extrapolation has no significant effect on the numerical results.

The ion production rates from the electron spectra presented above were computed with an early version of a computer code for the interaction of energetic electrons with the atmosphere developed by *Banks et al.* [1974]. Production rates for regions 2 and 9, representative of the cleft and nightside auroral regions, are shown in Figure 6.

The flow paths around which the plasma tubes were carried in the numerical simulation are those presented in an earlier paper by *Knudsen* [1974] and are reproduced as Figure 7. Results were obtained only for paths labeled II–VI. The flow paths define the motion of plasma tubes as seen by an observer in a nonrotating frame of reference looking down on the north polar cap. That is, the motion includes corotation so that the exposure of the plasma tubes to solar EUV photons is properly simulated. The tubes of plasma were convected across the dayside cleft at a velocity of 1 km/s and on across the cap at a velocity of 0.5 km/s. They were again convected across precipitation region 7 (Figure 3) at 1 km/s. Equatorward of the limit of closed field lines the tubes were convected between successive dots in 1 hour. Analysis of energetic electrons measured on Isis 2 at greater than 20 keV, greater than 40 keV, and greater than 200 keV indicates that the field lines were closed equatorward of 69°A (16 min, 40 s, Figure 3) and that no trapped distributions existed poleward of 70°A in the night

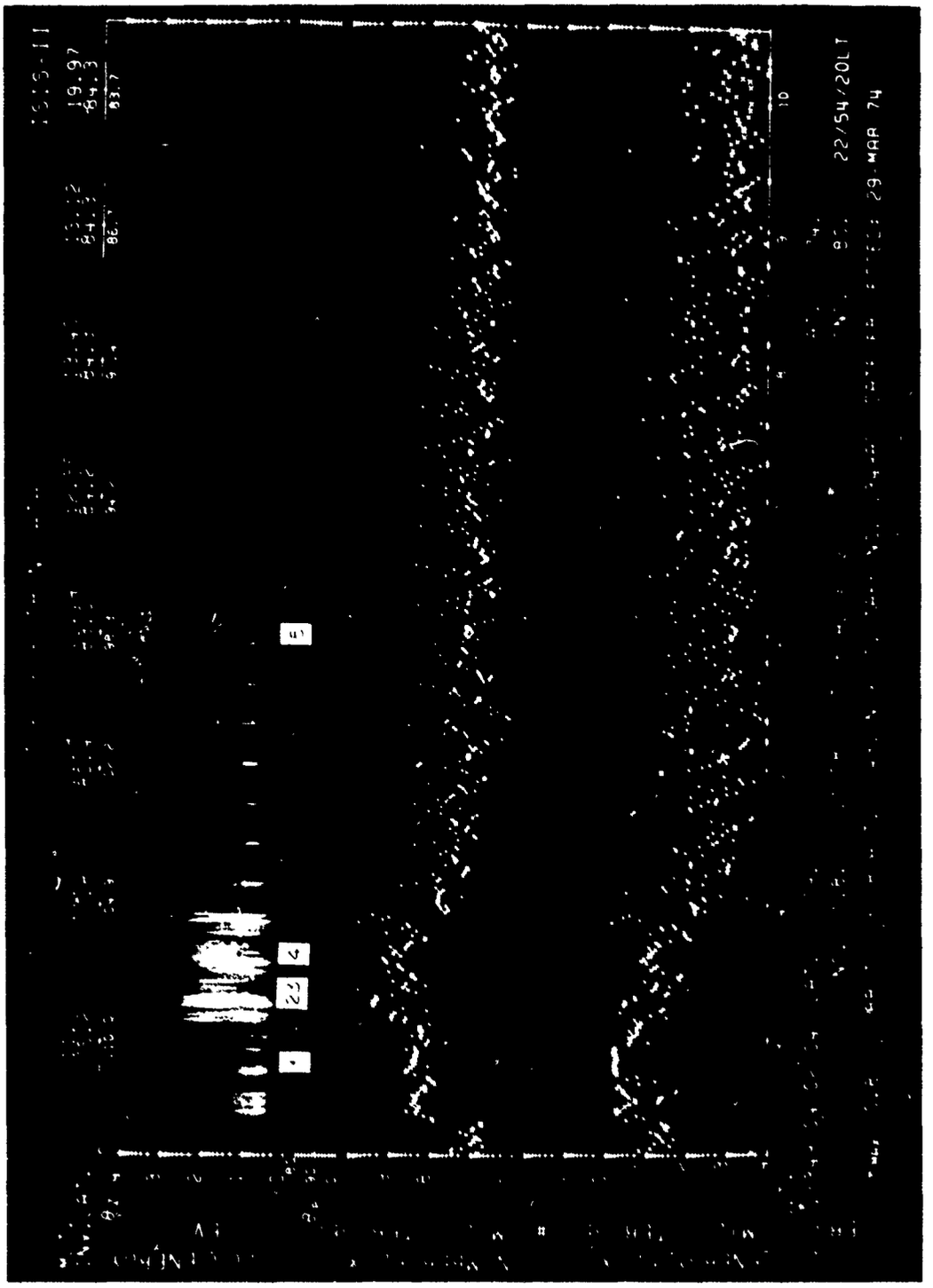

[illegible] from the [illegible] particle spectrometer December 15, 1971 local noon portion. Locations at which electron spectra were analyzed for use in the model are labeled

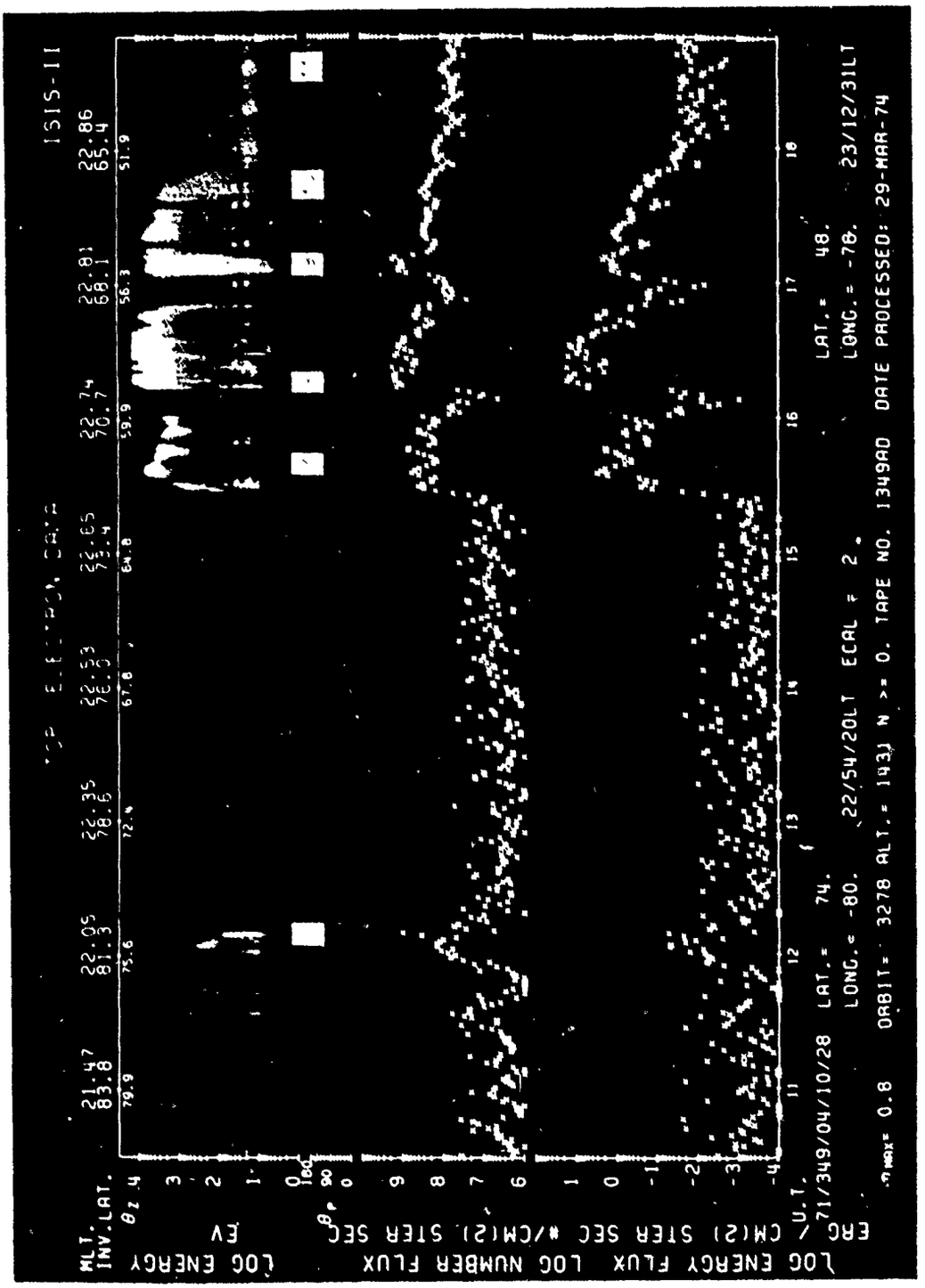
ISIS-II
MLT.
INV.LAT.
21.47
83.8
79.9
22.05
81.3
75.6
22.35
78.6
72.4
22.53
76.0
67.8
22.65
73.4
64.8
22.74
70.7
59.9
22.81
68.1
56.3
22.86
65.4
51.9
LOG ENERGY FLUX LOG NUMBER FLUX LOG ENERGY
ERG / CM(2) STER SEC #/CM(2) STER SEC EV
U.T.
71/349/04/10/28 LAT.= 74.
LONG.= -80.
22/54/20LT ECAL = 2.
LAT.= 48.
LONG.= -78.
23/12/31LT
ORBIT= 3278 ALT.= 193 N >= 0. TAPE NO. 1349AD DATE PROCESSED: 29-MAR-74

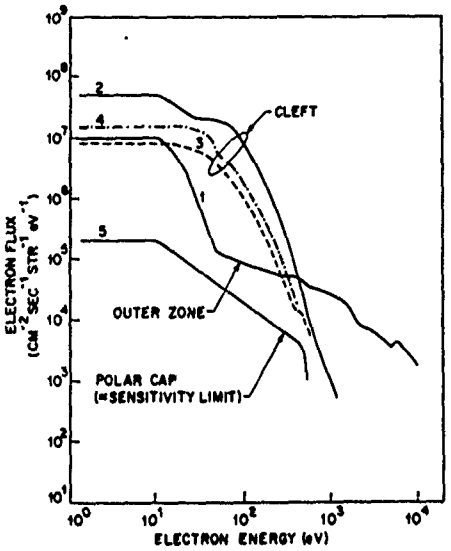

Fig. 4. Representative electron particle flux as a function of energy. Numbers refer to locations labeled in Figure 2.

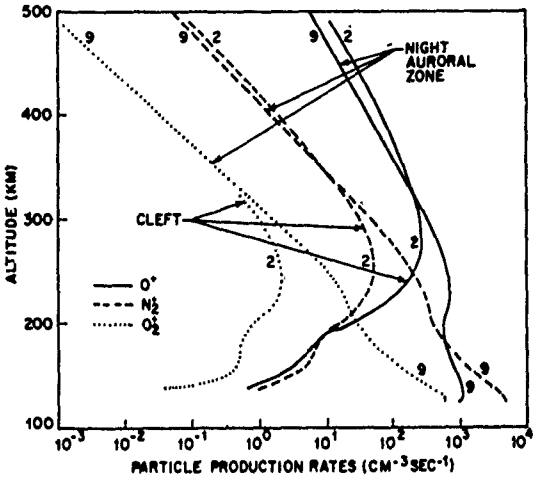

Fig. 6. Production rates of O^+, N_2^+, and O_2^+ ions by the electron particle fluxes at locations 2 and 9 of Figures 2 and 3.

sector (16 min, 20 s, Figure 3) (J. R. Burrows, private communication, 1976). The limit of closed field lines in the night sector of Figure 7 is consistent with this observed boundary. The tubes were convected slowly through precipitation regions 8–10 as required by the model, and as we shall see, these precipitation regions produced considerable ionization in the slowly convecting tubes.

The flow pattern of Figure 7 in the dayside cleft region and over the polar cap is reasonably consistent with that derived from vector ion velocity data by *Heelis et al.* [1976]. Flow across the cleft and into the polar cap is observed between approximately 0900 and 1500 MLT as has been assumed herein, and the general flow pattern of Heelis et al. presented with corotation removed in their Figure 8 would, with corotation restored, look similar to that of our Figure 7. The Harang discontinuity and stagnation points must exist in any reasonable model at approximately the locations indicated in Figure 7, and the flow must approach corotation in the vicinity of 55°Λ. The major discrepancy between experimental measurements and the 'time average' representation presented in Figure 7 appears to be in the magnitude of the velocity equatorward but in the near vicinity of the limit of the closed field lines. The measured velocity is of the order of 1 km/s, whereas the model velocities with corotation removed are of the order of 0.1 km/s. The measured velocity does approach corotation velocity somewhere between 70°Λ and 50°Λ [*Heelis et al.*, 1976]. The velocities with which the plasma tubes were trans-

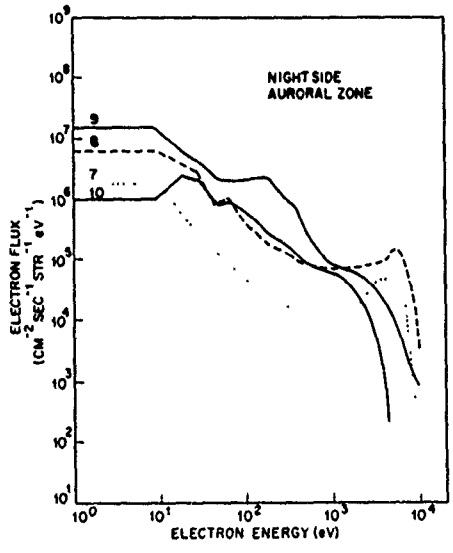

Fig. 5 Representative electron particle flux as a function of energy. Numbers refer to locations labeled in Figure 3.

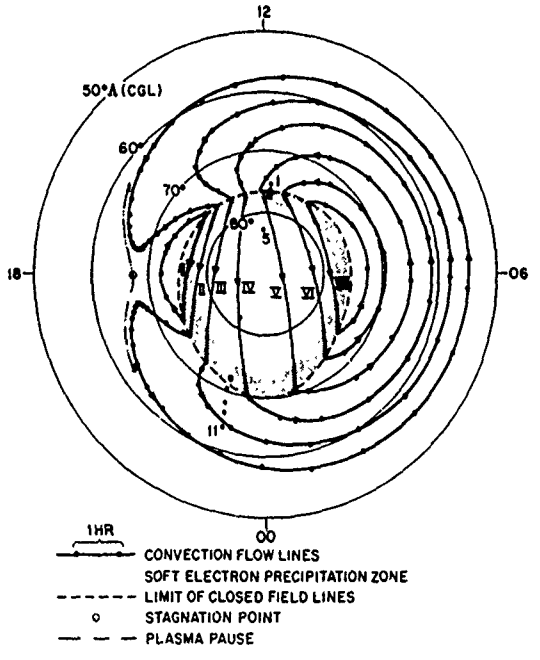

Fig 7. Flow paths around which time-dependent plasma response was computed Locations of electron spectra are indicated by the numbered dots. Numbers correspond to those in Figures 2 and 3.

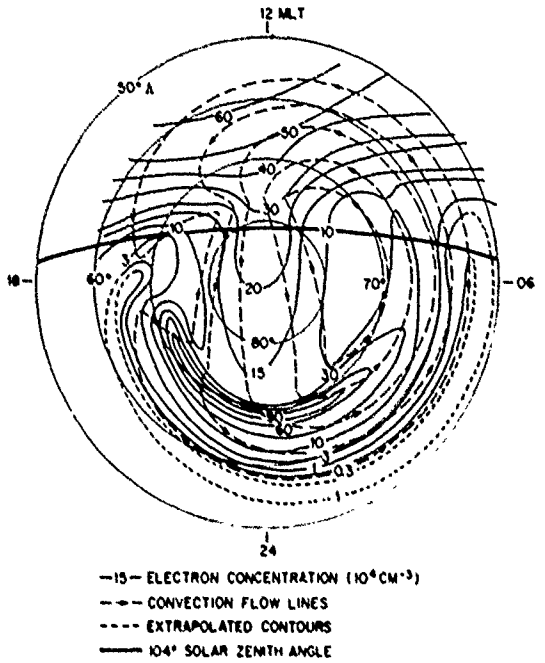

Fig. 8. Contours of N_mF_2 derived from the numerical analysis. The short-dashed portions of contours are extrapolated contours

ported across the cleft and polar cap are reasonably consistent with observation.

The finite time steps in the numerical analysis were less than or equal to 5 min. In regions where the ion production rate was changing rapidly, the time step was decreased appropriately.

RESULTS

Contours N_mF_2 derived from the numerical results are shown in map view in Figure 8. The maximum electron concentration in each vertical profile around the several flow paths was plotted and subsequently contoured. The short-dashed portions of the contours equatorward of the lowest latitude path on the nightside of the earth are extrapolated. Numerical

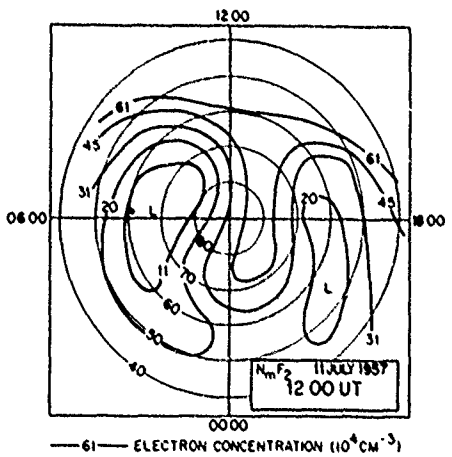

Fig. 9 Synoptic N_mF_2 contours for the Antarctic polar region (after *Sato and Rourke* [1963] and reproduced by *Thomas and Andrews* [1969]) Coordinates are geographic coordinates

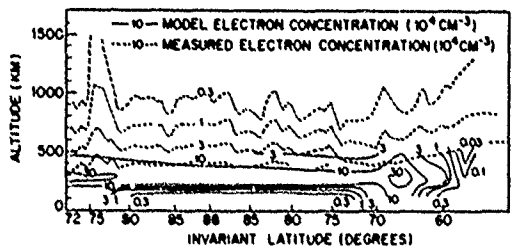

Fig. 10. Comparison of numerically computed electron concentration with that measured by the topside sounder experiment on Isis 2 in vertical profile.

computations for flow paths equatorward of the plasmapause were not performed for this study. Figure 9 shows experimental data included for later comparison.

A local noon–midnight vertical profile comparison of the numerically computed electron concentration with the observed electron concentration is shown in Figure 10. The observed data are from the topside sounder experiment on Isis 2 for the same pass as that from which the energetic electron flux data were derived. Comparison of the model results with the topside sounder data is meaningful in the altitude interval 350–500 km.

In Figure 11 we show a comparison of the computed electron concentration in vertical profile with the plasma tube convecting and with it stationary (steady state) at two locations along path IV. The observed electron concentration is also indicated. Figure 12 shows the computed electron concentration at midnight on path II. The plasma within the convecting tube in this region of path II is in a steady state condition.

DISCUSSION

The computed electron concentration shown in map view in Figure 8 shows several of the features characteristic of the polar ionosphere. First, a 'tongue' of plasma extends from the

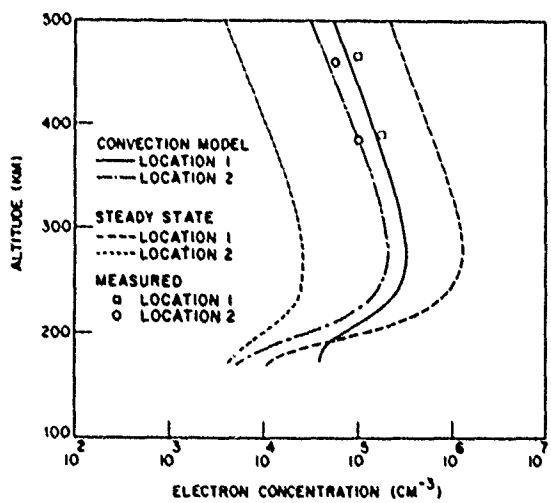

Fig. 11 Comparison of numerically computed electron concentration profiles, convecting and steady state, in the cleft (location 1) and within the polar cap (location 2) with measured concentration Location 1 corresponds to 77°Λ, 1154 MLT, 100° SZA, and particle spectrum 2 Location 2 corresponds to 84°Λ, 2100 MLT, 117° SZA, and particle spectrum 5

local noonside of the earth across the polar cap to the nightside. Manifestations of this tongue in time-averaged f_0F_2 data [*Pike*, 1971] and in Alouette 1 topside sounder data at 350-km altitude [*Nishida*, 1967] were presented in the previous paper [*Knudsen*, 1974]. In Figure 9 we have reproduced synoptic N_mF_2 data for the Antarctic polar region in geographic coordinates [*Sato and Rourke*, 1963; reproduced by *Thomas and Andrews*, 1969]. A tongue is clearly visible with low concentration regions on either side. The tongue and low concentration regions on either side are reproduced in the numerical results. Not present in Figure 9 are the ridge of ionization produced by auroral electron precipitation and the deep trough present in the numerical results. These discrepancies will be addressed hereafter. The region of low concentration on the local evening side of the tongue in the numerical model results from the presence of a stagnation point outside the region of particle precipitation (Figure 7) and direct solar photon production. Near the stagnation point in local winter the tubes of plasma move sufficiently slowly for the concentration to decay to low values. The region of low concentration on the morning side of the tongue in the numerical model results from lack of significant exposure of the plasma tubes to the sun and to the more intense nightside auroral electron precipitation at latitudes below 70°Λ in the present model.

The direct solar photons are able to produce a significant F layer for solar zenith angles from 0° up to approximately 104° (compare Figure 1). On the midnight side of the 104° SZA of Figure 8, only the scattered photons make a contribution to the ion production.

In the time-averaged data presented by *Nishida* [1967] a maximum existed in the evening sector at about 60°Λ. The cause of the maximum is uncertain, although *Nishida* [1967] assumed that it was a manifestation of the mid-latitude evening increase [*Evans*, 1965]. The data used for the averaging included data from August 29 to November 10, so that the stagnation point would have been illuminated by direct solar photons at nearly all universal times. The maximum is not evident in the data presented by *Pike* [1971] or by *Sato and Rourke* [1964].

No significant increase in N_mF_2 was evident in the numerical results in the cleft region (Figures 8 and 10). As has been pointed out previously [*Knudsen*, 1974], a large increase cannot be expected if the plasma is convected across the cleft at 1 km s^{-1} or the present example the maximum increase to be expected is

$$\Delta N_mF_2 \sim \beta r_i \sim 2 \times 10^{-9} \text{ cm}^{-3} \text{ s}^{-1} \times 120 \text{ s} \simeq 2.4 \times 10^{-7} \text{ cm}^{-3}$$

The value is only 10% of N_mF_2 prior to entry of the plasma into the cleft. Had the electron concentration been in a steady state in the cleft region, the value of N_mF_2 would have been a factor of 4 larger in the cleft than just equatorward of the cleft (Figure 11). The observed electron concentration at 400-km altitude does show a small increase in concentration at the cleft. We assume this to be primarily a result of the heating of the electron gas as the tube convects across the cleft. The increase in observed concentration in the cleft is small at 400 km but increases with altitude. This behavior indicates an increase in scale height and not an increase in N_mF_2. The increase would be independent of altitude if the electron and ion temperature were held constant, as is evidenced in the numerical results of Figure 11. As has been pointed out previously, the numerical model did not include energy balance, and the electron and ion temperatures were arbitrarily set equal to the neutral temperature.

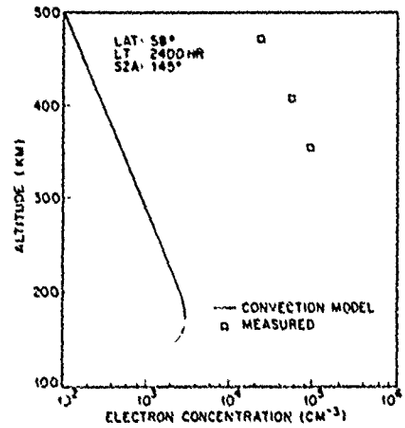

Fig. 12. Computed electron concentration profile at 2400 MLT on path II. The convecting and steady state solutions are the same. The observed electron concentration is also shown.

The computed electron concentration compares favorably with the topside sounder electron concentrations in the altitude interval in which the two sets of data overlap. The 10×10^4 cm^{-3} contours of both sets of data coincide rather well from 75°Λ on the dayside to 75°Λ on the nightside of the model. The prominent variations in concentration exhibited by the topside sounder data, especially at higher altitude, are produced by increases in the electron and ion temperatures. This is evidenced, as was previously mentioned, by the decrease in electron concentration variation as the altitude decreases. The model results are not expected to reproduce these variations because the electron and ion temperatures were held constant. The increase in concentration of the model results at 67°Λ in the night sector resulted from the increase in ion production rate produced by energetic electrons (regions 8–10). The concentration trough at ~57°Λ results from a lack of production and a long decay time. These latter features do not occur in the experimental data.

The nearly constant value of N_mF_2 over the polar cap evidently results from rapid convection of plasma from the dayside of the cleft. The concentration profiles that would occur without convection (steady state) are shown in Figure 11 and are compared with the profiles resulting from convection. The nonconvecting profile at location 2 is an upper limit profile computed from the production rates of ions for the upper limit particle precipitation flux labeled 5 in Figures 2 and 4. The profile would be identical to the steady state profile in Figure 12 were the particle flux zero.

Because the polar cap F layer statistically has a large concentration and decays across the cap from noon to midnight in a manner consistent with convection [*Nishida*, 1967; *Knudsen*, 1974], it is reasonable to infer that F layer plasma must be convected rather steadily across the cleft near the local noontime sector. Were convection of ionospheric plasma across the cleft and on across the polar cap to cease for a period of several hours, the polar cap F layer would decay by as much as an order of magnitude.

The ridge of high ion concentration occurring in the numerical results equatorward of 70° on the nightside of the earth (Figure 8) is produced by assumed slow convection of plasma through the intense particle precipitation zones represented by spectra 8 and 9 of Figure 3. This ridge of ionization is not

present in the observed electron concentration (Figure 10). Statistical studies also show little or no enhancement in the nightside auroral zone [see *Knudsen*, 1974]. Suppression of such a ridge could be accomplished by moving the plasma through these zones rapidly. Rapid convection would not permit buildup of ionization in a tube as it crossed the zone(s) of high particle precipitation. The buildup may also be suppressed through an increased loss rate within the auroral zone [*Schunk et al.*, 1976].

A trough region of low ion concentration was produced in the numerical results equatorward of the ridge of high ion concentration from approximately 1800 MLT to 0600 MLT. The trough resulted from the slow convection of plasma near the evening stagnation point at which location the solar zenith angle was too large for direct solar photons to maintain the F_2 layer ion concentration at a high value against the normal ion loss processes and polar wind escape. A 'steady state' level of ion concentration of flow line 11 around the nightside of the polar region was maintained by the scattered solar photon flux level assumed to be present in the model. The trough disappears on the morning side as the plasma tube emerges into the direct solar photon flux. The ionization level in the trough would be least near midnight and greater toward the evening and morning sectors in a more realistic model in which the scattered solar photon flux decreased with increasing solar zenith angle.

The deep trough evident in the numerical results (Figures 8 and 10) did not appear in the topside sounder data. The probable explanation is that variation of the convection electric field and hence flow paths with time prevents the development of the deep trough. The flow paths must be steady for periods of the order of 24 hours for a deep trough to develop in the manner suggested by *Knudsen* [1974] and demonstrated in the present numerical results. As was pointed out earlier, the magnetic AE index was small and steady except for two short excursions for 28 hours prior to the orbit selected for analysis. Hence the conditions for development of a trough by slow convection would seem to have been fulfilled as well as one could expect. Resolution of this discrepancy must await future studies.

SUMMARY AND CONCLUSIONS

The time-dependent behavior of the F layer plasma within a magnetic flux tube is computed for the tube carried around several flow paths in the polar regions. The flow paths are those proposed in a previous paper by *Knudsen* [1974]. As the tube traverses each path, it is subjected to time-dependent ionization rates from direct and scattered solar photons and precipitating energetic electrons. Ionization rates for the energetic electrons are computed from energy spectra observed by the Isis 2 soft particle spectrometer. The numerical results are presented in the form of a map view of N_mF_2 contours, electron concentration in vertical section over the magnetic pole from noon to midnight, and several vertical profiles of electron concentration at several locations for both convecting and nonconvecting flux tubes. The computed electron concentrations are compared with observed electron concentrations from topside sounder data obtained in the same satellite pass as the energetic electron flux data.

The proposed convection field produced a tongue of F layer plasma extending from the dayside of the cleft over the polar cap with concentrations consistent with the observed concentrations. Had the F layer been assumed to be stationary (nonconvecting) within the polar cap, the computed concentrations would have been a factor of 10 too small. Concentration 'lows' on either side of the tongue are consistent with some previously observed synoptic data. No significant increase in N_mF_2 occurred at the cleft in the model results. This behavior is consistent with the observed behavior. In diffusive equilibrium an increase of approximately 4 in concentration would have existed.

The presence of the polar cap F layer with peak electron concentrations typically in excess of 10^5 cm^{-3} implies, when it is interpreted in the light of the present study and a previous study [*Knudsen*, 1974], that F layer plasma is rather steadily convected across the cleft in the local noontime sector and on across the polar cap.

A ridge of ionization not present in the observed ionosphere was predicted by the numerical simulation in the nightside auroral zone. Several zones of particle precipitation were measured by the Isis 2 satellite, and the plasma tubes were transported at high velocity (1 km/s) only through the highest latitude zone. Evidently, the plasma tubes are transported rapidly across zones of high precipitation, and/or some additional loss mechanism is operative in the precipitation zones.

A trough of low electron concentration was predicted by the numerical model which extended from approximately 1800–2400 MLT to approximately 0600 MLT. The electron concentration in the trough was constant with local time and maintained by the assumed constant flux of solar EUV photons scattered into the night ionosphere. No trough was present in the Isis 2 topside sounder data. A satisfactory explanation for the latter discrepancy must await future studies.

Acknowledgments. The authors wish to thank J. H. Whitteker, C. D. Anger, and J. R. Burrows for supplying electron concentration, airglow, and energetic electron flux data, respectively. R. W. Schunk kindly made his computer program available and helped greatly with discussions of the program behavior. This research was supported by Lockheed independent research funds, NASA contract NASw-2550, NSF grant DES75-03985, and AFGL contract F19628-76-C-0005.

The Editor thanks J. A. Fedder and H. Rishbeth for their assistance in evaluating this paper.

REFERENCES

Banks, P. M., C. R. Chappell, and A. F. Nagy, A new model for the interaction of auroral electrons with the atmosphere: Spectral degradation, backscatter, optical emission, and ionization, *J. Geophys. Res.*, *79*, 1459, 1974.

Chen, W. M., and R. D. Harris, An ionospheric *E* region nighttime model, *J. Atmos. Terr. Phys.*, *33*, 1193, 1971.

Evans, J. V., Cause of the mid-latitude evening increase, *J. Geophys. Res.*, *70*, 1175, 1965.

Heelis, R. A., W. B. Hanson, and J. L. Burch, Ion convection velocity reversals in the dayside cusp, *J. Geophys. Res.*, *81*, 3803, 1976.

Hinteregger, H. E., L. A. Hall, and G. Schmidtke, Solar XUV radiation and neutral particle distribution in July 1963 thermosphere, *Space Res.*, *5*, 1175, 1965.

Jacchia, L. G., Revised static models of the thermosphere and exosphere with empirical temperature profiles, *Spec. Rep. 332*, Smithsonian Astrophys. Observ., Cambridge, Mass., 1971.

Knudsen, W. C., Magnetospheric convection and the high-latitude F_2 ionosphere, *J. Geophys. Res.*, *79*, 1046, 1974.

Lui, A. T. Y., and C. D. Anger, A uniform belt of diffuse auroral emission seen by the Isis-2 scanning photometer, *Planet. Space Sci.*, *21*, 799, 1973.

Nishida, A., Average structure and storm time change of the polar topside ionosphere at sunspot minimum, *J. Geophys. Res.*, *72*, 6051, 1967.

Pike, C. P., A comparison of the north and south polar *F* layers, *J. Geophys. Res.*, *76*, 6875, 1971.

Sato, T., and G. F. Rourke, Antarctic Research and Data Analysis, *Sci. Rep. 8*, AVCO Corp., Wilmington, Mass., 1963.

Sato, T., and G. F. Rourke, *F* region enhancements in the Antarctic, *J. Geophys. Res.*, *69*, 4591, 1964.

about a factor of 4 smaller than that introduced by the uncertainties in the measurements of the slant ranges, it has not been corrected in the final results. Uncertainties of ±10 km in the slant range and assumed altitude yield a spread of about ±0.4° in the latitude.

During the December period of observation, periodic measurements of the cleft location were also made by the Isis 2 satellite. The satellite measurements are shown by solid triangles in the plots of λ_c for December 4 and December 6. Absorption prevented ionosonde measurements at the time of the December 4 satellite crossing. Simultaneous measurements were obtained on December 6 and on another day later in the month when IMF data were not available. On these two occasions the ionosonde and satellite measurements of the cleft's position agreed to within 0.5°.

Magnetic conditions during the observations are shown in Table 2. The local K for College, a station near the magnetic longitude of the ionosondes, is shown as well as the planetary index Kp.

December 4, 1974

As is true throughout most of the periods to be covered, this time was fairly quite magnetically (Figure 4). The College magnetogram showed a small amount of activity at 2020, 2130, and 2350. Small positive bays (~50 γ) were recorded at Leirvogur from 2220 to 2250 and at 2340.

The z component of the IMF shows small fluctuations throughout the period; these fluctuations are probably due to waves propagating upstream from the bow shock [*Heppner et al.*, 1967]. B_z is mostly positive, but does turn significantly negative from 2128 to 2222 UT.

The cleft measurements are unfortunately prevented by D region absorption of the ionosonde signals from 1900 and 2100. Just prior to 1900, Δλ is between +1° and +2°. The cleft remains mostly poleward of its expected position until ~2200, when it begins to move equatorward. This motion continues until about 2240, when the equatorward edge comes to rest over Sachs Harbor. Equatorward motion resumes at 2330, and for the remainder of the period the equatorward edge was at least as far south as Cape Parry.

Because of the gap caused by the absorption it is difficult to associate with certainty the equatorward motion of the cleft at 2200 with the southward turning of B_z at 2128. The sudden equatorward movement of the cleft at 2330 is quite clear, however, and coincides (within the resolution available) with the onset of the small positive bay at Leirvogur.

December 6–7, 1974

At the time at which the IMF measurements begin, B_z is northward at about +4 γ and is slowly decreasing (Figure 5). Unfortunately, there is a large gap in the IMF data between 2100 and 2200. It is thus not possible to determine exactly when B_z first becomes negative.

The cleft first begins to move equatorward at about 2200 UT, possibly soon after B_z goes negative. This motion continues until about 2215, when both Δλ and B_z become more positive. B_z remains close to zero until 2313, when it turns sharply southward. During this time the cleft first moves poleward, peaking at ~2230, then moves equatorward until ~2250, and then moves poleward until 2309, when it moves sharply equatorward.

Because of the gap in the magnetic data it is not possible to establish the timing between the initial equatorward motion of the cleft at 2200 and the southward turning of the field. Nor is it clear why Δλ goes negative again after 2230. It may be that the motion of the cleft from 2200 to 2305 is related to oscillations in the position of the magnetopause, such as have been reported by, for example, *Aubry et al* [1970] and derived theoretically by *Holzer and Reid* [1975]. The period in the present case (~30 min) is longer by a factor of 2 or more than the reported periods, however.

The drop in Δλ at 2309 may be associated with the sharp change in B_z at 2313. Allowing for the assumed propagation delay, Δλ thus drops about 10 min before the change in B_z. The inconsistency may be due to the fact that the satellite was ~18 R_A above the ecliptic plane and that the discontinuity was in a plane other than that assumed. These circumstances may invalidate our simple model for the propagation of changes in B_z. Following this drop the cleft remains about 1.5° below its expected position and does not return poleward as it did following the decrease of 2200. This difference might be accounted for by the fact that B_z remains significantly southward after 2313, while it became more positive following the decrease at 2200.

Since the geomagnetic activity is so low prior to 2345, we assume that the motion of the cleft up to this time is due principally to changes in the IMF. On the other hand, from 2345 on, B_z remains southward, and one would not expect it to be responsible for the equatorward motion of the cleft at 0015. This motion may be associated with the weak geomagnetic activity from ~2400 on.

January 1–2, 1975

B_z is relatively smooth on this day and exhibits three well-defined southward turnings, one sharp drop at 2220 and two significant zero crossings at ~2242 and 2355 (Figure 6). The nightside magnetograms are again very quiet, but Leirvogur did record a sharp negative bay of < 100 γ beginning at 0135.

Although there is little magnetic activity and B_z is northward until ~2240, the cleft is found equatorward of its expected position throughout the period. The sharp drop in B_z near 2220 does not appear to provoke a response in λ_c, possibly because B_z does not go very negative or because the cleft is already somewhat equatorward. The cleft does move equatorward at 2245, about 5 min after the southward turning of B_z. B_z returns to positive values within several minutes, but Δλ remains at about −1.5° for the ensuing hour. Why Δλ stays depressed is not clear, there is only a very small amount of magnetic activity (ΔH < 50 γ) recorded on the nightside at this time.

When B_z becomes negative again at 2355, Δλ actually becomes more positive, in contrast to the earlier results. B_z remains near −1 γ throughout the rest of the period, but the cleft begins to move equatorward again at 0100. The cause of this motion is also unclear, it may be simply an extreme example of the diurnal motion.

January 9–10, 1975

During this interval, B_z again shows evidence of upstream waves and does not exhibit any well-defined sustained changes in direction (Figure 7). B_z is positive throughout most of the record. Aside from some small disturbances from ~2100 to ~2230, nightside magnetic activity is quiet.

During the first hour the cleft is moving poleward. At 2200, Δλ starts to become more negative, possibly in response to the geomagnetic activity occurring at that time. For the remainder of the period the cleft remains a degree or so equatorward of its expected position.

VOL. 82, NO. 1 JOURNAL OF GEOPHYSICAL RESEARCH JANUARY 1, 1977

Ionosonde Observations of the Northern Magnetospheric Cleft During December 1974 and January 1975

G. S. STILES,[1] E. W. HONES, JR.,[2] J. D. WINNINGHAM,[3] R. P. LEPPING,[4] AND B. S. DELANA[5]

During December 1974 and January 1975 the northern magnetospheric cleft was monitored by ionosondes at Cape Parry and Sachs Harbor, Northwest Territories, Canada, in support of rocket shots into the cleft. Ionograms were taken nominally at 15-min intervals but as rapidly as two per minute during times of particular interest. Analysis of 5 days of data shows the ionosphere at cleft latitudes to be very complex and dynamic. The ionograms often show considerable structure and can change appearance significantly in a minute or two. The cleft at times appears to move equatorward in response either to a southward turning of the interplanetary magnetic field or to the occurrence of geomagnetic disturbances. This response is in agreement with the conclusions of previous satellite studies. Behavior contrary to this generalization is not uncommon, however, and therefore it may not always hold on time scales considerably shorter than the satellite orbital period of ≥1 hour. The rate of the cleft's motion may vary from ~0.05 to ~0.5 deg/min.

INTRODUCTION

Since the initial discovery of the magnetospheric cleft by satellite instrumentation [*Heikkila et al.*, 1970; *Winningham*, 1970; *Heikkila and Winningham*, 1971; *Frank*, 1971; *Frank and Ackerson*, 1971; *Russell et al.*, 1971], considerable effort has been devoted to the investigation of this phenomenon (see the summary by *Vasyliunas* [1974]). This work has shown that the plasma found in the cleft is very much like that seen in the magnetosheath [e.g., *Winningham*, 1972]. The location of the cleft has been found to respond both to changes in the interplanetary magnetic field and to the occurrence of geomagnetic disturbances [*Burch*, 1972; *Kamide et al.*, 1976]. Much of the current study in this field is thus devoted to the relation between the interplanetary and cleft magnetic fields and the mechanism by which the magnetosheath plasma enters the cleft.

During December 1974 and January 1975 two groups launched rockets into the northern cleft in attempts to examine the particle populations, the magnetic field, and the convection of plasma. The success of these experiments depended upon an accurate knowledge of the location of the cleft prior to the launching of the rockets. Ground-based ionosondes were one of the techniques used to monitor the cleft's position. In this paper we describe the results of an analysis of the ionograms made in support of the rocket flights.

The rockets were launched from Cape Parry, located on the Arctic coast of Canada (Figure 1). The December flights were organized by a Canadian group and concentrated on making optical and particle measurements, the initial results are reported by *Shepherd et al.* [1976]. The January flights were a cooperative effort by the Los Alamos Scientific Laboratory (LASL) and the University of Alaska (UAK). Two rockets were launched whose primary purpose was to project barium ion clouds upward along the cleft field lines by means of shaped explosive charges. The rockets also carried particle detectors. The LASL-UAK experiments have been described by *Jeffries et al.* [1975].

A considerable amount of ground based data were taken in support of these flights to aid both in the location of the cleft and in the interpretation of the results. Ionosondes were located at Cape Parry and Sachs Harbor (see Figure 1). Ionosondes have proven most useful in locating the projection of the cleft upon the ionosphere [*Pike*, 1971, 1972; *Winningham and Pike*, 1972; *Pike et al.*, 1974; *Ungstrup et al.*, 1975; *Shepherd et al.*, 1976]. Ionograms were taken nominally at 15-min intervals; however, during periods of particular interest the spacing was decreased to a minute or so.

Optical phenomena were also monitored. Photometers were installed at Cape Parry and Sachs Harbor, and an all-sky camera was located at Sachs Harbor. Some of the photometric observations during this period are described by *Shepherd et al.* [1976]. *Whalen and Pike* [1973] had shown earlier that photometer measurements of 6300-Å emissions may be used to determine the position of the cleft.

Satellite data were used to check the ground-based measurements and to aid in the analysis of the results. The position of the cleft was measured on several passes by the soft particle spectrometer (SPS) aboard Isis 2 [*Heikkila and Winningham*, 1971]. Defense Meteorological Satellite Program satellite photos [e.g., *Pike and Whalen*, 1974] were used to monitor auroral activity. The interplanetary magnetic field (IMF) and solar wind velocity were measured by Imp 8 whenever that satellite was suitably located. One of the principal goals of the present study was to investigate the relation between changes in the IMF and the movement of the cleft. Earlier work [e.g., *Burch*, 1972] indicates that the motion of the cleft is correlated with changes in the z component of the IMF.

RESULTS

Since the ionospheric manifestation of the cleft may be a degree or more wide and since its poleward boundary may not be sharply defined, ionosondes are most useful in tracking the position of the cleft when it is poleward of the sounder. Under these conditions, oblique echoes of the ionosonde radio signals from the cleft's relatively sharp equatorward boundary of ionization will produce unique traces on the ionogram provided that the cleft is not too distant (examples are given by *Pike* [1971, 1972], *Pike et al.* [1974], *Ungstrup et al.* [1975], and *Shepherd et al.* [1976]). During the December and January period this condition was satisfied for 5 of the 7 days on which

[1] Center for Research in Aeronomy, Utah State University, Logan, Utah 84322
[2] University of California, Los Alamos Scientific Laboratory, Los Alamos, New Mexico 87545
[3] University of Texas at Dallas, Richardson, Texas 75080
[4] NASA Goddard Space Flight Center, Greenbelt, Maryland 20771
[5] Geophysical Institute, University of Alaska, College, Alaska 99701

Paper number 6A0690

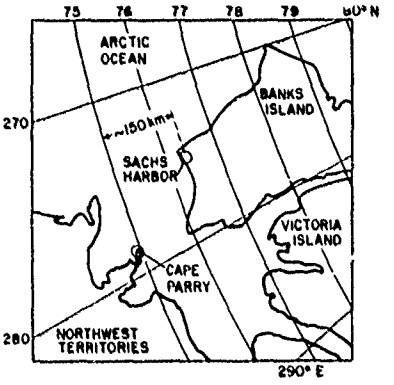

Fig. 1. Rockets were launched from Cape Parry, Northwest Territories, Canada. Ionosondes were located at Cape Parry and Sachs Harbor. Coordinates are invariant geomagnetic latitude and longitude [*Evans et al.*, 1969] at an altitude of 300 km.

IMF measurements were obtained by Imp 8. The discussion below will be limited to ionograms made on those days.

We first examine two sequences of ionograms to give the reader an idea of the type of data upon which the conclusions below are based. These sequences are intended to emphasize the rapid and dramatic variations that can occur in the ionograms and to indicate the problems that may arise when one tries to deduce the position of the cleft.

The first sequence (Figure 2) was made on December 6, 1974, from 2305 to 2325 UT. (The rocket flight described by *Shepherd et al.* [1976] began at 2332:06 UT.) The Sachs Harbor records do not show much change throughout this period. There is some evidence of the normal *X* and *O F* layer traces, but the critical frequencies are not particularly well defined (except at 2315, where the second-order trace is fairly clean). Throughout most of the records there is an irregular feature extending past 5 MHz between 300 and 400 km that shows

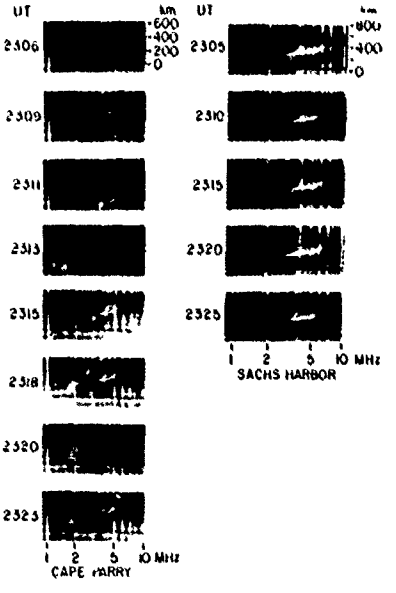

Fig. 2. Ionograms from Cape Parry and Sachs Harbor for December 6, 1974.

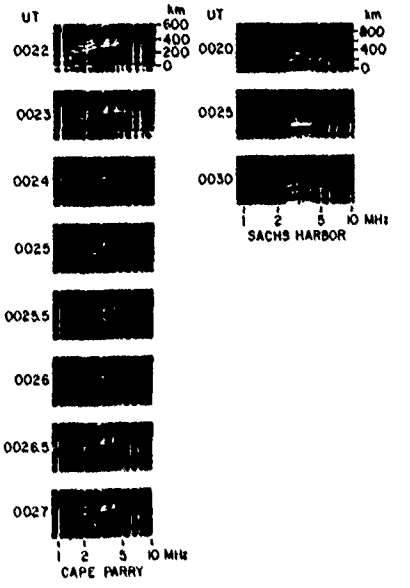

Fig. 3. Ionograms for January 11, 1975.

spreading and only a small amount of retardation at its high-frequency end. Such irregularities are characteristic of the cleft and, with the presence of the obscured *X* and *O* traces, suggest that the equatorward boundary of the cleft is located close to Sachs Harbor.

The Cape Parry records differ greatly from those made at Sachs Harbor. At 2306 the Cape Parry *O* and *X* traces are better defined. At this time the only evidence of the cleft at Cape Parry is several horizontal features just above 5 MHz between about 390 and 510 km. As is explained in the work by *Pike* [1971, 1972], these returns are interpreted as being oblique reflections from ionospheric features that are not directly above the sounder. The closest feature is presumed to be the equatorward edge of the cleft precipitation zone. The measured height (~390 km for the closest feature) thus gives the slant range along the oblique path to the edge of the cleft. The actual altitude of the cleft must be assumed. Note that at 2306, virtually no returns are visible between 300 and 400 km from ~2 to ~3.5 MHz.

In the next ionogram (2309 UT), however, there is a strong oblique return (with retardation at its high- and low-frequency ends) from the cleft between 2 and 5 MHz with a minimum range of ~360 km. It does not appear that this feature is the result of a simple equatorward motion of the cleft; the feature at 430 km (3.5 MHz) at 2306 actually seems to have moved poleward (to ~450 km) by 2309.

By 2311 there is a strong cleft return at ~315 km. There is a hint of a return near this altitude at 2309, and it is not clear whether the strong return at 2309 has moved equatorward or whether a new feature has appeared. The short feature at ~3.4 MHz, ~350 km may be the remains of the strong trace at 2309.

Throughout the remainder of the sequence the ionograms continue to show rapid variations. At times there may be only one predominant trace (2313, 300 km, 3 MHz, and 2320, 340 km, 3 MHz), while minutes later several weaker cleft returns may be detectable (2315 and 2323). (Note that the appearance of a strong sharp return at short range seems to preclude observation of weaker returns at longer ranges.) The virtual

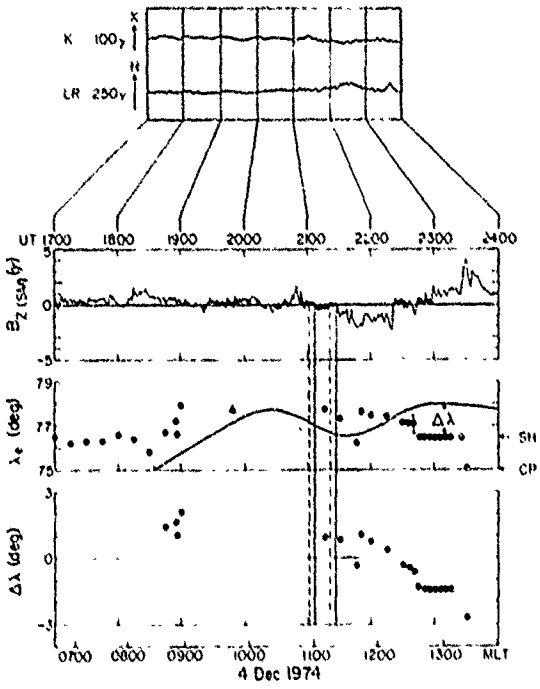

Fig. 4 Ground magnetograms, interplanetary magnetic field, and invariant latitude of the cleft for December 4, 1974. See text for explanation. Magnetic local time is shown along the bottom.

heights of the returns may vary by several tens of kilometers from record to record. It is difficult to account for these changes in height and appearance by assuming that the cleft as a whole is simply moving latitudinally.

The second sequence of ionograms (Figure 3) was made just prior to the second LASL-UAK barium release, which occurred at 0032 UT on January 11, 1975. As in Figure 2 the Sachs Harbor records indicate that the equatorward edge of the cleft is very close and possibly overhead. The *F* layer (*X* and *O*) traces show considerable frequency spreading. At 0020 a broad trace extending from about 2.7 MHz at 200 km to about 5.7 MHz at 230 km may be seen; this may be an auroral *E* layer seen obliquely. Five minutes later this feature has increased about 30 km in range. Note that the space between 200 and 300 km is almost filled at 3 MHz. At 0030 there are two strong traces, one like the first feature at 0020 at 200 km and another clefflike trace near 260 km. A fainter trace may be seen near 350 km.

The Cape Parry records in this interval show, as in the previous example, more variation than do those from Sachs Harbor. Throughout the sequence the *X* and *O* returns from the normal *F* layer may be seen. The traces at ~300 and ~350

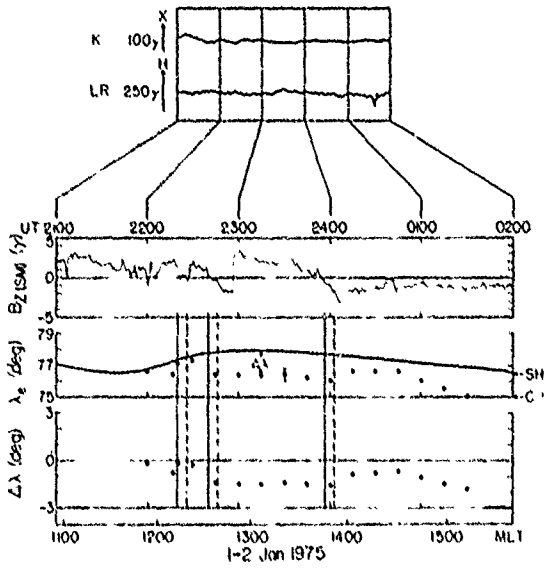

Fig. 6 January 1–2, 1975.

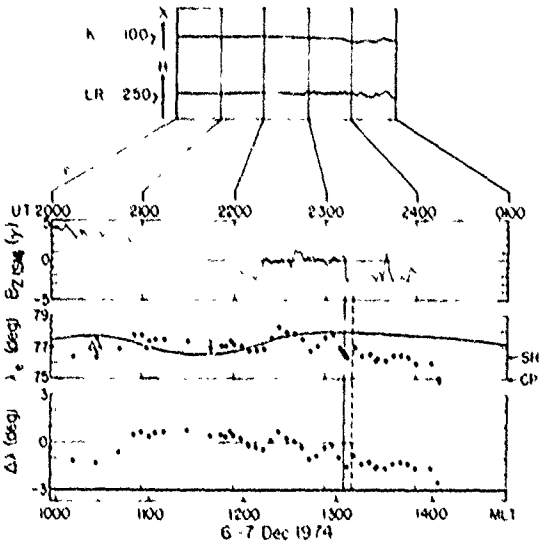

Fig. 5 December 6–7, 1974

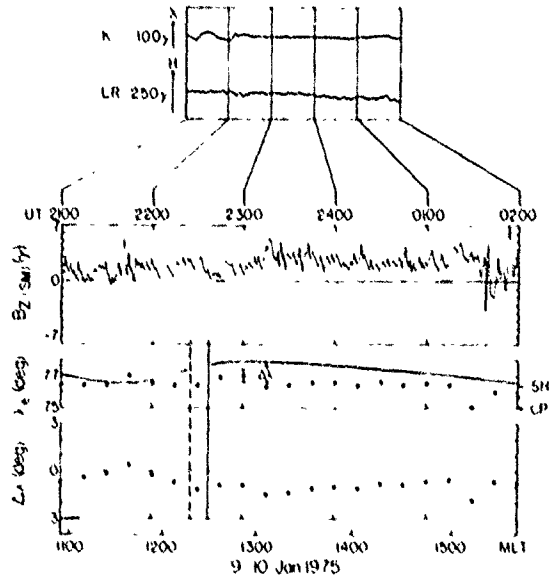

Fig. 7 January 9–10, 1975

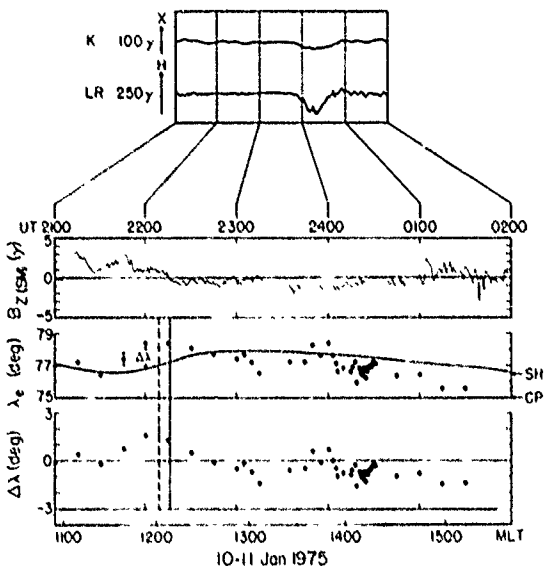

Fig. 8. January 10-11, 1975

km between 1.5 and 2.5 MHz, which show the same shape as the *O* trace, are probably returns from a tilted *F* layer poleward of the station and in the vicinity of the equatorward edge of the cleft.

The cleft returns in this sequence may be found between ~300 and ~500 km at frequencies above (to the right of) the *X* trace. At 0022 two cleft returns may be seen at 300 and 340 km. Over the next 5 min these returns change rapidly. It appears that all the traces may be drifting poleward at a rate (~0.5 km/s) sufficient to produce an increase in slant range of ~20 km/min. Drifts of similar magnitude and direction have been reported for the *F* layer plasma in the cleft [*Knudsen*, 1974] and dayside auroral features [*Vorobjev et al.*, 1975]. Note again that at several times, multiple cleftlike returns can be seen.

Before proceeding with the discussion of the analysis of ionograms of this type we should summarize briefly their more important characteristics. First, as is most obvious from the examples, the appearance of the ionograms may change significantly on a time scale of a minute or so, traces may appear and disappear rapidly. Second, the ionograms from the two stations may differ greatly (this is due to the different positions of the two stations relative to the cleft and may reflect significant changes in the nature of the cleft over distances of ~100 km). These factors greatly complicate the process of tracking the cleft by simply measuring the slant range of apparently oblique returns.

The results of scaling the ionograms are shown in Figures 4-8. At the top of each figure are shown nightside magneto-

TABLE 1. Position of Imp 8 in Solar Magnetospheric Coordinates

Date	r, R_E	ϕ, deg	θ, deg
December 4-5, 1974	33.6	303.2	6.4
December 6-7, 1974	27.6	21.3	42.9
January 1-2, 1975	31.2	83.4	15.1
January 9-10, 1975	33.2	259.1	-14.2
January 10-11, 1975	28.5	287.1	9.7

TABLE 2. College *K* and Planetary *Kp* Magnetic Activity Indices

Date	1800-2100 UT	2100-2400 UT	0000-0300 UT
December 4-5, 1974	1, 1	1, 1	1, 1
December 6-7, 1974	0, 0+	0, 1-	0, 2-
January 1-2, 1975	1, 2	1, 2-	0, 1+
January 9-10, 1975	1, 1-	0, 1+	0, 2-
January 10-11, 1975	1, 0+	0, 1+	0, 2

K is the first number in each entry, and *Kp* is the second.

grams from Kiruna (magnetic midnight, ~2100 UT) and Leirvogur (magnetic midnight, ~0000 UT).

In the second panel is shown the z component (in solar magnetospheric coordinates, positive northward) of the IMF. These measurements are 1.02-min averages. The data show occasional gaps of several minutes. The position of the satellite is given in Table 1. At all times of interest, Imp 8 was in the solar wind.

The solid vertical lines drawn across the panels mark approximate times when B_z goes negative. The dashed vertical lines are estimates of the times at which the changes in B_z should reach the nose of the magnetosphere if the associated change in the total field vector is primarily a latitudinal one and at approximately the fixed longitudinal direction of 135° (or 315°) and if this discontinuity (or gradient) moves radially outward from the sun at ~ 450 km/s. (The longitudinal direction and the solar wind speed have been checked against the available data and faithfully apply to most events within acceptable error limits.) Since we are limited to data from one satellite, we obviously cannot determine with certainty the surface of the change in B_z, the dashed lines are intended only as rough estimates.

The third panel gives the absolute location λ_c in corrected geomagnetic latitude of the equatorward edge of the cleft as determined by the method described below. The fourth panel gives the deviation $\Delta\lambda$ of the cleft from its expected position. The expected position, which is a function of magnetic local time, is a smoothed version of the results of *Winningham* [1972] and is shown as a solid line in the third panel. It may be that Winningham's curve should be shifted a degree or so to higher latitudes [see *Burch*, 1972] because of seasonal variations. We are more interested in the motion of the cleft than in its absolute position, however, and the correction for diurnal variations given by Winningham's curve is considered adequate.

The latitude of the cleft is calculated from the measured range of the closest echo and an assumed altitude of 260 km [see *Pike et al.*, 1974]. All ionograms containing oblique echoes are used. In the initial calculations a flat earth is assumed for convenience. The distance along the earth from the ionosonde to a point directly below the reflecting layer is derived and then translated into degrees of latitude. This value is then added to the invariant latitude of the ionosonde to give the location of the equatorward boundary of the cleft. The invariant latitudes of the ionosonde stations are taken from the 300-km altitude values of *Evans et al.* [1969] (see Figure 1).

For the relatively small ranges of latitude involved (~4°) the use of the flat earth approximation does not result in very large errors. The correction to the position of the cleft's lower boundary is less than 0.1° and approaches zero as the cleft moves southward toward the ionosondes. Since this error is

about a factor of 4 smaller than that introduced by the uncertainties in the measurements of the slant ranges, it has not been corrected in the final results. Uncertainties of ±10 km in the slant range and assumed altitude yield a spread of about ±0.4° in the latitude.

During the December period of observation, periodic measurements of the cleft location were also made by the Isis 2 satellite. The satellite measurements are shown by solid triangles in the plots of λ_c for December 4 and December 6. Absorption prevented ionosonde measurements at the time of the December 4 satellite crossing. Simultaneous measurements were obtained on December 6 and on another day later in the month when IMF data were not available. On these two occasions the ionosonde and satellite measurements of the cleft's position agreed to within 0.5°.

Magnetic conditions during the observations are shown in Table 2. The local K for College, a station near the magnetic longitude of the ionosondes, is shown as well as the planetary index Kp.

December 4, 1974

As is true throughout most of the periods to be covered, this time was fairly quite magnetically (Figure 4). The College magnetogram showed a small amount of activity at 2020, 2130, and 2350. Small positive bays (~50 γ) were recorded at Leirvogur from 2220 to 2250 and at 2340.

The z component of the IMF shows small fluctuations throughout the period; these fluctuations are probably due to waves propagating upstream from the bow shock [*Heppner et al.*, 1967]. B_z is mostly positive, but does turn significantly negative from 2128 to 2222 UT.

The cleft measurements are unfortunately prevented by D region absorption of the ionosonde signals from 1900 and 2100. Just prior to 1900, $\Delta\lambda$ is between +1° and +2°. The cleft remains mostly poleward of its expected position until ~2200, when it begins to move equatorward. This motion continues until about 2240, when the equatorward edge comes to rest over Sachs Harbor. Equatorward motion resumes at 2330, and for the remainder of the period the equatorward edge was at least as far south as Cape Parry.

Because of the gap caused by the absorption it is difficult to associate with certainty the equatorward motion of the cleft at 2200 with the southward turning of B_z at 2128. The sudden equatorward movement of the cleft at 2330 is quite clear, however, and coincides (within the resolution available) with the onset of the small positive bay at Leirvogur.

December 6-7, 1974

At the time at which the IMF measurements begin, B_z is northward at about +4 γ and is slowly decreasing (Figure 5). Unfortunately, there is a large gap in the IMF data between 2100 and 2200. It is thus not possible to determine exactly when B_z first becomes negative.

The cleft first begins to move equatorward at about 2200 UT, possibly soon after B_z goes negative. This motion continues until about 2215, when both $\Delta\lambda$ and B_z become more positive. B_z remains close to zero until 2313, when it turns sharply southward. During this time the cleft first moves poleward, peaking at ~2230, then moves equatorward until ~2250, and then moves poleward until 2309, when it moves sharply equatorward.

Because of the gap in the magnetic data it is not possible to establish the timing between the initial equatorward motion of the cleft at 2200 and the southward turning of the field. Nor is it clear why $\Delta\lambda$ goes negative again after 2230. It may be that the motion of the cleft from 2200 to 2305 is related to oscillations in the position of the magnetopause, such as have been reported by, for example, *Aubry et al.* [1970] and derived theoretically by *Holzer and Reid* [1975]. The period in the present case (~30 min) is longer by a factor of 2 or more than the reported periods, however.

The drop in $\Delta\lambda$ at 2309 may be associated with the sharp change in B_z at 2313. Allowing for the assumed propagation delay, $\Delta\lambda$ thus drops about 10 min before the change in B_z. The inconsistency may be due to the fact that the satellite was ~18 R_A above the ecliptic plane and that the discontinuity was in a plane other than that assumed. These circumstances may invalidate our simple model for the propagation of changes in B_z. Following this drop the cleft remains about 1.5° below its expected position and does not return poleward as it did following the decrease of 2200. This difference might be accounted for by the fact that B_z remains significantly southward after 2313, while it became more positive following the decrease at 2200.

Since the geomagnetic activity is so low prior to 2345, we assume that the motion of the cleft up to this time is due principally to changes in the IMF. On the other hand, from 2345 on, B_z remains southward, and one would not expect it to be responsible for the equatorward motion of the cleft at 0015. This motion may be associated with the weak geomagnetic activity from ~2400 on.

January 1-2, 1975

B_z is relatively smooth on this day and exhibits three well-defined southward turnings, one sharp drop at 2220 and two significant zero crossings at ~2242 and 2355 (Figure 6). The nightside magnetograms are again very quiet, but Leirvogur did record a sharp negative bay of < 100 γ beginning at 0135.

Although there is little magnetic activity and B_z is northward until ~2240, the cleft is found equatorward of its expected position throughout the period. The sharp drop in B_z near 2220 does not appear to provoke a response in λ_c, possibly because B_z does not go very negative or because the cleft is already somewhat equatorward. The cleft does move equatorward at 2245, about 5 min after the southward turning of B_z. B_z returns to positive values within several minutes, but $\Delta\lambda$ remains at about −1.5° for the ensuing hour. Why $\Delta\lambda$ stays depressed is not clear, there is only a very small amount of magnetic activity (ΔH < 50 γ) recorded on the nightside at this time.

When B_z becomes negative again at 2355, $\Delta\lambda$ actually becomes more positive, in contrast to the earlier results. B_z remains near −1 γ throughout the rest of the period, but the cleft begins to move equatorward again at 0100. The cause of this motion is also unclear, it may be simply an extreme example of the diurnal motion.

January 9-10, 1975

During this interval, B_z again shows evidence of upstream waves and does not exhibit any well-defined sustained changes in direction (Figure 7). B_z is positive throughout most of the record. Aside from some small disturbances from ~2100 to ~2230, nightside magnetic activity is quiet.

During the first hour the cleft is moving poleward. At 2200, $\Delta\lambda$ starts to become more negative, possibly in response to the geomagnetic activity occurring at that time. For the remainder of the period the cleft remains a degree or so equatorward of its expected position.

January 10–11, 1975

B_z is somewhat erratic but shows a fairly clean change in direction from northward to southward at about 2216 (Figure 8). Note that there is a sharp jump in B_z at 2105; the College magnetogram also shows a jump in H at the same time. Such changes in high-latitude magnetic records are often correlated with changes in the IMF [*Burch*, 1972]. This indicates that there may be little propagation delay for the solar wind between Imp 8 and the front of the magnetosphere.

Leirvogur recorded a substorm beginning at about 2350; the negative bay peaked at $\sim -130\ \gamma$ at 0020 and recovered by 0050. Small ($< 50\ \gamma$) fluctuations followed for the next hour. (Note that Leirvogur also detected the small jump at ~2105.)

Prior to 2200, while $B_z > 0$, the cleft is seen to be moving generally poleward. At 2215, close to the southward turning of B_z, the cleft begins to move equatorward. This motion continues for about another hour. The average rate of the motion until 2315, when the cleft appears to reach an equilibrium, is about 0.04°/min.

From 2330 to 2400 the cleft appears to be drifting poleward again. At about 2400, just after the onset of the negative bay at Leirvogur, the cleft rapidly moves about 2° equatorward. For the remainder of the observation, $\Delta\lambda$ remains negative, even though B_z becomes more positive after 0100.

Summary

There are eleven cases when the edge of the cleft shows significant equatorward motion. In agreement with the earlier work mentioned in the introduction it appears that the cleft responds both to changes in the polarity of B_z (four cases, 2200 and 2313 December 6, 2245 January 1, and 2216 January 10) and to the occurrence of geomagnetic disturbances (two cases, 2332 December 4 and 2400 January 10). In 2 of the 11 cases the motion of the cleft did not appear to be associated with either B_z or a magnetic disturbance (2230 December 6 and 0100 January 2). In the remaining cases (2200 December 4, 0015 December 7, and 2200 January 9) several factors precluded forming even tentative conclusions.

In examining eight cases where the cleft moves poleward we find only two (2215 December 6 and 2130 January 10) that may be associated with B_z becoming more positive. Three events occur when B_z does not show any clear change (2250 December 6, 2100–2140 January 9, and 2330–2400 January 10). The January 10 event, which occurs while B_z is negative, may be associated with the onset of a negative bay, there is also a small amount of geomagnetic activity on January 9. The remaining three cases occur either while B_z is positive and decreasing (1900 December 4 and 2030 December 6) or when it has turned southward (2400 January 1).

The cleft appears to respond fairly rapidly to changes in the IMF. The records of December 6–7, January 1–2, and particularly January 10–11 indicate that the cleft may begin to move equatorward within 10 min or less of the time when the change in B_z reaches the front of the magnetosphere.

The velocity of the equatorward motion, once it begins, varies significantly. On December 6–7 and January 1–2 the cleft moved equatorward at about 0.5° min. On December 4 and January 10–11 the rate was less than 0.1° min.

The duration of the motion also varied. When the motion was faster (December 6–7 and January 1–2), it ceased after about 15 min. In those cases of slower motion (December 4 and January 10–11) it continued for about an hour. The total change $\Delta\lambda$ for a single event varies from 1 to 3 deg.

The temporal relation between geomagnetic activity and the cleft's motion is less clear. The records suggest, however, that the cleft begins to move within 10 min or so of the onset of activity. On January 10–11, for example, the negative bay appeared at 2350, and the equatorward motion began at 2402.

Discussion

In the previous section we found evidence that the cleft may at times move equatorward in response to a southward turning of the z component of the IMF and to the occurrence of geomagnetic disturbances. These events agree with the conclusions of earlier work. *Burch* [1972, 1973] analyzed Ogo 4 particle measurements and found that the equatorward boundary of cleftlike precipitation moves to lower latitudes by several degrees during substorms and/or in the presence of negative B_z. *Pike et al.* [1974] monitored the cleft with an airborne ionosonde and found that the cleft typically moved equatorward following a southward turning of B_z. Recently, *Kamide et al.* [1976], combining the Ogo 4 and the Isis 1 data, also found a tendency for the cleft to move equatorward with southward B_z and the occurrence of substorms.

It is important to note that we also found several examples where the motion of the cleft does not correspond to these results. The earlier investigations do provide convincing evidence that on the average, the cleft moves equatorward in response to increasing geomagnetic activity and southward B_z. These conclusions are based largely upon satellite data, however, which provide no more than roughly one measurement of the cleft's position per hour, the conclusions may not hold on a time scale of several minutes.

In the only previous work [*Pike et al.*, 1974] in which the relation between B_z and the cleft's position was studied with high time resolution, it was concluded that the cleft responds to changes in B_z after a delay of about 15 min. Our results suggest that when the cleft does respond, the delay may be as short as ~10 min.

Burch [1972] gives an estimate of the rate at which the cleft moves equatorward following a southward turning of B_z. His value of ~0.1° min is based upon a single measurement of the cleft's position during each event (necessitated by the fact that the data were taken by satellite). In this study, where the measurements are ground based and may be made several times during each event, we have found that the cleft may move equatorward as rapidly as ~0.5° min. However, the rate of motion may fall as low as ~0.05° min.

One of the goals of earlier efforts has been to obtain a quantitative relation between the cleft's location and B_z. *Burch* [1973], for example, derives from his data an expression for the position of the cleft as a function of the average value of B_z over the previous 45 min. Such an expression may agree fairly well with the average behavior of the cleft and those instances where the cleft moves equatorward fairly slowly in response to a southward turning. Since a 45 min average of B_z is used, however, the expression will not be able to account for those cases where the cleft moves a degree or two in only a few minutes (e.g., December 6–7 and January 10–11). Nor will the expression account for those times when the movement of the cleft and B_z appear to be unrelated.

The variation in the response of the cleft implies that any scheme for predicting the cleft's position based upon a fixed length average of B_z will not be accurate at all times. It is important to note that any theoretical description of the mechanism linking the IMF and the position of the cleft must be able to account for such variations. Such a description will apparently have to include other factors, including geomag-

netic conditions [*Kamide et al.*, 1976] and perhaps the state of the ionosphere [*Holzer and Reid*, 1975].

CONCLUSIONS AND SUGGESTIONS

We have reported the results of the analysis of 5 days of ionogram data from two stations located in northern auroral latitudes. The ionospheric manifestation of the cleft has been found to be very complex and dynamic. The returns frequently show considerable structure and may change significantly in just a minute or two.

A clear relation between the position of the cleft and the IMF (or geomagnetic activity) has not emerged from the study of this small sample. Events have been found which agree with earlier conclusions that southward turnings of B_z and geomagnetic activity are associated with equatorward motion of the cleft. Other events, however, indicate that at times the motion may be contrary to that expected and may depend on other causes.

The results do suggest that a program of taking ionograms in high time resolution (spacing, $\lesssim$1 min) would improve our knowledge of the factors that control the cleft's position. The cleft has been found to change rapidly, and it may be that the key to its behavior will be found only when these rapid changes are better understood.

Acknowledgments. The LASL portion of this work was performed under the auspices of the U.S. Energy Research and Development Administration (ERDA). The University of Texas at Dallas portion of this work was supported by ERDA contracts KH-69046-1 and LC5-83449-1, Air Force Cambridge Research Laboratories contracts F19628-75-C-0032 and F19628-76-C-0005, and NASA contract NGR 44-004-124. University of Alaska operations were supported by NASA contract NGR02-001-087. The Kiruna and Leirvogur magnetograms were obtained through the World Data Center A for Solar Terrestrial Physics (geomagnetism). The authors thank the referees for their comments.

The Editor thanks J. A. Whalen and J. H. Whitteker for their assistance in evaluating this paper.

REFERENCES

Aubry, M. P., C. T. Russell, and M. G. Kivelson, On inward motion of the magnetopause during a substorm, *J. Geophys. Res.*, *75*, 7018, 1970.

Burch, J. L., Precipitation of low-energy electrons at high latitudes: Effects of interplanetary magnetic field and dipole tilt angle, *J. Geophys. Res.*, *77*, 6696, 1972.

Burch, J. L., Rate of erosion of dayside magnetic flux based on a quantitative study of the dependence of polar cusp latitude on the interplanetary magnetic field, *Radio Sci.*, *8*, 955, 1973.

Evans, J. E., L. L. Newkirk, and B. M. McCormac, North polar, south polar, world maps and tables of invariant magnetic coordinates for six altitudes 0, 100, 300, 600, 1000, and 3000 km, *DASA 2347*, Lockheed Palo Alto Res. Lab., Palo Alto, Calif., 1969.

Frank, L. A., Plasma in the earth's polar magnetosphere, *J. Geophys. Res.*, *76*, 5202, 1971.

Frank, L. A., and K. L. Ackerson, Observations of charged particle precipitation into the auroral zone, *J. Geophys. Res.*, *76*, 3612, 1971.

Heikkila, W. J., and J. D. Winningham, Penetration of magnetosheath plasma to low altitudes through the dayside magnetospheric cusps, *J. Geophys. Res.*, *76*, 883, 1971.

Heikkila, W. J., J. B. Smith, J. Tarstrup, and J. D. Winningham, The soft particle spectrometer in the Isis I satellite, *Rev. Sci. Instrum.*, *41*, 1393, 1970.

Heppner, J. P., M. Sugiura, T. L. Skillman, B. G. Ledley, and M. Campbell, Ogo-A magnetic field observations, *J. Geophys. Res.*, *72*, 5417, 1967.

Holzer, T. E., and G. C. Reid, The response of the dayside magnetosphere-ionosphere system to time-varying field line reconnection at the magnetopause, 1, Theoretical model, *J. Geophys. Res.*, *80*, 2041, 1975.

Jeffries, R. A., W. H. Roach, E. W. Hones, Jr., E. M. Wescott, H. C. Stenbaek-Nielsen, T. N. Davis, and J. D. Winningham, Two barium plasma injections into the northern magnetospheric cleft, *Geophys. Res. Lett.*, *2*, 285, 1975.

Kamide, Y., J. L. Burch, J. D. Winningham, and S.-I. Akasofu, Dependence of the latitude of the cleft on the interplanetary magnetic field and substorm activity, *J. Geophys. Res.*, *81*, 698, 1976.

Knudsen, W. C., Magnetospheric convection and the high-latitude F_2 ionosphere, *J. Geophys. Res.*, *79*, 1046, 1974.

Pike, C. P., A latitudinal survey of the daytime polar *F* layer, *J. Geophys. Res.*, *76*, 7745, 1971.

Pike, C. P., Equatorward shift of the polar *F* layer irregularity zone as a function of the *Kp* index, *J. Geophys. Res.*, *77*, 6911, 1972.

Pike, C. P., and J. A. Whalen, Satellite observations of auroral substorms, *J. Geophys. Res.*, *79*, 985, 1974.

Pike, C. P., C.-I. Meng, S.-I. Akasofu, and J. A. Whalen, Observed correlations between interplanetary magnetic field variations and the dynamics of the auroral oval and the high-latitude ionosphere, *J. Geophys. Res.*, *79*, 5129, 1974.

Russell, C. T., C. R. Chappell, M. D. Montgomery, M. Neugebauer, and F. L. Scarf, Ogo 5 observations of the polar cusp on November 1, 1968, *J. Geophys. Res.*, *76*, 6743, 1971.

Shepherd, G. G., J. F. Pieau, F. Creutzberg, A. G. McNamara, J. C. Gerard, D. J. McEwen, B. Delana, and J. H. Whitteker, Rocket and ground-based measurements of the dayside magnetospheric cleft from Cape Parry, N.W.T., *Geophys. Res. Lett.*, *3*, 69, 1976.

Ungstrup, E., A. Bahnsen, J. K. Olesen, F. Primdahl, F. Spangslev, W. J. Heikkila, D. M. Klumpar, J. D. Winningham, U. Fahleson, C.-G. Falthammar, and A. Pedersen, Rocket-borne particle, field, and plasma observations in the cleft region, *Geophys. Res. Lett.*, *2*, 345, 1975.

Vasyliunas, V. M., Magnetospheric cleft symposium, *Eos Trans. AGU*, *55*, 60, 1974.

Vorobjev, V. G., G. Gustafsson, G. V. Starkov, Y. I. Feldstein, and N. F. Shevnina, *Planet. Space Sci.*, *23*, 269, 1975.

Whalen, J. A., and C. P. Pike, *F* layer and 6300-Å measurements in the day sector of the noon oval, *J. Geophys. Res.*, *78*, 3848, 1973.

Winningham, J. D., Penetration of magnetosheath plasma to low altitudes through the dayside magnetospheric cusps, Ph.D. dissertation, Tex. A&M Univ., College Station, 1970.

Winningham, J. D., Characteristics of magnetosheath plasma observed at low altitudes in the dayside magnetospheric cusps, in *Earth's Magnetospheric Processes*, edited by B. M. McCormac, p. 68, D. Reidel, Dordrecht, Netherlands, 1972.

Winningham, J. D., and C. P. Pike, In situ observations of the effects of magnetosheath particle precipitation on the dayside ionosphere (abstract), *Eos Trans. AGU*, *53*, 361, 1972.

(Received April 15, 1976;
accepted September 8, 1976.)

VIII. Papers in Press

Energetic Particle Precipitation into the High Latitude Ionosphere and the Auroral Electrojets

1. Definition of Electrojet Boundaries Using Energetic Electron Spectra and Ground-based Magnetometer Data

by

J. D. Winningham

and

Koji Kawasaki and Gordon Rostoker

Abstract

Data from the University of Alberta meridian line of magnetometers are utilized to define the poleward and equatorward borders of the eastward electrojet in the evening sector. Soft particle spectrometer data from the ISIS-2 polar orbiting satellite are organized in the framework of the eastward electrojet for cases where the satellite orbital path took it close to the meridian line of ground-based magnetometer stations. It is shown that in the late evening hours the equatorward border of the eastward electrojet coincides with the equatorward edge of the central plasma sheet (cps) as marked by electrons of $E > 1$ keV. The boundary plasma sheet (bps) spans the poleward portion of the eastward electrojet and a region up to a few degrees poleward of the eastward electrojet where the westward electrojet is known to penetrate on average. A level shift in the Y'-component of the ground magnetometer data exists across the portion of the electrojet region marked by bps; this level shift is interpreted as net

upward field-aligned current flow. In the hours between noon and dusk the correlation between the equatorward border of the eastward electrojet and the equatorward edge of the cps deteriorates completely and the magnetic latitude profiles exhibit anomalous behavior. This problem will be discussed in paper 2 of this series. On the basis of this study we conclude that in the evening sector the cps is threaded by field lines carrying current flowing into the ionosphere while the bps is threaded by field lines carrying current flowing out of the ionosphere. The electric field transition from the auroral oval to the polar cap must occur in the heart of the bps under average conditions.

Energetic Particle Precipitation into the High Latitude Ionosphere and the Auroral Electrojets

2. Eastward Electrojet and Field-Aligned Current Flow at the Dusk Meridian

Gordon Rostoker, J. D. Winningham, Koji Kawasaki,

J. R. Burrows and T. J. Hughes

Abstract

Soft particle spectrometer and energetic particle detector data from the ISIS-2 polar orbiting satellite are organized in the framework of the eastward electrojet flowing in the local time range around dusk. The structure of the ionospheric electrojets is inferred from ground based magnetic data using a meridian line of magnetometers through western Canada. Irregularities in latitude profiles of the magnetometer data near the dusk meridian indicate that there is a double structure within the current flow, with strong eastward current flow in the poleward portion of the electrojet. Precipitating energetic electron fluxes are found within this region of strong eastward current flow in the poleward portion of the electrojet. No significant energetic electron or proton fluxes are found in the

equatorward portion of the eastward electrojet. Using realistic models of the ionospheric and field aligned currents flowing in the evening sector, it is demonstrated that a portion of the eastward electrojet in the post-noon quadrant flows up the field lines into the magnetosphere at the dusk meridian. It is suggested that this segment of the eastward electrojet exists because of the presence of a poleward electric field in the sunlit ionosphere and that upward field-aligned current flow occurs at the conductivity discontinuity between the sunlit and dark ionospheres.

IX. Oral Presentations at Meetings

1. Comparison of Backscattered Electrons with a Parallel Electric Field Model, T. W. Speiser, D. S. Evans, and J. D. Winningham, presented at International Symposium on Solar-Terrestrial Physics, Boulder, Colorado, June, 1976.
2. Entry of Solar Wind Plasma into the Magnetotail, E. W. Hones, Jr., and J. D. Winningham, presented at the Second Magnetospheric Cleft Conference, St. Jovite, Quebec, October, 1976.
3. Rocket Measurements of the Dayside Cleft Plasma, J. D. Winningham, presented at the Second Magnetospheric Cleft Conference, St. Jovite, Quebec, October, 1976.
4. Substorm Probability as Functions of Interplanetary Magnetic Field and the Size of the Auroral Oval, Y. Kamide, P. D. Perreault, and J. D. Winningham, AGU Meeting, Spring 1977.
5. Field-Aligned Current Flow Near the Dusk Meridian Associated with the Eastward Auroral Electrojet, K. Kawasaki, J. D. Winningham, J. R. Burrows, G. Rostoker, and J. Kisabeth, IAGA, Seattle, August, 1977.
6. Definition of Electrojet Borders and Field-Aligned Currents Using Energetic Electron Spectra, J. D. Winningham, K. Kawasaki, and G. Rostoker, IAGA, Seattle, August, 1977.
7. Empirical Dependence of 6300A Emission Rate on Electron Energy and Energy Flux in Aurora, G. G. Shepherd, J. D. Winningham, L. E. Bunn, and F. W. Thirkettle, IAGA, Seattle, August, 1977.
8. The Relationship of Particle Precipitation to Auroral Forms, J. L. Burch and J. D. Winningham, IAGA, Seattle, August, 1977.

9. Electron Density and Temperature Measurements in an Artificial Ionospheric Hole: Project Lagopedo, J. D. Winningham and N. Eaker, A.G.U. Meeting, Spring, 1978.

10. Electron Angular Distributions During an Auroral Break-up, D. M. Klumpar, W. E. Sharp, and J. D. Winningham, A.G.U. Meeting, Spring, 1978.

11. Corpuscular Fluxes at Midlatitudes, An Examination of the Storm Period 1 November 1972, Fred A. Morse, J. D. Winningham, and J. R. Burrows, A.G.U. Meeting, Spring, 1978.

12. Electrons in the Earth's Magnetosphere, J. D. Winningham, Fifth European Geophysical Society Meeting, Strasbourg, France, August, 1978.

13. Electrons in the Earth's Magnetosphere, J. D. Winningham, AGU Chapman Conference, Magnetospheric Substorms and Related Plasma Processes, Los Alamos, New Mexico, October, 1978.

X. REFERENCES

Anger, C. D., T. Fancott, J. McNally, and H. S. Kerr, ISIS-2 scanning auroral photometer, Appl. Opt., 12, 1753, 1973.

Arnoldy, R. L., and P. B. Lewis, Correlation of ground-based and topside photometric observations with auroral electron spectra measurements at rocket altitudes, J. Geophys. Res., 82, 5563, 1977.

Banks, P. M., C. R. Chappell and A. F. Nagy, A new model for the interaction of auroral electrons with the atmosphere: spectral degradation, backscatter, optical emission and ionization, J. Geophys. Res. 79, 1459, 1974.

Bunn, F. E., PhD. Thesis, York University, 1974.

Deans, A. J. and G. G. Shepherd, Rocket measurements of oxygen and nitrogen emissions in the aurora, Planet. Space Sci. 26, 319, 1978.

Donahue, T. M., T. Parkinson, E. C. Zipf, J. Doering, W. G. Fastie and R. E. Miller, Excitation of the auroral green line by dissociative recombination of the oxygen molecular ion: Analysis of two rocket experiments, Planet. Space Sci. 16, 737, 1968.

Hays, P. B. and C. D. Anger, The influence of ground scattering on satellite auroral observations, Appl. Opt. 17, 1898, 1978.

Heikkila, W. J., J. B. Smith, J. Tarstrup, and J. D. Winningham, The soft particle spectrometer in the ISIS-1 satellite, Rev. Sci. Instrum., 41, 1393, 1970.

Mantas, G. P. and J. C. G. Walter, The penetration of soft electrons into the ionosphere, Planet. Space Sci. 24, 409, 1976.

McEwen, D. J. and D. A. Bryant, Optical-particle characteristics of pulsating aurora, J. Atmos. Terr. Phys. 40, 871, 1978.

Rees, M. H. and D. Luckey, Auroral electron energy spectra derived from ratio of spectroscopic emissions, 1. Model computations, J. Geophys. Res. 79, 5181, 1974.

Rees, M. H., A. I. Stewart, W. E. Sharp, P. B. Hays, R. A. Hoffman, L. H. Brace, J. P. Doering, and W. K. Peterson, Coordinated rocket and satellite measurements of an auroral event, 1. Satellite observations and analysis, J. Geophys. Res. 82, 2250, 1977.

Rusch, D. W., J.-C. Gerard, and W. E. Sharp, The reaction of $N(^2D)$ with O_2 as a source of $O(^1D)$ atoms in aurorae, Geophys. Res. Lett., 1979.

Sharp, W. E., M. H. Rees, and A. I. Stewart, Coordinated rocket and satellite measurements of an auroral event: 2. The rocket observations and analysis, J. Geophys. Res. 1979.

Shepherd. G. G., T. Fancott, J. McNally, and H. S. Kerr, ISIS-2 atomic oxygen red line photometer, Appl. Opt. 12, 1767, 1973a.

Shepherd, G. G., C. D. Anger, L. H. Brace, J. R. Burrows, W. J. Heikkila, J. Hoffman, E. J. Maier, and J. H. Whitteker, An observations of polar aurora and airglow from the ISIS-2 spacecraft, Planet. Space Sci. 21, 819, 1973b.

Shepherd, G. G., J. F. Pieau, T. Ogawa, T. Tohmatsu, K. Oyama, and Y. Watanabe, Direct measurement of conjugate photoelectrons and predawn 630 nm airglow, Plant. Space Sci. 26, 211, 1978.

Shepherd, M. M. and R. H. Eather, On the determination of auroral electron energies and fluxes from optical spectral measurements, J. Geophys. Res. 81, 1407, 1976.

Sivjee, G. G. and D. J. McEwen, Rocket observations of the interaction of auroral electrons with the atmosphere, Planet. Space Sci. 24, 131, 1976.

Solheim, B. H. and E. J. Llewellyn, An indirect mechanism for the production of $O(^1S)$ in the aurora, Planet. Space Sci., accepted for publication, 1979.

Yau, A. W. and G. G. Shepherd, Energy transfer from excited N_2 and O_2 as a source of $O(^1S)$ in the aurora, accepted for publication, Planet. Space Sci., 1979.

PERSONNEL

A list of scientists, engineers, technicians, and programmers who contributed to the work reported is given below:

J. David Winningham, Research Scientist
Principal Investigator

Walter J. Heikkila, Professor of Physics
Co-Investigator

Gordon G. Shepherd, Professor of Physics
York University, Toronto

Nick Eaker, Research Scientist Associate

Charley R. Thompson, Technical Staff Assistant

Jack R. Frazier, Jr., Technical Staff Assistant

Louis B. Wadel, Senior Programmer

Frank Thirkettle, Senior Programmer